Astronomy Unit

School of School of Physics and Astronomy

Queen Mary University of London

Collisional Features in Saturn's F Ring

Nicholas Oliver Attree

Supervised by C.D Murray

Submitted in part fulfilment of the requirements for the degree of
Doctor of Philosophy in School of Physics and Astronomy of the University of
London

1

Declaration

I, Nicholas Attree, confirm that the research included within this thesis is my own work or that where it has been carried out in collaboration with, or supported by others, that this is duly acknowledged below and my contribution indicated. Previously published material is also acknowledged below.

I attest that I have exercised reasonable care to ensure that the work is original, and does not to the best of my knowledge break any UK law, infringe any third party's copyright or other Intellectual Property Right, or contain any confidential material. I accept that the College has the right to use plagiarism detection software to check the electronic version of the thesis.

I confirm that this thesis has not been previously submitted for the award of a degree by this or any other university.

The copyright of this thesis rests with the author and no quotation from it or information derived from it may be published without the prior written consent of the author.

Signature:

Date:

Details of collaboration and publications: Material from Chapter 4 has been previously published as a letter to the *Astrophysical Journal* (Attree et al., 2012), which I wrote and performed the analysis for.

Material in Chapter 5 has been previously published as an article in the journal *Icarus* (Attree et al., 2014), which I wrote and performed the analysis for.

Material in Chapter 8 was published in the journal *Icarus* (Murray et al., 2014), for which I was a coauthor and contributed to discussions.

<div align="right">Nicholas Oliver Attree</div>

Abstract

The role of physical collisions in shaping Saturn's F ring is explored using a mixture of dynamical theory, image analysis and computer simulations. The F ring is highly dynamic, being perturbed by the nearby moons, Prometheus and Pandora, and by a population of small bodies, whose presence is inferred by their influence on the ring, charged particle data and, occasionally, direct detection.

Small-scale features, termed 'mini-jets', are catalogued from images taken by the Imaging Science Subsystem of the Cassini spacecraft. More than 1000 are recorded, implying a population of ~ 100 objects on nearby orbits, colliding with the ring at velocities of a few $\mathrm{m\,s^{-1}}$. Many are seen to collide several times, forming repeated structures, and must have enough physical strength, or self-gravity, to survive multiple passages through the core.

Larger features, called 'jets', share a similar morphology. They are likely caused by a more distant population which collide at higher velocities (~ 10 $\mathrm{m\,s^{-1}}$) and are roughly an order of magnitude less common. Differential orbital motion causes jets to shear out over time, giving the ring its multi-stranded appearance. Jets have different orbital properties to mini-jets, probably because they result from multiple, overlapping collisions.

Simulations using an N-body code show that the shape of collisional features depends heavily on the coefficient of restitution, particularly the tangential component. When both components are < 1 large objects merely sweep up small particles. Features like jets and mini-jets require large particles in both the target and impactor, as is the case for two similarly-sized aggregates colliding.

A single population of aggregates is proposed, ranging from large, unconsolidated clumps, embedded in the core, through mini-jet-forming objects to the more distant, jet-forming colliders. Prometheus may be ultimately responsible for all of these features as its gravity can trigger clump formation as well as perturb particles.

Acknowledgements

First and foremost I would like to thank my supervisor, Carl Murray, whose expertise and knowledge helped guide me through this project. Without him this thesis would, of course, not have been possible.

I would also like to thank my officemates and co-workers at Queen Mary University of London for many useful discussions and helpful pieces of advice. In particular, I would like to thank my coauthors on the publications that have come out of this research: Nick Cooper and Gareth Williams.

Finally, I would like to thank my friends and family for their continued support and encouragement, particularly my mother and father (Caroline and Mike) and also my partner Charlotte.

Contents

List of Figures

List of Tables

1. Introduction

1.1. Background

Planetary rings provide a useful testing ground for Newton's theories of gravity and motion as well as providing us with local examples of an astrophysical disk, analogous to those from which planetary systems form. Saturn's extensive ring system is the most famous example but all the giant planets, and now several small bodies, are known to have rings. This thesis will focus on a particular ring in the Saturn system, designated the F ring, which has a range of interesting properties.

Located at a distance of about 2.33 planetary radii from Saturn's centre, the F ring is a narrow, dusty ring containing a variety of dynamic structures. Discovered by Pioneer 11 in 1978 (Fig. 1.1) it lies between the E and A rings, separated from the latter by the 3400 km Roche Division (Gehrels et al., 1980). This location, near Saturn's Roche limit for ice, places it between the competing regimes of tidal disruption and gravitational accretion. Two nearby moons, Prometheus and Pandora, further complicate the ring's dynamics by gravitationally perturbing its constituent particles, creating the so-called streamer-channel phenomenon (Murray et al., 2005; Beurle et al., 2010). In addition, the F ring region is home to a population of small bodies, the first evidence for which was again found by the Pioneer spacecraft (Cuzzi and Burns, 1988). Subsequent observations by Voyagers 1 and 2, in 1980 and 1981, respectively (Smith et al., 1981, 1982), and from Earth (McGhee et al., 2001) showed the gravitational and collisional influence of these bodies on the ring and, in some cases, the objects themselves.

The arrival of the Cassini spacecraft, in July 2004, provided unprecedented spatial and temporal coverage. Observations by Cassini's Imaging Science Subsystem (ISS, see Fig. 1.2 for an example image) reveal the ring to be even more complex and dynamic than previously thought, with changes occurring over timescales from hours to years (Porco et al., 2005; French et al., 2012). Jets of material are seen extending several hundred kilometres either side of the ring and are thought to be caused by collisions with small, local objects (Charnoz et al., 2005; Murray et al., 2008).
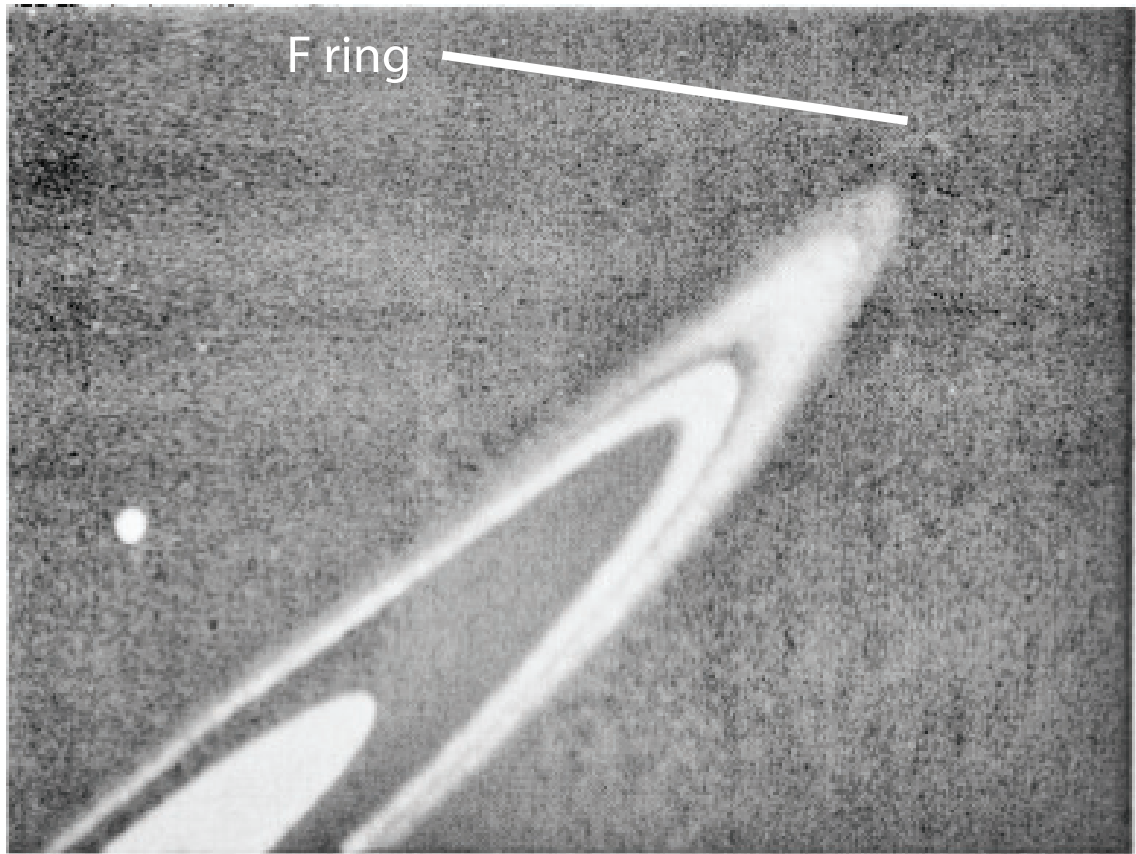
Figure 1.1.: Discovery image of the F ring taken by the imaging photomultiplier onboard Pioneer 11 on September 1st, 1979 (from Gehrels et al., 1980). The F ring is just visible at the ansa, outside the edge of the A ring. The moon at lower left is Janus. Range to the ring is estimated at 943,000 km and the phase angle 8.6°. Contrast has been enhanced to aid visibility.

Differential orbital motion shears out these jets and gives the ring its multi-stranded appearance. Smaller features, with a range of morphologies and unknown origins, are also seen protruding from the ring. Some examples of these are shown in Fig. 1.3. Moonlets and dense clumps have also been detected when they occult background stars, as seen by Cassini's other instruments (Meinke et al., 2012; Hedman et al., 2011b). Finally, Cassini has provided evidence for ongoing renewal of the F ring by the aggregation and accretion of new bodies (Beurle et al., 2010).

All these lines of evidence point to a dynamic environment shaped by a variety of nearby objects: Prometheus, Pandora and the mostly unseen small bodies. Interactions occur between them and the F ring core, both gravitationally and by physical collisions. Studying the F ring can therefore put constraints on the properties of this local population as well as improve our understanding, in general, of interactions between rings and moons as well as of embedded objects within astrophysical disks.

1.2. Scientific Goals

The F ring is clearly a dynamic environment shaped by interactions between small particles and larger moonlets and clumps. Cassini images provide excellent coverage and resolution, allowing features relating to these interactions to be tracked and surveyed. The rest of this thesis will explore, in detail, the specific interaction mechanism of physical collisions.

Chapter 2 gives a more detailed overview of the F ring, describing its morphology and structure, particle size distribution, orbit and stability over time.

Following on from this, Chapter 3 outlines the dynamics needed to understand and interpret the results in the rest of the thesis. This includes discussions of the relative motions between two small bodies orbiting a larger one, the effects of a small perturbing force on such motions and the dynamics of physical collisions. Laboratory experiments and computer simulations of such collisions are then reviewed.

Chapter 4 briefly describes the Imaging Science Subsystem of the Cassini spacecraft and the process of acquiring, and making measurements from, images of the F ring. Observations of a particularly interesting F ring feature, termed a mini-jet, are then presented. The feature is seen for over half an orbital period and its evolution, formation mechanism and implications for the local object population are discussed.

A survey of similar features, found in Cassini images, is presented in Chapter 5. Their distribution in space and time, proximity to other ring features and morphology are all analysed in an effort to understand the object population. A number of
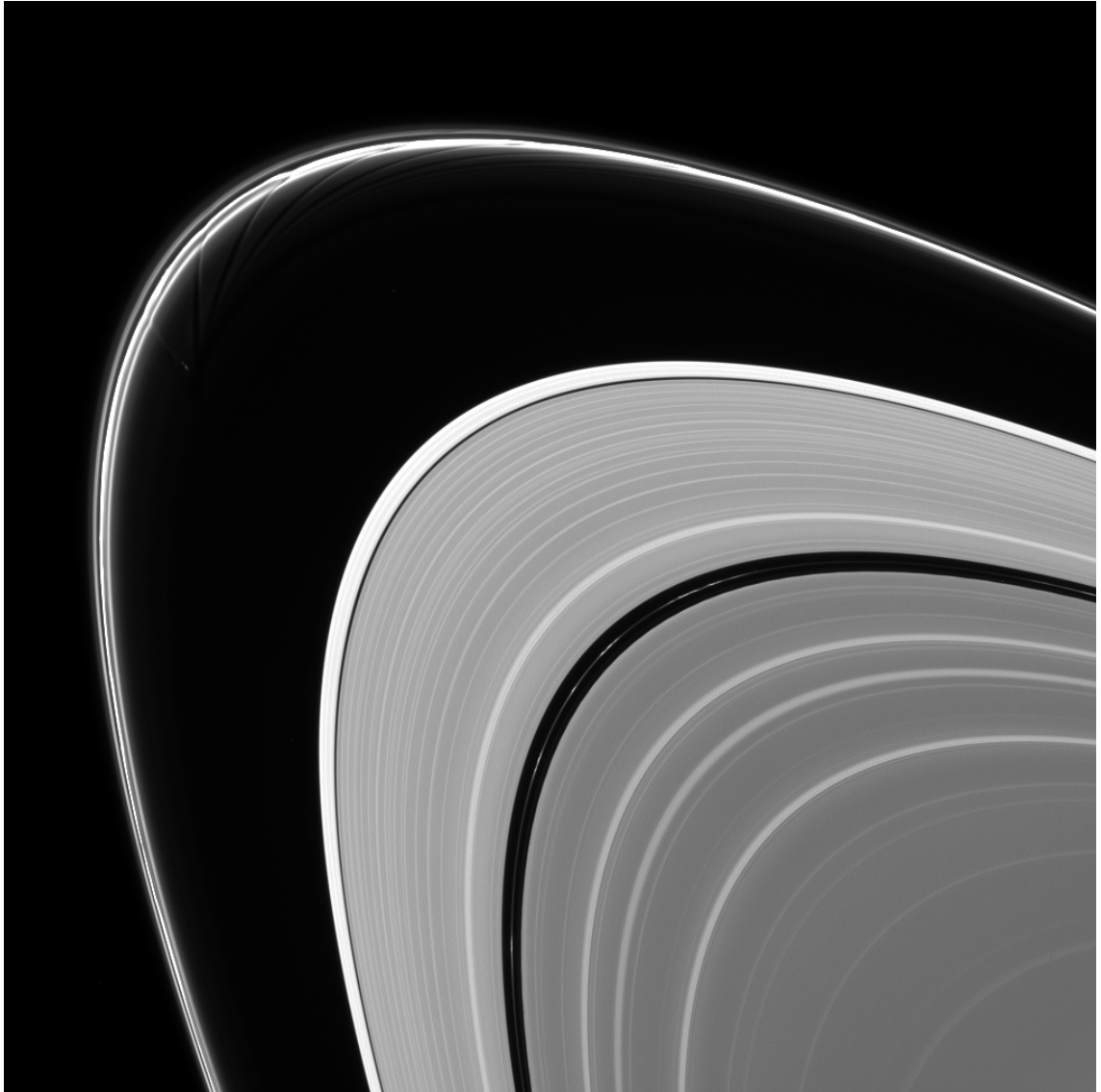
Figure 1.2.: Cassini ISS image number N1770770563 of the F ring, taken on February 11th, 2014 at a distance of 2.1 million kilometres from Saturn. Streamer-channels, caused by Prometheus (just inside the F ring) are visible near the ansa, as well as the Roche division, A ring edge, Keeler and Enke gaps. Contrast has been enhanced to aid visibility.
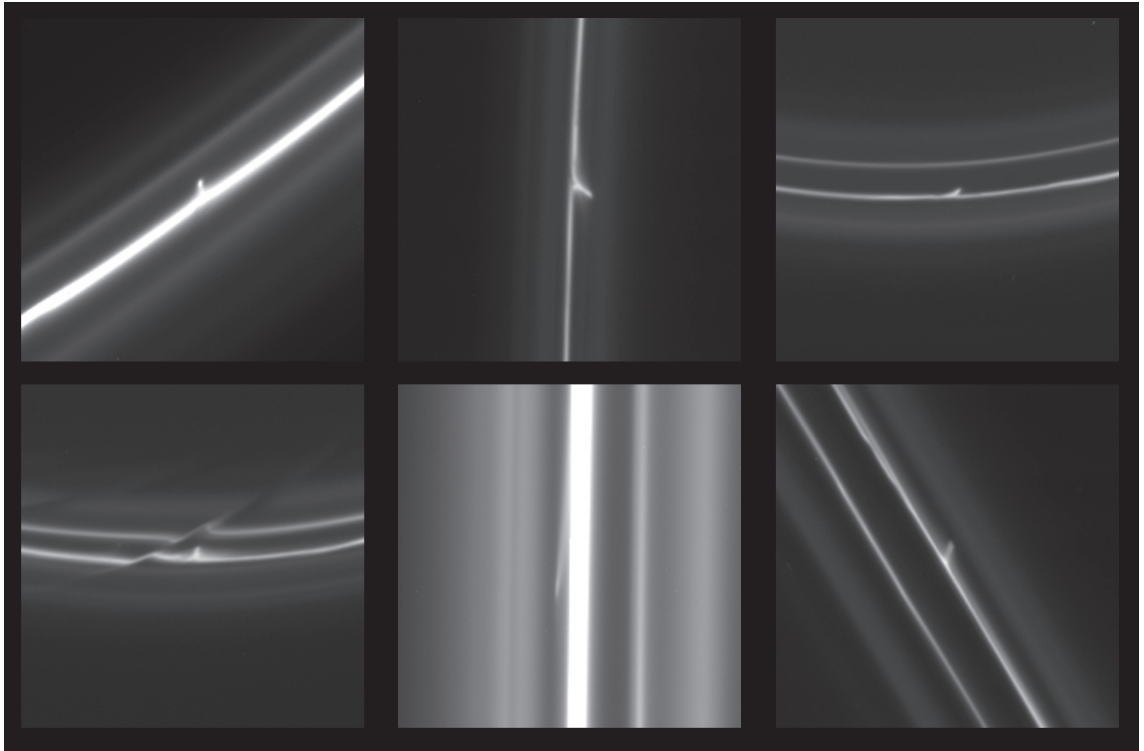
Figure 1.3.: Examples of small F ring features seen in Cassini ISS images. The image numbers and dates are from left, top: N1501710723 (Aug. 2, 2005), N1542050711 (Nov. 12, 2006), N1578411831 (Jan. 7, 2008), bottom: N1578427113 (Jan. 7, 2008), N1589117591 (May 10, 2008), N1597907705 (Aug. 20, 2008). The corresponding approximate lengths are 29, 136, 155, 43, 129 and 32 km. Previously published in Attree et al. (2012).

interesting case studies are examined in detail.

In Chapter 6 the larger jet features are surveyed using a subset of mosaics created from Cassini observations. Their distribution and morphology are compared to the smaller mini-jets and a number of features are tracked over time to see how they evolve.

Computer simulations of both jet and mini-jet forming collisions are presented in Chapter 7. These are performed using the REBOUND N-body code and results are compared to the predictions of theory (Chapter 3). Implications for the physical properties of the impactors are then discussed.

Chapter 8 presents a summary and conclusions. Other locations in the solar system where similar collisional processes may be occurring, and potential future work, are also briefly discussed.

2. Properties of Saturn's F ring

This chapter gives a more detailed overview of the properties of the F ring, including observations from space and the Earth. In Section 2.1 the overall morphology and structure of the ring are reviewed. In Section 2.2 the size distribution of its constituent particles and photometry are discussed. In 2.3 the focus is on the orbit, stability and short- and long-term evolution of the ring.

2.1. Morphology and Structure

The first image of the F ring, taken by Pioneer 11's imaging photomultiplier (Gehrels et al., 1980), immediately revealed its irregular nature. Imaging by Voyagers I and 2 and then by Cassini confirmed it to have several narrow components with clumpy, irregular structure embedded within a ~ 700 km wide dust envelope (Smith et al., 1981, 1982; Porco et al., 2005). These narrow components were described as braided in appearance, $20 - 50$ km in width and dynamic, varying between the fly-bys of Voyager I in November 1980, Voyager 2 in October 1981 and the arrival of Cassini in 2004. The most persistent, and typically brightest, of these narrow components is identified as the F ring core.

Some of the structure described by the early imaging results can now be explained in terms of the following types of feature, most of which are unique to the F ring.

Streamer-Channels

As the closest moon to the F ring Prometheus was long suspected of being associated with its braided, multi-stranded appearance. Early models were hampered by uncertainties in the orbits and structure of the ring and there was confusion as to whether or not Prometheus physically entered the core (see for example Murray and Giuliatti Winter, 1996). With a better understanding of the F ring structure from Voyager imagery it became apparent that Prometheus's orbit carried it into the extended envelope and inner strands but not the core itself (Murray et al., 2005 and references therein). Images from the Cassini ISS provided much better reso-
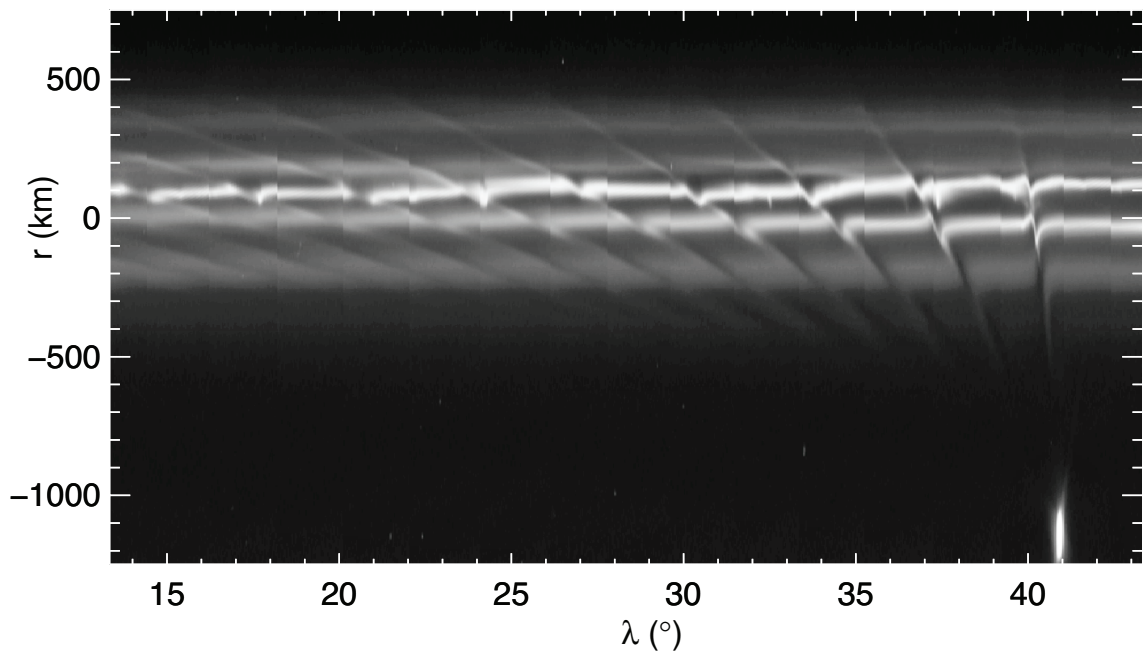
Figure 2.1.: Mosaic of Cassini ISS images showing streamer-channels induced in the F ring core and strands by Prometheus. The images are re-projected into a radius/longitude frame, relative to a model of the F ring's orbit, so that the core appears as a bright horizontal line (see Chapter 4 for details). Prometheus is visible in the lower right, distorted because of the aspect ratio. Images are from the ISS_055RI_LPMRDFMOV001_PRIME sequence, taken January 7th, 2008.

lution and coverage and showed 'streamers' of material extending from the F ring towards the moon (Porco et al., 2005). The process was then finally understood by a combination of analysis of images re-projected into a radius, longitude frame (see Fig. 2.1) and numerical modelling (Murray et al., 2005 and references therein).

Prometheus's eccentricity means it periodically approaches the core, perturbing a section of ring before receding away. The minimum radial distance, and hence magnitude of this perturbation, is modulated on decade-long timescales by the precession of the periapse longitudes of Prometheus and the F ring. This minimum separation varies between $\sim 200 - 800$ km (Murray et al., 2005). A close approach happens once every Prometheus orbit (14.7 hours) but the difference in orbital speeds means that a distinct section of ring is perturbed each time, separated by $3\pi\Delta a \approx 3.3°$. Here Δa is the difference in semi-major axis between Prometheus and the F ring (using the Cooper et al. (2013) orbit from Table 2.1 and the latest JPL ephemeris, see Section 4.1). A periodic structure at this wavelength is readily detectable in images and photometry. Every 3.3° material is perturbed onto differing orbits (forming a streamer pointing towards the moon), removing it from a roughly radial section of ring (leaving a dark channel). The channel subsequently shears out, due to the gradient in orbital velocities across it, in a process known as 'Keplerian shear' while the streamer becomes more or less visible with orbital phase because of its eccentricity. The result is a series of sheared streamers or channels separated by 3.3° and all pointing towards the guiding centre of Prometheus's orbit, as can be seen in Fig. 2.1. The whole streamer-channel structure moves along the ring with Prometheus, taking 67.56 days (the synodic period) to complete one cycle and return to the same longitude. Pandora produces a similar effect but, with its lower mass and greater semi-major axis separation, it is much more difficult to detect.

Beurle et al. (2010) modelled the streamer-channel mechanism in greater detail with numerical integrations. These show how the induced kick in semi-major axis given to the F ring particles changes with relative longitude to Prometheus. Those particles located just upstream from Prometheus (greater longitude) have their semi-major axis decreased while those just downstream have their semi-major axis increased. The largest changes are felt by particles within $\pm 0.5°$ of closest approach (see their figure 4). The particles also receive corresponding changes to their eccentricity and longitudes of pericentre, and the combination of these lead to channels which open and close over an orbit. The magnitude of the eccentricity kick is equal to the fractional change in semi-major axis for all the particles, meaning they return to their original orbital radius at some point in their orbits. The magnitude of this kick is dependent on the orbital configuration with maximum values occurring when
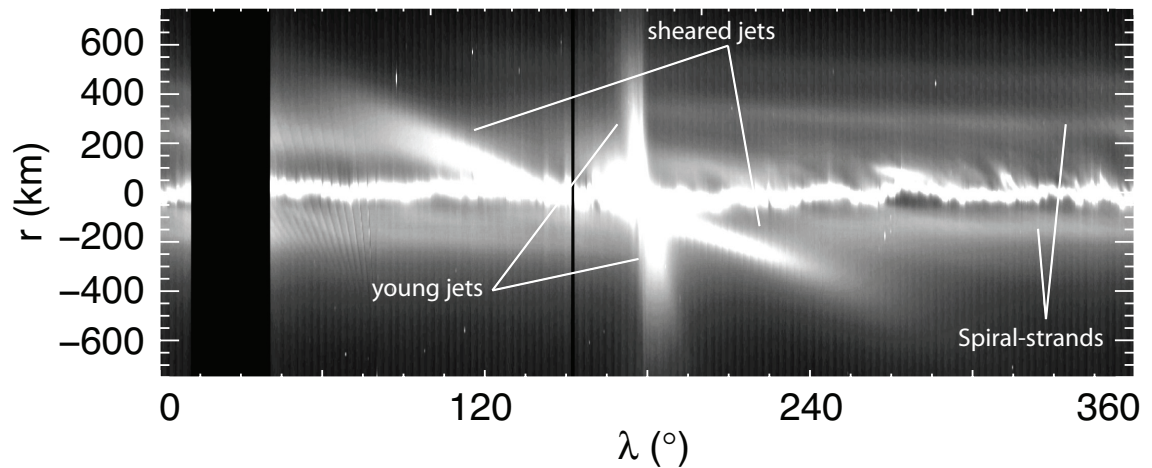
Figure 2.2.: Mosaic of re-projected Cassini images showing jets of material emanating from the F ring core and shearing to spiral/strands. Contrast has been enhanced to aid visibility.

Prometheus's apocentre is aligned with the F ring's pericentre (leading to the closest radial separation). At this anti-alignment, reached in late 2009, the maximum kick given to particles is ±19 km in semi-major axis, $\pm1.3 \times 10^{-5}$ in eccentricity and $\pm4°$ in longitude of periapse (Murray et al., 2008), respectively.

Finally Beurle et al. (2010) found that particle concentration at the edges of the channels was actually enhanced and that times of highest density corresponded to minima in particle dispersion velocities. This supports the idea of Prometheus triggering aggregation of material and possibly leading to the formation of clumps and objects. This, and the effects of Prometheus and Pandora on the global stability of the ring, are discussed further in the next section.

Jets, Spirals and Strands

With the full 360° coverage provided by ISS observations the strands lying on either side of the core (which were at first thought to be separate ringlets) were discovered to be connected to it in the form of a 'kinematic spiral' (Charnoz et al. (2005) and see Fig. 2.2). This results from a roughly radial displacement of material over a range of semi-major axes, followed by the naturally occurring Keplerian shear. The intersections of various strands with the core explains the appearance of braids. The question then became: what caused the initial displacement?

Charnoz et al. (2005) and Murray et al. (2008) quickly ruled out the gravitational perturbation of an undetected satellite, which would have to have the mass (and rough size) of Prometheus, as well as Prometheus itself, since it does not enter the

core. Physical collisions were then proposed with close agreement noted between the locations of the spiral intersection points, large 'jets' of material (Murray et al., 2008) and the core crossings of the newly discovered object S/2004 S 6 (Porco et al., 2005). This small object, referred to hereafter as S6, was noted to have an orbit which not only intersects the core's but extends to radial distances comparable to those of the jets and strands. Charnoz (2009) showed in analytical calculations that dissipative collisions at S6's $\sim 30\mathrm{ms}^{-1}$ relative velocity could easily spread material over several hundred kilometres in radius and confirmed this with numerical simulations. Murray et al. (2008) noted additional jets not associated with S6, suggesting further colliding objects. The collision model provides the best explanation for jets and strands but the details of the physical interaction are still not fully understood. Charnoz (2009) modelled two extreme scenarios, that of massless core particles and that of massless S6 particles, neither of which fully capture the collision physics. The process is understood in general but the details will be explored more in this thesis.

The formation of spiral-strands can then be summarised as the following (shown in Fig. 2.2): S6, or another nearby object, impacts the ring at tens of metres per second, spreading material over a range of semi-major axes. This bright jet of material then undergoes Keplerian shear, decreasing in brightness as it spreads around the ring. Eventually the shear takes it all the way around, through $> 360°$, and it appears almost parallel to the core as a strand. Meanwhile the object continues to intersect the ring, triggering a series of features along the length of the core which may overlap one another.

Extended Clumps

As well as the mostly radial disturbances of streamer-channels and jets the brightness of the F ring is found to vary with longitude along its core and strands. Both Voyager and Cassini show large longitudinal variations in brightness in addition to the 3.3° signal from Prometheus. The relatively low-resolution Voyager images revealed only the large-scale structure and 'clumps' (also called 'extended clumps') in this context describe features several degrees to tens of degrees in length ($1° \approx 2440$ km at the F ring). On the smaller scale the much higher-resolution Cassini ISS images show longitudinal variation down to kilometre levels. Some of these small, bright clumps are related to fans and kinks (see below) but many appear morphologically distinct and may represent individual objets or their dust envelopes. Occultation studies have also shown evidence for dense clumps and moonlets embedded in the core as discussed further in the next section.

In terms of the larger features, analysis of Voyager images showed two or three
large clumps, several times brighter than the ring average, as well as many smaller
features at any one time (Showalter, 1998, 2004). These were found by radially and
longitudinally averaging the observed ring brightness, reducing the 2D image to a
1D brightness/longitude profile. No large clumps were seen to survive in the nine
months between Voyagers 1 and 2 but most persisted for around 30 days during each
observing period. Those that could be tracked between profiles had a range of mean
motions, centred on that of the core but spread over ~ 100 km in semi-major axis.
Showalter (1998) found that several very bright clumps had high spreading rates,
dissipating quickly compared to the average, and called these 'burst' events. French
et al. (2014) applied the same brightness profiling method to ISS images, effectively
'downscaling' Cassini data to aid comparison with Voyager, and found similar num-
bers of the smaller extended clumps (a few degrees) with a similar distribution in
mean motions and brightnesses. Very bright clumps were much rarer however with
only two being detected in six years of Cassini data. French et al. (2014) also found
several fast spreading clumps and noted that the longitude of their clumps showed
no relation to that of Prometheus.

Showalter (1998, 2004) suggested that extended brightness features, especially
the burst events, were caused by dust released by interplanetary meteoroid impacts.
Showalter (1998) noted that the material in a typical $\sim 5°$ clump could come from
the complete disruption of a body just ~ 12 m in radius or a 10 cm regolith layer
on one ~ 80 m in radius and that ejection velocities from hypervelocity impacts are
quite capable of spreading material across ~ 100 km. Barbara and Esposito (2002)
instead argued for collisions with an embedded population, citing evidence from
other studies for such a population's existence and the non-detection of many smaller
brightness increases expected in the meteoroid model. Higher-resolution Cassini im-
ages did in-fact reveal many small features but also provided additional evidence for
a local population. Further, the discovery of S6 and the jet/spiral-strand formation
mechanism showed that nearby objects could indeed produce quickly spreading,
large magnitude brightness increases over several degrees of ring.

Extended clumps are now mostly viewed as having a local collisional origin (French
et al., 2014). Returning to the full 2D images they found several of their clumps
could be associated with jets, naturally explaining their spreading rates and mean
motions (the centre of brightness of a jet can easily move in longitude as it shears,
mimicking a detached clump with large relative semi-major axis). Nonetheless many
clumps cannot be tied directly to a particular jet or collision and some of their prop-
erties remain mysterious. They are mostly found 'fully formed' over a longitudinally
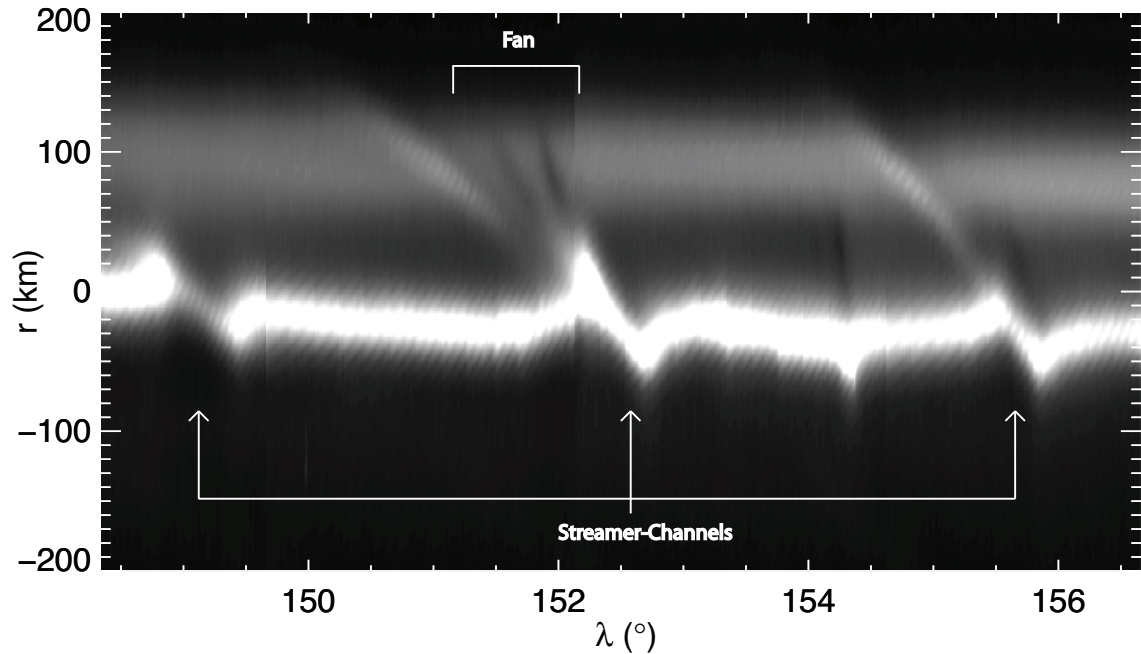
Figure 2.3.: Mosaic of re-projected Cassini images showing a fan. The association
with the left-hand side of a streamer-channel (three of which are visible
here) is clear. Images are from the ISS_039RF_FMOVIE001_VIMS se-
quence, taken February 27th, 2007. Contrast has been enhanced to aid
visibility.

extended region as opposed to spreading from a point source as might be expected
from a collision. Additionally the decrease in the number of large features may
imply a change in the population of colliding objects (French et al., 2014).

Fans and Kinks

Fans (Fig. 2.3) are a series of dark, sheared channels which intersect at a point in
the core (Murray et al., 2008). They are the result of the gravitational influence of
a small embedded object that has an eccentricity relative to the material around
it (making fans an extension of the 'propeller' features seen in the main rings by
Tiscareno et al., 2006). Numerical simulations (Williams, 2009) show how, on each
orbit, the embedded object undergoes a close encounter with a radial section of
material, scattering it away to leave a channel which subsequently undergoes Keple-
rian shear. The mechanism is very similar to the Prometheus perturbation, indeed
streamer-channels can be thought of as large fans caused by an object outside of
the ring. The Prometheus channels and those in fans open and close on orbital
timescales (due to the induced relative eccentricities) but at maximum extension

their width is found to be approximately ten times the scattering object's Hill radius (see Section 3.1 for an explanation of Hill spheres). Numerous fans have been spotted in Cassini images, implying objects ranging from ~ 7 to ~ 35 km in diameter embedded in the F ring core, assuming Prometheus-like densities (Murray et al., 2008). It is interesting to note that often only one side of the fan is seen, implying objects embedded at one edge of the core, and that fans are preferentially found on one side (left-hand) of the edge of streamer-channels (Beurle et al., 2010). The association between fans and streamer-channels further implicates Prometheus in the formation of the embedded objects, but the asymmetry is puzzling.

Kinks, where the linear structure of the core changes radial position over a small distance before gradually returning to its previous value, were noted by Porco et al. (2005). When seen at the opposite ring ansa (a separation in time of half an orbital period) they are mirrored in the radial direction, pointing inwards instead of outwards or *vice-versa*, implying particles with a relative eccentricity. When seen at 90° orbital phase, kinks can appear merely as a bright clump. Murray et al. (2008) explain kinks by the presence of embedded masses which, once perturbed by a Prometheus encounter, are slow to damp their eccentricity by collisions or self-gravity. They thereby maintain a small relative eccentricity, perturbing ring material as it shears past and exciting it to similar radial motions as themselves. Kinks are often relatively bright but the embedded objects must be too small, or the material too dynamically hot (Winter et al., 2007), to form fans.

Objects

In addition to the indirect detections of embedded objects from fans and kinks, and the presence of large extended clumps, individual objects much larger than an average ring particle have been found at the F ring. The first evidence came from the depletion of magnetospheric charged particles measured by Pioneer 11 and interpreted as the action of dust clouds released by inter-object collisions (Cuzzi and Burns, 1988). They proposed a population of 10,000 to 100 million 0.1–10 km moonlets spread over the whole 2000 km-wide region between Prometheus and Pandora. Such objects were not seen by Voyager but have been directly imaged by the Hubble Space Telescope (HST) in 1995/6. During this period Earth passed through the ring plane, as viewed from Saturn, providing an edge-on viewing geometry. McGhee et al. (2001) saw numerous ~ 10 km, extended objects spread across the whole region. However objects of this size or number have not been seen by either Voyager or Cassini to date. The most common interpretation is that the objects represent tem-

porary clumps, rather than permanent moonlets, raising the possibility of significant long-term changes in the ring.

Cassini has found several objects by direct imaging, including the aforementioned S6. This moonlet, as well as S/2004 S 3 and S/2004 S 4, orbit within a few hundred kilometres of the F ring, with S6 and S4 inside of it and S3 at greater semi-major axis (Porco et al., 2005). Assuming roughy spherical moonlets, image photometry suggests they are ~ 5 km across but all three may be temporary clumps. S6 has been recovered in images dating to at least 2007 but its current status, and those of the other two, are unknown. All three have orbits which are probably chaotic and most likely undergo collisions with the F ring core. Images of S6, meanwhile, reveal it to be composed of a chain of objects, rather than a single moonlet, and to have a large dust envelope. The presence of jets not linked to S6 suggests there may be more, as yet undiscovered, objects like these.

Near the core itself objects can be masked by surrounding dust and direct imaging is more difficult. Nonetheless their presence can be inferred by their gravitational influence and, at certain times, by the shadows they cast. Around equinox ISS images showed numerous bright features casting shadows up to several hundred kilometres in length onto surrounding material (Beurle et al., 2010), implying optically thick objects extending $\sim 5 - 10$ km from the ring plane. Shadow widths were ~ 70 km so the objects must be extremely azimuthally extended and quite large. As with the fan objects they most likely represent aggregate clumps with masses equivalent to $\sim 5 - 20$ km radius moonlets. Although they may be temporary structures many are seen to survive for at least one Prometheus synodic period (Beurle et al., 2010).

Stellar occultations, where the F ring passes between an observer and a background star, blocking some of the light, reveal objects embedded in the dust. Occultation measurements have been made by Voyager's photopolarimeter (PPS) as well as Cassini's Visual and Infrared Mapping Spectrometer (VIMS) and Ultraviolet Imaging Spectrograph (UVIS).

UVIS found 15 semi-transparent clumps and two opaque moonlets, with radial widths from tens of metres to a few kilometres (Esposito et al., 2008; Meinke et al., 2012). All but one fall within a few kilometres of the core with one of the moonlets found in an inner strand and one of the semi-opaque features confirmed by VIMS. These types of feature are probably temporary aggregates, with increasing optical depth corresponding to longer lifetimes, and may evolve into moonlets (Meinke et al., 2012). The two moonlets are noted to have 'skirts' of material, where the optical depth swiftly increased towards opaque, and these are interpreted at loose regolith layers of ~ 200 m and ~ 150 m thick. Various lines of evidence also point

to the objects being azimuthally extended, with azimuthal to radial length ratios of $\sim 1.7 - 10$. Meinke et al. (2012) find a power law distribution for the cumulative number of objects (moonlets and clumps) with size, suggesting around a thousand objects with radial widths greater than a kilometre and $\sim 30{,}000$ larger than 100 m. Opaque moonlets are about an order of magnitude less common. Finally, one UVIS occultation, in late 2008, showed periodic optical depth variations that Albers et al. (2012) interpret as the occultation track cutting across either a fan or propellor structure. The inferred object size is ~ 240 m, significantly smaller than the fan objects seen in imaging. The higher spatial resolution of occultations may be probing a smaller population.

Other Features

Despite recent successes in understanding streamer-channels, jets and strands the detailed structure of the F ring remains perplexing. Many features are visible in high-resolution Cassini images which do not fit neatly into one of the categories described above. Some are shown in Murray et al. (2008) figure 4 and include complicated loops and protrusions of core material and a possible narrow core component. Many are associated with bright objects, implying a dynamical link. With S6 now known to interact directly with ring material it is reasonable to suggest that physical collisions may play an important role in the formation of these structures and in shaping the ring itself.

A number of features have been seen which appear morphologically very similar to jets, but on scales that are much smaller (~ 50 km radial extent), as shown in Fig. 1.3. They are therefore termed mini-jets and are observed throughout the Cassini dataset. For example Fig. 2.4 shows one such feature, seen just after Cassini's Saturn orbit insertion manoeuvre. It takes the form of a ~ 140 km long jet extending about 54 km in radius from the bright F ring core. The tip of the feature is brighter than the rest and it also seems to be associated with a bright, kinked section of core. Interpreting the origin of mini-jets, such as this, has been difficult as they are usually only seen in perhaps 2–4 consecutive images. In this thesis a survey of such features is undertaken in order to catalogue their distribution and morphology with a view to explaining their origin.
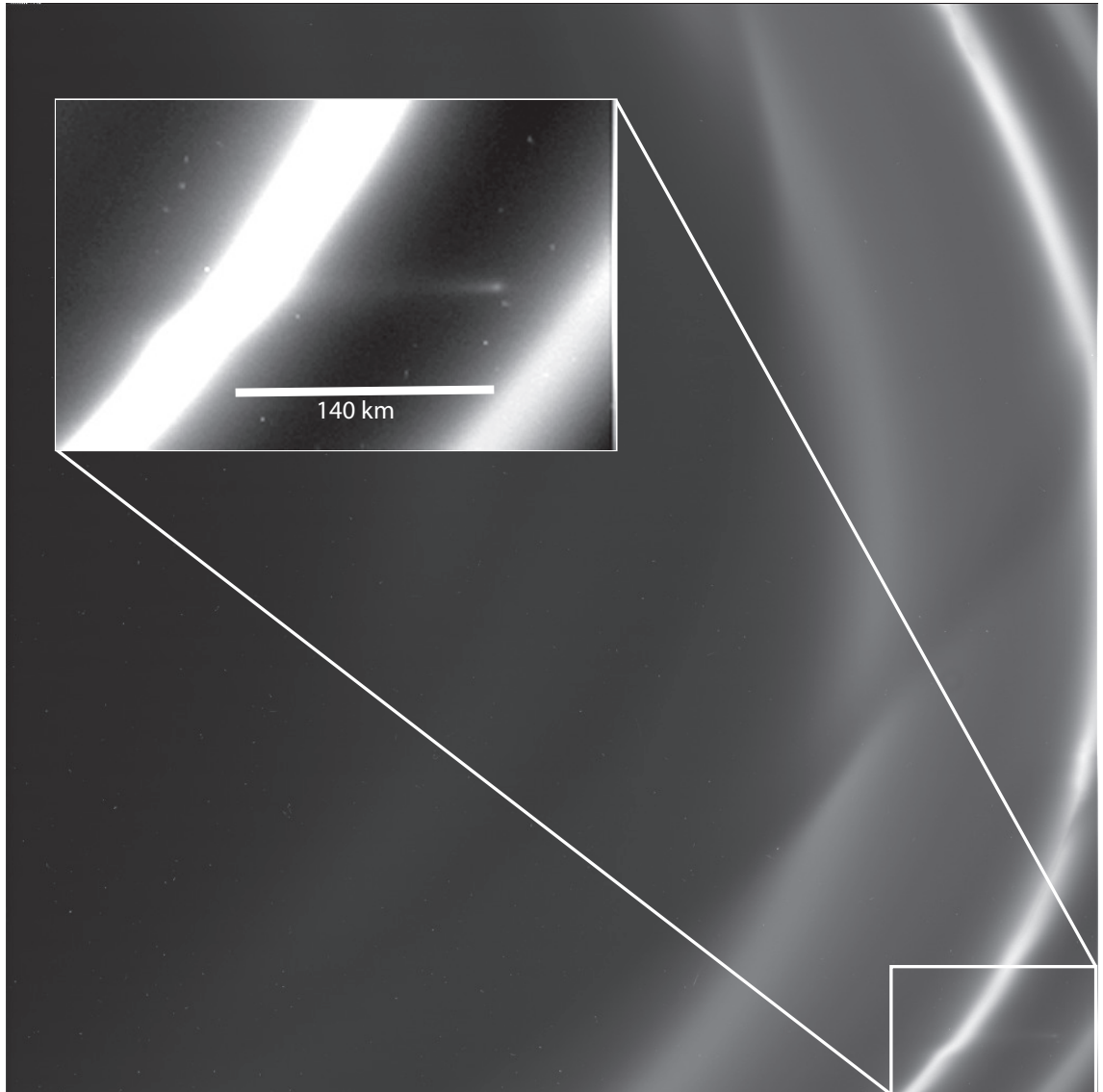
Figure 2.4.: Raw Cassini image N1467350502, taken at 04:57:27 on July 1st, 2004, just after Saturn orbit insertion, showing a 'mini-jet' feature. The inset shows a closeup with its contrast stretched to enhance visibility. Strands and a streamer-channel are also visible. Range to the ring is 116,613 km and image phase angle is 126°.

2.2. Photometry and Particle Sizes

Based on ISS photometry the core has a mean optical depth $\tau \approx 0.033$ but is highly variable and can appear optically thick in certain configurations (French et al., 2012). UVIS report a median optical depth from occultations of $\tau = 0.31$, varying between 0.05 and 3.45, and Voyager 2's PPS found a similar $\tau = 0.43$ (Albers et al., 2012). The full-width-at-half-maximum of the optical depth profile is also recorded and Albers et al. (2012) report core FWHM as 15 km for UVIS and 25 <FWHM< 45 km for VIMS. These are comparable with the visual appearance noted above and with estimates from HST photometry of 10 ± 4 km FWHM (Scharringhausen and Nicholson, 2013). Scharringhausen and Nicholson (2013) also model the vertical extent of the core and find it to have a similar FWHM in the vertical direction of 13 ± 7 km. Jets and strands have correspondingly smaller optical depths with Albers et al. (2012) finding them to be, on average, ~ 10 times wider and ~ 10 times dimmer than the core.

Evidence exists for a further component to the F ring system in addition to the core, strands and envelope: a narrow inner core. This is seen in both high-resolution imaging (Murray et al., 2008) and UVIS occultations (Albers et al., 2012; Meinke et al., 2012) as a ~ 1 km thick, discontinuous and high optical depth (occultation $\tau > 0.5$) feature. High-resolution images also show objects embedded within it (Murray et al., 2008). The feature was detected sporadically in occultations by Voyager's PPS and Radio Science Subsystem (RSS) (Albers et al., 2012; Marouf et al., 1986) as well as by the RSS on Cassini (Marouf et al., 2010). Cassini's RSS detected the narrow component in 15 of 49 occultations while UVIS saw it in 16 of 87 cases. Both Cassini and Voyager's RSS, sensitive only to particles larger than around a centimetre in size, detected only the narrow inner component, not the broad visible component. Therefore the larger F ring particles may be confined to this inner core, embedded within a more diffuse, visible envelope. Albers et al. (2012) note however that there was no improvement to their orbit fit (see next section) using only this inner core.

Most of the F ring's visual brightness is concentrated in the core or strands. The dust envelope extending several hundred kilometres either side has optical depths fading slowly to as low as $\tau = 0.002$ (Albers et al., 2012). French et al. (2012) measured the total integrated width and brightness from ISS image photometry and found, on average, 90% of the intensity within a ring of 580 ± 70 km centred on the core. This is nearly three times the 200 ± 40 km width found from a similar measurement of Voyager 1 images. Likewise, the optical depths integrated over

this radial width and the peak values were both consistently higher as observed by Cassini than by Voyager. Despite this difference the average ring photometry did not change significantly over the course of the Cassini tour (2004-2009).

The F ring as a whole is brighter at high phase angles implying strong forward scattering and small particle sizes (Smith et al., 1981). French et al. (2012) also noted their measured total ring widths increasing with increasing phase angle implying more small particles in the outer envelope than in the core.

Showalter et al. (1992) performed a photometric study from Voyager images, modelling the ring as two populations: one of very small, micron-sized particles, and one of much larger particles. The best fit result indicated 98% of the visual brightness arising from this small 'dust' with the 2% fraction of larger $\sim$ cm and above sized particles restricted to the $\sim$ 1 km inner core. Showalter et al. (1992) found a power-law size distribution for the small population with more particles at ever smaller sizes. In contrast to this, Vahidinia et al. (2011) found a relatively narrow size distribution for the dust particles from Cassini VIMS spectra, with most limited to between 10 and 30 μm in size. They also confirm the dust to be made, almost exclusively, from crystalline water ice.

Hedman et al. (2011b) used VIMS occultations (rather than imaging) to investigate the ring's transmission spectra. They identity a particular spectral feature that is sensitive to particles between 1 and 100 μm and note that it is inversely correlated with optical depth across the ring, implying dense clumps have fewer small particles. 14 individual features with strong peaks in optical depth are identified as possible clumps and their spectra show an increase in the number of 'big' particles ($> 30\ \mu$m) relative to small ($< 30\ \mu$m). Showalter et al. (1992) had argued that the extended envelope arises from dust released by impacts on the larger particles embedded in the core followed by Poynting Robertson drag (a radiation absorption/re-radiation effect, see Burns et al., 1979) inwards. The VIMS spectral results indicate that accretion of small particles back onto the larger ones may also be occurring. This may be significantly enhanced in the regions of low relative velocity and high density triggered by Prometheus. Hedman et al. (2011b) did not find a relationship between the longitude of the spectral features and Prometheus but note that this does not rule out the clumps having formed there and drifted apart due to their random velocities.

2.3. Orbit and Stability

Despite all this variability the orbit of the F ring core can still be well approximated as a single, uniformly precessing, inclined ellipse. Furthermore, measurements made via different techniques and instruments produce reasonable agreement despite the different components discussed above. Bosh et al. (2002) fitted combined HST and Voyager RSS occultation data to find a semi-major axis of $a = 140223.7 \pm 2.0$ km, corresponding to a mean motion of 581.96 degrees per day and an orbital period of about 14.7 hours (with the other orbital elements listed in Table 2.1). Albers et al. (2012) updated this using Cassini UVIS occultations and found a very similar set of orbital elements. Their large RMS residuals of 24 km are concluded to be a real feature of the ring, reflecting the non-Keplerian features visible in imaging. Although Albers et al. (2012) found the core orbit to be stable over time they did find these residuals to be time dependent, increasing between 2005 and 2009, which they attribute to the changing distance between Prometheus and the ring.

Cooper et al. (2013) used a different technique: measuring the position of the bright core in ISS image sequences which tracked Prometheus around its orbit and fitting a geometric, inclined, precessing ellipse to this. Ten such sequences were analysed producing ten independent fits, each to a small (few degrees) section of the ring. Individually each fit resembles the previous solutions but with a scatter between them of up to ~ 20 km, again revealing the differing orbits of different parts of the ring. It must be noted that no obvious features such as jets or fans are seen in these images; to all intents and purposes the fits are to quiet, 'undisturbed' ring but still show scatter. Combining all the measurements (9805 points) into a single averaged fit produces the orbital elements shown in Table 2.1 with RMS residuals of 8.2 km. Semi-major axis and eccentricity are roughly consistent with the Albers et al. (2012) and Bosh et al. (2002) models but the ascending node and periapse show large differences. Cooper et al. (2013) tried excluding points near to Prometheus in an effort to remove the effect of its perturbation. They found similar a and e but the two longitudes converging towards the Albers et al. (2012) fit. They conclude that individual parts of the ring each have their own orbit (with a scatter consistent with the perturbation from Prometheus) which, when combined together, approach a stable 'average' F ring orbit. On the other hand the individual periapses all appear locked together so that the ring precesses uniformly. This may be because of self-gravity or a collisional effect.

The long-term stability of the F ring as a whole presents further questions: without some mechanism to radially confine them narrow rings should spread over time.

	a (km)	e ($\times 10^{-3}$)	I ($° \times 10^{-3}$)	Ω (°)	ϖ (°)
A	$140\,223.7 \pm 2.0$	2.54 ± 0.05	6.5 ± 0.7	16.1 ± 3.6	24.1 ± 1.6
B	$140\,221.3 \pm 1.8$	2.35 ± 0.02	6.43 ± 0.15	15.4 ± 1.4	24.2 ± 0.8
C	$140\,223.92 \pm 0.09$	2.3636 ± 0.0004	5.68 ± 0.05	5.3 ± 0.6	8.8 ± 0.3

Table 2.1.: Orbital models of the F ring core: A) is Fit 3 from Bosh et al. (2002), B) is Fit 2 from Albers et al. (2012), C) is Fit 11 from Cooper et al. (2013). The columns are the six standard orbital elements: semi-major axis (a), eccentricity, (e), inclination (i) and the longitudes of the ascending node (Ω) and periapse (ϖ). All three are referenced to the J2000 epoch.

This is due to collisional diffusion (Tiscareno, 2013) and, in the case of very small particles, radiation and plasma effects (see Burns et al., 1979 and Burns et al., 2001 for an overview). For the F ring Poynting Robertson (PR) drag causes $\sim 1\ \mu$m sized dust to spiral in towards Saturn on 100,000 year timescales (Burns et al., 2001).

Goldreich and Tremaine (1979) proposed the now famous 'shepherding' mechanism whereby the perturbing force of two nearby moons constrains a narrow ring between them. Prometheus and Pandora seemed, at first, to work for the F ring, however Showalter and Burns (1982) showed that the torques on the ring do not balance as required by the mechanism. Furthermore, several works have shown that the so-called 'shepherding' moons interact chaotically (Goldreich and Rappaport, 2003a,b), changing their semi-major axes approximately every 6.2 years. Winter et al. (2007) showed that the whole region between the two moons is chaotic with particles, from ~ 5 km moonlets down to dust, experiencing sudden $10 - 100$ km jumps in semi-major axis on orbital time periods or less during their integrations. Despite this, most of the particles remained within the region between the two moons and there was much faster longitudinal diffusion (with a characteristic time ≈ 100 orbital periods) than radial (characteristic time $\sim 10^6$ orbital periods) so the shepherding moons may well help to contain particles between them in a general way.

Cuzzi et al. (2014) propose a novel stability mechanism around stable 'antiresonances' involving the F ring's fast periapse precession rate ($\sim 2.7°$ per day) and the Prometheus synodic period. At locations where these two periods are integer multiple of each other the 'kick' given to particles by Prometheus can be cancelled out with an equal and opposite kick at the next encounter, leading to a region of enhanced stability compared to neighbouring semi-major axes. Cuzzi et al. (2014) point out that the averaged a values of Albers et al. (2012) and Cooper et al. (2013) fall on one of these locations, which are extremely narrow, ~ 1 km or less in semi-major

axis, and separated by ~ 8 km from each other. Cooper et al. (2013) independently found their model's mean motion to fall into such a location but point out the variability of, not only the ring's semi-major axis but that of Prometheus as well. The answer, as suggested by Cuzzi et al. (2014), may be that the large particles of the true, inner core sit in a stable antiresonance while the small dust component, visible to ISS, UVIS and VIMS, is a temporary and irregular cloud of impact ejected material chaotically evolving. The dust is quickly reabsorbed or scattered away and constantly replenished, explaining why its average orbit approaches that of the larger bodies. Cuzzi et al. (2014) note finally that their stability mechanism does not in any way constrain the apse values so the apparent periapse-locking of the whole F ring still needs to be explained by a further mechanism such as collisions or self-gravity.

A number of authors have speculated on the F ring's formation and long-term survival. Early works tended to assume the ring to be a recent phenomenon with Cuzzi and Burns (1988) suggesting the core is the spread-out remains of a recent, especially large collision among their moonlet belt. Barbara and Esposito (2002) agree with this interpretation of the core as a transient feature created from a more permanent moonlet belt. They model the evolution of its size distribution in a statistical way and find that, starting from a power law, tidally modified accretion (see section 3.2.2 below) drives it towards a bimodal distribution. That is, there exists a balance between collisional disruptions and mergers where there is a large population of small particles alongside a number of $\sim$ km-sized moonlets. There are some limitations to their model however: collisions are parameterised by a single relative velocity, rather than a spread, and the accretion probability is a simple cutoff in mass ratio (given by Canup and Esposito, 1995), whereas the truth is probably more complicated: as discussed below in section 3.2.2 both accretion, disruption and bouncing collisions are expected to happen at the F ring. This bimodal distribution has not been seen in the objects detected in occultations, although Meinke et al. (2012) note that they do not expect to be able to sample the largest sizes. Guimarães et al. (2012) consider a more detailed model of aggregate interactions and suggest the F ring should instead possess a trimodal distribution with a population of small dust, medium sized centimetre or decimetre sized aggregates and a few large ~ 1 km sized bodies, possibly as seen by Showalter et al. (1992).

With the important role of Prometheus better understood, more cyclical models have been proposed for the F ring's evolution. Esposito et al. (2012) developed a 'predator-prey' model of clump formation whereby aggregation is triggered by Prometheus before dispersion velocities are increased though mutual gravitational

interactions of the newly concentrated material. This 'stirring up' of velocities leads to increased fragmentation in collisions, breaking the clumps up, ready for the next cycle to repeat the process. The system cycles periodically but with a phase offset from that of the perturbation (i.e. the Prometheus close approach every $\sim$ 68 days). Esposito et al. (2012) suggest the expected distribution of clumps relative to Prometheus, including the phase offset, can be seen in the UVIS occultation data of Meinke et al. (2012), but the correlation is statistically weak. Hedman et al. (2011b) also found no correlation in clumps detected by VIMS. Esposito et al. (2012) further explain the rarity of solid moonlets, relative to translucent clumps, by a stochastic process of compaction or adhesion from one into the other (which is itself relatively rare) leaving the steady-state populations unequal.

If material is recycled almost indefinitely then the F ring can survive for much longer timescales. Several authors, including French et al. (2012), Albers et al. (2012) and Cuzzi et al. (2014), have attempted to reconcile the differences between Voyager, HST and Cassini data with cyclical processes. All three make note of the $\sim$ 17 year Prometheus precessional cycle which resulted in especially close approaches between the moon and the F ring in early 1975, mid 1992 and late 2009.

French et al. (2012) speculate that close approaches trigger a dynamical heating of the ring, releasing large quantities of dust and causing it to increase in brightness and width (as observed by Cassini relative to Voyager) before 'cooling' back down to a narrower, dimmer state (as seen by Voyager 1 and 2). Meanwhile, some of this material can spread beyond the gravitational influence of the core (which is assumed to lock precession values to itself) and is free to coalesce into distant objects like the clumps seen by HST and the, relatively rare, S6. Differential precession then causes these to re-impact into the ring, with some lag time, creating the large 'burst' events seen by Voyager, but not by Cassini (French et al., 2014), and depleting their number. The model is testable, with future Cassini observations predicted to see a return to conditions more like Voyager and HST. Nothing like this has thus far been seen.

Albers et al. (2012) also present a testable theory. Unlike French et al. (2012) they do see changes during the Cassini tour, specifically an increase of RMS residuals from the fit to UVIS occultations as Prometheus and the ring approached antialignment. If Prometheus does control the ring's dynamic 'temperature' then residuals should decrease again as the two recede over the remainder of the mission.

Cuzzi et al. (2014) suggest a similar, self-perpetuating model for the formation of S6-like objects, assuming some population of large bodies to start from. Collisions between them and the core will spread material in a similar manner to the French

et al. (2012) model but with coalescence further enhanced at their antiresonance locations. Material will aggregate at these semi-major axes forming new S6 or HST-like clumps. Eventually chaos in their orbital evolution or differential precession will again trigger orbit crossing, resulting in further collisions with the core. The presence, or not, of bright clumps at antiresonance locations should also make this model falsifiable.

3. Orbital and Collisional Dynamics

In this chapter the orbital and collisional dynamics needed to understand and interpret the data in the rest of the thesis are reviewed. Section 3.1 reviews the basic orbital dynamics of the 2- and restricted 3-body problems, introducing Hill's coordinates and motion in a local, co-rotating frame. In Section 3.1.2 the effects of a small, instantaneous perturbation on such motions are discussed. Section 3.2 outlines the hard sphere model of physical collisions before laboratory- (Section 3.2.1) and simulation- (Section 3.2.2) based experimental results are reviewed.

3.1. Orbital Dynamics

3.1.1. Motion in Hill's Co-Ordinates

The motion of one point mass (m_1) with respect to another point mass (M_c, the central body), when both are moving only under the influence of their mutual gravitational attraction, has the well-known solution of Keplerian orbits. That is, an elliptical path where the radial separation, r_{kep}, is described by

$$r_{\text{kep}} = \frac{a(1 - e^2)}{1 + e \cos(f)}, \tag{3.1}$$

where f is the true anomaly and a and e are the semi-major axis and eccentricity, which are determined by the initial conditions. The average angular speed around the orbit, the mean motion, is given by $n = \sqrt{G(m_1 + M_c)/a^3}$, with G the gravitational constant, and the orbital period is $P_0 = 2\pi/n$.

In general adding a third body, m_2, to the problem results in a lack of analytical solutions. However, if the masses of the second and third bodies are kept small ($m_1, m_2 \ll M_c$) then the gravitational influence of the central body dominates and progress can be made. It is useful to describe the motions of the two small bodies in a local cartesian co-ordinate frame (r, l, z) which rotates with them around the

central body at angular frequency n and radial distance a. Here the r direction points radially outwards, the positive l axis is in the direction of orbital motion and the vertical z axis orthogonal to both (Nakazawa and Ida, 1988). These are Hill's coordinates, first used by Hill (1878) in his work on the orbit of the moon. The assumption of small secondary masses is the first of the so-called Hill's approximations, the others being:

$$\begin{aligned}
|r|, |z| &\ll a, \\
|\dot{r}|, |\dot{l}|, |\dot{z}| &\ll an, \\
|\ddot{r}|, |\ddot{l}|, |\ddot{z}| &\ll an^2,
\end{aligned}$$
(3.2)

where dots and double dots indicate first and second derivatives with respect to time. The local radial and vertical length scales, i.e. the relative separations between the two small bodies, must be much less than the semi-major axis and their relative motions much smaller than their overall orbital velocities (note the lack of restriction on the scale of the l axis).

Under these assumptions a set of equations of motion can be constructed for the motion of the bodies in the local frame. These three equations, accurate to first order, contain a number of terms including the gravitational attraction of the central body, the centrifugal and the Coriolis forces. An additional term containing the relative position vector of m_2 from m_1 refers to their mutual gravitational interaction. In the limit of massless particles ($m_1, m_2 \to 0$) or when this separation is large (but still $\ll a$), this term disappears and Hill's equations of motion have the exact solution of epicyclic motion. The position of each particle at some time is given by (Nakazawa and Ida, 1988)

$$\begin{aligned}
r &= \Delta a - a\Delta e \cos M, \\
l &= 2a\Delta e \sin M - \frac{3}{2}M\Delta a, \\
z &= a\Delta i \sin(nt - \omega),
\end{aligned}$$
(3.3)

and its velocity by

$$\begin{aligned}
\dot{r} &= na\Delta e \sin M, \\
\dot{l} &= 2na\Delta e \cos M - \frac{3}{2}n\Delta a, \\
\dot{z} &= na\Delta i \cos(nt - \omega),
\end{aligned}$$
(3.4)

where $M = n(t - t_0)$ is the mean anomaly, with t_0 the time of pericentre passage,

and $\Delta a, \Delta e$ and Δi are the relative orbital elements. These are defined by

$$
\begin{aligned}
\Delta a &= a_1 - a_2, \\
\Delta e^2 &= e_1{}^2 + e_2{}^2 - 2e_1 e_2 \cos \Delta \varpi, \\
\Delta i^2 &= i_1{}^2 + i_2{}^2 - 2i_1 i_2 \cos \Delta \omega,
\end{aligned}
\tag{3.5}
$$

where $\Delta \varpi = \varpi_1 - \varpi_2$ and $\Delta \omega = \omega_1 - \omega_2$ contain the differences in the longitudes of pericentre, ϖ, and arguments of periapse, ω, of the two bodies, respectively. Relative eccentricity can be considered the difference between the two eccentricity vectors, with magnitudes e_1 and e_2, using the cosine rule. It can be shown (Williams, 2009) that, to first order, the relative motion between two particles on Keplerian orbits with small eccentricities is equivalent to one particle having a circular orbit and the other a relative eccentricity of Δe. Likewise for inclination

In the case of massive particles the gravitational interaction term in Hill's equations is non-negligible and there are no analytical solutions: the equations must be integrated numerically. Even in this case, however, it can be shown that the particle motions can still be expressed in the same form as Eqns. 3.3 and 3.4 with the relative orbital elements now functions of time (Nakazawa and Ida, 1988). Relative trajectories can then be understood as a series of piece-wise motions, each with their own $\Delta a, \Delta e$ at any given moment

The trajectories described by Eqns. 3.3 and 3.4 can be decomposed into two components: motion of the guiding centre and epicycle motion. This guiding centre rotates around the central mass in a circle of radius a with the mean motion n. Meanwhile, the body in question travels in the opposite direction around an ellipse, with semi-major axis $2a\Delta e$ and semi-minor axis $a\Delta e$, centred on the guiding centre in the same period (Murray and Dermott, 1999). The superposition of the two motions, particle around guiding centre, and guiding centre around central mass, then recovers the full Keplerian orbit, as shown in Fig. 3.1.

For a small difference in semi-major axis, Δa, between the body and the origin of the Hill co-ordinates there will be a small difference in mean motions

$$
\frac{dn}{da} = -\frac{3}{2} \sqrt{\frac{G(m_1 + m_2)}{a^5}} = -\frac{3n}{2a}.
\tag{3.6}
$$

If the two start off at the same longitude, λ, at t_0 they will slowly drift apart at a rate, $\dot{\lambda} = -3n\Delta a/2a$, which corresponds to the last term in the second part of Eqn. 3.4. After time t this will have built up to a difference in longitudes of $\Delta\lambda = -3nt\Delta a/2a = -3M\Delta a/2a$, corresponding to the last term in the second part
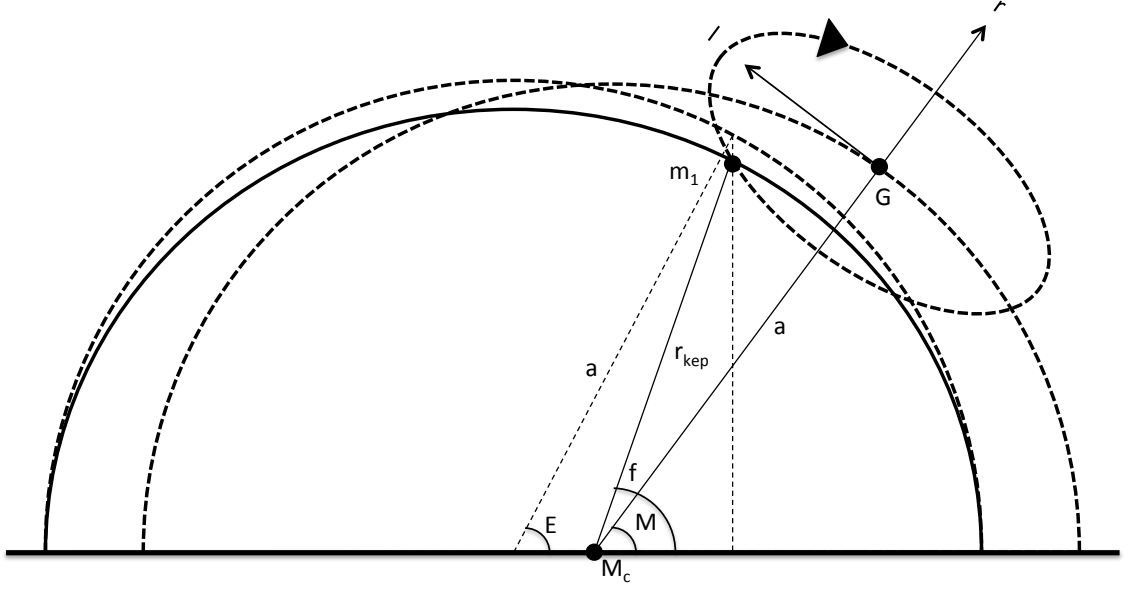
Figure 3.1.: The guiding centre approximation: m_1 follows a Keplerian orbit (solid black line) around M_c. This can be broken down into motion of the guiding centre, G, around a circle of radius a (dashed line) combined with a rotation of m_1 around a 2:1 ellipse. The Hill coordinate frame as well as the angles f, M and E, the true, mean and eccentric anomalies, are also labelled. E is referenced to the centre of a circumscribed circle of radius a, concentric to the Keplerian orbit (dashed).

of Eqn. 3.3. This process is known as Keplerian shear as it leads to the 'shearing' out of radial features (those separated by a Δa) in the longitudinal direction. When combined with the epicycle motion it leads to the radially looping trajectories described by Eqns. 3.3 and 3.4.

A useful derived quantity is the angle made by the line connecting two particles experiencing Keplerian shear and the longitudinal axis. This gradient (called the cant angle in Tiscareno et al., 2013) is obtained by taking the arctangent of the ratio r/l from Eqn. 3.3 with Δe set to zero;

$$\theta = \tan^{-1}\left(-\frac{2}{3M}\right). \tag{3.7}$$

If Δe is not zero but is instead assumed to be equal to $\Delta a/a$ then the gradient is instead

$$\theta = \tan^{-1}\left(\frac{1-\cos M}{2\sin M - 3/2M}\right) \tag{3.8}$$

Figure 3.2 compares how these two gradients evolve. In the case with no eccentricity
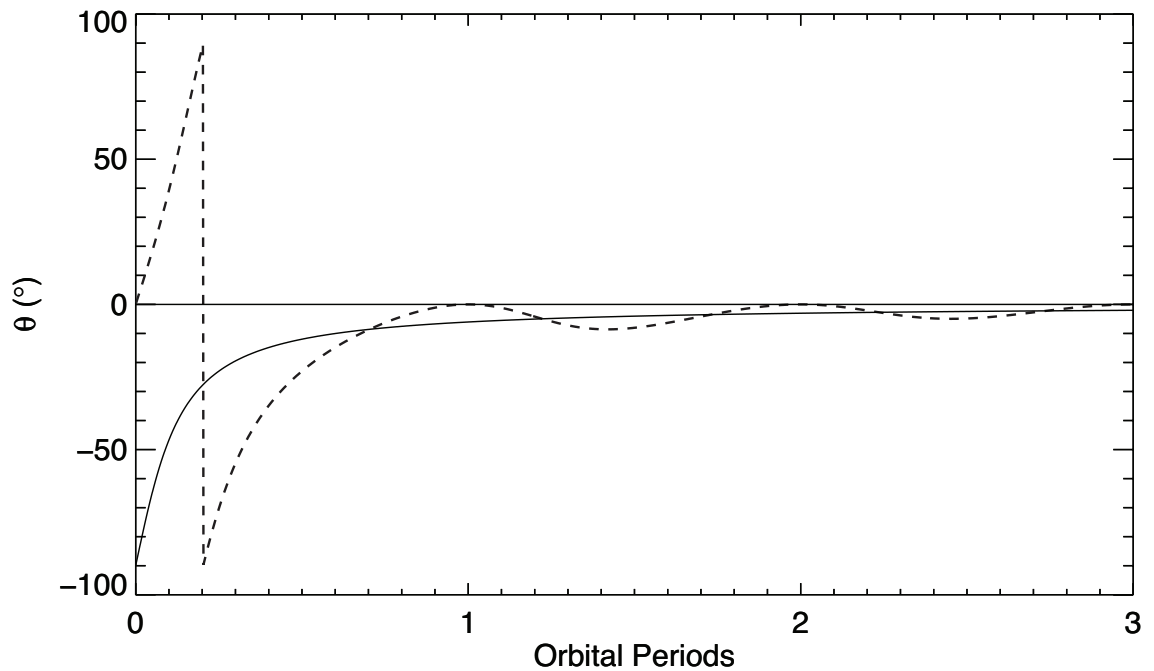
Figure 3.2.: Gradient, or cant angle θ, between two particles on differing orbits over time. The solid line is for circular orbits with differing semi-major axes, given by Eqn. 3.7. The dashed line is for both differing semi-major axes and eccentricities with $\Delta a = a\Delta e$, given by Eqn. 3.8.

(solid line) the angle simply decreases with time as the particles shear apart. In the case of $\Delta a = a\Delta e$ (dashed line) the angle oscillates, around the previous curve, once per orbit whilst its magnitude decreases with time. These curves present two useful cases that will be compared to observations later.

Another useful parameter relating to these equations is Hill's radius: (see for example Ohtsuki et al., 2013)

$$R_H = a \left(\frac{m_1 + m_2}{3M_c} \right)^{1/3}. \tag{3.9}$$

This length can be used to scale Hill's equations in order to re-write them in a dimensionless form but it also has a physical interpretation as the equilibrium point between the mutual attraction of the two small bodies and the tidal force (Murray and Dermott, 1999). A sphere of radius R_H then defines the volume of space dominated by the gravity of the small bodies, with respect to the central object. As R_H shrinks with decreasing semi-major axis there will come a point where it equals the physical size of the objects. This defines the Roche limit, inside of which objects will exceed their Hill spheres, becoming gravitationally unbound, and disrupt.

3.1.2. Perturbations to an Orbit

The rates of change of the instantaneous (osculating) elements of an orbit due to a small disturbing force can be derived by elementary dynamics (Burns, 1976) as given in Section 2.9 of Murray and Dermott (1999). The disturbing force per unit mass is split into its three components in the same local frame as above: r, l and z. Assuming that this force is applied for a short duration (i.e. much less than an orbital period, $\Delta t \ll P_0$) then the other variables can be held constant and the force per unit mass equated to an instantaneous change in velocity in the same three components, $\Delta \boldsymbol{v}_r, \Delta \boldsymbol{v}_t$ and $\Delta \boldsymbol{v}_z$, where bold face indicates these are vector quantities. The perturbation equations can then be re-written in terms of these specific impulses[1] as

$$\delta a = \frac{2}{n\sqrt{1-e^2}} \left[e\Delta\boldsymbol{v}_r \sin f + \Delta\boldsymbol{v}_l(1 + e\cos f) \right] \tag{3.10}$$

$$\delta e = \frac{\sqrt{1-e^2}}{na} \left[\Delta\boldsymbol{v}_r \sin f + \Delta\boldsymbol{v}_l(\cos f + \cos E) \right] \tag{3.11}$$

$$\delta\varpi = \frac{\sqrt{1-e^2}}{ena} [\Delta\boldsymbol{v}_l \sin f \frac{2 + e\cos f}{1 + e\cos f} - \Delta\boldsymbol{v}_r \cos f] \tag{3.12}$$

$$\delta i = \frac{\sqrt{1-e^2}}{na(1 + e\cos f)} [\Delta\boldsymbol{v}_z \cos(\omega + f)] \tag{3.13}$$

where $\delta a, \delta e, \delta\varpi$ and δi are the instantaneous changes in the elements of the orbit subjected to these impulses at a true anomaly f, eccentric anomaly E and argument of pericentre ω. Expressions for the change in the longitude of the ascending node and time of pericentre passage can also be derived but are not used here. A final term referring to the change in nodal longitude is also excluded from Eqn. 3.12.

In the limit of initially circular orbits $e \to 0$, $E = f$ and the equations become

$$\delta a = \frac{2\Delta\boldsymbol{v}_l}{n} \tag{3.14}$$

$$\delta e = \frac{\Delta\boldsymbol{v}_r \sin f + 2\Delta\boldsymbol{v}_l \cos f}{na} \tag{3.15}$$

$$\delta i = \frac{\Delta\boldsymbol{v}_z \cos(\omega + f)}{na} \tag{3.16}$$

---

[1]'Impulse' and 'specific impulse' will be used interchangeably in this thesis but impulse should technically have units of mass times velocity.

where there is no equivalent to Eqn. 3.12 as changes to the longitude of pericentre are unspecified for circular orbits.

These changes in orbital elements are written with lower case δ to distinguish them from the relative orbital elements described above. If no other perturbations occur, however, then the orbit of the perturbed particle relative to its old, unperturbed, orbit will be described by Eqns. 3.10 to 3.13 so $\Delta a = \delta a$ while δe and $\delta \varpi$ combined give Δe.

These equations have a number of implications. Firstly only impulses out of the plane of the orbit can change its vertical structure (inclination). Conversely, out of plane impulses cannot change the semi-major axis or eccentricity, though they may change the pericentre through the omitted term in Eqn. 3.12. For a purely longitudinal impulse ($\Delta \boldsymbol{v}_r = \Delta \boldsymbol{v}_z = 0$) it can be seen from Eqns. 3.14 and 3.15 that the magnitude of the induced Δa equals $a\delta e$. A perturbed particle will always return to the orbital radius where it experienced the perturbation. Adding a radial impulse to this will, in general, increase the induced eccentricity, so that $a\delta e > \Delta a$, but this depends on where in its orbit the particle is perturbed. Figures 3.3, 3.4 and 3.5 show the results of a one metre per second impulse applied, in various directions, to a particle, orbiting with F ring values of n, a and e, at various points in its orbit.

In the case of a purely longitudinal impulse (Fig. 3.3) Δa is simply a constant 18 km while $a\delta e$ varies across the orbit between $\pm\Delta a$. $\delta\varpi$ also varies across the orbit between about $\pm3°$ and is out of phase with the eccentricity. The combined relative eccentricity is therefore a constant equal to the relative semi-major axis change, i.e. $\Delta a = a\Delta e$.

With a purely radial impulse (Fig. 3.4) there is no Δa and a smaller $a\delta e \approx 8.5$ km. Induced eccentricities and pericentre shifts are again out of phase so that relative eccentricity is again constant at all points in the orbit and $a\Delta e \gg \Delta a$, always. The point in the orbit where the perturbation occurred merely specifies how much of the relative eccentricity is through e and how much is through ϖ.

When the impulse is angled at $45°$ to the longitudinal direction (Fig. 3.5) it has both radial and longitudinal components, resulting in a slightly lower Δa and a slightly higher δe than the purely longitudinal case. Again $a\Delta e > \Delta a$ always.

These figures demonstrate that the perturbations to a particle's orbit depend not only on the magnitude and direction of the applied force but also on the particle's position around its own, starting orbit. To zeroth order, however, some patterns emerge: 1) changes in semi-major axis are controlled primarily by the longitudinal component, 2) both the radial and longitudinal components produce changes in eccentricity and pericentre and 3) when these are combined, $a\Delta e \geq \Delta a$.
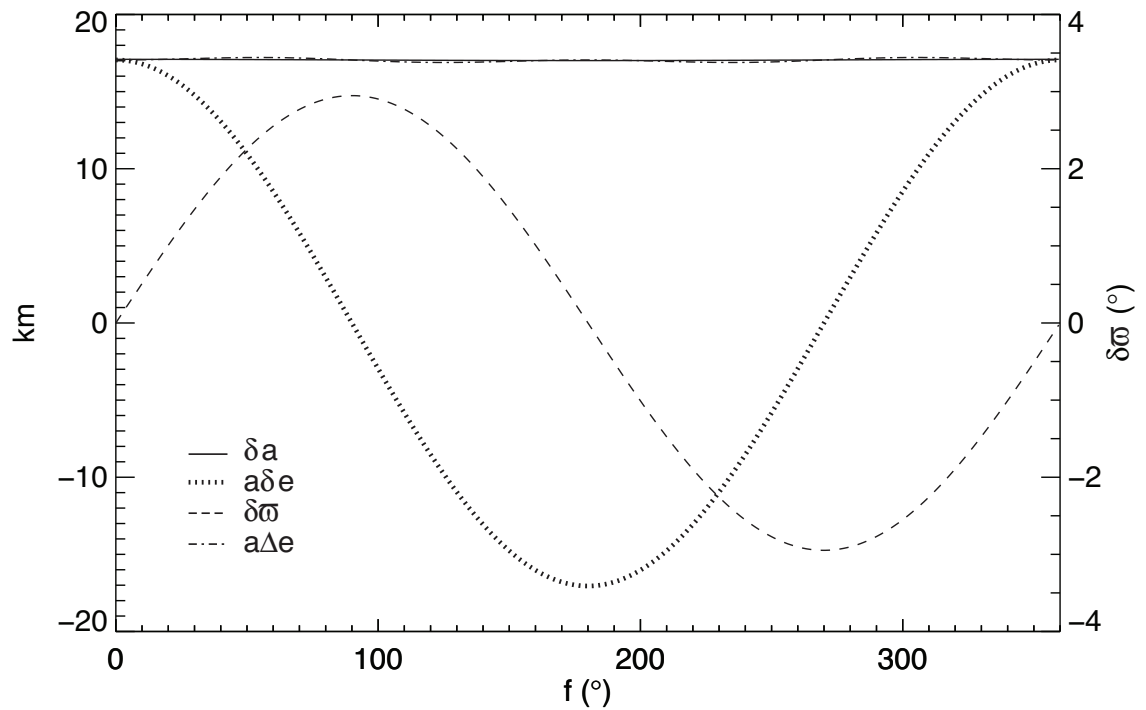
Figure 3.3.: Changes in the orbital elements of a particle with the F ring's orbit when perturbed by a 1 ms^{-1} longitudinal impulse at various points in its orbit. The solid line is δa (from Eqn. 3.10); dotted line is $a\delta e$ (Eqn. 3.11); dashed line is $\delta\varpi$ (Eqn. 3.12); and dot-dashed line is the combined relative eccentricity (Eqn. 3.5) times a.
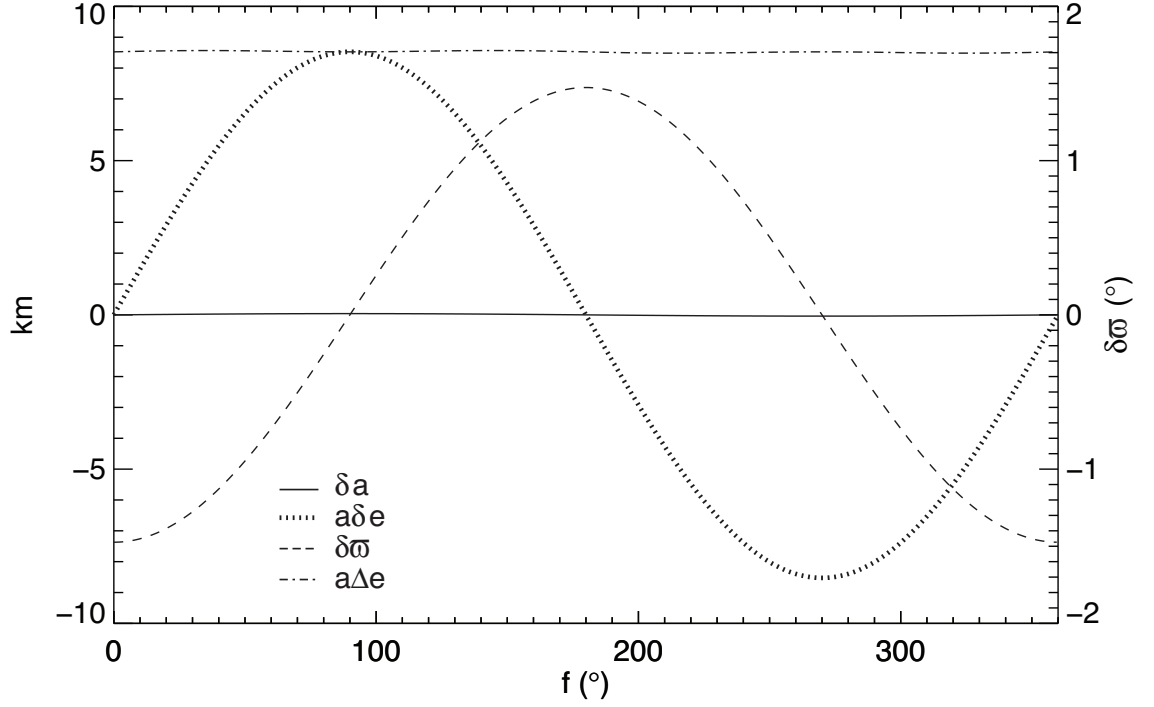
Figure 3.4.: Changes in the orbital elements of a particle with the F ring's orbit when perturbed by a 1 ms^{-1} radial impulse at various points in its orbit.

A cartoon picture of the results of a distribution of velocity impulses delivered to a group of particles can now be constructed. Consider an isotropic distribution of $\Delta\boldsymbol{v}$ in the plane of the orbit ($\Delta v_z = 0$) given to a group of particles. The components of $\Delta\boldsymbol{v}$ in, and opposite to, the orbital direction induce positive and negative changes in semi-major axis, respectively. Relative eccentricities with equal magnitudes are also induced so that $a\Delta e = \Delta a$ across the particles. The radial components of the $\Delta\boldsymbol{v}$ will slightly alter these eccentricities but have little effect on Δa, resulting in a cloud of particles with $a\Delta e \approx \Delta a$. The evolution of such a cloud, in the co-rotating frame, is then governed by Eqns. 3.3 and shown in schematic form in Fig. 3.6: it will shear away, lengthening in both the positive and negative longitudinal directions whilst the relative eccentricity causes its constituent particles to oscillate radially on their epicycles. Since $a\Delta e \approx \Delta a$ the size of these ellipses means that each particle will return to the original orbital radius, or thereabouts, once per orbit. Since all the particles are perturbed at the same time they will all be in phase, starting at periapse for those with a positive Δa and apoapse for negative. The whole cloud will therefore oscillate together, 'bouncing' up to a maximum radial extent and collapsing down to the l axis once per orbit whilst lengthening all the while. The angle it makes with the l axis will follow Eqn. 3.8, plotted in Fig. 3.2. More complicated velocity
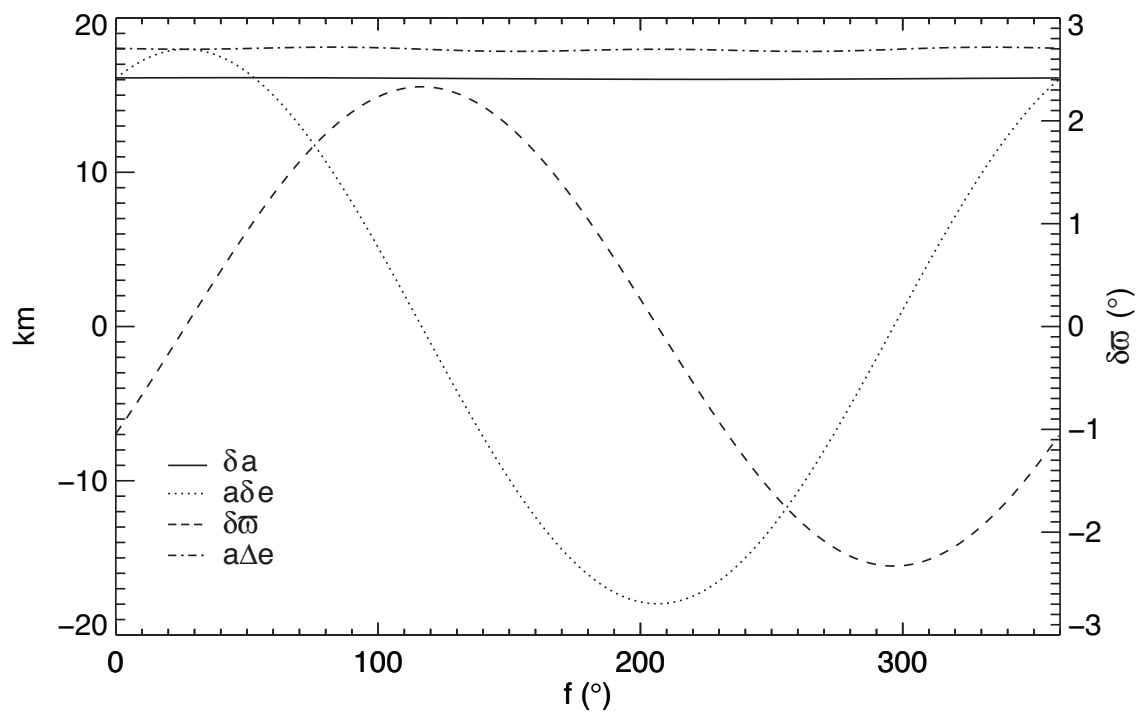
Figure 3.5.: Changes in the orbital elements of a particle with the F ring's orbit when perturbed by a 1 ms^{-1} impulse at 45° to the longitudinal direction at various points in its orbit.

distributions will produce different clouds of particles but their gradients should always decrease as they shear out in a manner resembling those in Fig. 3.2.

3.2. Collisional Dynamics

Having derived the effects of a velocity impulse on a particle's orbit one must now consider what sort of impulses physical collisions can deliver. Impacts by objects from outside the Saturn system or on very different orbits will be at hypervelocity (tens of kilometres per second), leading to cratering events with specific ejecta patterns, for which there is an extensive literature (see Melosh, 1989 for an overview). This thesis will primarily be concerned with much lower velocity impacts for which the inelastic, hard sphere (meaning no deformation or fragmentation of the particles) model provides a reasonable description.

Following Richardson (1994), but ignoring particle spin, consider two particles with masses m_1, m_2 radii R_1, R_2 and position and velocity vectors $\boldsymbol{r}_1, \boldsymbol{r}_2$ and $\boldsymbol{v}_1, \boldsymbol{v}_2$, respectively. Relative positions and velocities are $\boldsymbol{r} = \boldsymbol{r}_2 - \boldsymbol{r}_1$ and $\boldsymbol{U} = \boldsymbol{v}_2 - \boldsymbol{v}_1$. Figure 3.7 illustrates the two particles, showing a coordinate frame centred on the impact point. The axes are in the direction connecting the two spheres' centres (normal component, n, defined by $\hat{\mathbf{n}} = \mathbf{r}/\mathbf{r}$), and transverse to this, t. Relative velocity can be split into its components in each of these directions, $\boldsymbol{U}_n$ and $\boldsymbol{U}_t$.

The inelasticity of the particles is quantified by the parameters ϵ_n and ϵ_t, the coefficients of restitution in each direction. The post-impact relative velocity is then

$$\boldsymbol{U'} = \epsilon_n \boldsymbol{U}_n + \epsilon_t \boldsymbol{U}_t \tag{3.17}$$

where primed symbols indicate post-impact quantities. $\epsilon_n = \epsilon_t = 1$ for perfectly elastic collisions, where particles rebound with no change in speed, and $\epsilon_n = \epsilon_t = 0$ for perfectly inelastic collisions, which result in merger of the two with zero rebound velocity.

Solving for conservation of linear and angular momentum and Eqn. 3.17 produces the following expressions for the change in linear velocity of the two particles after the collision (equations 14 and 15 of Richardson, 1994)

$$\Delta \boldsymbol{v_1} = \boldsymbol{v_1}' - \boldsymbol{v_1} = \frac{m_2}{M_{\text{tot}}} \left[(1 + \epsilon_n)\mathbf{U}_n + \beta(1 - \epsilon_t)\boldsymbol{U}_t \right], \tag{3.18}$$

$$\Delta \boldsymbol{v_2} = \boldsymbol{v_2}' - \boldsymbol{v_2} = -\frac{m_1}{M_{\text{tot}}} \left[(1 + \epsilon_n)\boldsymbol{U}_n + \beta(1 - \epsilon_t)\boldsymbol{U}_t \right], \tag{3.19}$$
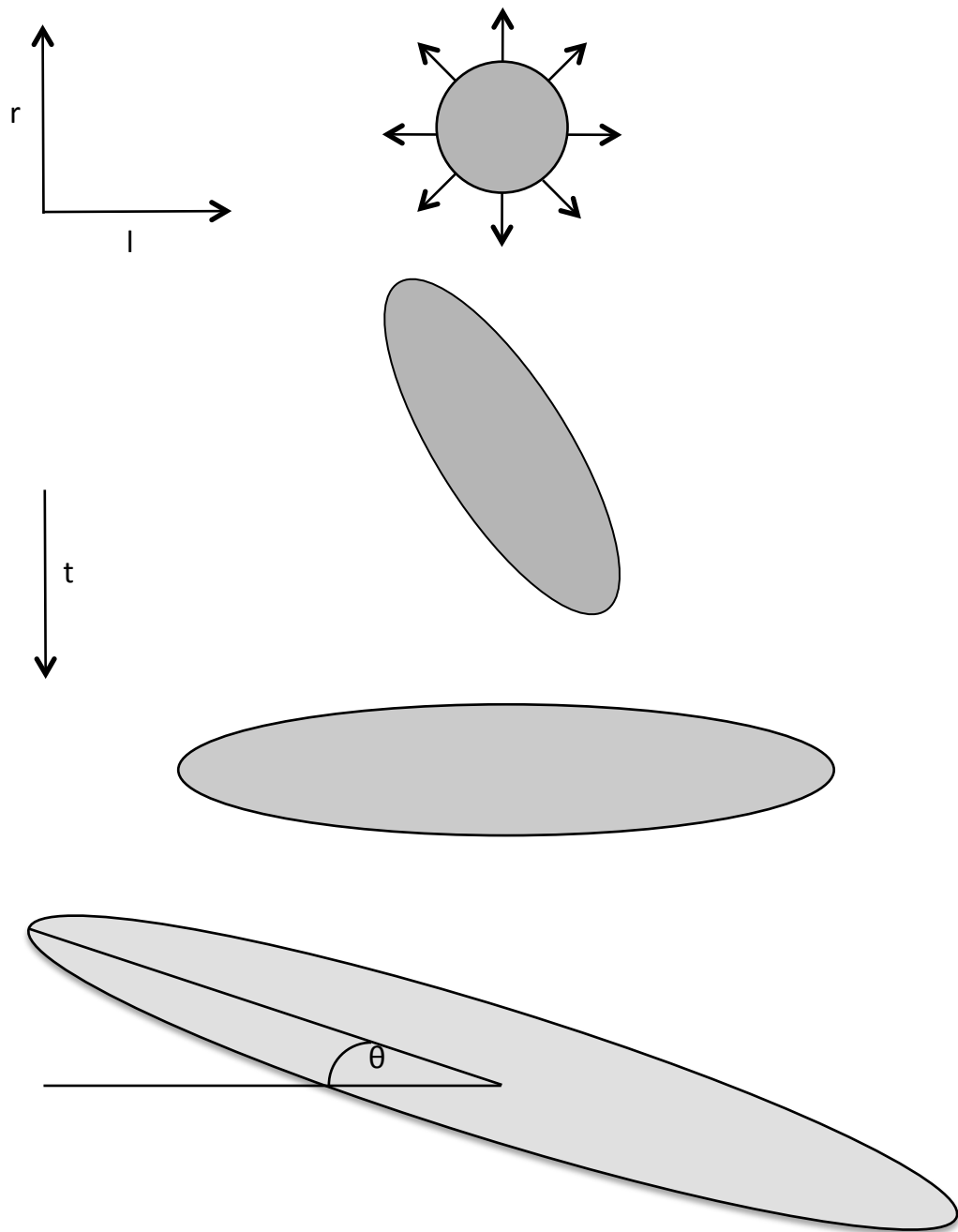
Figure 3.6.: Evolution, in the co-rotating frame, of a cloud of particles given an isotropic distribution of velocity impulses. The particles shear in the l direction, whilst oscillating once per orbit in the r direction and the brightness of the feature decreases as they are spread over a larger area. Gradient, or cant angle θ, is also labelled.
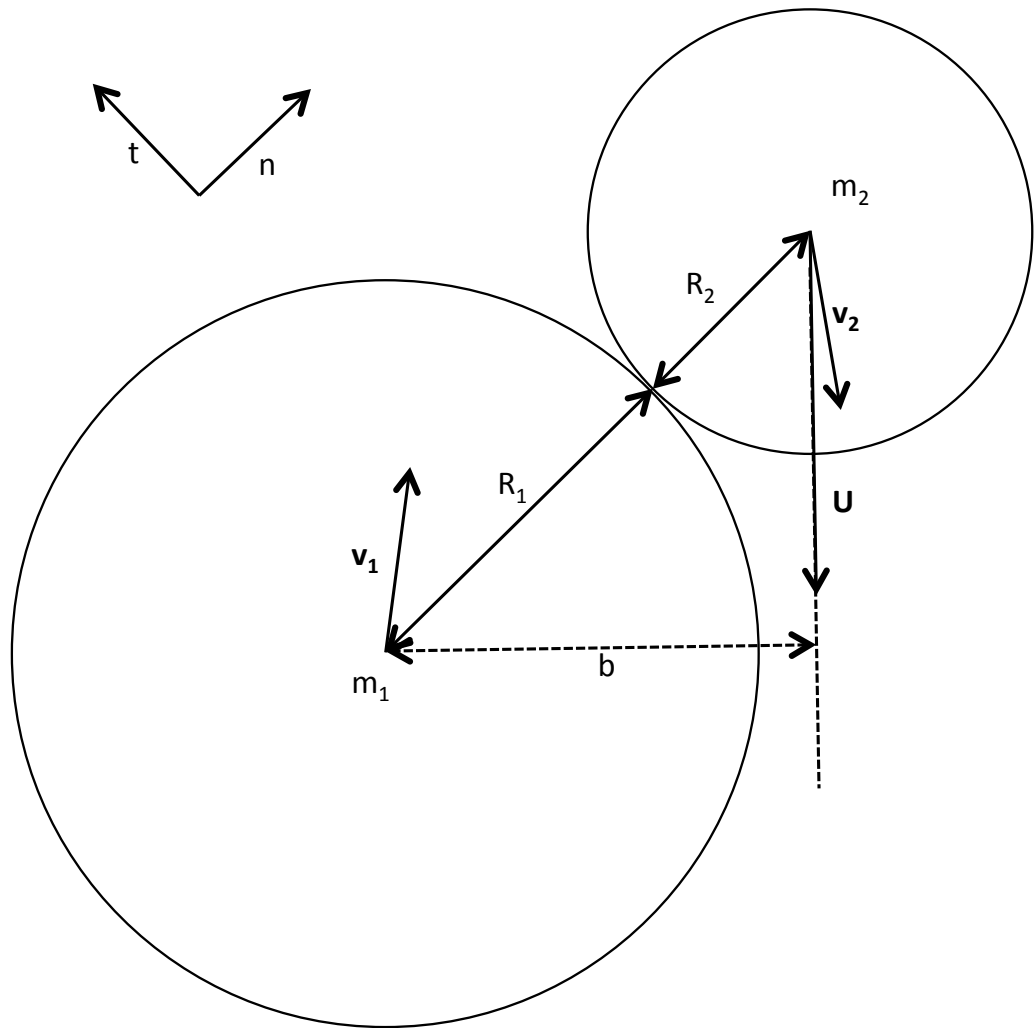
Figure 3.7.: Diagram of a collision between two hard spheres m_1 and m_2. The relative velocity and a collision-centred coordinate system are shown, as described in the text. Also shown is the impact parameter, b, defined as the closest separation of the two particle centres in the plane normal to the relative velocity vector $\mathbf{U}$.

where $M_{\mathrm{tot}} = m_1 + m_2$ is the total mass and β is a dimensionless quantity between zero and one, relating to the moments of inertia of the two particles. $\beta = \frac{2}{7}$ for two uniform spheres and is equal to one for point masses or non-rotating bodies. Two more expressions can be constructed for the change in spin rate of the two particles but these are not considered here.

Equations 3.18 and 3.19 are the general result of an inelastic collision between two particles but for some specific arrangement further simplifications can be made.

One interesting case is that of a much more massive particle encountering a smaller one (e.g. a moonlet of a kilometre or more in radius encountering dust), say $m_2 \gg m_1$ so that $m_2/M_{\mathrm{tot}} \to 1$ and $m_1/M_{\mathrm{tot}} \to 0$. Therefore $\Delta \boldsymbol{v_2} = 0$, the moonlet's velocity is unchanged by the encounter, and 3.18 is reduced to just the terms in the square bracket. Of these, $\beta = 1$ for non-rotating bodies. Charnoz (2009) argued that this is justified for the case of dissipative collisions between dust and a moonlet because any β less than one results in an effective tangential coefficient of restitution, even when $\epsilon_t = 0$. This may be accurate for perfectly smooth spheres but small moons will be irregularly shaped and possibly possessing a regolith layer, all of which should serve to damp out tangential velocities as well as normal ones. With $\beta = 1$ the normal and tangential components of the impact are treated symmetrically and, assuming $\epsilon_n \approx \epsilon_t \approx \epsilon$, Eqn. (3.18) becomes

$$\Delta \boldsymbol{v}_1 \approx \boldsymbol{U} + \epsilon(\boldsymbol{U}_n - \boldsymbol{U}_t) \sim \boldsymbol{U}, \tag{3.20}$$

i.e. the impulse received by the dust particles is equal to the relative velocity with which they encounter a large object plus some factor, determined by the specific geometry. For highly dissipative collisions (small ϵ) this factor will be small and the dust will be given approximately the velocity of the collider. Dust particles will, therefore, follow the colliding object's orbit with some small scatter around it determined by the geometry and coefficient of restitution.

3.2.1. Experimental Evidence

Coefficients of restitution can vary with impact velocity, particle size, mechanical and chemical composition and temperature but are likely to be low ($\epsilon \sim 0.1$) for icy ring particles. Coefficients of restitution for kilometre sized bodies in microgravity are difficult to determine experimentally, for obvious reasons, but extensive work has been done to measure those of smaller objects. This is because continuous low velocity collisions in the main rings (where typical particle sizes and relative

velocities are centimetres to metres and less than centimetres per second - Colwell et al., 2009) help determine stability by the amount of kinetic energy they dissipate.

Experiments with pendulums and ice targets (Bridges et al., 1984; Supulver et al., 1995) have found decreasing coefficients of restitution with increasing velocity. Bridges et al. (1984) found a power law decrease with an exponent of -0.234 for collisions involving centimetre-sized frosty ice spheres at centimetres per second. With impact speeds of $\sim 1\mathrm{ms}^{-1}$ Bridges et al. (1984) predicts $\epsilon \sim 0.1$. Supulver et al. (1997) found that a surface frost layer reduced the coefficient or restitution further. Supulver et al. (1995) measured both the tangential and normal coefficients of restitution, for similar targets and velocities, and found both to decrease linearly with increasing velocity. They also found a dependence on impact angle for the combined coefficient with it increasing with increasing angle away from head-on collisions. Supulver et al. (1995) noted high tangential coefficients, $\epsilon_t \sim 1$, suggesting very little rolling or sliding friction and little loss of energy in glancing collisions

Experiments in free space include those flown on parabolic flights, in drop towers and onboard the space shuttle. Heißelmann et al. (2010) collided 1.5 cm-sized ice spheres at similarly low speeds (0.06 ms^{-1} to 0.22 ms^{-1}) in a drop tower but found little dependence on velocity and a uniform scatter in ϵ between 0.06 and 0.84. Hill et al. (2015) repeated the experiment with both spheres and irregularly shaped, millimetre sized particles at slightly higher velocities (still $<$ ms^{-1}) and again found scatter in ϵ between 0.08 and 0.64 (mean of 0.36). Hill et al. (2015) attribute this scatter to surface roughness present in their particles but not in the pendulum experiments, which used smooth spheres, and note that, although there was no correlation with velocity *within* each experiment the upper value of ϵ did decrease with increasing velocity *between* the experiments. Hill et al. (2015) also note tangential coefficients of restitution much lower than Supulver et al. (1995) in many cases and no dependence on impact parameter for the overall ϵ.

Colwell (2003) and Colwell et al. (2008) impacted $\sim$ cm sized brass spheres into regolith targets (composed of $\sim 100~\mu$m irregular silica particles) under microgravity conditions aboard the space shuttle and parabolic flights. Bearing in mind the different materials, these results are interesting in showing ejecta cones similar in appearance to those of hypervelocity impacts (Melosh, 1989). Ejecta velocities, however, were similar in magnitude to the impact velocities and were seen to scale roughly with kinetic energy of the impactor to the power 1/2, i.e. roughly linearly with impact velocity but with a dependence on the impactor mass. Neither total ejecta mass nor ϵ could be measured but the former also appeared to scale with kinetic energy.

Another important parameter may be porosity, usually quantified as the percentage filling factor of ice in the particle. Shimaki and Arakawa (2012) performed experiments in a drop tower in air with centimetre sized 'fluffy' snowballs. They also found little dependence on impact parameter or velocity, which they varied between $0.44 - 4.12$ ms^{-1}, and instead found a strong dependence on porosity; ϵ decreased with increasing porosity. At very low speeds there can be a transition from bouncing to sticking (effective $\epsilon = 0$) but Shimaki and Arakawa (2012) found this at all speeds with porosities of over 70%. Gundlach and Blum (2015) found smaller, micrometer sized, particles to be efficient at sticking together into aggregates under low temperature and pressure conditions, even up to 9.6 ms^{-1}, but that this decreased with increasing particle size to a metre per second or less for F ring sized dust (see their figure 12) and even less for the larger particles.

Conversely, for higher velocities particles may undergo fragmentation. This is quantified in terms of a critical specific kinetic energy, Q^*, in J/kg. This is usually defined as where half the mass is fragmented, leaving the largest remnant with 50% of the starting target mass, and it can vary with size and composition (Durda et al., 1998). Shimaki and Arakawa (2012) produce a map of collision outcomes, including Q^*, for various velocities and porosities (their figure 11) but only for equal cm-sized colliders. Hill et al. (2015) note small amounts of fragmentation at various velocities in their experiments but no critical disruptions.

All of this presents a confused picture, especially when considering the necessity of extrapolating to much larger objects. For real, icy ring particles colliding at metres per second a number of features seem likely however: low coefficients of restitution, with a weak trend for decreasing coefficient with increasing velocity, considerable scatter and an independence on impact parameter due to surface roughness. For collisions between large aggregate 'rubble piles' one must rely upon the results of computer simulations as will be discussed next.

3.2.2. Aggregate Collisions

Rubble piles (loosely bound aggregates of smaller objects) have been extensively studied in the context of both the asteroid belt and protoplanetary disks. Their interactions fall into two regimes: strength, where the outcome is governed by the material strength, and gravity, where gravitational attraction is the dominant cohesive force. Larger objects fall into the gravity regime with the change-over point uncertain but generally predicted to be around a few hundred metres to a kilometre in size (Durda et al., 1998). The critical disruption criteria in the gravity regime is

usually defined as the specific energy needed to scatter half the total mass with ve-
locities greater than the combined escape speed (Leinhardt et al., 2000). Aggregate
collisions are studied with a range of methods from lab based techniques (in the
strength regime, like those described above) to simulations using N-body codes and
smoothed particle hydrodynamics (SPH), which is most-often used for high velocity
cratering impacts (e.g. Benz and Asphaug, 1999).

A typical N-body approach is that taken by Leinhardt et al. (2000) who simulate
the collision of kilometre sized rubble piles at speeds less than ten metres per sec-
ond in free space. The aggregates are assembled from a large number (~ 500) of
randomly packed spherical particles (with densities of $2000 \ \mathrm{kg \, m^{-3}}$, corresponding
to rocky bodies) and their motion integrated with the N-body code PKDGRAV.
Two such aggregates are given bulk velocities in order to collide with each other and
the individual collisions resolved using the hard-sphere model with $\epsilon_n = 0.8, \epsilon_t = 1$.
Leinhardt et al. (2000) report a range of outcomes from complete merging, through
partial disruptions to catastrophic fragmentations, with the result being highly de-
pendent on collision speed and impact parameter. A variety of re-accreted remnants
are formed, including contact binaries and secondary and tertiary clumps, and in
cases with different sized impactors the smaller object generally completely dis-
rupts. Based on this, and other work, Stewart and Leinhardt (2009) proposed a
universal law for the mass of the largest remnant in a catastrophic disruption as a
function of collision energy. They first use the reduced mass, $M_{\mathrm{red}} = m_1 m_2 / M_{\mathrm{tot}}$,
to extend the specific kinetic energy to take into account unequally sized impactors:
$Q_R = 0.5 M_{\mathrm{red}} U^2 / M_{\mathrm{tot}}$. The critical disruption energy, Q_R^*, is then Q_R where the
mass of the largest fragment is $0.5 M_{tot}$. The universal law then states that this
largest remnant mass is a linearly decreasing function of Q_R / Q_R^* with a gradient of
-0.5. This result is 'universal' in the sense that it applies to impactors of different
masses, densites and mass ratios, but only for catastrophic disruptions and not low
speed merging and bouncing events.

Korycansky and Asphaug (2006, 2009) ran similar simulations using irregular
polyhedra instead of spherical elements, as well as a power law size distribution to
build up more realistic aggregates. The results were very similar: head-on collisions
led to merging at low speeds with increasing fragmentation as the impact velocity
increased until catastrophic disruption occurred. The largest fragment then followed
the universal law. Off-centred collisions typically resulted in two similarly massed,
re-accreted objets, departing from one another at higher than escape speed while
increasing the impact velocity led, once again, to complete disruption. When us-
ing the same coefficients of restitution as Leinhardt et al. (2000), Korycansky and

Asphaug (2006) did find a slightly lower Q_R^*. When using more dissipative values, including a tangential coefficient, they found a value approximately twice as large.

While the above simulations were performed in free space (i.e. with no external forces involved) planetary rings exist in a tidal environment which can significantly alter the outcomes of low velocity collisions. For accretion in free space the two particles' rebound velocities must be lower than their mutual escape velocity (constraining ϵ) whereas in a tidal field an additional constraint is imposed such that the particles' combined radius, $R_1 + R_2$, must not exceed their mutual Hill radius, R_H (Ohtsuki et al., 2013). The ratio of these quantities, $r_p = (R_1 + R_2)/R_H$, is a useful parameter for determining the outcome of collisions and Ohtsuki (1993) found that, from three-body calculations, accretion was prohibited for $r_p \geq 1$, difficult for $1 > r_p > 2/3$ and possible for $r_p \leq 2/3$. This scaled radius can be written

$$r_p = \frac{R_c}{a} \left(\frac{\rho}{3\rho_c} \right)^{-1/3} \frac{1 + \mu^{1/3}}{(1+\mu)^{1/3}} \qquad (3.21)$$

(Ohtsuki, 1993; Canup and Esposito, 1995), where R_c and ρ_c are the radius and density of the central body and ρ the density of the small objects, showing explicitly its dependence on the particle mass ratio, μ. Thus at a fixed density and radial distance from the central body only bodies of significantly differing sizes may aggregate. Large particles may accrete smaller ones but the merging of two large objects is impeded.

Walsh and Richardson (2003) investigated N-body collisions between aggregates in a tidal environment appropriate for the F ring by colliding spherical rubble piles (similar to those of Leinhardt et al., 2000 but with particle densities of 500 and 1000 $\mathrm{kg\,m^{-3}}$) at $1 - 10$ $\mathrm{m\,s^{-1}}$. In general they noted the density and coefficient of restitution (with values of $\epsilon_n = 0.5$ and 0.8) as being more important than mass ratio in determining collision outcomes. Complete accretion was rare but present (even for equal mass impactors) at low speeds but with a sharp cut-off with increasing velocity ($2 - 4$ $\mathrm{ms^{-1}}$ depending on ϵ_n and particle density). Walsh and Richardson (2003) did not investigate fragment size and velocity distributions but did find significant erosion at high velocities and mass ratios. In addition their figure 1 shows ejected particles strung out between two partially fragmented, equal sized aggregates.

Karjalainen (2007) made a more detailed study of collision outcomes with conditions appropriate for 135 000, 140 000 and 145 000 km radial distances from Saturn. They allowed aggregates to form in the tidal field (resulting in elongated ellipsoidal shapes) before placing them on circular orbits to collide with a range of impact

parameters, an ϵ_n from Bridges et al. (1984) and $\epsilon_t = 1$ based on Supulver et al. (1995). Karjalainen (2007) found a range of outcomes at the F ring distance, all with increased aggregation when compared to the three-body calculations of Ohtsuki (1993) and Canup and Esposito (1995) (i.e. looser constraints on r_p) due to the aggregates' ability to adjust their shapes to stay within their Hill spheres. Constructing the aggregates from a power law size distribution of particles further enhanced this. In partial disruption events 'bridges' of material again formed between the two large fragments (see their figure 2). Reducing the coefficient of restitution to $\epsilon_n = 0.1$ increased aggregation, equivalently to shifting the location radially outwards, as did setting $\epsilon_t = 0.9$. Finally, Karjalainen (2007) note that post-collision aggregates quickly settled down into synchronous rotation and that aggregate shape was important; more elongated aggregates were easier to disrupt.

Hyodo and Ohtsuki (2014) extended this work to collisions between eccentric and inclined objects by considering impacts in different directions. They used a similar setup of 1 km radius tidally accreted aggregates with $\epsilon_n = 0.5, \epsilon_t = 1$ and collided them at a range of velocities between 1 and 8 ms^{-1} in the orbital, radial and vertical directions in Hill's co-ordinates. Tidal effects were important for low velocities, with radial collisions, in general, less disruptive than longitudinal ones. This is because in the latter, material was spread radially by the impact and experienced Keplerian shear away from the clump whereas in the former it spread longitudinally and did not shear. Tidal effects decreased in importance as radial distances from Saturn, and collision velocity, increased. Higher velocity collisions led to decreasing remnant masses and, at large radial distances, agreement with the Stewart and Leinhardt (2009) universal law was found.

Both Hyodo and Ohtsuki (2014) and Karjalainen (2007) note that aggregation, partial fragmentation and disruptions are all present at F ring distances depending on the other parameters. In summary: at this fixed radial distance and assuming a fixed particle density the outcome of a collision between two aggregates will strongly depend on the collision velocity and direction, the mass ratio between the aggregates, the shapes and packing fractions of the aggregates and the normal and tangential coefficients of restitution, which may themselves depend on the particles' surface roughness.

4. Detection of Low-Velocity Collisions from Cassini

This chapter presents an overview of observing small-scale features in the F ring using the Imaging Science Subsystem (ISS) of the Cassini spacecraft. A particularly interesting feature, thought to be collisional in nature, has been discovered and is described in detail here. This feature is observed for approximately half an orbital period, revealing, in unprecedented detail, its evolution and orbit, relative to the F ring core, and shedding light on the process of collisions and the unseen population of nearby objects. Analysis of this feature has previously been published as a letter to the *Astrophysical Journal* (Attree et al., 2012) but additional discussion is presented here.

Section 4.1 gives a brief overview of the ISS instrument and details how the images are navigated ('pointed'), analysed, and measurements made from them. The different types of observing sequences used, and the process of turning them into mosaics, are described in Section 4.2. Next, the detection of the interesting feature is presented in Section 4.3, with the analysis techniques used in 4.3.1. Possible formation mechanisms and their implications are discussed in Section 4.4 before conclusions are drawn in Section 4.5.

4.1. Cassini's Imaging Science Subsystem

ISS consists of two separate cameras: the wide angle camera (WAC) and the narrow angle camera (NAC). Both are mounted together on the remote sensing pallet with the same, fixed, pointing direction but differ in their optical properties. The WAC is a refracting telescope with a 0.2 m focal length and a wide, 3.5°, field of view. The NAC is a reflecting, 2 m focal length telescope with a much narrower 0.35° field of view (Porco et al., 2004). Each camera has a pair of filter wheels that can rotate a variety of colour filters in front of the detector to observe at different wavelengths. Detectors are the same for both cameras: charge coupled devices (CCDs) with

1024 by 1024 pixels giving an angular pixel size of 59.749 and 5.9907 μradians, respectively, for the WAC and NAC. The point spread functions are slightly larger than one pixel at 1.8 and 1.3 pixels, respectively. Images are sampled at 12 bits but many are down-sampled to 8 bits, giving either 256 or 4095 discreet brightness levels, or data numbers (DN), per pixel.

4.1.1. Processing Cassini Images

Images are downlinked from Cassini via NASA's Deep Space Network and stored locally as VICAR files, with the $.IMG$ extension. Each has an associated $.LBL$ label file giving the timing, pointing and camera information at the time of exposure. Images are numbered sequentially, proceeded by an 'N' for NAC or 'W' for WAC images. Bespoke software written in IDL, called CAVIAR for CAssini VIsual Image Analysis Release, is used for viewing and analysing the images. Figure 4.1 shows what a typical raw image looks like when loaded into CAVIAR. Also shown is the image plane co-ordinate frame used to describe the location of feature within an image. The centre of each pixel is described by its line and sample coordinates, (l, s), both of which run from one to 1024[1]. The optical axis is through the centre of the image at $(l, s) = (511.5, 511.5)$ pixels. Positions of real objects in inertial space can be transformed to line and sample pixel coordinates, using the camera matrix (Porco et al., 2004), provided that the position of the spacecraft and the vector direction of the optical axis are known. Default navigation involves using the predicted positions of Cassini and pointing information (right ascension, RA, and declination, DEC, of the optical axis) from the label file. Cassini's position is based on ephemeris files called kernels provided by the SPICE system of the Navigational and Ancillary Information Facility at `ftp://naif.jpl.nasa.gov/pub/naif/toolkit_docs/C/info/intrdctn.html`. Small errors of position and orientation are always present in these reconstructed orbits, however, which can lead to significant pixel offsets. In order to make accurate measurements they must be corrected and the pointing information updated in a process called 'pointing' an image. This is done manually, usually using background stars, following the method described below.

- The 'unpointed' image is loaded into CAVIAR. The default pointing information is used to plot predicted locations of ring edges and moons, from ring models and ephemerides built into the SPICE kernels, and stars, from the

---

[1]Note that this is different to the standard IDL image coordinate system which would here run from zero to 1023.

Tycho 2 and UCAC 2 surveys (Høg et al., 2000; Zacharias et al., 2004) onto it. Fig. 4.1a shows this.

- The predicted positions are manually navigated (clicking and dragging with a mouse) so that they line up with the visible features in the image. In effect one is dragging the pointing vector of the optical axis around.

- An iterative procedure is then used to fit the predicted positions to the centroids of bright peaks, identified by the software as stars, by incrementally varying the pointing vector RA, DEC and $Twist$ (a rotation angle around the optical axis).

- The best fit RA, DEC and $Twist$ are saved in a $.QMPF$ Queen Mary Pointing File which is used instead of the default pointing whenever the image is subsequently loaded into CAVIAR. The image is now considered pointed (shown in Fig. 4.1b).

Typical RMS residuals are ~ 0.1 NAC pixels or 0.59907 μradians. Some images have very few visible stars and are harder to navigate but pointing inaccuracies seldom approach or exceed a single pixel.

Once an image has been accurately pointed its pixels can be mapped to positions in the ring plane, assuming a model for Saturn's pole direction and the radii of ring features, both of which are provided in the kernel files. Angles such as the normal to the ring plane, elevation angle of the spacecraft with respect to it and phase angle (Sun to ring-plane intercept to spacecraft angle) can also be computed. Positions in the ring plane are measured in a planetocentric, cylindrical polar co-ordinate frame with radius, r, (in kilometres from Saturn's centre) and inertial longitude, λ. Zero inertial longitude is referenced to the position of the ascending node of Saturn's equatorial plane on the Earth's mean equator at the J2000 epoch. Longitudes can also be defined relative to a point which rotates around the planet with a certain angular speed, n. This co-rotating longitude, λ_n, is then related to inertial longitude by

$$\lambda_n = (\lambda + n\Delta t) \bmod (360°), \tag{4.1}$$

where Δt is time, in Julian days (JD), since some reference epoch and mod is the modulo function, which ensures that the longitude is between zero and 360°. The reference time and angular speed used here are 12:00:00 on January 1st, 2007 (JD = 2454102.5) and $n = 581.96°\mathrm{d}^{-1}$, respectively.

(a)

(b)
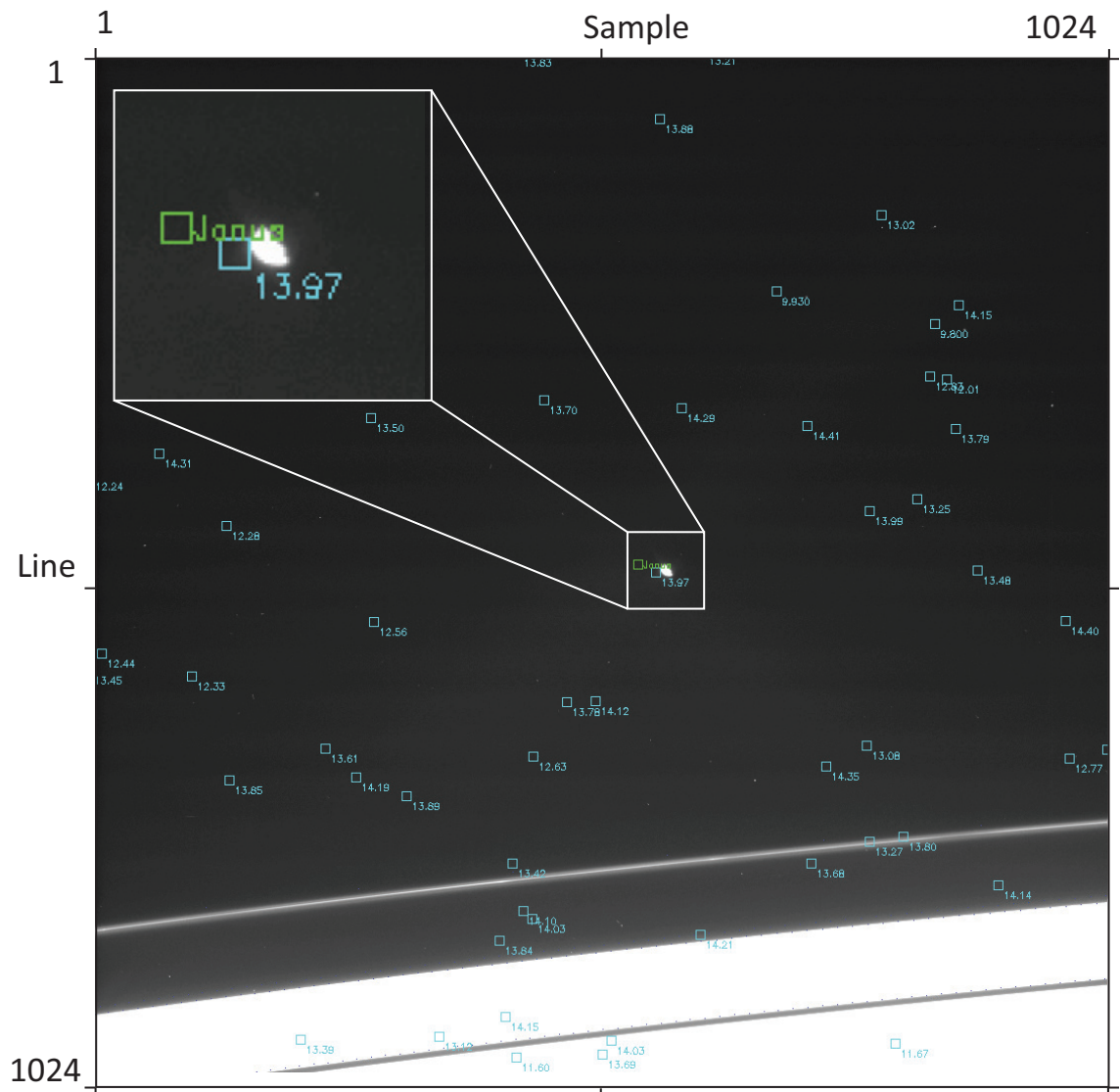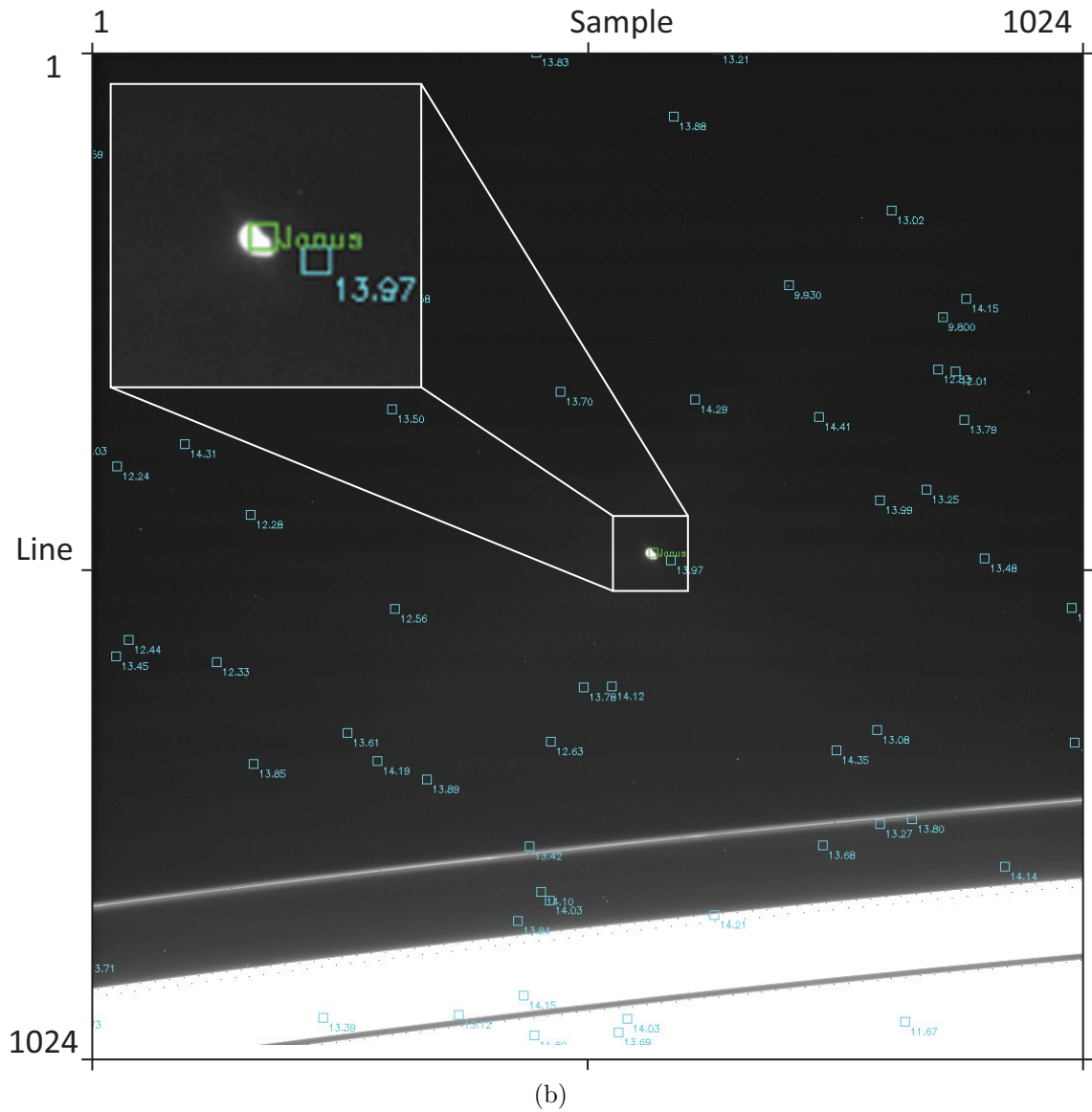
Figure 4.1.: Example of pointing an ISS image, number N1801731368, taken February 4th, 2015. a) image displayed in CAVIAR with the default pointing information. Teal boxes highlight predicted locations of background stars (numbers are their magnitude) and green, predicted location of moons. b) after pointing by manually matching predicts to stars, followed by iterative refinement. The predicted location of Janus now matches, but note, only the background stars were used for pointing. RMS residuals are 0.17136 pixels. Contrast and brightness have been enhanced to find the stars.

4.2. F Ring Observations

Observations of the F ring are mostly made though the clear filters, with the NAC and WAC, at a variety of geometries and distances. NAC images are used here, almost exclusively, due to their higher resolution. Exposure times vary with observing phase and are typically between 100 and 1800 ms. Images are taken in groups called observation sequences. These contain anywhere between two and several hundred images and are given a name based on the target, the primary instrument being used and the Cassini orbit (rev) number. For example, sequence ISS_085RF_FMOVIE003_PRIME was taken during rev 85 with ISS as prime instrument and is the third of the FMOVIE, i.e. F ring movie, type sequences proposed for this rev. Observations of the F ring usually fall into one of the following categories:

- FMOVIE, or F ring movies, typically contain ~ 100 NAC images taken over a period of several hours. Pointing is at a fixed inertial longitude allowing the F ring to rotate through the field of view and the imaging frequency ($\sim$ every four minutes) is chosen such that each image captures a new co-rotating longitude of ring, with some small overlap. Imaging for a full F ring orbital period then builds up complete coverage in co-rotating longitude, all at approximatetely the same inertial longitude and orbital phase[2].

- FRSTRCHAN, or F ring streamer-channel movies, are designed to track Prometheus's perturbation on the ring around its orbit. Camera pointing is updated before each image to follow a single piece of ring through inertial space. The ~ 100 or so images in a typical streamer-channel movies then sample roughly the same co-rotating longitude at a range of inertial longitudes and orbital phases.

- AZSCAN, or azimuthal scans, are similar to FMOVIES but scan along the ring in inertial space with each image to build up full or near full longitude coverage. AZSCAN images therefore sample a range of both inertial and co-rotating longitudes and were only taken near the beginning of the mission.

- SATELLORB, or satellite orbit observations, do not target the F ring at all but rather track Saturn's moons for astrometric purposes. When observing nearby moons such as Prometheus or Pandora, however, the F ring is often visible. SATELLORBs consist of pairs of NAC images, separated by a few

---

[2]M will actually vary slightly across the images of the FMOVIE due to precession of the periapse, at a rate of $\sim 2.7°$ d^{-1}, but the difference is small for a single orbit.

minutes, taken sporadically in time and longitude. They provide random, intermittent coverage in co-rotating and inertial longitude.

- A small number of miscellaneous other types, such as high-resolution F movies, HIRESFRNG, some of which follow a section of the ring in a similar way to streamer-channel movies. Others include ride-along images of stellar occultation events, for example L2PUPOCC, where L2 Puppis is the name of the star.

The various methods of observation are complimentary to one another. FMOVIEs and AZSCANs typically provide the best co-rotating longitude coverage, producing large scale 'maps' of the F ring which show the overall structure at a particular time. Streamer-channel movies and HIRES movies, on the other hand, show the time evolution of a limited section of ring, revealing how specific structures change over their orbit. SATELLORBs provide an additional tool for sampling the ring in a random way or, when fortunately timed, tracking individual features.

For each FMOVIE and AZSCAN a mosaic composed of every image in that sequence is constructed. This is done by re-projecting the images into a radius-longitude frame by mapping each pixel onto a cartesian grid corresponding to its ring-plane coordinates. A sampling of 1px/km in radius and 300px/deg in longitude is used with bi-linear interpolation. Images are re-projected to ± 750 km in radius, relative to that of the predicted F ring core at that time and longitude, based on the Cooper et al. (2013) model (see Table 2.1), thus removing the eccentricity from the resulting mosaic. Images are then placed according to their co-rotating longitude (computed using the epoch and mean motion from above) and stitched together into a single image file at a common resolution and frame. Where image coverage overlaps the portion of the image with the best radial resolution is manually chosen. The result is a single *.png* image file for each observation sequence measuring 1501×108000 pixels. Features with a semi-major axis corresponding exactly to n will sit at a certain longitude between mosaics while those with a Δa will shift left or right at a rate given by Eqn. 3.6. Relative eccentricity will cause features to move up and down in radius but their longitudinal epicycle motion is compressed by the aspect ratio. The F ring's own eccentric motion causes a slight longitude difference between features in different mosaics, of up to $\pm 2ae \approx 712$ km (about 87 pixels) which can be seen in some, especially opposite ansa, sequences.

Mosaics have been generated over the duration of Cassini observations (165 as of the beginning of 2015), providing an invaluable 'map' of the F ring. Mosaics are given a short name (compared to the full sequence designation) corresponding to

the first four digits of the first image number in them. Where subsequent mosaics would have the same four digits they are given an alphabetical letter extension, e.g. 1756-A. Opposite ansa sequences, or those with two different exposure times, are split into two separate mosaics and labelled 1 and 2, e.g. 1750-1 and 1760-2.

Mosaics are particularly useful for looking at large-scale structure and so will be used extensively later in this thesis. The rest of this chapter is concerned with features at the smaller scales, however, so individual images are predominantly used here.

Collisional Features

Mini-jets, like the feature in Fig. 2.4, are seen in all types of imaging sequence throughout the Cassini tour. For the purposes of identification they are defined as small-scale, roughly linear features, typically $\sim$ 20–150 km in radial extent and $\ll 1°$ in longitude, emanating from the core. This excludes kinks and bright clumps which lie entirely within the core, as well as identifiable fans, but includes a variety of morphologies, as will be discussed in the next chapter. Visible numbers are $\sim$ 10 in the ring at any one time but most are only observed in one or two images over the course of $\sim$ 10 minutes, and are not seen again. Any relative orbital motion is small over such a short timeframe, limiting the opportunity to interpret the features and discern their orbital elements. Streamer-channel movies provide the best hope for seeing the evolution of a mini-jet over an extended period. Examining these sequences, a single clear mini-jet has been found, visible for $\sim$ 7.5 h in ISS_102RF_FRSTRCHAN001_PRIME. The rest of this chapter presents analysis of this feature.

4.3. Study of a Time-Resolved Collisional Feature

The ISS_102RF_FRSTRCHAN001_PRIME sequence contains 201 NAC images, tracking Prometheus and its perturbation around the ring over a full orbit on January 30th, 2009. The mini-jet appears in 138 images, each separated by $\sim$ 4 minutes, meaning it is visible for approximately half an orbital period: $\sim$ 7.5 h. The first frame in which it appears is N1612002457 at 09:47:26, shown in Fig. 4.2.

The feature appears as a linear protrusion at an angle from the F ring core. This angle is seen to decrease with time whilst the tip moves radially inwards towards the ring. The feature is relatively narrow ($\sim$ 30 km across), with sharply defined edges, where the image DN drops to background levels, at the tip and trailing edge

(opposite to orbital direction). On the leading edge (positive l direction) there is a faint 'spray' of material (see enhanced inset to Fig. 4.2) connecting the feature, at an angle, to the core upstream of it. Also visible is a faint object, located just past the tip of the feature at a similar radius but slightly greater longitude. The object is about two pixels across, corresponding to ~ 10 km, and may be a solid moonlet or a particularly bright clump of dust. Both the 'spray' and the object follow the feature as it collapses back into the core, so are most likely associated with it.

Measurements of the location of the tip, object and base of the feature have been made in each image. This is done by hand in CAVIAR with the images first pointed as above. Pixels then correspond to radius/longitude coordinates in the ring plane and their positions are recorded in both l, s and r, λ coordinates by zooming in and clicking. An attempt is made to select the same portion of the feature for measurement each time but there is significant scatter as its appearance and the viewing geometry change. The tip is measured as the single bright pixel at the end of the feature before the sharp drop in brightness. The base is taken as a pixel in the rough centre of the core where the line of the feature, extrapolating by eye, intersects it. The object is measured at the brightest pixel in the small cluster of bright pixels just past the tip. The measured ring-plane co-ordinates for the tip (r_{tip} and λ_{tip}) and base (r_{base} and λ_{base}) are listed in Appendix A. Uncertainties are assumed equal to the pixel sizes: ~ 5 km in the radial direction by $\sim 0.01° \approx 30$ km in the longitudinal direction.

A portion of each image is also re-projected into radius/longitude space and a movie constructed from the resulting frames. This is done by selecting a region ± 200 km in radius and ± 400 km in longitude from the measured base position in each image. The pixels in this region are each mapped to a ring-plane coordinate and re-projected so that they lie on a cartesian grid according to this radius and longitude. Pixels are sampled at one kilometre resolution in both directions, using bi-linear interpolation, producing an equal aspect ratio re-projection. The left-hand side of Fig. 4.3 shows three frames from this movie. The mini-jet appears as a linear feature at an angle from the vertical (i.e. radially outwards direction) which increases with time whilst its tip moves radially inwards towards the ring.

4.3.1. Analysis

Measurements of l, s coordinates in each image, combined with the known spacecraft position, allow an orbit to be fitted. Fits of the orbital elements for the tip of the mini-jet, the object next to it and the F ring core at the time of observation are
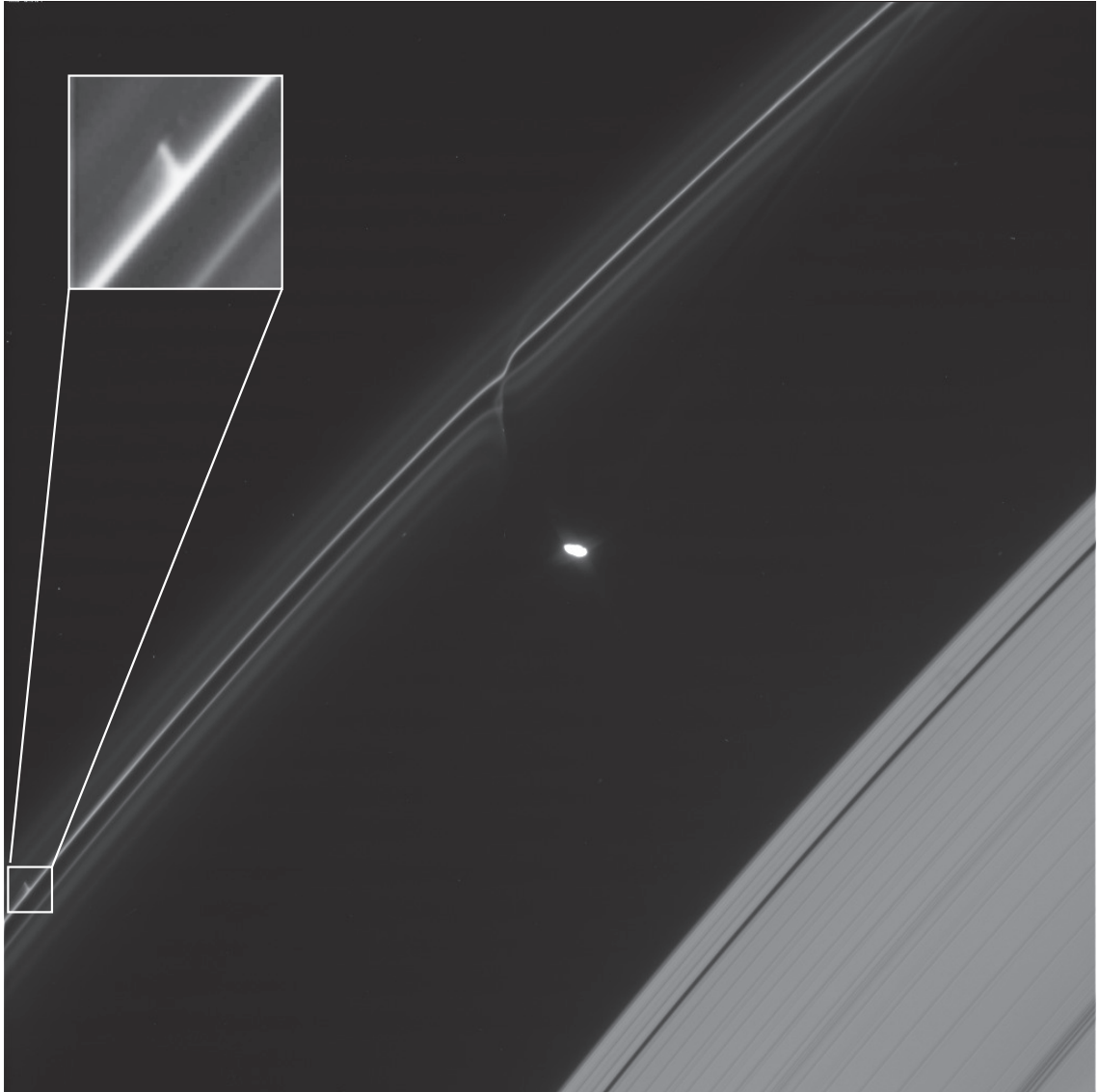
Figure 4.2.: NAC image N1612002457, taken January 30, 2009 at 09:47:26 with a 1.5
s exposure and showing $\sim 6°$ of ring. A ~ 50 km mini-jet is highlighted
and enhanced in the inset. Note the faint but traceable object which
appears just beyond the jet 'tip' as well as the faint 'spray' of material
which connects the leading (left) side of the jet to the F ring core. This
is the first in a sequence of 138 images, each separated by ~ 4 minutes,
which capture the evolution of this feature. Previously published in
Attree et al. (2012).
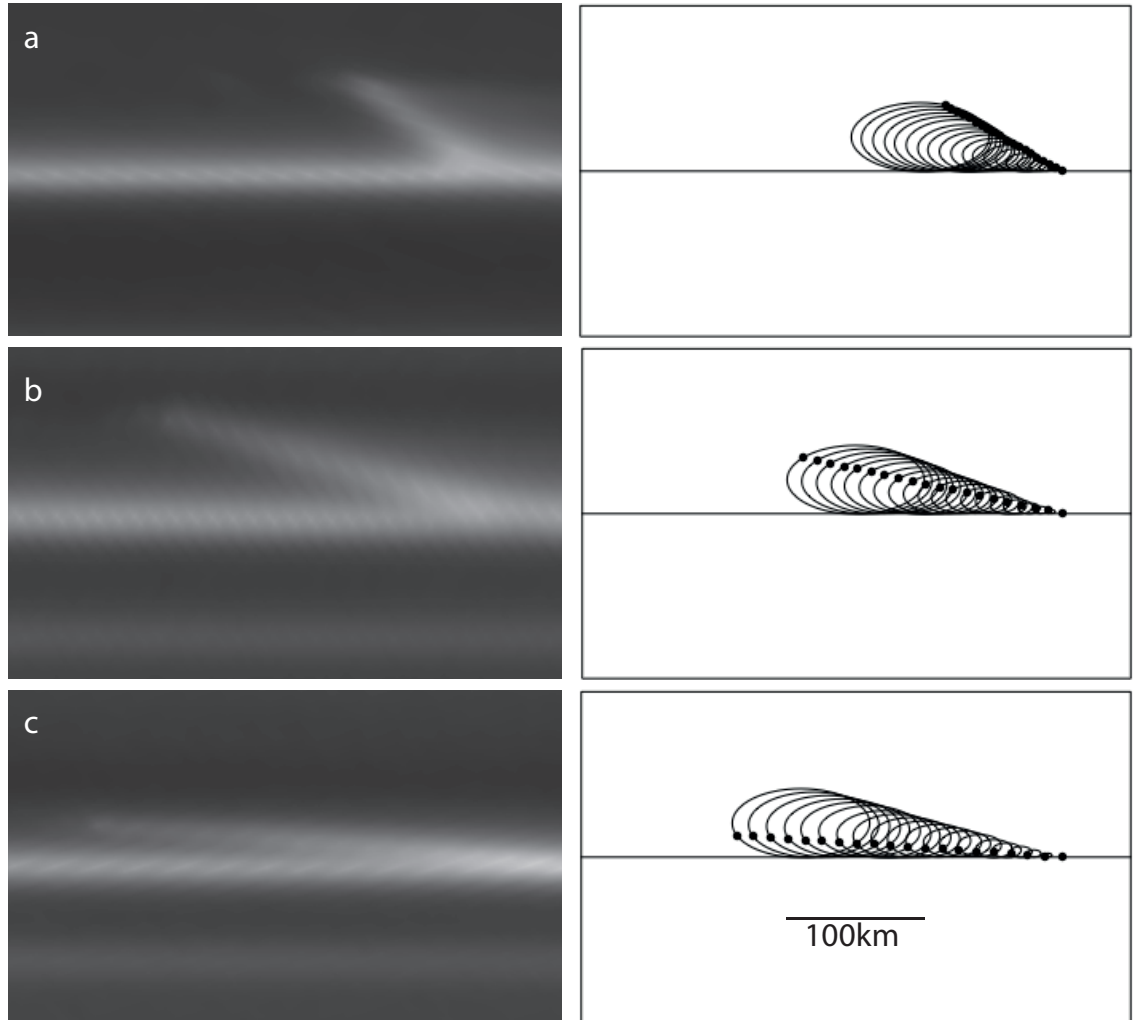
Figure 4.3.: Left: Re-projected ISS NAC images separated by $\sim$ 3 hours. Images are (a) N1612002457 (b) N1612013501 (c) N1612022286. Right: corresponding frames from an animation of particles (denoted by filled black circles), displaced from the ring by a range of Δa and Δe, undergoing relative orbital motion. The particles follow epicyclic paths around the ellipses with centres that drift downstream (to the left) at a constant rate due to Keplerian shear. The re-projected images and the animation are to the same scale and each covers 400×220 km. Previously published in Attree et al. (2012).

	a (km)	e ($\times 10^{-3}$)	i ($^\circ \times 10^{-3}$)	Ω ($^\circ$)	ϖ ($^\circ$)
Core	$140\,215.1 \pm 0.2$	2.3108 ± 0.0008	6.3 ± 0.1	$102.3 \pm\ 0.7$	341.98 ± 0.02
Tip	$140\,242\ \pm 4$	$2.51\ \pm 0.03$	$5\ \pm 1$	$70\ \pm 10$	$340.9\ \pm 0.5$
Object	$140\,246\ \pm 8$	$2.51\ \pm 0.05$	$4\ \pm 2$	$86\ \pm\ 9$	$340.8\ \pm 0.7$

Table 4.1.: Orbital elements for the F ring core, mini-jet tip and mini-jet object at the epoch January 30th, 2009 at 09:45:00:00. Orbit fits performed by Nick Cooper.

presented in Table 4.1. The F ring core orbit is derived from a geometric fit to the bright core, over one orbit, from the same image sequence, as in the method of Cooper et al. (2013). It therefore represents a precise local snapshot of the core orbit in the vicinity of the mini-jet rather than using the global average of Table 2.1. The tip of the mini-jet is displaced from the core by $\delta a = 27 \pm 4$ km in semi-major axis and $\delta e = 1.992 \pm 0.3 \times 10^{-4}$ in eccentricity, for a combined relative eccentricity of $a\Delta e \approx 28$ km (uncertainties are derived from the tip measurement errors which dominate). The rest of the mini-jet material must have similar, but smaller, relative orbits with $\Delta a \approx a\Delta e$ for the whole structure.

The evolution of the feature with respect to the F ring core, as shown in Fig. 4.3, can now be understood as a combination of Keplerian shear and epicycle motion. As shown in Chapter 3, objects on moderately eccentric orbits can be thought of as travelling on ellipses of semi-axes, ae, and, $2ae$, around a guiding centre which itself follows a circular path around the primary (Murray and Dermott, 1999). The mini-jet is composed of a number of particles displaced from the F ring by a range of Δa, Δe which will each follow their own centred ellipse relative to the ring. At the same time the Δa offset leads to Keplerian shear of the guiding centres of each ellipse. The combined effects lead to the motion of the jet radially inwards towards the ring whilst it simultaneously lengthens downstream in longitude. This is exactly half of the motion of the example ejecta cloud sketched in Fig. 3.6, i.e. only the ejecta in one hemisphere (the negative Δv_l one) is present. A further illustration of the epicycles is shown to the right of the re-projections in Fig. 4.3.

In order to compare the feature with the theory of Section 3.1 its gradient in each image is calculated. From the measurements

$$\theta = \tan^{-1}\left(\frac{r_{\text{tip}} - r_{\text{base}}}{a(\lambda_{\text{tip}} - \lambda_{\text{base}})}\right), \tag{4.2}$$

where a is the F ring semi-major axis and the longitudes are converted to radians. Gradient is plotted against day-of-year in Fig. 4.4. The theoretical curve for the
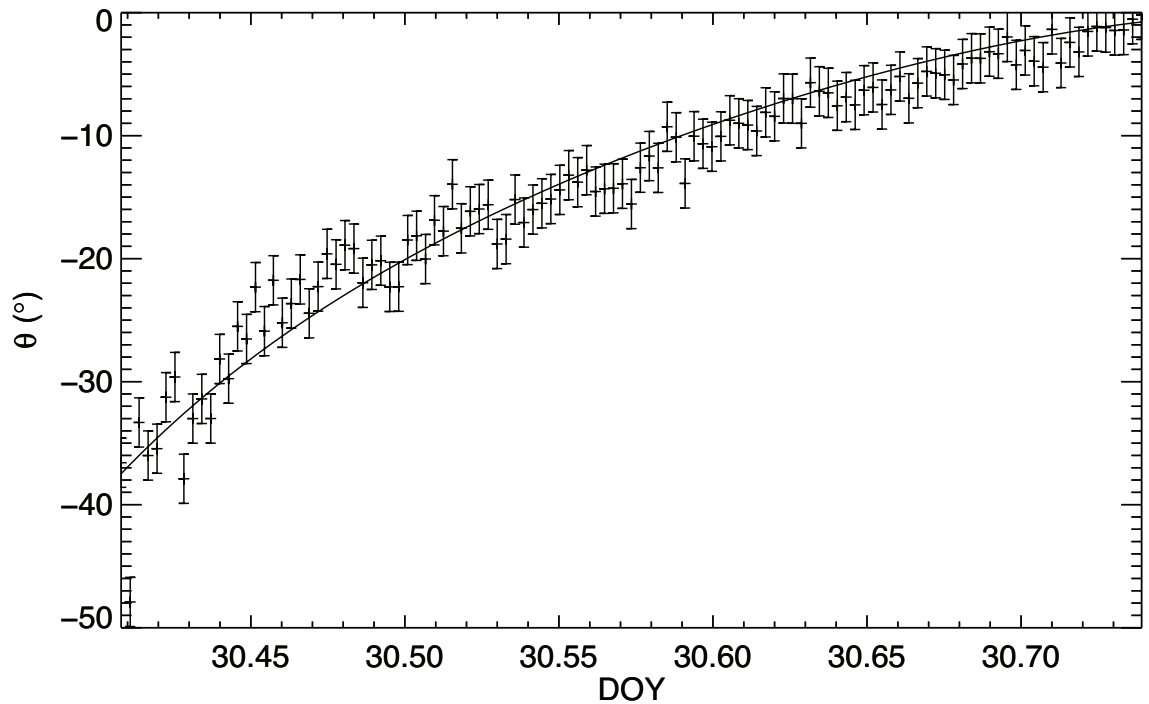
Figure 4.4.: Measured gradient, θ, of the mini-jet feature over time (day-of-year). The curve from Eqn. 3.8 is over-plotted, fitted to the data for the formation time t_0. Uncertainties are taken as $\pm 2°$.

time-evolution of a $\Delta a = a\Delta e$ feature (Eqn. 3.8) is then over-plotted. The curve has been fitted to the data for t_0, the time when all the particles were in the core together at periapse, and yields excellent agreement ($\chi^2/DOF = 1.18$). Here uncertainties are taken as a constant $\pm 2°$, rather than carrying through the uncertainties in measured coordinates, as these formal errors are much smaller ($< 0.3°$) than the visible uncertainty in the gradient. This is because of the feature's blurred, extended appearance, relative to an infinitesimally thin line, and is reflected in a much better chi-squared fit statistic for $\pm 2°$ than with the formal errors.

The formation time is $t_0 = 30.171 \pm 0.00148$ DOY, with the derived error from the fitting routine, assuming that the feature is on its first cycle. This is 5.69 hours before the first observation so the mini-jet is observed between 38% and 92% of its orbital cycle. The orbital phase of the ring at the formation time is $f \approx 328.43°$.

Towards the end of the movie the mini-jet re-enters the ring and becomes difficult to resolve. If the particles' orbits are unchanged they will follow their epicycles radially outwards towards apoapse again and the feature should re-emerge from the core. However, it is possible that the mini-jet may not survive re-collision with the F ring core. In this example the issue is complicated by the presence of Prometheus

which, by chance, reaches its closest approach near the longitude of the mini-jet and most likely perturbs it gravitationally. The relevant section of co-rotating longitude has been examined in the preceding and succeeding sets of observations and no definitive detection of a re-merging mini-jet, or any precursor feature, has been made.

4.4. Discussion

What physical processes can result in a ~ 27 km change in a ring particle's semi-major axis and eccentricity on a short timescale? The mini-jet is clearly a local phenomenon, with the particles making it up coming from an essentially point source. It is not associated directly with the Prometheus perturbation, being located upstream from it in a section of ring which has not undergone a close encounter for much longer than the feature's observed lifetime. Other large bodies capable of such gravitational interactions have not been detected and in any case would produce features with positive *and* negative values of Δa (Beurle et al., 2010), more similar to fans or streamer-channels. Non-gravitational forces such as radiation pressure, Poynting-Robertson and plasma drag are not expected to be important on such short timescales (hours or days versus thousands or tens of thousands of years Burns et al., 2001), or over such limited sections of ring. This does not rule out such processes having a subsequent effect on the dissipation of the feature.

Physical collisions, however, *are* able to create similar, and even larger, features over short timeframes (Charnoz, 2009). Following the method of Chapter 3, a collision should deliver an effectively instantaneous velocity impulse, $\boldsymbol{\Delta v}$. One can work backwards from the orbital elements of the tip of the mini-jet to find this: rearranging Eqn. 3.10 and substituting into Eqn. 3.11 gives

$$\Delta v_l = \frac{na\delta e/\sqrt{1-e^2} - (\delta an\sqrt{1-e^2})/2e}{2\cos f - (1 + e\cos f)/e};$$

(4.3)

an expression for the longitudinal velocity impulse in terms of the observed orbital changes. Likewise, rearranging Eqn. 3.11 and substituting into Eqn. 3.10 gives

$$\Delta v_r = \frac{an\delta e/\sqrt{1-e^2} - 2n\delta a\cos f\sqrt{1-e^2}/2 + 2e\cos f}{\sin f - 2e\cos f\sin f/1 + e\cos f}$$

(4.4)

for the radial component.

Using the F ring orbit from Table 4.1, with $f \approx E \approx 328°$ at t_0, with values of δa

and δe from above, Eqns. 4.3 and 4.4 give

$$\Delta v_l = 1.6 \pm 0.2 \text{ ms}^{-1}, \qquad \Delta v_r = -1.1 \pm 1.7 \text{ ms}^{-1}$$

for the maximum impulse, where errors have been estimated using the uncertainties in δa and δe quoted above. The rest of the particles which make up the jet receive impulses of smaller magnitudes, between this and zero. The ratios of the two components (vertical impulses are ignored for now), i.e. the orientations of the $\boldsymbol{\Delta v}$ vectors for the remaining particles, are unknown. Considering the feature's linear, $\Delta a \approx a\Delta e$, shape and relatively narrow width (small spread in relative eccentricities) the velocity distribution must be primarily in the longitudinal direction and the orientations similar. The specific orientation and position of each particle may vary but is clearly less sensitive to the radial component.

The velocity vector of the collider remains unknown, and degenerate, without further assumptions. Two possible models for delivering this $\boldsymbol{\Delta v}$ present themselves; that of high velocity, external impacts or that of low-velocity local collisions.

Meteoroids from outside the Saturn system are expected to bombard the rings, producing a range of features such as spokes (Smith et al., 1981, 1982), optical depth variations due to ballistic transport and bright, shearing clouds in the main rings (Tiscareno et al., 2013). Impact velocities at Saturn depend on the source of the material (e.g. Oort cloud or elsewhere) but are of order the escape speed (Cuzzi and Durisen, 1990), ~ 23 kms^{-1}, at the F ring. At these high velocities ring particles are likely to fragment if struck by meteoroids with a mass $> 10^{-7}$ their own (Benz and Asphaug, 1999), forming a cloud of ejecta. Otherwise a cratering event will take place with ejecta particles excavated from the target. In either case material ejected from the ring can easily be given velocities of a few metres per second. For targets and impactors of similar density the mass ratio above corresponds to a size ratio of ~ 200 so $\sim$ cm-sized meteoroids can fragment ring particles several metres in radius. This is the mechanism posited by Showalter (1998) to release dust in the bright, extended clumps.

Clouds of debris released from comets also strike the rings, producing kinematic spirals in Saturn's C and D rings and Jupiter's main ring (Hedman et al., 2007, 2011a; Showalter et al., 2011; Hedman et al., 2015). In these cases a large mass of dust is thought to impact over several days, displacing most of the ring material in a region perhaps $\sim 10°$ by thousands of kilometres in radius. Impacts on this scale are clearly not applicable to the mini-jet here but may be relevant when discussing the larger F ring features, as later in Chapter 6.

In the case of catastrophic disruptions ejecta distributions approach an isotropic form, producing a circle in $\Delta v_l, \Delta v_r$ space. Experiments sometimes show this offset in the direction of the incoming trajectory and elongated in the perpendicular direction (Zappalà et al., 1996; Leinhardt et al., 2000). Ejection velocities vary with impact energy and are a decreasing function of fragment size, with small particles ejected at very high velocity (kilometres per second) along the impact direction (Cuzzi and Durisen, 1990). Larger ejecta particles are given much lower velocities, $\sim 1 - 100$ ms^{-1} (Cuzzi and Durisen, 1990), with the largest fragment moving the slowest: around the original target body's escape speed for gravitationally dominated impacts (Benz and Asphaug, 1999). As impact energy increases above the catastrophic disruption threshold ejecta particles will decrease in size, as per the universal law, and ejection velocities increase.

At lower energies, below the disruptions threshold, material is ejected from the impact point in a cone shaped spray, excavating a crater on the surface of the ring particle. This ejecta cone is centred on the incoming trajectory for normal impacts (i.e. the majority of material is ejected back in the direction of the impact) and canted away from it, by the impact angle, in oblique events (Cuzzi and Durisen, 1990). The cone opening angle is seen to be around 120° in experiments (Zappalà et al., 1996) with most of the ejecta concentrated within 45° (Cuzzi and Durisen, 1990). Ejection velocities are, again, $\sim 1 - 100$ ms^{-1} and the total mass of material in the cone, normalised by impactor mass (the yield factor), varies with impact velocity and material but is typically $10^4 - 10^6$ (Cuzzi and Durisen, 1990).

Thus, hypervelocity impacts can easily generate enough material at appropriate velocities to form the mini-jet. Some details of the feature are difficult to explain in this model however. Fragmentation is expected to create isotropic distributions, resulting in double sided features, like that sketched in Fig. 3.6 and seen by Tiscareno et al. (2013) in the main rings. An offset in the impact direction could shift the distribution to being mostly one sided but it is unlikely for no particles at all to be ejected the 'wrong way'. Cratering events with narrow ejecta cones will lead to a tight 'jet' of ejecta in one direction but, with roughly isotropic impacts, this will be randomly oriented in space. Orientations purely along, or against, the orbital direction would lead to a distribution like the mini-jet but, considering the cone opening angles, some material is expected to be ejected in the other direction, again at odds with the single sided feature seen. Additionally there should be a size distribution across the length of the feature with larger particles near the base (low ejection velocity) decreasing to smaller particles at the tip (higher ejection velocity), as well as a population of extremely high velocity ejecta. The observed mini-jet is

relatively uniform across its length and also has a large object near the tip. If this is the largest ejected fragment it should not be found here in this model.

What about a low-velocity collision involving a nearby moonlet? This will follow different physics from hypervelocity impacts but might also be expected to spread material at $\sim$ metres per second from collisions of a similar velocity.

Microgravity cratering experiments, with regolith targets at low-velocity ($\sim$ 1 ms^{-1}), also produce ejecta cones (Colwell, 2003; Colwell et al., 2008). Ejected velocities are ~ 1 ms^{-1} with a power law fall off and cone angles and orientations similar to the hypervelocity case. Excluding the high-velocity ejecta component then, the results of all cratering impacts will appear similar and the same comments from above apply here.

What about larger impactors? As shown in Chapter 3, the dynamics of hard sphere collisions between a massive moonlet and an essentially massless dust particle gives the dust grains a $\boldsymbol{\Delta v}$ approximately equal to the impact velocity. Such a moonlet, ploughing through the F ring at ~ 1 ms^{-1}, would therefore pick up dust, scattering it from its surface (depending on the coefficient of restitution and specific geometry) to form a shearing structure, like Fig. 3.6, but centred on the moonlet. The mini-jet may be such a structure with the colliding moonlet embedded within it, somewhere in its bright centre. In the converse scenario, simulated by Charnoz (2009), a loose clump of dust on a nearby orbit instead strikes a moonlet embedded in the core. Scattering from its surface leads, again, to a mini-jet like structure centred on the moonlet which, this time, would lie at the base of the feature, in the core. Simulations in Charnoz (2009) typically show double-sided features but these used the orbit of S6 which, with its large relative eccentricity, crosses the core. A dust clump with a $\Delta a \approx a\Delta e$ orbit, striking an embedded moonlet head on, could potentially result in only positive Δv_l. If local moonlets are themselves aggregates of smaller particles, loosely bound by gravity, then they are liable to breakup, even in low-velocity collisions. This may be the case both for the colliding object and a hypothetical target aggregate, embedded in the ring. Simulations of such disruptions were reviewed in Section 3.2.2 and typically show spreading of material perpendicular to the impact direction at similar velocities to those discussed here (Hyodo and Ohtsuki, 2014). Partial disruptions, where two large remnants survive or re-accrete after the collision, have been shown to spread ejecta between the orbits of the two (Leinhardt et al., 2000; Walsh and Richardson, 2003; Karjalainen, 2007; Hyodo and Ohtsuki, 2014). If the bright object is the remnant of the colliding aggregate, with the target clump hidden in the core, then this scenario is an extremely plausible one for dragging out ejecta between them to form the mini-jet. The object is thus

a good candidate for the colliding body and, if this mini-jet is typical, for one of a population of such nearby objects.

4.5. Conclusions

This chapter investigated the phenomenon of mini-jets— small-scale, irregular features in Saturn's F ring. Cassini observations have shown the time evolution of a mini-jet to be a combination of Keplerian shear and epicycle motion resulting from an initial displacement in semi-major axis and eccentricity. This displacement is consistent with the impulse from a collision with a small (~ 1 km) object on a nearby orbit. If this is typical of small-scale F ring features it reinforces the notion of Murray et al. (2008), and other authors, that the ring is shaped by a local moonlet swarm, in addition to the gravitational effect of Prometheus.

ISS has been used to obtain 10 streamer-channel movies to date, and together they represent 27.99° d of coverage (time and longitude coverage are both important for observing over significant portions of an orbit). With only one mini-jet event observed, this is a frequency, $\nu = 0.036°^{-1}\mathrm{d}^{-1}$ or ~ 13 in the entire ring per day. The number of mini-jets observed at any one time in the ring should be $N_{mj} = \nu \tau_{mj}$, where τ_{mj} is the average lifetime. In addition mini-jets will only be visible when radially extended outwards or inwards from the core, which is the case for 70–80% of a cycle for $\Delta a = 27$–50 km size jets and a 10 km thick core, respectively. With a lifetime of ~ 1 cycle $= 0.6196$ d, ~ 8 mini-jets should visible in the F ring at any one time.

A population of objects originating in the F ring but gravitationally perturbed by Prometheus should be spread around the ring with a range of orbital parameters up to a maximum of $\Delta a = \pm 19$ km, $\delta e = \pm 13 \times 10^{-5}$ and $\Delta \bar{\omega} = \pm 4°$ (Murray et al., 2008), with the relative eccentricity $\Delta e \approx \Delta a / a$ (Williams, 2009). They will return to the ring, or thereabouts, roughly once per orbit, near periapse or apoapse, with impact velocities of a few metres per second. If the ~ 13 mini-jets estimated per day are each from one object that collides, on average, once an orbit then at least ~ 8 such objects are required. If only a fraction of collisions produces an appreciable mini-jet, because of a clumpy, irregular core, then the total number of impacting objects could be much larger.

A number of features need to be studied to confirm this model. A statistical analysis of their distribution, morphology and lifetimes, etc. would help to understand better the collisional process and constrain the underlying impactor population.

From the discussion above it is clear that many different collisional scenarios can result in a linear, shearing feature like the one seen. Without further observations it is difficult to rule out any one model (e.g. hypervelocity meteoroid impacts) as the cause. Such a survey is presented in the next chapter.

5. Surveying Low-Velocity Collisional Features

The F ring core contains many small, irregular features and is changeable on time-scales ranging from hours to years (Porco et al., 2005; French et al., 2012). In the previous chapter a 'mini-jet' feature was examined in detail, as it evolved over a period of half an orbit. Low velocity (~ 1 ms^{-1}) collisions with local objects appear a good model for the formation mechanism, although hypervelocity impacts by meteoroids cannot be ruled out. Here a much more detailed study of the full population of mini-jets observed to date is presented in an attempt to investigate the collisional theory and put constraints on the underlying moonlet population. Parts of this survey have been published in the journal *Icarus* (Attree et al., 2014) but here it is extended to include observations through 2013, raising the total number of features from 857 to 1088. A more detailed analysis of a number of case study features is also presented.

Section 5.1 describes how the features are catalogued with measurements made from Cassini ISS images. Section 5.2 presents the raw results. These are analysed in 5.3, in particular the distribution of features in space and time (Section 5.3.1), their morphology (Section 5.3.2) and the characterisation of features observed more than once (Section 5.3.3). Finally some interesting case study features are discussed in more depth (Section 5.3.4). Further analysis and the implications for the impactor population are discussed in Section 5.4 before the concluding remarks are presented in Section 5.5.

5.1. Observations

A search of all Cassini ISS sequences containing resolved images of the F ring has been performed. This includes images from observation sequences of all types, both targeted at the F ring, like FMOVIEs and AZSCANs, and those with fortuitous coverage. For each sequence the beginning and end times are taken as the mid-times
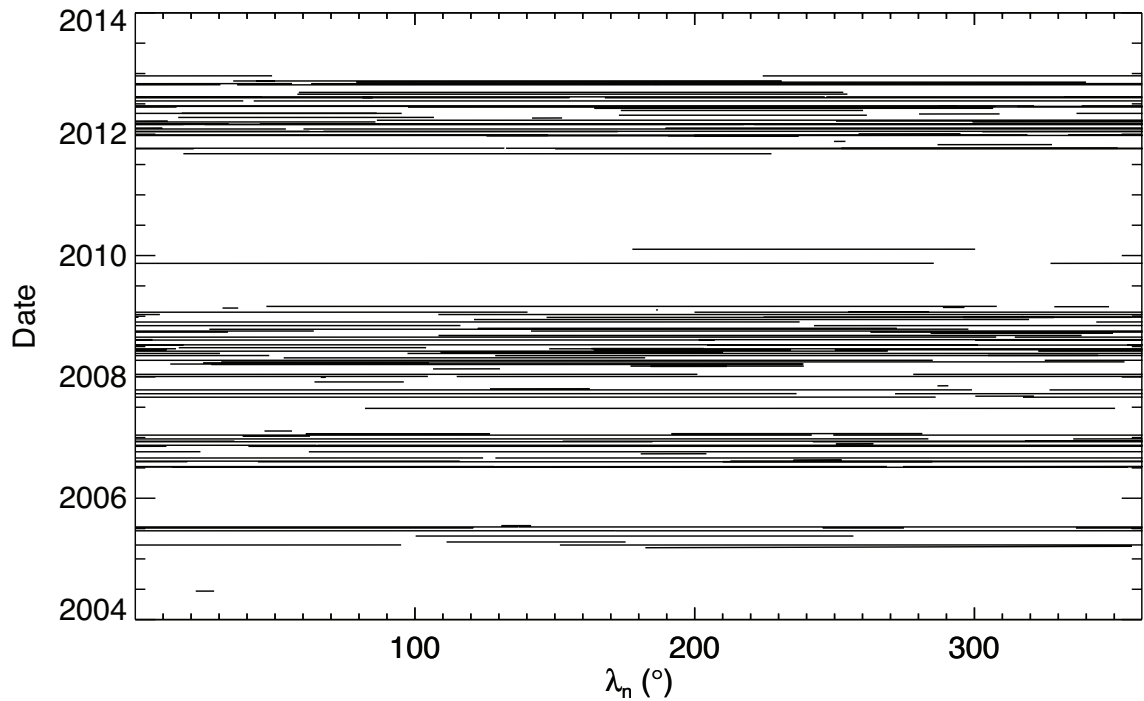
Figure 5.1.: Coverage of the F ring. Black lines show the co-rotating longitude (Eqn. 4.1 with a mean motion of $n = 581.96°d^{-1}$) covered by resolved Cassini images up until the end of 2013.

of the first and last images, respectively, and the maximum and minimum inertial longitudes in these images are recorded. These are converted to co-rotating longitude (using Eqn. 4.1 and the mean motion and epoch from Section 4.1) and taken as the start and stop longitudes, with longitude coverage between them. Longitude coverage of all sequences containing a feature is shown in Fig. 5.1. Several gaps in coverage are apparent: Cassini arrived in July 2004 and the survey is conducted only until the end of 2013. Additionally, the spacecraft was in the ring plane, and hence F ring observations impossible, during most of 2010 and 11 and periods of 2006 and 9. Outside of these times good coverage of most of the ring is obtained for extended periods.

As before, small features (typically $\sim$ 10–200 km in radial extent and $\ll 1°$ in longitude) emanating from the core are identified by eye, excluding bright kinks and clumps within the core itself and the larger jet features. After pointing the images using background stars a portion of each image containing a feature is re-projected in an equal aspect radius-longitude plot. This aids direct comparisons between features seen at different geometries and phases. For each feature a measurement of the tip and base ring-plane coordinates is made in the same way as in the previous chapter.

5.2. Results

As of the end of 2013 the catalogue contains 1088 features. This is the total number including those observed repeatedly which, in Attree et al. (2014), were separated out and counted only once. Here the total is used for convenience because the repeated features are few (~ 50), compared to the total, so do not unduly affect the statistics. The full catalogue is tabulated in Appendix B. Entries are named by the Cassini image number that they appear in while multiple features in the same image are labelled alphabetically e.g. N1557026084a, N1557026084b etc.

Based on their morphology in the re-projections each feature is assigned to one of three classes: (i) classic mini-jets, (ii) objects and (iii) complex features; each is described in detail below. Representative examples of each are shown in Figs. 5.2, 5.3 and 5.4. A number of features (~ 50) are found clustered close together in 'multiple' structures and, for these, an attempt is made to identify individual mini-jets within them. In some cases, however, this proved impossible due to poor resolution or the number of individual features (sometimes dozens) and these were placed in the 'complex' category. Some examples of multiple features are shown in Fig. 5.5. Both repeatedly observed and multiple features are of special interest and are discussed in more detail, in Section 5.3.3, below.

5.2.1. Classic Mini-Jets

Features with a clearly defined linear structure at a measurable angle from the longitudinal direction are defined as classic mini-jets like the one discussed in the previous chapter. As shown in Fig. 5.2 they are seen at a variety of angles and lengths and a sub-category has been identified as 'bright-heads'; these are classic mini-jets with a particularly bright tip or head. Such a head may represent the colliding object itself or simply a concentration of ejecta at that location. 518 mini-jets, including 46 bright-heads have been found.

5.2.2. Objects

'Objects' are identified as bright features separate from, but close to, the F ring core. As seen in Fig. 5.3 most are extended longitudinally in a similar way to S6 and some are connected to the core by a faint dust sheet or, in some cases, a mini-jet-like linear trail. The dividing line between objects with a faint trail and mini-jets with a bright head is therefore somewhat blurred and it is possible that these actually represent
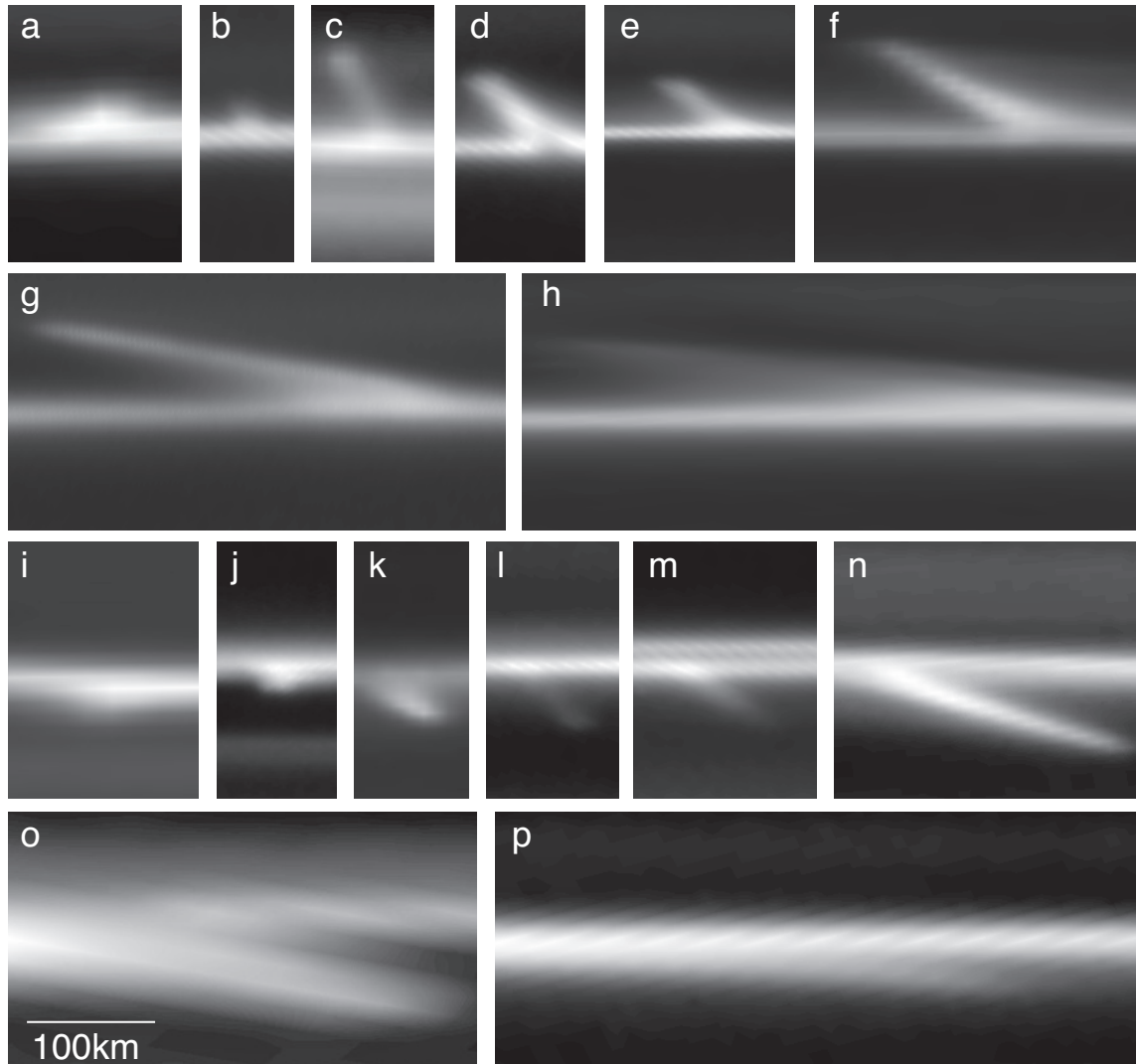
Figure 5.2.: Classic mini-jets re-projected in a radius/longitude frame to the same scale and ordered by age. Outwards mini-jets: (a) N1577813677a, (b) N1604028396, (c) N1733559846, (d) N1613003098, (e) N1597907705, (f) N1612005469, (g) N1623284964, (h) N1623331766c. Inwards mini-jets: (i) N1726901763a, (j) N1607629518, (k) N1605396128a, (l) N1616541581, (m) N1615488367, (n) N1610401148b, (o) N1727800548, (p) N1734593691. Contrast has been adjusted in each case to enhance visibility. Previously published in Attree et al. (2014).
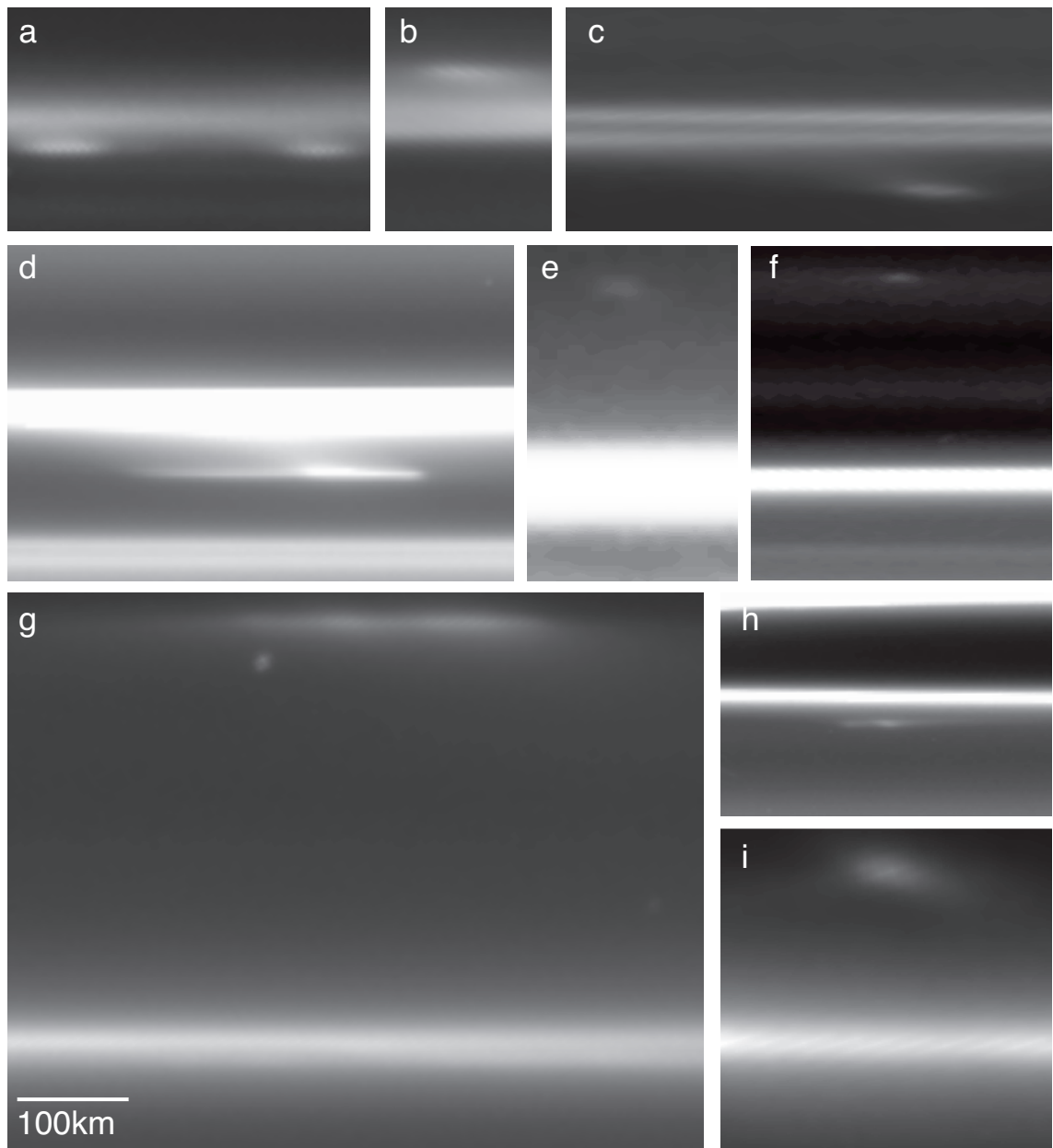
Figure 5.3.: Objects re-projected in a radius/longitude frame to the same scale. (a) multiple objects N1616523599a,b, (b) N1501710723, (c) object which could be a bright head mini-jet N1623351880, (d) N1589120162, (e) N1549820347 (f) N1610593686 which could be a clump in the outer strand, (g) large, S6-like, object N1616506283 (artefact visible below this object), (h) N1589119327b, (i) N1618601283. Contrast has been adjusted in each case to enhance visibility. Previously published in Attree et al. (2014).

the same phenomenon imaged at different geometries or orbital phases. 214 objects have been identified.

5.2.3. Complex Features

As shown in Fig. 5.4 some features are difficult to fit into either of the above classes and are instead described as 'complex'. Some are most likely mini-jets or objects imaged at poor resolution or difficult geometries but some may be more interesting features. A number of these appear in the very highest-resolution images, for example there are 14 in one early sequence with just over 1 km radial resolution and 10^{-3} degrees longitudinal resolution. These may reveal a complicated substructure present in all mini-jets but not normally resolved. Several others have the appearance of a superposition of several classic mini-jets on top of one another and resemble close multiple features. These are placed in the complex category when the resolution is insufficient to separate the individual components. Altogether there are 310 complex mini-jets.

5.3. Analysis

Classic mini-jets are assumed to represent the same kind of structure as the feature from the previous chapter, i.e. material with a range of Δa and Δe relative to the core (the Cooper et al., 2013 model is used; see Table 2.1), with $\Delta a \approx a\Delta e$, ranging from 0 up to some maximum at the tip. Radial and longitudinal positions of the tip, relative to the collision point, (r_{mj} and l_{mj}) will then obey Eqns. 3.3. Figure 5.6 shows a simple schematic, overlaid on a re-projected image, denoting these lengths and the mini-jet gradient, θ, as well as their theoretical trajectory over time. θ will follow Eqn. 3.8 for any mini-jet, irrespective of size, as long as the relationship between relative eccentricity and semi-major axis holds.

Mini-jets start out pointing the 'wrong way', against the direction of Keplerian shear, before quickly passing through the radial direction and looping away down the ring. The gradient follows this, starting positive before passing through an asymptote at the vertical point ($\pm 90°$) early in the first cycle. θ then increases towards zero whilst oscillating in and out at ever smaller angles. The minimum of the second cycle is $\theta = -8.56°$. All mini-jets with angles less than this are on their first cycle while those with greater angles are degenerate and could be any number of cycles old.

The radial extent of the mini-jet is determined by the maximum velocity impulse
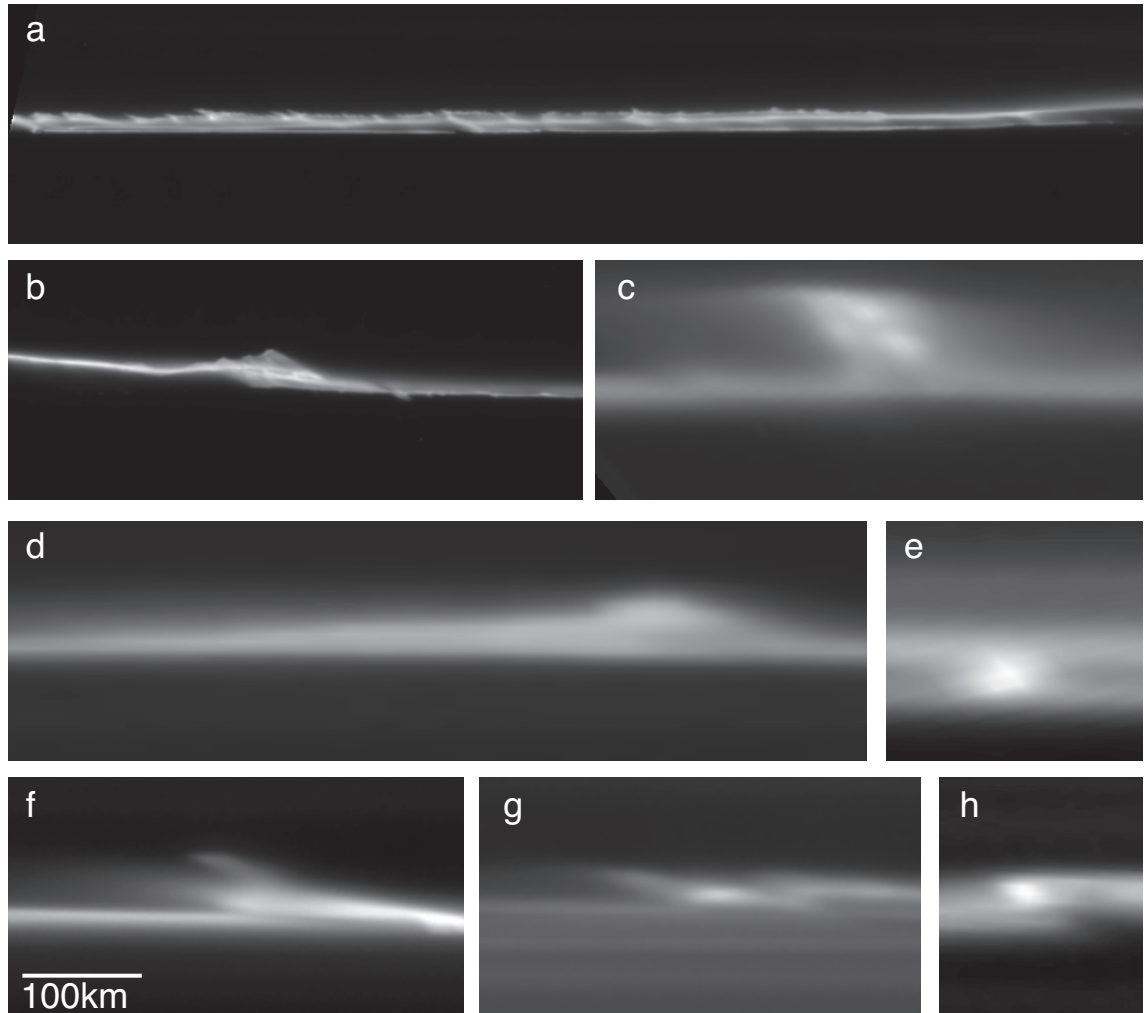
Figure 5.4.: Complex features re-projected in a radius/longitude frame to the same scale. (a) numerous small mini-jets in N1537899083 and (b) N1537898708. Complex and poorly resolved mini-jets in (c) N1589620046 and (d) N1493639016 and possible object in (e) N1627640563. Complex mini-jets in (f) N1605531856, (g) N1623226701 and unknown feature in (h) N1601512734. Contrast has been adjusted in each case to enhance visibility. Previously published in Attree et al. (2014).
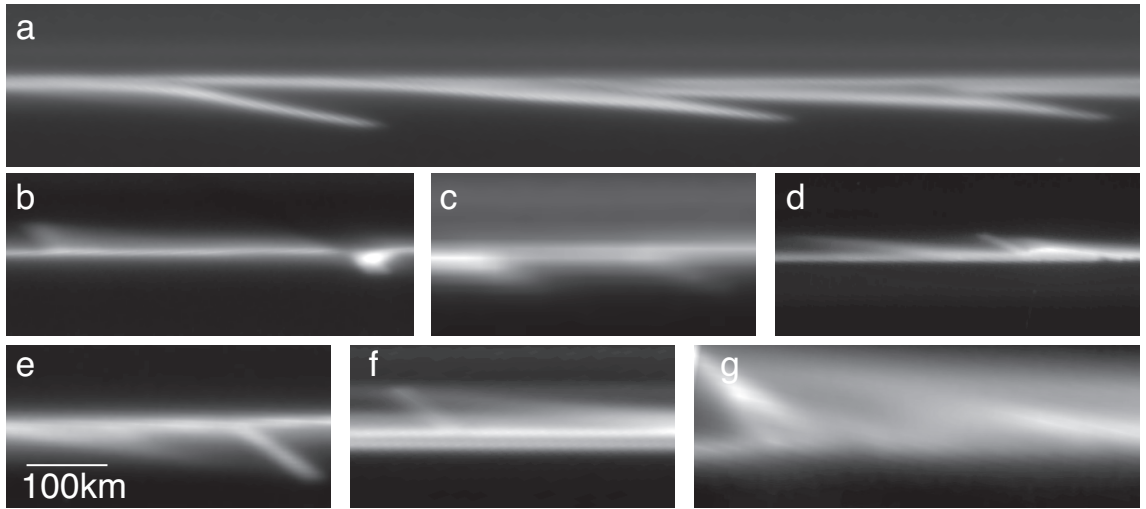
Figure 5.5.: Multiple features re-projected in a radius/longitude frame to the same scale. Mini-jets with similar ages (a) N1597902245a,b,c, (b) N1623224391a,b, (c) N1554046873a,b. Possible repeat collisions (c) N1729259467a,b, (d) N1615511698, (e) N1727132335a,b, (g) N1733524214a,b. Contrast has been adjusted in each case to enhance visibility. Previously published in Attree et al. (2014).
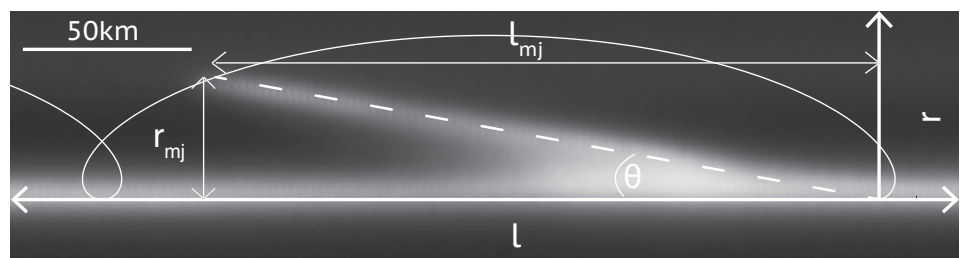
Figure 5.6.: Schematic overlaid on a typical outwards mini-jet. The origin is centred on the point of collision and the white curve is the trajectory of the tip. The mini-jet starts out pointing the 'wrong way', against the direction of Keplerian shear, before quickly passing through the vertical and continuing its progress down the ring. Previously published in Attree et al. (2014).

imparted in the collision, $\boldsymbol{\Delta v}$. Assuming dissipative, low-velocity impacts this is roughly equal to the impact velocity $\boldsymbol{U}$, i.e. assuming the tip of the mini-jet is put onto an orbit approximating that of the colliding object while the rest of the material is dragged out between this and the F ring. This assumption allows the simplification of Eqn. 3.14 to be used with $\Delta a = \delta a$;

$$U \sim \Delta v \approx \frac{n\Delta a}{2}. \tag{5.1}$$

It seems likely that the complex features are also collisional in nature but with more complicated ejecta patterns due to multiple objects or differing collision geometries. A general theory for their time evolution has yet to be developed and instead they are analysed on an ad-hoc basis.

For classic features the gradient is computed from the measured lengths. For complex features and objects only the coordinates of the centre of the feature are measured (listed as r_{tip}, λ_{tip} for objects and r_{base}, λ_{base} for complex in Appendix B). Uncertainties in these measurements vary with image geometry and resolution, with a typical pixel being 5 km in the radial and $0.01°$ in the longitudinal direction. This pixel error is carried forward when calculating the angle θ but the blurred, extended appearance of most features means it is an underestimate and, as with the previous chapter, typical errors are instead estimated, by eye, as $\pm 2°$. In the analysis below the derived quantities should then be taken as order of magnitude estimates.

5.3.1. Distribution

The 1088 features are found in 138 different imaging sequences. The number in each sequence is highly variable, ranging from one (only sequences with at least one feature are listed here) to 59, with a median of 5 and a mean and standard deviation of 8 ± 8.8 respectively (note the lack of change from Attree et al., 2014, even with the extra features here). Features are found on both sides of the core and in both inner and outer strands (~ 60 in the strands) and at a range of phase angles ($13° - 163°$) and viewing geometries.

Examining the numbers of features at each co-rotating longitude, λ_n, reveals no noticeable trends (in an inertial frame the number is biased to where Cassini makes its observations). Likewise, when examining the Fourier transform of the distribution no traces of periodicity are detected. No particular trends are detected within the subclasses of feature and no significant differences between their distributions have been noted.

Mini-jets and similar features, then, are distributed randomly around the F ring, as might be expected from a stochastic, collisional process. The average separation between adjacent features in the same sequence is $26° \pm 20.5°$, where the error is the standard deviation, which is large because the number of features in each sequence is so variable. A test for clustering is performed by taking the ratio of this value to the expected 'degrees per feature' (the sequence coverage divided by number of features seen in it). For nearly all sequences this is around one (mean of 1.01, median of 0.90). A value of one would be expected for no clustering as the observed average distance would match that of uniformly spaced features (e.g. following a Poisson distribution with a mean separation). On the large scale at least, the distribution is fairly uniform around the ring. On the small scale, however, there are over 50 'multiple' features where the separation between adjacent features is $\ll 1°$, much less than the average. This suggests that the components of 'multiples' are related to each other rather than being randomly distributed mini-jets that happened to be seen close together. For features with a mean separation of $\sim 20°$ the probability of finding two $< 1°$ apart is given by Poisson statistics as negligible ($\sim 10^{-6}$) even with over a thousand features.

Figure 5.7 shows the number of features per sequence, adjusted by the varying amount of the F ring covered in each. This is done by dividing the number of features by the co-rotating longitude coverage and then multiplying by 360 degrees to get the expected number in the whole F ring; this is reasonable if features are distributed randomly on the large scale. Only sequences with a longitude coverage of $> 50°$ are deemed representative of the whole ring and are included in this plot. A similarly shaped histogram is seen for just the raw number of features, suggesting the validity of the adjustment method.

The mean and standard deviation of the adjusted number are 14 ± 13.4 and the median is 10, slightly larger than the mean of the raw count, which is weighted down by the large number of small longitude coverage observations with a single feature. ~ 13 in the whole F ring would match the average of $26°$ per feature mentioned above. Thus the average number of features visible in the F ring at any one time (N_{mj}) is between 10 and 15. A Poisson distribution with a mean of 10 is over-plotted in Fig. 5.7 for comparison, however, and the agreement is poor. There are more sequences with few, or zero (not shown), features than Poisson statistics predict as well as a large tail where many are seen. The number of features is clearly highly variable and not particularly well correlated with any other observing statistic (no trends are detected with phase angle and only a very weak trend for more features at better imaging resolution is found; see below). This is partly because mini-jets are
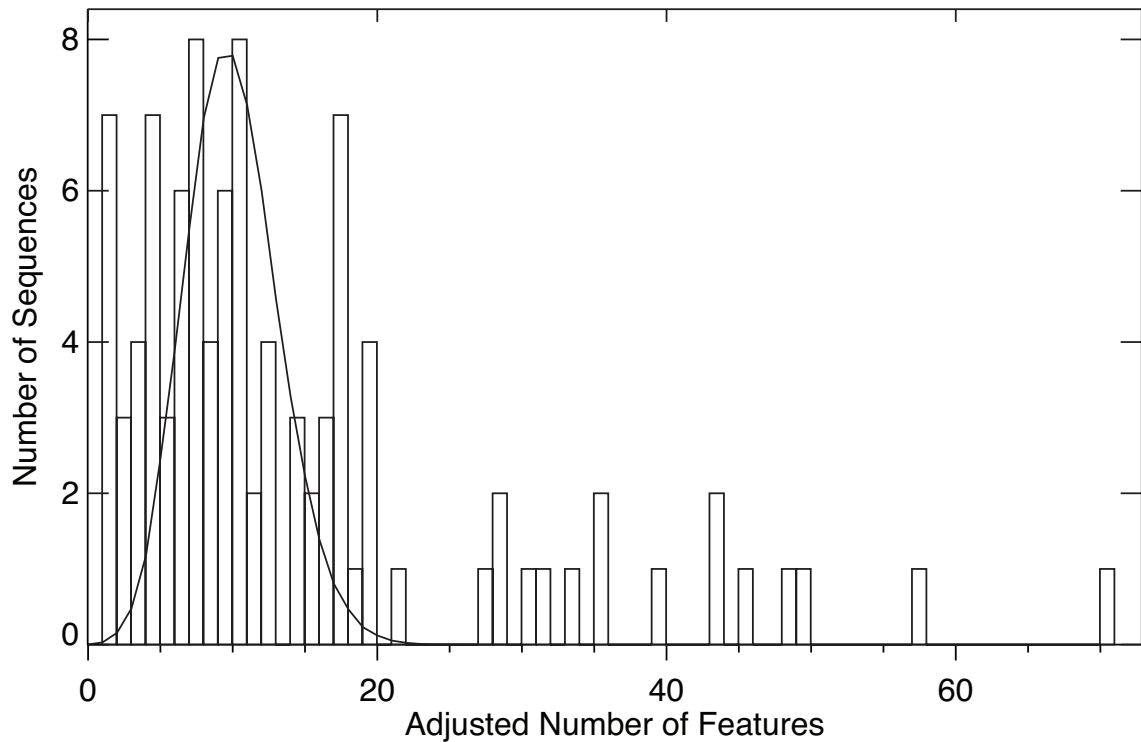
Figure 5.7.: Histogram of the number of features per observation sequence with >
50° coverage. The number of features has been adjusted by longitude
coverage as described in the text. A Poisson distribution of mean 10 is
over-plotted for comparison.

only visible at certain points in their orbit, depending on phase and geometry, and
partly because of the difficulties of visual identification, especially when confronted
with multiple features.

Finally, in terms of spatial distribution, the mean longitude of Prometheus is cal-
culated at the time of each feature's observation, subtracted from its base longitude
and plotted in Fig. 5.8. The mean number of features in each 2° bin is 6 ± 2.72. The
distribution is generally random and noisy but, with half of the bins within 10° of
Prometheus more than one standard deviation less than the mean, there is a slight
dip in the number of features here. One might expect mini-jets to be more difficult
to observe in the highly disturbed streamer-channel region and this may account
for the dip, however there is some evidence that the decrease persists upstream of
Prometheus, where the ring should be relatively undisturbed. In this case the fea-
ture would be real although the physical mechanism for a depletion in collisional
features near Prometheus is, as yet, unexplained (one possibility is a phase-lag ef-
fect as in the 'predator-prey' model of Esposito et al., 2012). When considering the
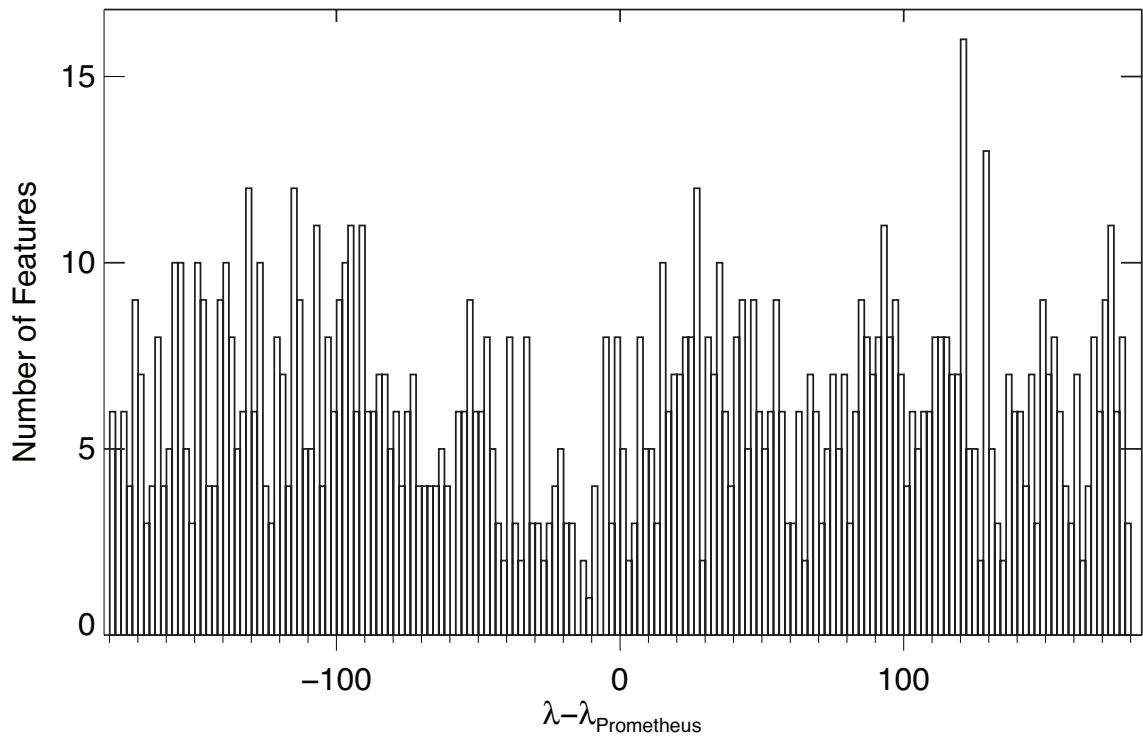
Figure 5.8.: The number of features seen in 2° bins relative to Prometheus's mean
longitude. There are no statistically significant trends. Updated from
Attree et al. (2014).

scatter in the rest of the data set it is suggested that the decrease is around the level of the noise and any trend here is weak at best.

The distribution of the features in time is examined by plotting the adjusted number, per sequence, against date in Fig. 5.9. The symbols show range from the spacecraft to the ring, as a proxy for resolution. The date of closest approach between the F ring and Prometheus (due to their eccentricities and differing precession rates) is also highlighted in Fig. 5.9 and there is a hint of an increase in the number of features in the year leading up to it. Unfortunately there is little coverage of the F ring at the actual closest approach and after it, and any increase preceding it must be treated with caution because of the large number of observations here. The 2008/09 observations are among the best in terms of coverage, number and resolution and, while attempts have been made to remove any biases by the methods above, it should, perhaps, come as no surprise that the best observations produced the most entries in the catalogue. As above, when considering the large scatter, it is suggested that the increase in 2008/09 is at the level of the noise (6 sequences above 2 standard deviations and none above 3) and any trend for greater numbers
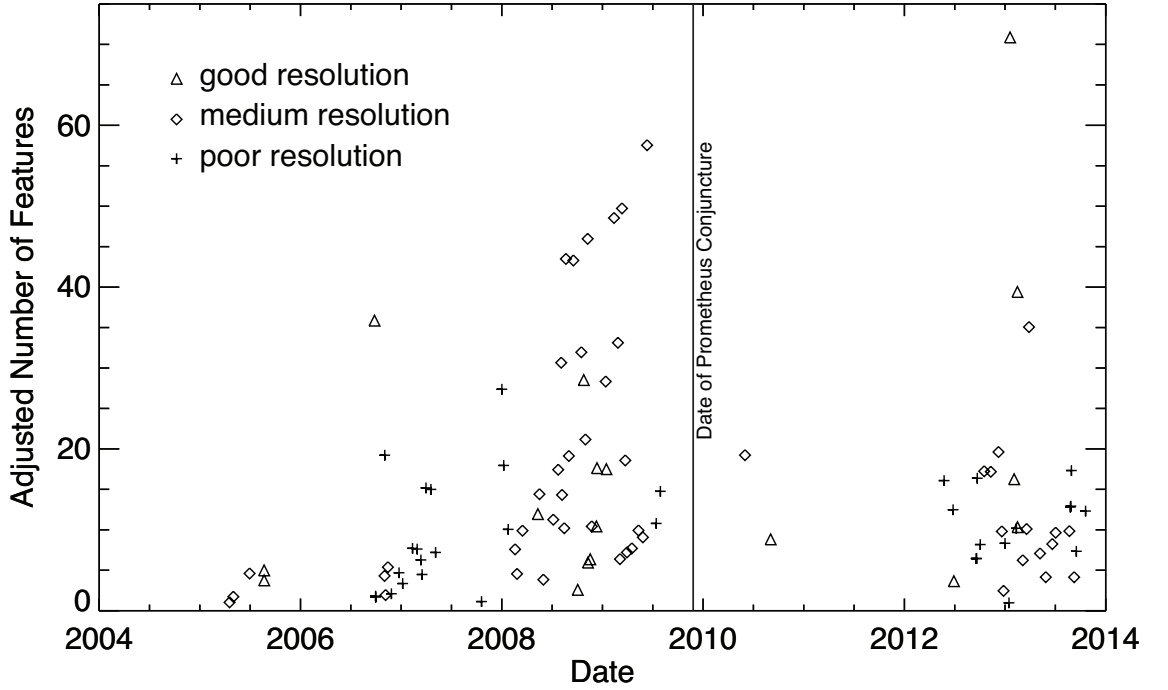
Figure 5.9.: The number of features, per observation sequence with $> 50°$ coverage, as a function of time. The number of features has been adjusted by longitude coverage as described in the text. There are no statistically significant trends. Good resolution refers to sequences imaged from a mean range of $< 8 \times 10^5$km (radial resolution $\lesssim 5$km per pixel), medium is between 8×10^5 and 1.6×10^6km and poor is $> 1.6 \times 10^6$km (radial resolution $\gtrsim 10$km per pixel). Updated from Attree et al. (2014).

of mini-jets here is weak at best.

5.3.2. Morphology

For the subset of 518 'classic' mini-jets the measured angle, θ, is used to solve Eqn. 3.8 for the age of the feature, $t - t_0$. Equations 3.3 and 5.1 are then used to find the Δa and an approximate collision velocity.

As shown earlier, in Fig. 3.2, for small angles ($< 8.58°$) there are multiple solutions for mini-jet age as it could be collapsing on its first cycle or rising on its second or subsequent cycle. There is a degeneracy here e.g. a large, young mini-jet can appear similar to a small, old one. In these cases an age and Δa are computed for each solution before the second part of Eqn. 3.3 is used to predict a length l for each. Predicted lengths are then compared to the measured length and the closest fit chosen as the preferred age/Δa solution. This is a best guess at the real properties

of the mini-jet and is the best that can be done from a single image. The chosen solution is checked for self-consistency by ensuring the predicted length is between the maximum and minimum lengths that a mini-jet of that Δa and number of cycles could be. Nonetheless there are still a small number (18) of derived Δa values which are very large; these outliers are poorly fitted by the above method. Checking their gradients these are all young, 'wrong-way' (against the direction of Keplerian shear) or large, jet-like, features which are difficult to measure. This is especially true for young and small features which lie almost entirely within the core.

Figure 5.10 shows the distribution of measured angles along with a typical predicted distribution for comparison. This is created by generating a population of mini-jets with random ages (weighted by number of cycles as found from the best fit ages) then using Eqn. 3.8 to produce a predicted angle for each. This serves to highlight the observational bias inherent in detecting mini-jets by eye: many more are found at medium angles ($10° - 50°$) and many fewer at low angles ($< 10°$) than predicted, simply because low angles are harder to spot in amongst the irregular F ring core. Apart from this discrepancy the measured angles are consistent with a population of mini-jets with ages ranging from a few hours to a few days although fewer young, 'wrong-way' mini-jets are detected than might be predicted. This is probably because they are very difficult to measure, as mentioned above.

Figure 5.11 shows the best fit solutions for Δa omitting these outliers. Nearly all the mini-jets derived with confidence lie within $\Delta a = \pm 100$ km of the core with roughly equal numbers positive and negative and a mean $|\Delta a| \approx 28$ km. This is a collision speed of $U \sim 1.2$ ms^{-1}, assuming $\Delta a = a\Delta e$ colliders impacting at peri- or apoapse. The corresponding ages have a mean of 1.22 orbital periods or 0.76 days and a little over a quarter (161/563) of mini-jets appear to have survived more than one cycle suggesting $\sim 3/4$ are disrupted when re-entering the core at the end of their first cycle.

Many multiple mini-jets, like those in Fig. 5.5a and c, have similar gradients and sizes implying that they formed at roughly the same time with the same collision velocities. A cluster of objects on very similar orbits, but stretched out in longitude by Keplerian shear, would impact the ring in a chain creating just such a series of features. Multiple, parallel mini-jets are most likely evidence for groups of objects or objects disrupted into swarms. By contrast, mini-jets like those in Fig. 5.5d to g have different angles (ages), where the tips of each jet all seem to point towards the same spot (Fig. 5.5d has three features showing both types). This would be expected if an object survives to re-collide with the core one orbit later (at the next loop in Fig. 5.6) creating a second mini-jet, in phase with, and following the tip of
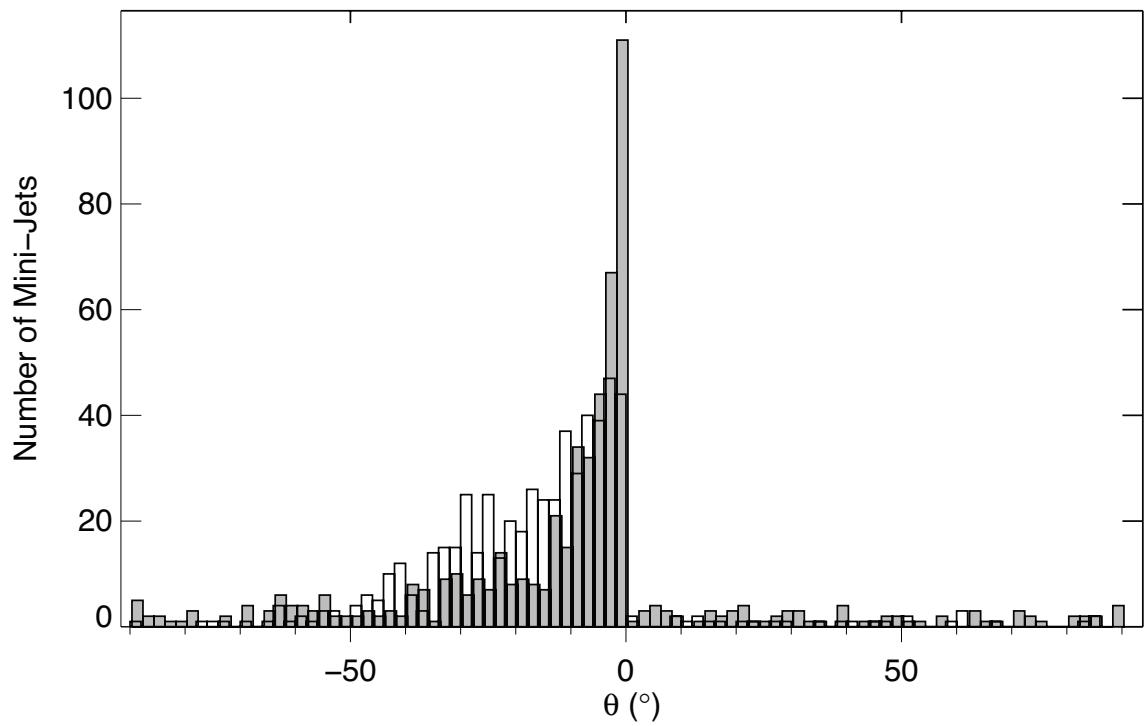
Figure 5.10.: Histogram of the measured mini-jet angles, θ, in 2° bins and a typical predicted distribution (shaded). See text for details. Updated from Attree et al. (2014).
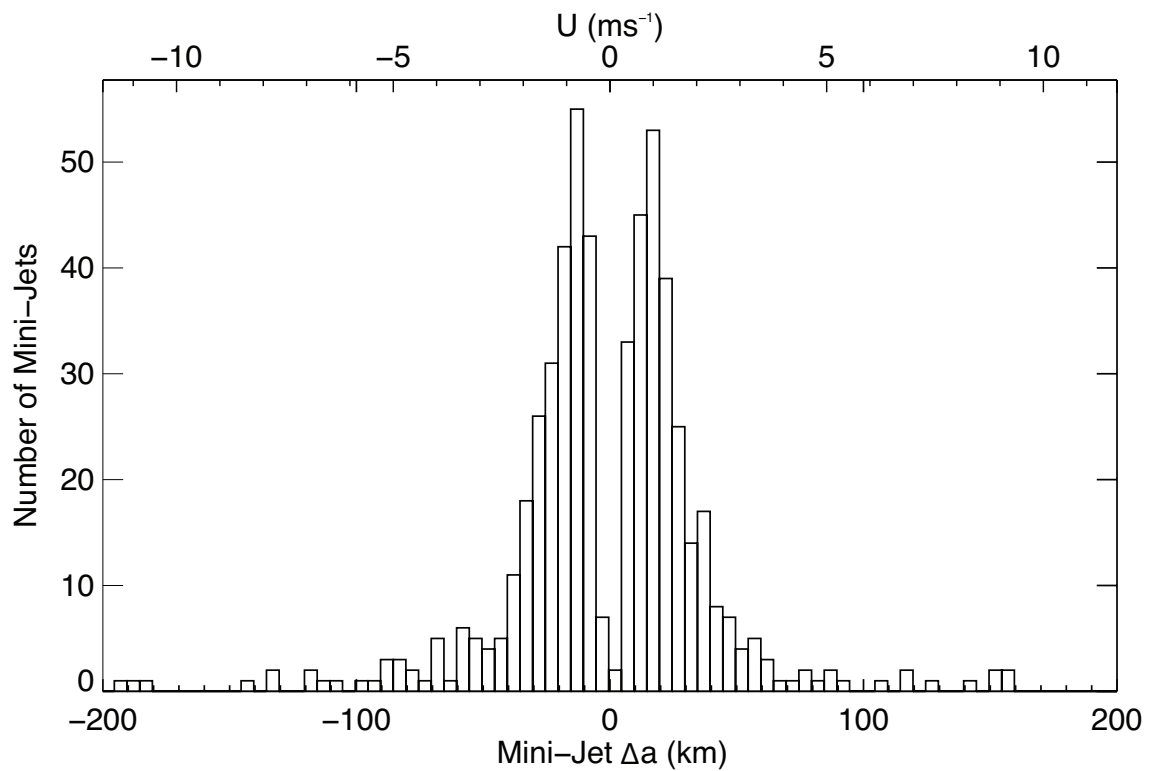
Figure 5.11.: Histogram of the calculated mini-jet Δa (semi-major axis relative to the F ring core) in 5 km bins. The corresponding velocity from Eqn. 5.1 (which assumes $\Delta a = a\Delta e$ colliders, impacting at peri- or apoapse) is also shown. Updated from Attree et al. (2014).
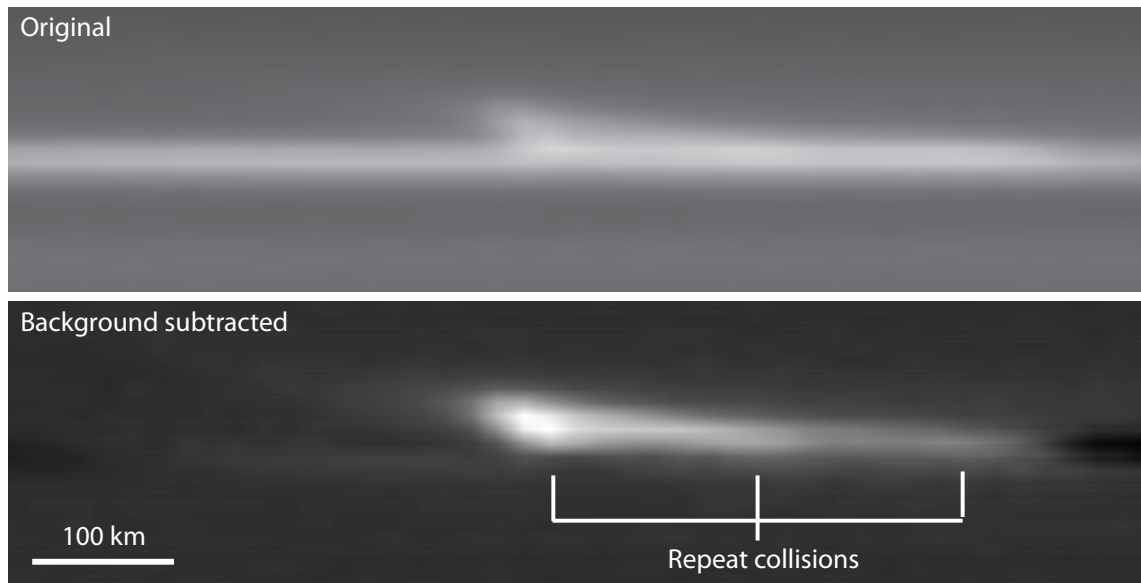
Figure 5.12.: Background subtraction of re-projected image of feature N1538184238. A mean radial profile is extracted from the original re-projection (top) and subtracted from every column, revealing the repeated collisions (bottom). Distances between collision points roughly correspond to the $3\pi\Delta a \approx 187$ km length inferred for this feature from its gradient fit.

the first. Thus the objects in Fig. 5.5d-g may be re-colliding.

The mini-jet closely examined in the previous chapter had a faint excess of material on its leading edge, referred to as 'spray', which followed the feature as it collapsed back into the core. A number of mini-jets here also show this, including many which are known to be older than one cycle (because they have been observed repeatedly, see below, or because of their angles and lengths). Using a background subtraction method to remove the averaged F ring core reveals these 'spray' features to be sheared-over and faint, but connected to the core at bright intersection points, much like mini-jets themselves. An example of this is shown in Fig. 5.12, where the mean radial profile has been subtracted from each column in the re-projected image of feature N1538184238. This, rather crude, background subtraction is quite effective at highlighting the spray here but, in general, is limited by the variability of the F ring core. The distances between intersection points in Fig. 5.12 roughly corresponds to this feature's inferred $3\pi\Delta a$ length, as expected for repeated collisions. It therefore seems likely that 'spray' is older mini-jets, from previous collisions by the same object, in the same way as the much more obvious examples of this in Fig. 5.5. The only difference here is the faintness of the older mini-jet.

Taking the combined number of mini-jets with tips that point together in multiples and those with prominent spray results in 57 features thought to be the result of repeated collisions. This is $\sim 5.2\%$ of the total number of features or $\sim 10\%$ of classic mini-jets, though likely this is an underestimate as the older features fade, becoming harder to identity. This means that a significant fraction of observed mini-jets are not caused by the first collision of a given object with the core.

5.3.3. Repeatedly Detected Features

Nearly all of the catalogued features are seen in only 2 to 3 images as the F ring rotates through the ISS field of view over the course of a few minutes. However some observation sequences are taken within hours or days of each other and cover the same section of ring (i.e. the same range of co-rotating longitude) raising the possibility of repeated observations of the same feature. In principle this means more data points to fit to the curve in Fig. 3.2, allowing better constraints on mini-jet properties, whilst also directly measuring their lifetimes and any subsequent collisions.

To this end the catalogue is searched by co-rotating longitude and date before comparing the morphology of features which are close in space and time. 52 possible matches (up from 25 in Attree et al., 2014) are found, including 148 (up from 64) individual features, listed in Appendix C. Features are detected between two and six times over timespans of ~ 15 hours to ~ 6.7 days. No special distribution in time or longitude is found in these features, suggesting that it is only by chance and good coverage that they are repeatedly observed.

Visually the repeated features appear more sheared, as expected, being both longer (larger l) and at a lower angle (smaller θ). However they prove difficult to fit to the predicted evolution of θ. As noted in Appendix C many are classified as complex with large uncertainties in their angles, while classic mini-jets imaged more than one cycle apart also proved difficult to fit. This might imply that morphological changes occur when a mini-jet re-enters the core, e.g. the release of more ejecta or re-collision and displacement onto differing orbits. Another possibility is that the morphologically similar feature seen at a later date actually represents a new collision, at a similar geometry, after the first feature has dissipated. The extent to which colliding objects survive and go on to re-collide provides information about their physical properties and those of the core.

Observations made during 2013 provide an interesting subset of repeatedly detected features which will now be examined in more detail. Between late August

Sequence	Δt (d)	Formed	Rate (d^{-1})	Dissipated	Rate (d^{-1})
ISS_196RF_FMOVIE003_PRIME	-	-	-	-	-
ISS_196RF_FMOVIE004_PRIME-A	2.89	4	1.38	2	0.69
ISS_196RF_FMOVIE005_PRIME-B	1.37	3	2.19	1	0.73
ISS_196RF_FMOVIE006_PRIME	1.33	8	6.00	4	3.00
ISS_197RF_FMOVIE007_PRIME	9.36	3	0.32	15	1.60
ISS_197RF_FMOVIE002_PRIME	7.55	2	0.27	1	0.13
ISS_198RF_FMOVIE001_PRIME1	32.77	12	0.37	4	0.12
Mean			1.75		1.05

Table 5.1.: September 2013 sequences, over which features have been tracked. Δt is the time, in days, from one sequence to the next. 'Formed' and 'Dissipated' list the number of features which appeared or were not seen when they should have been, respectively, as described in the text. The rate columns are then simply these numbers divided by Δt.

and early October, 2013 a series of FMOVIE sequences were acquired at similar geometries and co-rotating longitudes and closely spaced in time. These sequences (listed in Table 5.1 and with their corresponding mosaics shown in Fig. 5.13) provide an excellent opportunity for tracking features over time and directly measuring mini-jet formation and dissipation rates. There are 75 entries in the catalogue within these seven sequences, starting from feature N1755734445. Of these 27 can be positively matched, by location and morphology (see Appendix C), as 14 discrete features seen multiple times over a range of lifetimes.

When a new feature, which does not match anything in the previous sequence, is found it is counted in the 'Formed' column in Table 5.1 whilst those which disappear and are not seen again are listed in 'Dissipated'. The phase of the feature is calculated from its gradient, as before, to rule out a non-detection through the feature being in the core. The numbers in each of these columns are then divided by Δt, the number of days since the last sequence, to get an estimate for the formation and dissipation rates at the time of each sequence, respectively. The mean observed formation rate is about two per day whilst the dissipation rate, which should roughly match, is about one per day. Over the full 55.27 days 20 new features are seen to form and 27 dissipate. These totals do not match the mean formation/dissipation rates exactly because 55.27 days is much longer than an average lifetime so some features will have formed and dissipated between observations. As seen in the table the individual formation rates range between ~ 0.3 and ~ 6 d^{-1}, somewhat lower than the ~ 13 d^{-1} estimated from streamer-channel movies in the previous chapter. The highest formation rates are seen where the time between sequences is smallest,
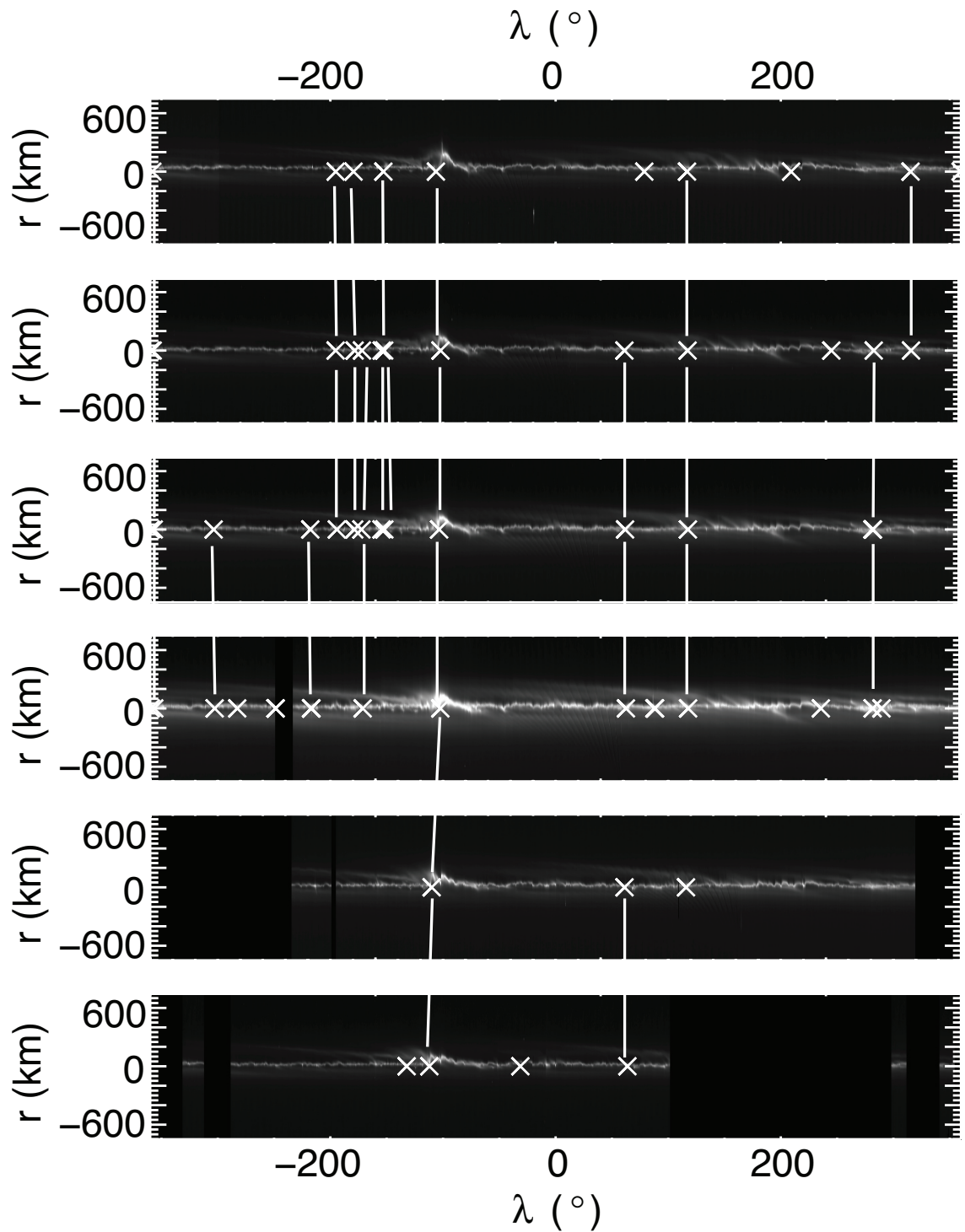
Figure 5.13.: Mosaics from the September 2013 series with survey features tracked between them. From top mosaics are: 1755, 1756-A, 1756-B, 1756-C, 1757-A and 1757-B, corresponding to the sequences listed in Table 5.1, minus ISS_198RF_FMOVIE001_PRIME which no features survived until.
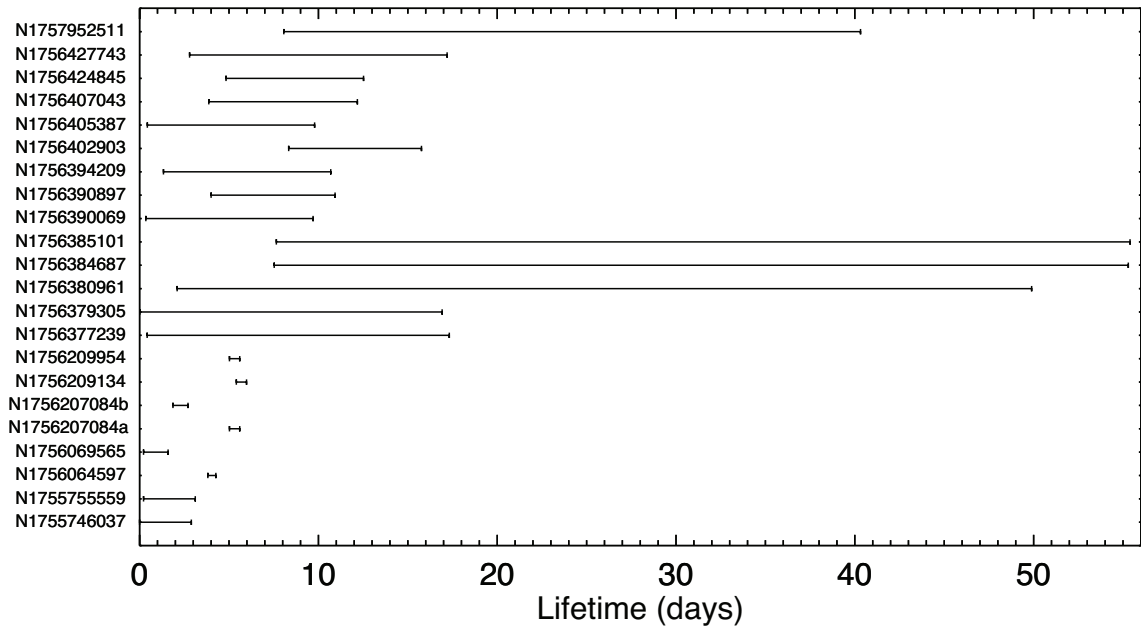
Figure 5.14.: Lifetime constraints placed on the named features by tracking them through the seven sequences listed in Table 5.1. Minimum and maximum lifetimes are found by the method described in the text.

consistent with the above statement about lifetimes. It is difficult to estimate a typical formation rate, because of this sampling problem, but a rate of ~ 2 d^{-1}, combined with a typical $N_{mj} \sim 15$ mini-jets visible at any one time, would suggest an average lifetime of ~ 7.5 d, longer than the ~ 1 d taken in the previous chapter.

Constraints can be placed directly on this lifetime by tracking the features across several sequences until they are no longer seen. The lower limit is then the estimated age of each feature when it is first observed (from an angle evolution fit) added to the total time they are observed for. The upper limit is this lower limit added to the Δt to the next sequence in which they should be visible (i.e. where there is longitude coverage and the mini-jet phase is checked to rule out it being in the core) but are not observed. Performing this analysis for all the repeatedly detected features in these sequences results in the constraints shown in Fig. 5.14. Most features last between about 2 and 15 days ($3.2 - 24.2$ orbital periods). Without assuming an underlying distribution, an average lifetime cannot be derived from these data but the results in Fig. 5.14 are consistent with a figure of a few days. By comparison a large, complex jet feature is seen in all the sequences, over at least 55.27 d, and many other small clumps and kinks also survive tens of days.

By eye there appears to be no correlation between ring appearance and the loca-

tions of features or their lifetimes (see Fig. 5.13). This is checked quantitatively by examining the core brightness profiles with longitude (see next chapter) and, again, no clear trends are found. Mini-jets and similar features appear in parts of the core which are both brighter and darker than the average and survive for varying amounts of time in both. Additionally, from these sequences, it is clear that repeated observations are needed to distinguish between clumps in the core and features that will develop into mini-jets. From a single image it is very difficult to tell if a feature is a local enhancement in ring material or the expanding cloud of material from a very recent impact, or even a multiple-cycles old mini-jet, very close to the core. Some mini-jets seem to arise from clumps while others show no evidence for precursors. It is also difficult to say when a mini-jet has fully dissipated as they tend to gradually fade away and become more and more blurry and indistinct.

5.3.4. Case Studies

A number of particularly interesting features are now described in detail. Each of these has been observed several times, revealing their evolution with time, and each represents a unique challenge, the explanation of which helps to constrain the formation theory.

Firstly, feature N1765064931, found in sequence ISS_199RF_FMOVIE002_PRIME on December 6th, 2013. This particular sequence is one of several FMOVIEs to track a segment of ring for one full orbital period, in a manner more similar to a streamer-channel movie. These were acquired specifically for the purposes of tracking the evolution of features. The feature found here is the clearest in these tracking sequences and has the appearance of a classic mini-jet. As shown in Fig. 5.15 it appears from the core at about 21:40 hours, in image number N1765060635, before extending radially and shearing. The feature is visible until the end of the sequence, just after midnight, for a total of about 2 h 45 m. Its visual appearance is very similar to the streamer-channel feature from the previous chapter (except that it points radially inwards rather than outwards) but the resolution of these images is not as good, with pixel size approximately 13 km in the radial and 0.001° in the longitudinal, meaning the feature is more blurred and harder to discern. As the mini-jet extends towards its maximum extent there is a hint of a bright-head (see Fig. 5.15, bottom panel). Unfortunately the images just before its first appearance fall into the planet's shadow but previous images, from N1765055305 (taken 20:11 hours) onwards, may show a small, bright clump, hinting at the beginnings of the feature. Due to the resolution and local conditions the core is about ~ 40 km across

in these images and features within it are difficult to resolve.

The tip and base coordinates of the feature are recorded and the gradient fitted to find the formation time, as with the previous mini-jet. The results are shown in Fig. 5.16 with the best-fit solution $t_0 = 340.75 \pm 0.0027$ DOY, approximately 16:00 hours, or four hours before the first observation. A good fit is achieved ($\chi^2/DOF = 1.042$) using gradient uncertainties of $\pm 5°$, a conservative estimate based on the feature's fuzzy appearance. The tip of the mini-jet also moves radially away from the core, as expected for a young feature on its first cycle, and lengthens in the correct way. Overall then this feature is in very good agreement with the mini-jet from the previous chapter.

The next case-study is a pair of features, found in the ISS_198RF_FMOVIE001-PRIME sequence, with designations N1760846184 and N1760853154. Both have the appearance of large, sheared jets with a number of sub-features within them, as shown in the bottom panels of Fig. 5.17. With lengths of over a degree and radial extents of ~ 120 and ~ 180 km, respectively, both these features could be classified as jets, rather than mini-jets, however they share several properties with the smaller structures and so are discussed here, rather than in the next chapter. Morphologically, both fit with the repeated collisional mini-jets discussed above, with three mini-jets measured within each (a, b and c) and more probably present but hard to disentangle. All the sub-components point together to the same point which, in the case of N1760846184 may be a bright head, and have bright intersections with the core. Distances between these base points, which should be equal to $3\pi\Delta a$, seem to vary considerably. This image sequence provides coverage at both ansae and the corresponding sections of co-rotating longitudes are shown in the top panels of Fig. 5.17. Nothing of note is seen extending from the core and the only visible presence of the large collisional features half an orbital period before their first detection is a slight clumpiness in the core. The measured gradients and phases (see Appendix B) are entirely consistent with the features being in the core, i.e. at their apoapse, at this time, explaining the lack of any detection here.

N1760846184 and N1760853154 then represent large jets with mini-jet like behaviour. That is to say each shows repeated, discrete collisions by a single object, looping along the core on its epicycles, creating jets of material with $\Delta a \approx a\Delta e$, which oscillate in and out in radius. A natural explanation for the differing base separations is multiple passes by the objects through these sections of core but, due to its clumpy nature, only a few, random, collisions resulting in a mini-jet. This would also explain the large distances between sub-components, which are $\sim 1°$, versus the, $\lesssim 1000$ km $\approx 0.41°$, inferred $3\pi\Delta a$ lengths. Despite the fact that
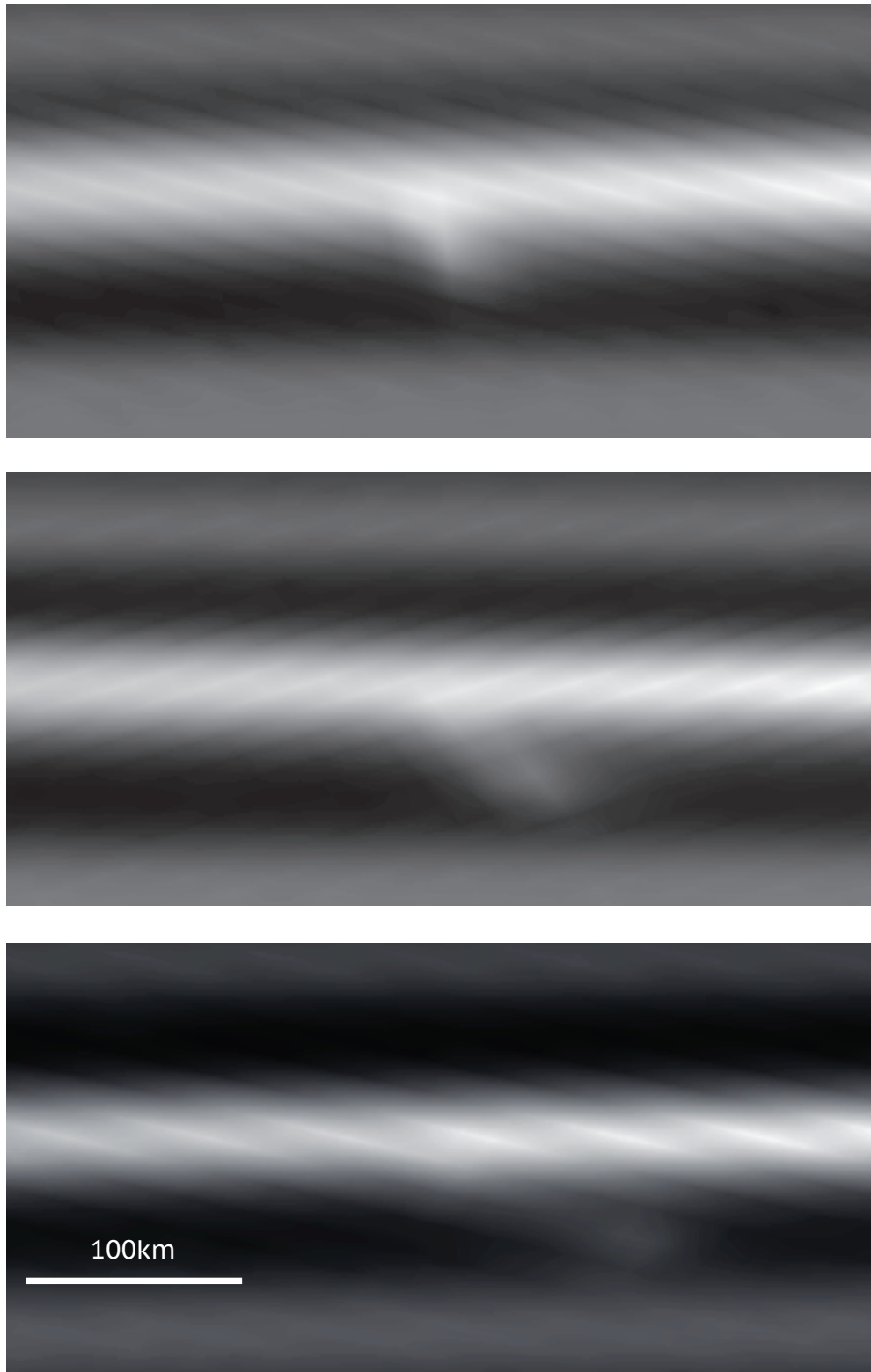
Figure 5.15.: Re-projections of an evolving mini-jet, tracked in the ISS_199RF_FMOVIE002_PRIME sequence. From top images are N1765060635, N1765064931 and N1765070521, taken at 21:40:09.817 and 22:51:45.775 on December 6th and 00:24:55.739, December 7th, 2013, respectively (~ 1.4 hours between them). All images are 1200 ms exposures and contrast has been adjusted in each case to aid visibility.
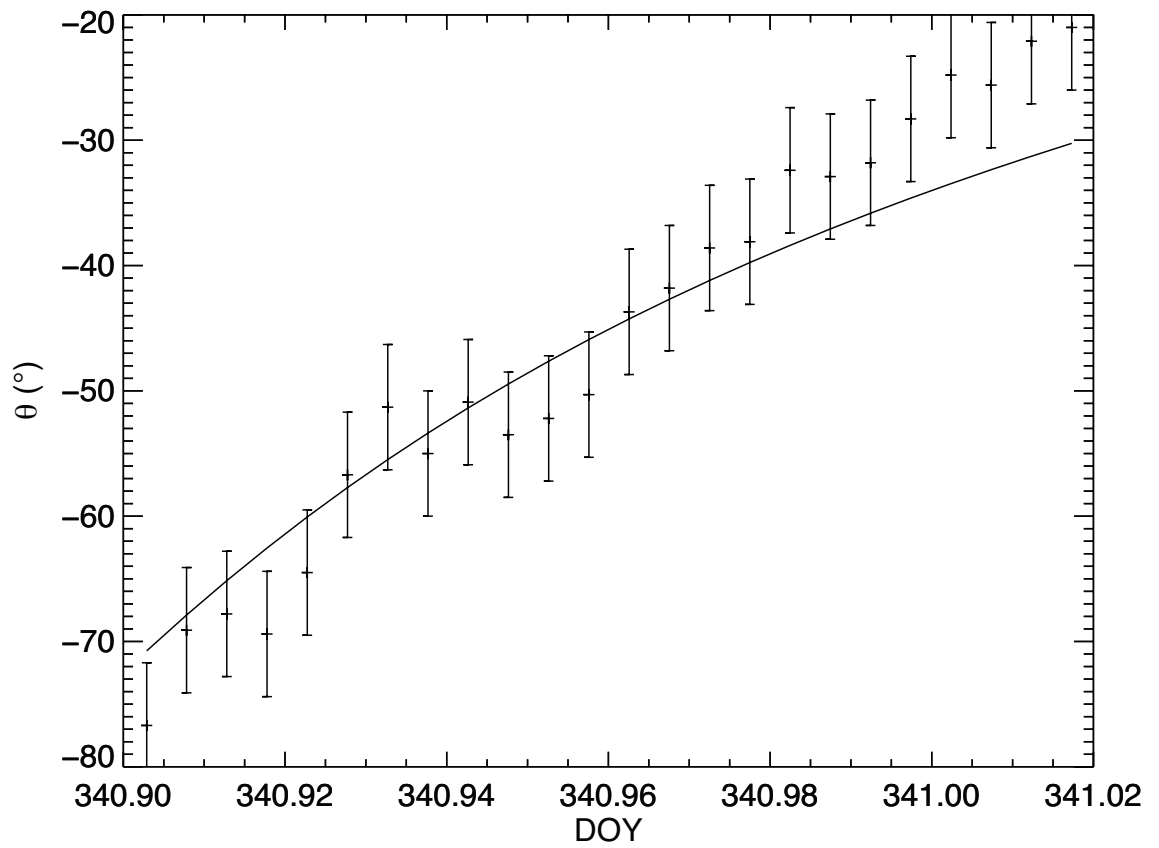
Figure 5.16.: Measured gradient, θ, of feature N1765064931 over time (day-of-year). The curve from Eqn. 3.8 is over-plotted, fitted to the data for the formation time t_0. Uncertainties are taken as $\pm 5°$.
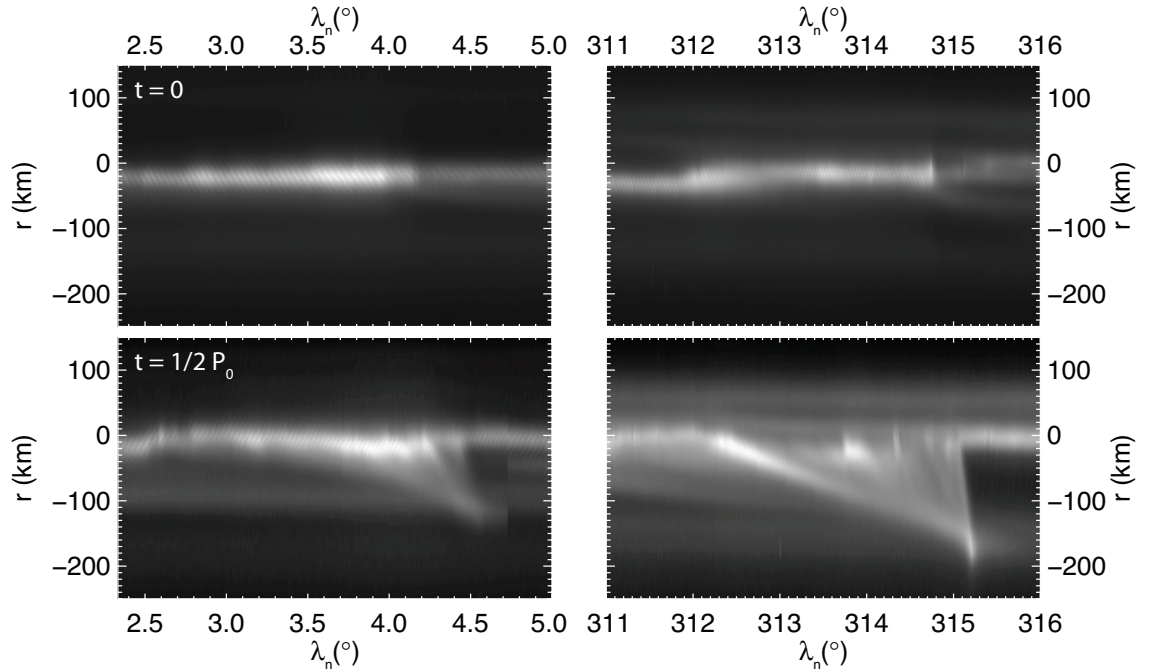
Figure 5.17.: Re-projections of repeated collision features N1760853154a,b and c (left-hand column) and N1760846184a,b and c (right-hand column). Panels in the top row are parts of mosaic 1760-1 and, in bottom row, from 1760-2, half an orbital period later. Contrast has been adjusted to aid visibility.

ISS_198RF_FMOVIE001_PRIME is one of the sequences studied in detail above, these features are not seen in any of the preceding, or succeeding, observations. This is hampered by a lack of coverage (see gaps in mosaics 1757-A and B in Fig. 5.13 above) but the $\Delta t \approx 33$ days time difference is enough for the, perhaps, dozens of orbital cycles needed to form them.

The next feature, designation N1739126746, is an example of a mini-jet imaged twice, one orbital period apart. It was found in sequence ISS_181RF_FMOVIE001-PRIME, taken in early 2013, which contains greater than 360° coverage. The feature fortunately occurred in the section of ring imaged twice, almost exactly one orbit apart. The re-projected images are shown in Fig. 5.18 and the tip of the feature can be seen to have moved about 600 km between frames. This, and the angles, are consistent with a $\Delta a \approx 65$ km mini-jet, the theoretical path of which, according to Eqn. 3.3, is superimposed on the figure. The tip and/or colliding object itself must have re-entered the F ring core in the time between images and one might expect a new mini-jet, in phase with the original, to have formed. Instead, visible in the second image is a dark, sheared channel in the core located roughly at the
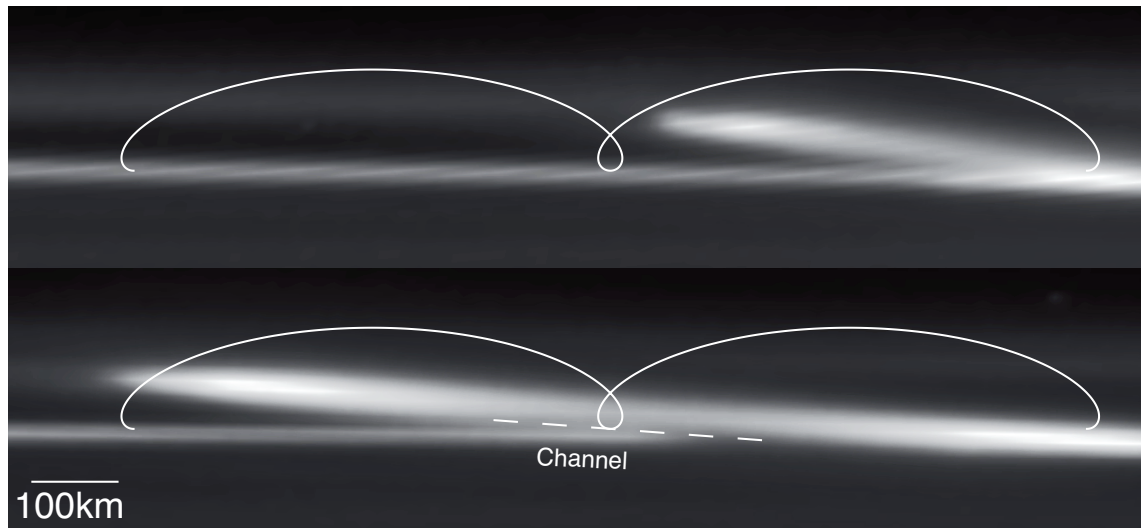
Figure 5.18.: Mini-jet imaged twice, one orbital period apart; the image numbers are top: N1739126746, taken at 17:51:25.327 on February 9th and bottom: N1739180046, taken at 08:39:44.988 on February 10th, 2013. The path of the tip/object is superimposed, assuming $\Delta a \approx 65$km which matches the location of the bright head in both images and the dark channel in the core in the second. This then represents an object re-colliding with a sparsely populated piece of ring and sweeping up material rather than impacting to form a second mini-jet. Previously published in Attree et al. (2014)

point of re-collision. It is suggested that this is a re-collision feature, as above, but one which happened to occur in an under-dense section of ring thus resulting in the sweep-up and scattering of fine grained material, leaving a depleted dark channel, rather than collision with a solid clump, leaving a mini-jet. This would be similar to the irregular gaps between the sub-components of N1760846184 and N1760853154 in the previous case-study. Finally it is noted that the appearance of the F ring before collision is uniform and bright so it is not immediately apparent that this is an under-dense region. This shows the difficulty in assessing the 'clumpiness' of the core from images.

Finally a repeated feature, seen in May 2007, is examined which presents an interesting challenge for mini-jet theory. Seen at first (top left of Figure 5.19) as a large double mini-jet, or jet, with a bright head, it has evolved to a triple mini-jet by the time of the second image, approximately one orbital period later (bottom left of Fig. 5.19). Also visible in Fig. 5.19 are a number of dark, sheared channels in the strands either side of the core up- and down-stream of the mini-jets, two in the first image and four in the second. All these features can be explained by multiple
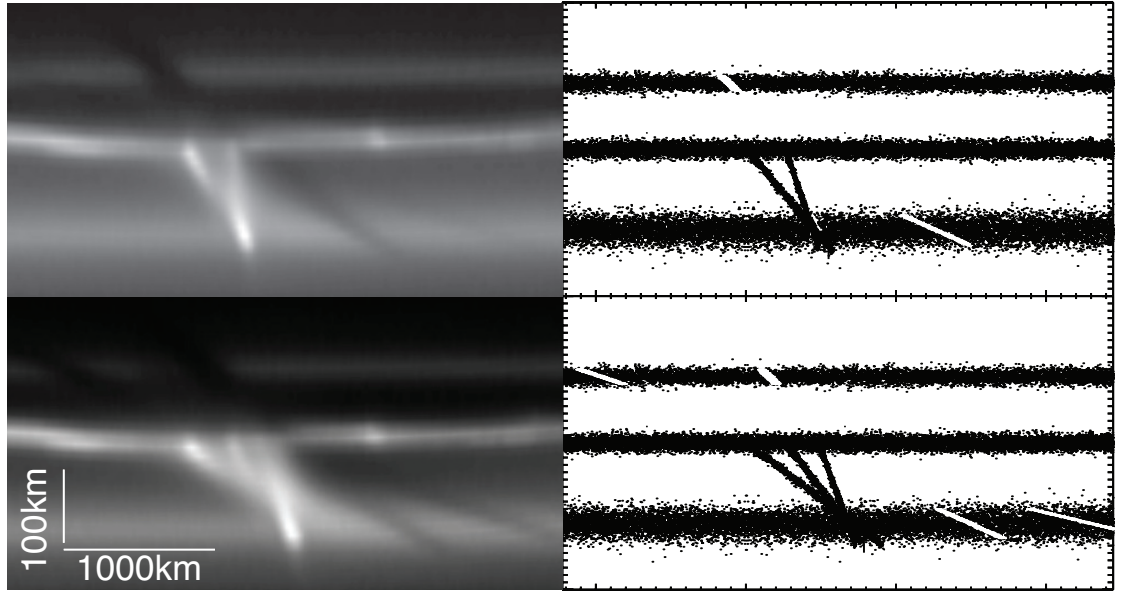
Figure 5.19.: Multiple mini-jet feature imaged twice approximately one orbital period apart. Left: re-projected image N1557026084, taken at 02:40:53.219 and N1557080024, taken at 17:39:52.877 both on May 5th, 2007. Right: corresponding frames from a formation model. A single object with a Δa, Δe and Δi loops along from left to right, creating a new mini-jet each time it moves through the core and sweeping out a dark channel on each pass through the strands. These subsequently shear to form the observed structure. Previously published in Attree et al. (2014)

collisions with a single object if, on colliding with the dense, clumpy core, it creates a mini-jet but while moving through the more diffuse strands it merely sweeps up or scatters material leaving behind a dark channel.

The right-hand panels of Fig. 5.19 show corresponding frames from an animation of a simple model: mini-jets and channels are generated so that when they evolve, according to Eqns. 3.3 and 3.8, they then match the angles and locations of the observed features. Mini-jets are a number of particles given linear $\Delta a = a\Delta e$ distributions while channels are particles, coloured white, with simple Δa spreads. A single object will pass through the locations, in the right sequence and at roughly the correct time, to form these features if it has $\Delta a \approx -25$km, $a\Delta e \approx 110$km and $\Delta i \sim 10^{-3}$ degrees, where Δi is relative inclination. For the object to pass through strands both inside and outside of the core it must have a relative eccentricity greater than its Δa, i.e. $\Delta a < a\Delta e$ contrary to what has been assumed for all mini-jets above. This is not ruled out by the dynamics but could have implications for the

derived mini-jet ages if some of them deviate from Eqn. 3.8. Indeed it may help explain the poorly fitted outliers mentioned above if these are, in fact, eccentric mini-jets on the 'wrong' side of the ring. This relative eccentricity also means that the object will pass through the core twice per cycle and a relative inclination is needed to explain why only one mini-jet is formed: the object loops above or below (i.e. out of the orbital plane) the core in one direction and collides with it in the other. The three dimensional nature has not been considered until now because the F ring's inclination is very small ($i = 0.0067°$) but collisions and gravitational interactions should induce small inclination differences between objects. To a first approximation one might expect Prometheus to induce inclinations comparable to its own of $i = 0.008°$. From Eqn. 3.3 a relative inclination of only $\Delta i = 8.17 \times 10^{-4}$ degrees is needed to produce a vertical offset of $z = 2$ km at the F ring, enough for $\lesssim 1$km radius objects to 'miss' each-other and pass by without colliding. Even such an initially complex feature as this can then be accounted for by a single colliding object with a few reasonable assumptions.

5.4. Discussion

As discussed in the previous chapter, high velocity meteoroid impacts cannot be ruled out as the formation mechanism for a particular mini-jet feature. Tiscareno et al. (2013) argue that elongated features observed in the A ring are dust clouds formed by impacts from cm- to m-sized meteoroids. They are best fit as evolving purely by Keplerian sheer (rather than epicyclical motion combined with shear as in Eqn. 3.8) and it is suggested that this implies "the impact of a compact stream" of material from a broken up object striking an area tens of kilometres in radius over some time. The radial extent of these clouds is between ~ 40 km and 300 km with most covering one hundred kilometres or more in radius (see Tiscareno et al., 2013 supplementary information), consistent with ejection velocities of ~ 20 ms^{-1}.

Tiscareno et al. (2013) calculate a flux of $\approx 10^{-15} - 10^{-18}$ s^{-1}m^{-2} for impactors between one and ten centimetres, respectively, which, depending on the cross-sectional area of the F ring (see below), corresponds to impact rates varying between tens per day and ~ 1 per year, across this range. All impacts should be roughly at the same velocity. Due to the physics of hypervelocity collisions (see Chapters 3 and 4) different sized impactors should eject particles at similar speeds but with differing total ejecta mass from the yield factor. This is approximately what is seen between ejecta clouds in the main rings with similar radial sizes but integrated brightnesses

(proportional to total mass) varying over 6 orders of magnitude.

On the contrary, in the F ring features studied here there is a rough gaussian distribution in radial sizes and, qualitatively at least, no power-law brightness distribution. Additionally, as pointed out before, isotropic cratering impacts and fragmentations should produce double-sided ejecta clouds, totally unlike the mini-jets presented here. Finally the presence of bright heads, objects and re-collision features strongly suggests a population of local objects colliding with the ring with velocities of order several metres per second. Such a model implies small bodies on orbits similar to the F ring's (Δa values of tens of km). These would have to be ~ 1 km, or less, in diameter in order not to be resolved in ISS imaging, although the 'object' class may represent some of the larger ones or those with accompanying dust envelopes.

Repeated collisions suggest that at least some of these objects survive passing through the F ring. These must have enough mass for self-gravity or material strength to resist fragmentation, so they are not just clumps of dust on similar orbits. Where repeated collisions *do not* occur it is difficult to say whether this is due to weak objects or the highly variable F ring core. Multiple impact features are relatively common, suggesting groups of objects moving together on related orbits. Similar complex structure is visible in the larger S6 collisions and is also highly suggestive of clusters of objects. These likely represent those objects that have been partially disrupted into a swarm of smaller objects, either by previous collisions with the core or by tidal forces. Keplerian shear swiftly stretches out an initial clump into a long, extended chain. It also makes sense that objects should repeatedly encounter the core if they must last long enough to go through multiple Prometheus interactions (or chaotic orbital evolution: see Winter et al., 2007), as suggested by their Δa spread (Fig. 5.11).

No association between the location of mini-jets and the visual appearance of the ring is noted. Features tracked across multiple imaging sequences do not seem to be found in bright (or especially dark) regions of the ring and their lifetimes seem entirely random, with some persisting for tens of days but other, bright features, disappearing in ~ 1 day. There is also the example of the third case study in which an object appears to sweep up material rather than forming a mini-jet in an, otherwise normal-looking, section of core. French et al. (2014) compared the locations of 889 of the features here (those published in Attree et al., 2014) to their 'Extended Clumps' and found slightly more mini-jets inside clumps. However the statistics were inconclusive. This may be further evidence that ISS images are not seeing the 'true' F ring core, containing the larger particles which are involved in

collisions, merely a dust envelope, in which mini-jets do not form.

One can crudely estimate the number of colliding objects with a particle in a box method using

$$N_{obj} = \frac{2\pi a H W \nu}{\sigma U}, \qquad (5.2)$$

where N_{obj} is the required number of objects, with average dispersion velocity U and collisional cross-section σ, to result in a collision frequency of ν events per second in a box of height H, width W and length $2\pi a$ (where a is semi-major axis as before). The box size is assumed to be 50×50 km and the relative collision velocity can be estimated from the mean mini-jet $|\Delta a|$ as $U \approx 1.2$ ms^{-1}. The frequency of mini-jet forming collisions is variable but taking the rough average of the sequences tracked in detail, $\nu \sim 2$ d^{-1}. This corresponds to the average feature lifetime of ~ 7.5 d, also seen in these sequences, rather than the lifetime of an individual mini-jet of ~ 1 orbit.

The collision cross-section between two discrete objects of equal radius, R_{obj}, is $\sigma = \pi(2R_{obj})^2$, ignoring gravitational focussing. Substituting this into Eqn. 5.2 with $R_{obj} = 500$ m requires $N_{obj} \approx 3 \times 10^7$, while $R_{obj} = 5$ km still needs $\sim 3 \times 10^5$ objects. These very large numbers correspond to a moonlet belt, like that proposed by Cuzzi and Burns (1988), and are unlikely given the detection limits placed by occultation studies (Meinke et al., 2012). The collisional cross-section between a continuous ring of width x and a single spherical object is $\sigma = \pi R_{\mathrm{obj}}^2 + 2\pi a x$, assuming collisions are equally likely from all directions, i.e. taking the core as a flat 'ribbon' of width x all the way around its orbit. With $R_{obj} = 500$ m and $x = 10$ km, as the nominal core width from imaging, $N_{obj} \approx 3$. However the core is not uniform and simple, having clumps and under-dense sections. If mini-jet features form only during collisions with a narrow, 1 km, inner core, containing the larger F ring particles (Murray et al., 2008) then $N_{obj} \approx 30$. Further restricting this by the discontinuous nature of the inner core, using the fraction of RSS occultations in which it is detected (~ 0.3), results in $N_{obj} \approx 100$. Showalter (1998) made a similar estimate when calculating the collisional cross-section for meteoroids, extrapolating $x = 20$ m for metre sized objects from the equivalent depths of Voyager RSS occultations. Using this cross-section leads to $N_{obj} \approx 2400$.

Overall then the inferred number of colliding objects depends heavily on the nature of the collisions. Each mini-jets is always seen connected to the core, implying the core must be one of the two colliders involved, but dense clumps or moonlets could be hidden within it. Considering the lack of association between mini-jets and core brightness features, and the cases of 'non collisions' (where material is merely swept

up) discussed above, this seems likely. Thus the estimates taking discontinuities into account seem like the best guess for impactor numbers. $N_{obj} \sim 100$ would fit nicely with the occultation results of Meinke et al. (2012) if the number of impactors corresponds to that of their rarer moonlets, i.e. one order of magnitude smaller than their ~ 1000 total objects with diameters greater or equal than a kilometre. Assuming that mini-jet numbers are a lower estimate, because the survey may have missed low-gradient features, the F ring region contains a steady population of at least ~ 100 small objects interacting with the core. More conservatively the number of objects can be described as $N_{obj} = 10^{2\pm1}$.

Such a population would have to be continuously replenished as its members are eroded or broken down by collisions. This is further evidence for ongoing accretion in the F ring core, as investigated by Canup and Esposito (1995), Karjalainen (2007) and others. There is already evidence that Prometheus may aid in triggering clump formation (Beurle et al., 2010; Esposito et al., 2012) and perturbing objects onto their colliding orbits. Although features found here are not correlated with Prometheus's location this does not rule out its influence as objects perturbed onto differing orbits would naturally spread around the ring (Hedman et al., 2011b; French et al., 2012).

Because the tip of a mini-jet is placed on an orbit similar to that of the colliding object Fig. 5.10 approximates the distribution of the object population in relative semi-major axis. For comparison, the maximum Δa perturbation exerted by Prometheus is ~ 20 km, when it and the F ring are at closest approach (Murray et al., 2008). This means multiple encounters are necessary to place some objects onto their mini-jet forming orbits, if indeed this is the mechanism. Subsequent encounters would be equally likely to perturb an object back towards the ring, depending on its exact orbit and the phase of closest approach, meaning objects could undergo a chaotic random walk in Δa around the core. Likewise their solidity and size would evolve by collisions in a random way over time with only a lucky few aggregating into solid moonlets as described in Esposito et al. (2012). This is a likely formation mechanism for S6, which must be a relatively young object.

An overall picture then emerges of mini-jet forming colliders being a subset of the total population of F ring objects. With some solidity, and on orbits differing by tens of km from the core, they are intermediate between temporary aggregates forming in the core and in the process of becoming larger, more solid moonlets on more distant orbits like S6. Mini-jets and jets would then represent two extremes of a continuum of collisional features, formed by steadily increasing impact velocities from steadily increasing Δa.

5.5. Conclusion

Small, irregular features have been found all around the F ring throughout the time that Cassini has observed it. Their numbers are highly variable, but average ~ 15 in the ring at any one time. Based on the analysis of over one thousand catalogued features they are randomly distributed but with a tendency to clump together in multiple structures. There may be fewer near the location of Prometheus but this trend seems weak at best. No long-term changes in their number with time are detected. Those with a resolvable linear structure (mini-jets) have angles consistent with a range of ages, from a few hours to a few days, and with around three quarters being less than one orbital period (≈ 15 hours) old. At least $\sim 10\%$ of mini-jets have evidence of older structures from previous collisions, however, and tracking them in detail over a subset of the observations revealed average lifetimes of $\sim 1-15$ days. Many showed significant morphological changes between images, including the creation of new mini-jets. Individual mini-jets, then, survive on the order of a single orbital period before dissipating, while structures created by repeated collisions by the same object last much longer, up to tens of days.

Collisions with a local moonlet population present the most likely explanation and the lifetime and numbers mean that several mini-jet forming collisions must happen each day. Depending on assumptions about the structure of the F ring core, and the nature of the collisions, this implies a population of order tens to hundreds of $\lesssim 1$km radius objects. Some of these moonlets have enough strength or self-gravity to survive multiple collisions but others are disrupted into groups of smaller objects on similar orbits. It is suggested that they are likely formed in the F ring itself, possibly due to the action of Prometheus, and are subsequently perturbed onto colliding orbits by further interactions. Those that survive may continue to grow and go on to form the larger visible objects such as S6. Mini-jets, therefore, represent one end of a continuum of collisional features with the other end being the large jets and spiral strands.

6. Large-Scale Collisional Features

In this chapter an analysis of the larger jet features is presented for comparison with the mini-jet survey of the previous chapter. Jets and strands were identified early in the exploration of the F ring but it was not until Charnoz et al. (2005) that the strands' spiral nature was noted and the two features tied together as being collisional in nature. Charnoz (2009) and Murray et al. (2008) then examined the jets in more detail, looking particularly at the role of S6, forming the basis for the discussion of mini-jets presented in Chapter 5. This chapter returns to the formation and evolution of jets with the additional knowledge gained from looking at their smaller cousins.

The next section lists the mosaics to be surveyed before the analysis method is outlined in Section 6.2. Section 6.3 presents the results for the statistics and distribution of the jets, with particular attention paid to features observed more than once. These results, and their implications for the collisions, are discussed in Section 6.4 before conclusions are drawn in Section 6.5.

6.1. Observations

Jets are typically much larger than a single NAC image, in which they appear as nearly parallel strands to the core, making their identification and measurement very difficult. The survey methods of the previous chapter are no longer appropriate and instead the F ring mosaics are used in this analysis.

Eight mosaics from December 2006 to May 2007, listed in Table 6.1, are surveyed. These are the same sequences examined by Murray et al. (2008) and are used here for the same reasons; they offer good, repeated coverage of most of the ring at reasonable resolution during a period where S6 was interacting regularly with it. The presence of additional jets, which do not appear to be associated with S6, also allows a variety of features to be analysed. Each mosaic is surveyed in turn using the methods presented below to find all the major jets. The statistics are then analysed and repeatedly observed jets are matched-up so that their time evolution can be

Mosaic	Imaging Sequence	Mid-Time	Images
1545	ISS_036RF_FMOVIE001_VIMS	2006-358-00:28:48.00	145
1546	ISS_036RF_FMOVIE002_VIMS	2007-005-21:12:57.60	130
1549-A	ISS_039RF_FMOVIE002_VIMS	2007-041-18:44:38.40	124
1551	ISS_039RF_FMOVIE001_VIMS	2007-058-15:01:26.40	143
1552	ISS_041RF_FMOVIE002_VIMS	2007-076-10:30:43.20	169
1554	ISS_041RF_FMOVIE001_VIMS	2007-090-15:51:50.40	130
1555	ISS_043RF_FMOVIE001_VIMS	2007-108-10:26:24.00	95
1557	ISS_044RF_FMOVIE001_VIMS	2007-125-10:23:31.20	178

Table 6.1.: Mosaics used in the jet survey.

tracked. Mini-jets and other small features are not discussed here.

6.2. Method

In Chapter 5 mini-jets were identified, and their base and tip locations measured in CAVIAR, by eye. Jets present more of a challenge as they often have very extended, messy base regions and fade to background levels gradually rather than having a well defined tip. They can also have extremely small gradients ($\sim \times 10^{-3\circ}$) making angle measurements by eye impossible. Instead a more robust semi-automated measurement technique is used by least-squares fitting to peaks in the mosaics' radial brightness profiles. The process is as follows:

- A mosaic file is loaded into IDL and stored as a 1501×108000 array with a raw brightness value, DN, between zero and 255 for each element. Row indices either side of the central row (751) then correspond to radial distance, r, in km away from the core model and columns are increasing co-rotating longitude, λ,[1] with each column $(1/300)^\circ \approx 8.16$ km wide.

- A peak-finding routine is run on each column of the mosaic and the maxima are ranked in order of their peak DN value.

- The brightest peak is identified as the F ring core and its r coordinate recorded as r_{core}. The second brightest peak is labeled jet number one, the third as jet two and the fourth as jet three, with corresponding radial coordinates r_{jet1}, etc.

---

[1]Note that references to 'longitude' from now on in this chapter will refer to co-rotating longitude, unless explicitly stated.
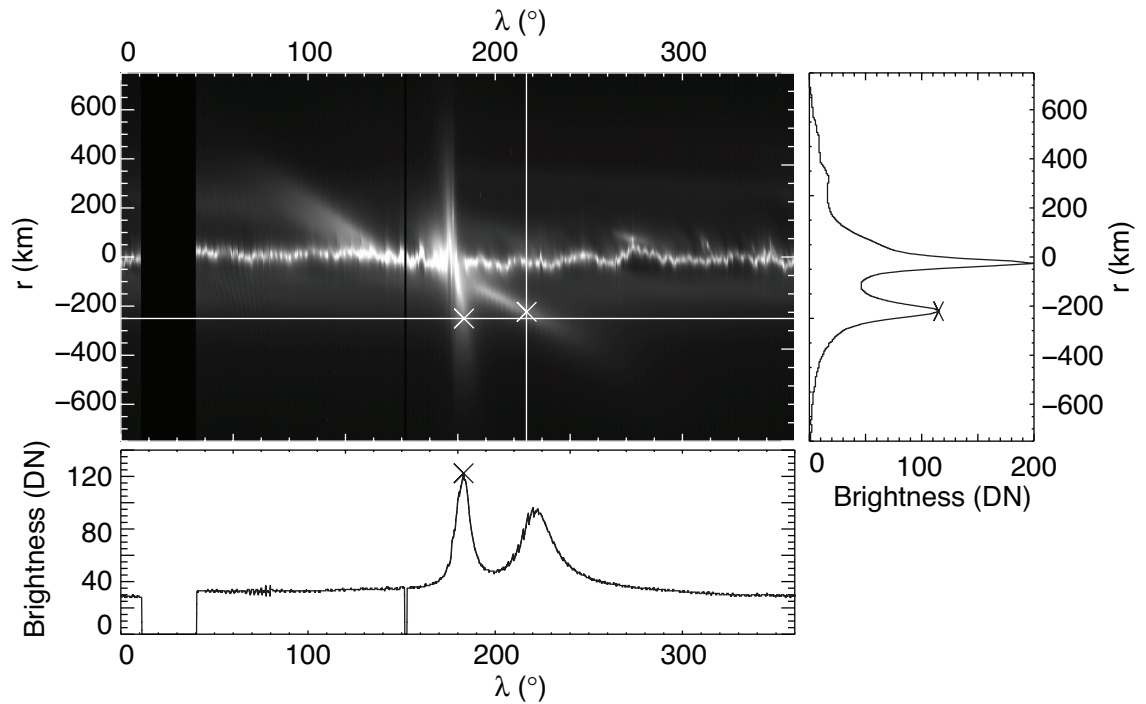
Figure 6.1.: Typical radial and longitudinal profiles from mosaic 1549-A. The radial profile is taken along the white, vertical line at $\lambda \sim 215°$ and shown on the right. r_{jet} is marked by an '$\times$'. The longitudinal profile is taken along the horizontal line at $r \sim -250$ km and shown below the mosaic with λ_{jet} marked.

- The radial locations of the 'core', 'jet 1', etc. ($r_{core}, r_{jet1}, ...$) are plotted on-top of the image to check that they match the bright areas and are not contaminated by stars or other features (see below). Linear trends in the jet peaks are then identified by eye and a straight line is fitted through each using *mpfit.pro* (Markwardt, 2009).

Figure 6.1 shows typical radial and longitudinal profiles extracted from 1549-A, the third mosaic in the sequence.

In almost all cases the brightest peak corresponds to the F ring core. The small number of exceptions are where bright stars or Prometheus appear in the mosaic or where jets or strands are especially bright and the 'core' jumps to these instead. Here a simple cut-off in radius (say no more than ± 100 km from the central row) is used with all 'core' locations falling outside this set to the mean core value in radius and brightness. This adjustment is only applied to a few columns in 108000 so should not bias the results. The mean core values all fall around 751, within one or two pixels, demonstrating the accuracy of the Cooper et al. (2013) core model.

Secondary and tertiary peaks can jump around between bright jets, both inside and outside the core, but tend to stay with one jet for enough longitudinal coverage for measurements to be made. Peaks are often confused and overlapping where jets encounter the core and these, and other contaminated sections, are excluded from the fits by eye. This means that only parts of some jets are measured, and the possible biases from this are discussed below. Longitudes where a particular jet, say jet 1, is measured are recored as, for example, λ_{jet1}.

The following measurements are made for each jet identified:

- The peak-finder is run again on the radial section between the jet and the core to identify the minimum DN. The distance between the jet and this minimum is taken as an approximation of the jet's width and the mean of these along the jet's length is recorded as its average width, W.

- A straight line is fitted to the measured jet positions, r_{jet} against λ_{jet}. Thus a model of the jet is created (r_{fit} against λ_{jet}) by finding the best-fit parameters, m and c, in the equation $r_{\mathrm{fit}} = m\lambda_{\mathrm{jet}} + c$. The mean jet width, W, is used as an estimate of the uncertainty in radial location for each point. m is converted to degrees, taking into account the mosaics' aspect ratio (1:8.16), and recorded as the jet gradient θ.

- The maximum radial extent, $R = |r_{\mathrm{max/min}} - r_{\mathrm{core}}|$, where $r_{\mathrm{max/min}}$ is either the smallest or largest value of r_{jet} for inwards or outwards jets, respectively, is recorded.

- The brightness (DN) values at each point in the jet are divided by the mean core brightness for that mosaic and the mean of these taken as the average normalised jet brightness B.

- The jet's intersection with the uneven core is found by extrapolating the fitted model, r_{fit}, to 360° in longitude and then performing a second linear fit to ($r_{\mathrm{fit}} - r_{\mathrm{core}}$) against longitude. The zero point where this new fitted solution goes from positive to negative or negative to positive values (i.e. where the model and core intersect) is then the jet's base longitude, λ_{base}. For some jets the gradient is so small that the jet actually 'wraps-around' through more than 360° before intersecting the core. For these features an estimate of the intersection is made by extrapolating r_{fit} to 720 or 1080°.

A typical jet and its associated best fit model are shown in Fig. 6.2.
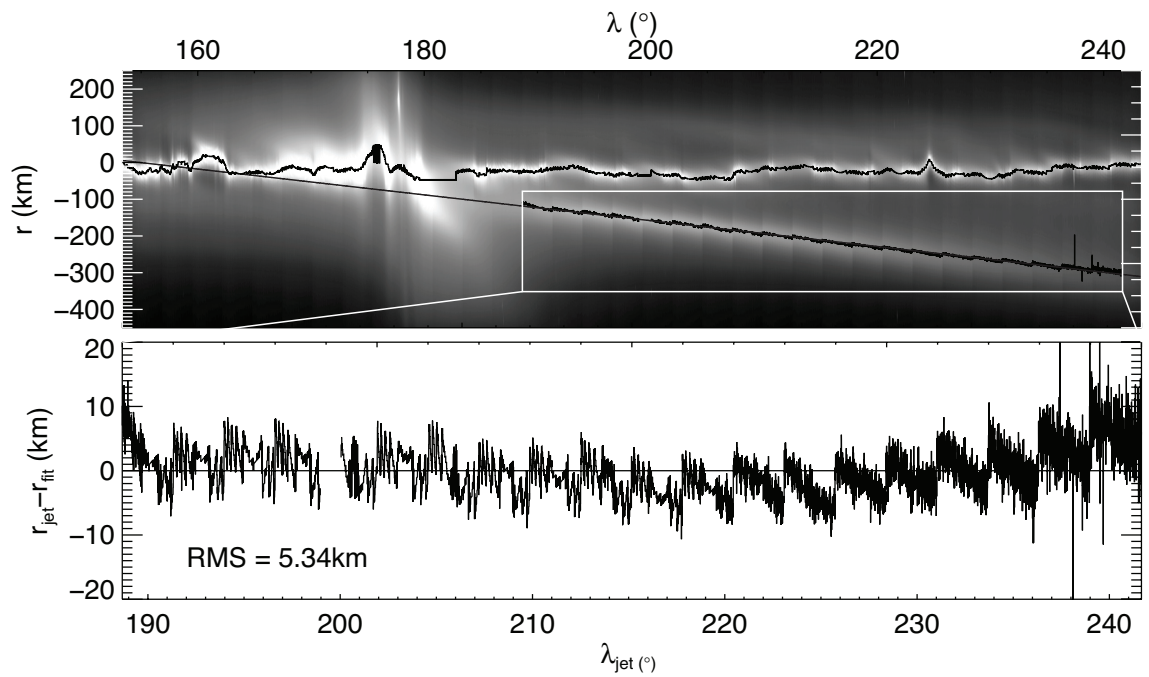
Figure 6.2.: Top: portion of mosaic 1549-A showing several large jets. r_{core} is over-plotted in black, along with r_{jet} for a selected jet ($I8$ from table 6.2) and the best-fit gradient, r_{fit}, and its intersection with the core. Bottom: best-fit residuals ($r_{fit} - r_{jet}$). The periodic 'jaggedness' is caused by imperfect joins between the constituent images of the mosaic.

The uncertainty in jet width, σ_W, is simply taken as the standard deviation of the measured width values along its length.

The uncertainty in angle, σ_θ, is the estimate of σ_m, provided by $mpfit.pro$ from the straight-line fit, again converted into degrees and adjusted for the aspect ratio.

R is a minimum estimate of the jet's radial extent, as faint parts of it could extend further out but not be measured, therefore no uncertainty is quoted for it.

σ_B is the standard deviation in brightness values along the jet's length combined with the standard deviation in core brightness, σ_{coreB}, using the normal error combination equations.

σ_λ is estimated by repeating the procedure for finding λ_{base} using the extremised versions of the straight-line model allowed by the fitting uncertainties. For example λ_{upper} is estimated by fitting $(r_{\mathrm{up}} - r_{\mathrm{core}})$ to longitude and finding its crossing point, where $r_{up} = (m - \sigma_m)\lambda_{\mathrm{jet}} + (c + \sigma_c)$ and σ_m and σ_c are the uncertainties from the straight-line fit for the gradient above. For 'wrap-around' features the procedure is the same except where $\lambda_{\mathrm{upper}} - \lambda_{\mathrm{lower}} > 360°$, i.e. the uncertainty is so large it is not known how many times the feature wraps around. Here upper and lower estimates of zero and 360 degrees are quoted.

The use of the mean jet width, W, for the uncertainty in jet radial position is a deliberate choice, taken to ensure a conservative estimate for the gradient error σ_θ. Theoretically the brightest point in the jet can be found with pixel, or greater, precision (~ 1 km), rather than the typical $W \approx 10 - 20$ km, but this significantly underestimates the true uncertainty. For example: linear fits to sections of a jet typically have residuals of $\sim \pm 10$km (see Fig. 6.2) and formal gradient errors of $\sigma_\theta = 10^{-2}$–10^{-4} ° but selecting a different section of a jet (λ_{jet}) can result in gradients which differ by more than this uncertainty. This can be seen in the residuals in Fig. 6.2 where a different trend, with a shallower gradient, is possibly seen after $\lambda \sim 220°$.

This is because real jets are not idealised, infinitely narrow lines with a single gradient, but complex, extended, collisional features. Their brightness can vary across their width and this can change significantly with longitude; they can contain clumps and mini-jets, like the core, and these may not be aligned with the centre of the jet. Additionally the centre of brightness, recorded by r_{jet}, is not always aligned with the axis of the jet where jets overlap with one another or the core. The second half of the jet in Fig. 6.2 is probably overlapping with another, older, jet which is difficult to see in the mosaic. An attempt is made to exclude sections like this by eye but the jets are often difficult to spot, resulting in systematic errors which can be greater than the formal statistical errors quoted above. Typically jets are

measured several times using different longitude ranges and the solution which best matches the average gradient, by-eye, is taken. Jet width is then used to provide a pessimistic estimate of the angle uncertainty which will be further discussed in the results section below. Finally the averaged jet width is used, rather than the width at each data point, so as not to unnecessarily weight certain parts of the jet above others.

Many of the mosaics contain young features, which are essentially radial in gradient (at this aspect ratio), and are not picked up by the method of radial profiling described above. These are instead identified by eye (they are obvious in the images) and measured with a modified method, illustrated in Fig. 6.3:

- Rows of pixels, limited to the neighbourhood of the feature, are examined to find the longitude of the brightest pixel, λ_{jet}, at each radius, r_{jet} (see Fig. 6.1). The longitudinal profiles are much more noisy than radial ones so before the peak value is found the profile is smoothed in IDL over 50 pixels.

- The same linear fit as before is performed except this time with the equation $\lambda_{\text{fit}} = m_1 r_{\text{jet}} + c_1$, fitting for λ_{jet}.

- The best-fit solutions are transformed back to be compatible with the radially searched jets by $m = 1/m_1$ and $c = 1/c_1$ and the rest of the process (measuring gradients, finding intersects, etc.) is identical.

Smoothing the profiles introduces an additional uncertainty in λ_{jet} which is conservatively estimated as twice the smoothing length, 100 px $\approx$ 1000 km. The young, radial jets are observed to be very longitudinally extended, sometimes by several thousand kilometres (see Fig. 6.3), so this does not reduce the accuracy needlessly. Jet widths, W, are set to 1000 km and R is set to $> |750|$ km to reflect the fact that traces of these features can be found in profiles all the way to the inner and outer edges of the mosaics. σ_θ is calculated as before but, with these large widths, is expected to be large. Gradients for these young features should then be considered order of magnitude estimates, in keeping with their blurred, extended appearance.

Experiments were performed with Gaussian and Lorentzian fits to the radial profiles to find centroids and full widths at half maxima for the peaks. The extreme variability of the F ring profile, sometimes with a single broad peak, sometimes with many similarly sized peaks, however, made this extremely difficult and the fit often failed. Combining this with the increased computation time (fitting two or three peaks 108000 times) and the systematic errors described above, it was decided not to pursue this method.
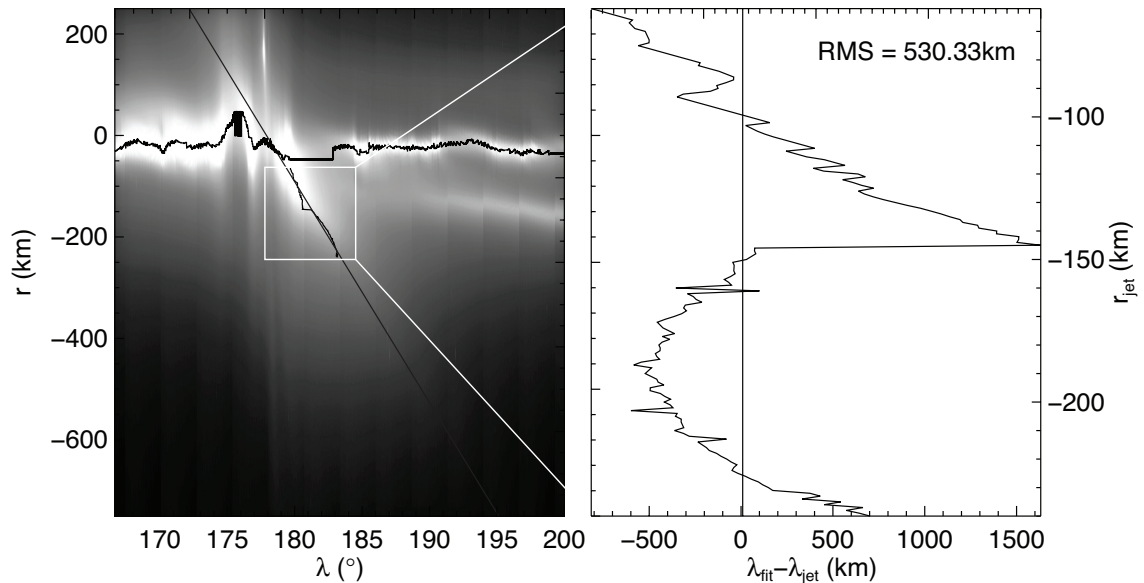
Figure 6.3.: Left: portion of mosaic 1549-A showing several large jets. r_{core} is over-plotted in black, along with r_{jet} for a selected young jet ($I7$ from table 6.2), its best-fit gradient, r_{fit}, and intersection with the core. Right: best fit residuals ($\lambda_{fit} - \lambda_{jet}$), in kilometres, which are much larger than those of older jets (e.g. Fig. 6.2 above), showing the uncertainty in the axis of this large, extended feature.

6.3. Results

A total of 97 jets, shown in Fig. 6.4 and listed in Table 6.2, are identified in the eight sequences. They are numbered in order of increasing base longitude for each sequence, proceeded by an 'I' or 'O' for inwards or outwards pointing jets, respectively. There are more outwards jets (59 versus 32) than inwards. The average of ~ 12 jets per sequence is similar to mini-jets.

Jets have a variety of morphologies, from young, blurred features, like $I7$ in Fig. 6.3, to extremely old features, like $O1$, which have wrapped around multiple times and appear as 'strands', almost parallel to the core. Immediately apparent is the jet complex associated with S6, as it progresses along the core. Young jets form at the newest collision points, increasing in longitude over time, overlapping older, more sheared, features. The disturbance is visible on both sides of the core as a large perturbed region, several degrees long. Identifying individual jets within this is discussed in more detail below but for now the statistical properties of the whole population are examined.

(a)

(b)
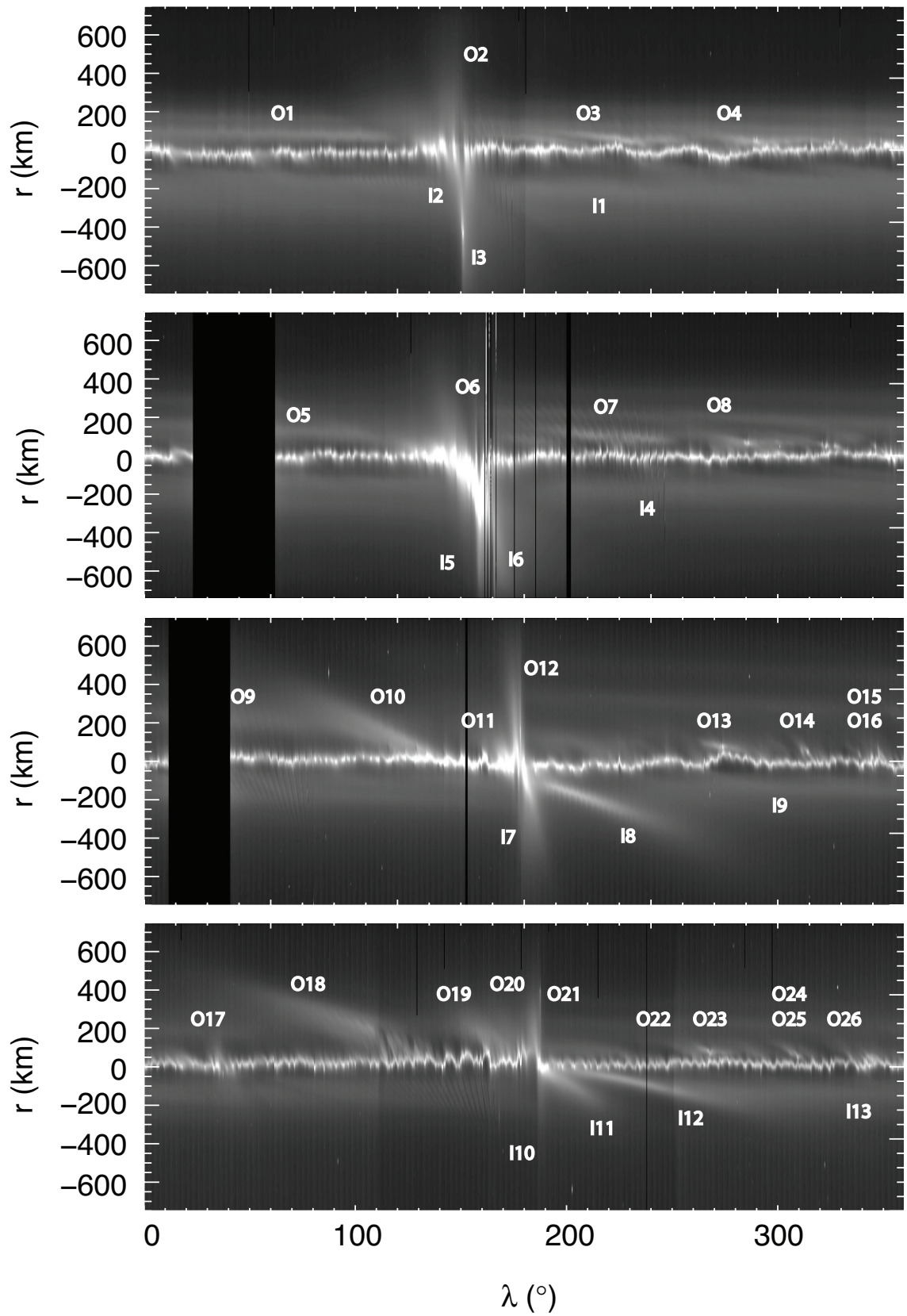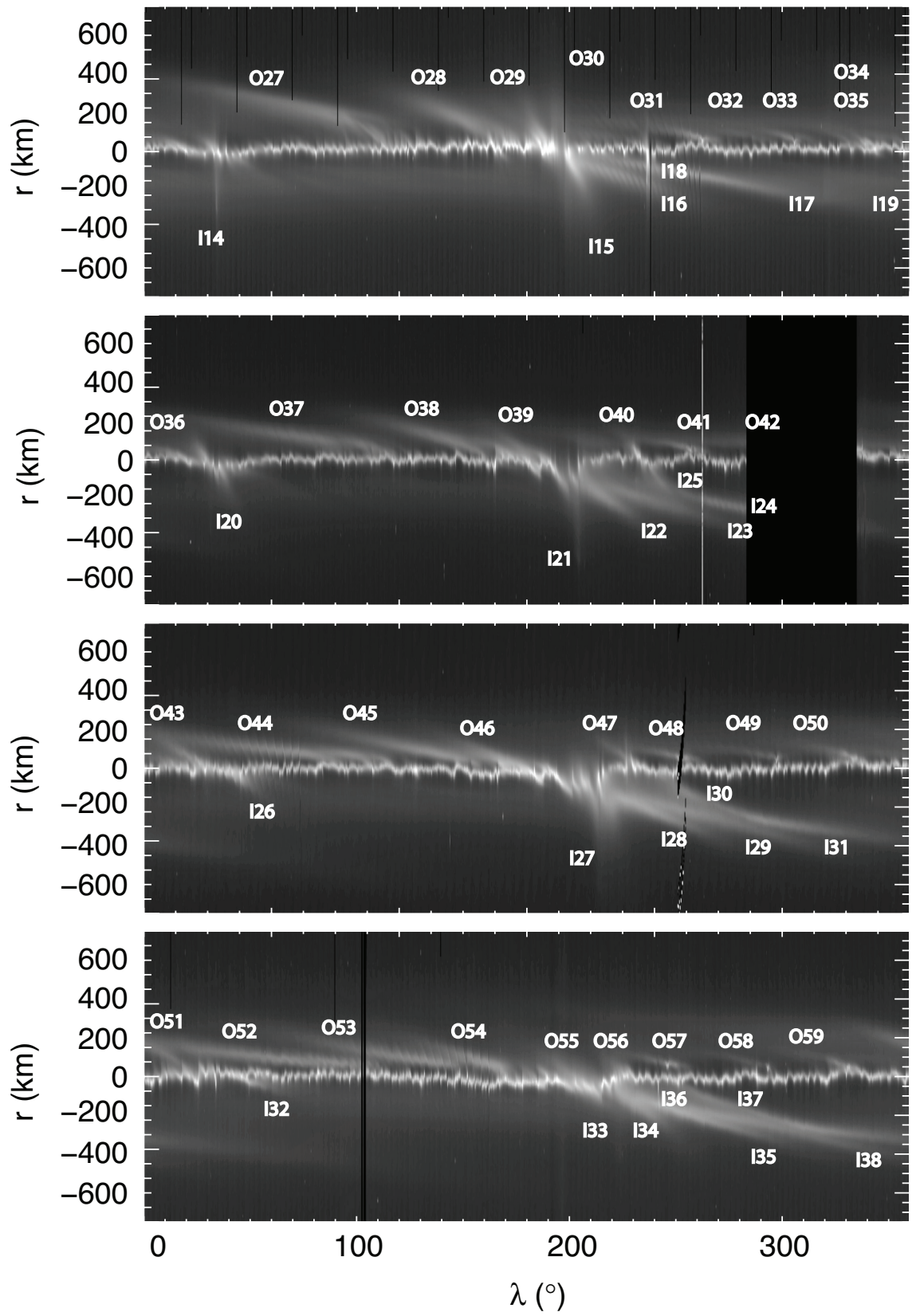
Figure 6.4.: The eight mosaics used in this survey: a) 1545, 1546, 1549-*A* and 1551,
b) 1552, 1554, 1555 and 1557 with the jets labelled. Contrast has been
enhanced to aid visibility.

Name	Mosaic	θ	λ_{base}	R	W	B
		(°)	(°)	(km)	(km)	
$I1$	1545	-0.0091 ± 0.0014	$89^{+57.03}_{-74.1}$	-230	92 ± 16	0.3 ± 0.3
$I2$	1545	-1.4158 ± 76.5545	$147^{+2.25}_{-2.25}$	-750	1000 ± 1000	1.00 ± 0.98
$I3$	1545	-48.9943 ± 32.3525	$151^{+0.24}_{-0.25}$	-750	1000 ± 1000	0.60 ± 0.62
$O1$	1545	-0.0042 ± 0.0004	$176^{+35.19}_{-30.55}$	128	46 ± 6	0.50 ± 0.47
$O2$	1545	7.3007 ± 10.8577	$145^{+0.15}_{-0.15}$	750	1000 ± 1000	0.20 ± 0.15
$O3$	1545	-0.0306 ± 0.0025	$267^{+4.77}_{-4.07}$	102	30 ± 5	0.6 ± 0.6
$O4$	1545	-0.0362 ± 0.0022	$313^{+2.13}_{-1.9}$	86	33 ± 5	0.60 ± 0.57
$I4$	1546	-0.0027 ± 0.0003	$276^{+275.64}_{-275.64}$	-243	71 ± 30	0.20 ± 0.25
$I5$	1546	-11.4763 ± 39.6720	$158^{+0.38}_{-0.38}$	-750	1000 ± 1000	1.40 ± 1.36
$I6$	1546	-1.1152 ± 43.4556	$156^{+0.41}_{-0.4}$	-750	1000 ± 1000	0.80 ± 0.76
$O5$	1546	-0.0042 ± 0.0041	$53^{+53.17}_{-53.17}$	149	63 ± 5	0.30 ± 0.33
$O6$	1546	-1.1048 ± 58.3683	$148^{+1.12}_{-1.12}$	750	1000 ± 1000	0.30 ± 0.34
$O7$	1546	-0.0199 ± 0.0004	$342^{+12.3}_{-11.78}$	148	41 ± 14	0.40 ± 0.41
$O8$	1546	-0.0377 ± 0.0006	$323^{+9.89}_{-9.57}$	142	29 ± 16	0.40 ± 0.42
$I7$	1549	-1.0203 ± 67.0369	$178^{+1.3}_{-1.3}$	-750	1000 ± 1000	1.00 ± 0.96
$I8$	1549	-0.0857 ± 0.0011	$159^{+4.94}_{-4.81}$	-335	90 ± 28	0.6 ± 0.6
$I9$	1549	-0.0003 ± 0.0007	0^{+0}_{-0}	-327	63 ± 10	0.30 ± 0.34
$O10$	1549	-0.067 ± 0.002	$160^{+8.14}_{-7.66}$	461	82 ± 18	0.50 ± 0.46
$O11$	1549	-30.2381 ± 78.3102	$178^{+3.34}_{-3.34}$	750	1000 ± 1000	0.80 ± 0.83
$O12$	1549	-8.9572 ± 83.3146	$176^{+6.37}_{-6.37}$	750	1000 ± 1000	0.30 ± 0.27
$O13$	1549	-0.0489 ± 0.0013	$313^{+16.45}_{-15.57}$	125	19 ± 12	0.50 ± 0.53
$O14$	1549	-0.3015 ± 0.0737	$316^{+1.87}_{-1.13}$	93	34 ± 4	0.50 ± 0.45
$O15$	1549	-0.2553 ± 0.0276	$319^{+0.65}_{-0.52}$	82	26 ± 5	0.70 ± 0.69
$O16$	1549	-0.3250 ± 0.0701	$341^{+0.79}_{-0.51}$	58	19 ± 6	0.6 ± 0.6
$O9$	1549	-0.0064 ± 0.0035	$115^{+244.51}_{-115.49}$	464	99 ± 26	0.30 ± 0.27
$I10$	1551	-3.3754 ± 23.6049	$186^{+0.19}_{-0.2}$	-750	1000 ± 1000	0.1 ± 0.1
$I11$	1551	-0.1444 ± 0.0020	$186^{+5.45}_{-5.3}$	-148	21 ± 12	0.70 ± 0.69
$I12$	1551	-0.0538 ± 0.0008	$190^{+6.13}_{-5.96}$	-169	54 ± 23	0.60 ± 0.62
$I13$	1551	-0.0002 ± 0.0013	0^{+0}_{-0}	-176	73 ± 22	0.40 ± 0.36
$O17$	1551	-0.0051 ± 0.0021	$0^{+272.05}_{-190.33}$	238	43 ± 19	0.20 ± 0.24
$O18$	1551	-0.0750 ± 0.0023	$161^{+7.99}_{-7.51}$	354	138 ± 32	0.40 ± 0.39
$O19$	1551	-0.0616 ± 0.0101	$218^{+73.53}_{-52.64}$	285	75 ± 14	0.30 ± 0.28
$O20$	1551	-2.3884 ± 68.4148	$186^{+1.71}_{-1.71}$	750	1000 ± 1000	0.80 ± 0.78
$O21$	1551	80.8634 ± 72.1622	$187^{+2.38}_{-2.38}$	750	1000 ± 1000	0.20 ± 0.19
$O22$	1551	-0.0961 ± 0.0023	$272^{+13.05}_{-12.43}$	194	28 ± 11	0.30 ± 0.29
$O23$	1551	-0.0465 ± 0.0026	$300^{+34.07}_{-30.42}$	101	22 ± 8	0.50 ± 0.53
$O24$	1551	-0.1609 ± 0.0041	$314^{+16.37}_{-15.54}$	108	22 ± 11	0.50 ± 0.47
$O25$	1551	-0.1518 ± 0.0243	$321^{+1.43}_{-1.03}$	76	18 ± 9	0.30 ± 0.32
$O26$	1551	-0.2423 ± 0.0225	$338^{+0.57}_{-0.47}$	90	21 ± 6	0.40 ± 0.42
$I14$	1552	-18.1648 ± 1.0477	$34^{+0.64}_{-0.64}$	-372	1000 ± 1000	0.30 ± 0.27
$I15$	1552	-0.5564 ± 69.2732	$197^{+1.51}_{-1.51}$	-750	1000 ± 1000	0.80 ± 0.76
$I16$	1552	-0.0683 ± 0.0024	$180^{+14.3}_{-13.33}$	-169	36 ± 10	0.80 ± 0.76

$I17$	1552	-0.0466 ± 0.0006	$192^{+6.33}_{-6.16}$	-283	73 ± 30	0.60 ± 0.57
$I18$	1552	-61.8014 ± 3.7017	$235^{+2.38}_{-2.38}$	-204	1000 ± 1000	0.40 ± 0.43
$I19$	1552	-0.0023 ± 0.0026	$71^{+71.32}_{-71.32}$	-330	82 ± 24	0.40 ± 0.37
$O27$	1552	-0.0549 ± 0.0014	$161^{+5.85}_{-5.56}$	442	130 ± 36	0.40 ± 0.38
$O28$	1552	-0.0989 ± 0.0019	$183^{+6.47}_{-6.23}$	253	80 ± 23	0.40 ± 0.38
$O29$	1552	-0.5205 ± 75.1431	$189^{+2.55}_{-2.55}$	750	1000 ± 1000	$0.5 \ \pm 0.5$
$O30$	1552	40.9542 ± 48.7075	$193^{+0.84}_{-0.84}$	750	1000 ± 1000	0.20 ± 0.18
$O31$	1552	-0.0524 ± 0.0011	$287^{+11.94}_{-11.44}$	119	26 ± 26	0.50 ± 0.46
$O32$	1552	-0.0313 ± 0.0033	$336^{+6.86}_{-5.58}$	122	33 ± 6	0.30 ± 0.33
$O33$	1552	-0.0879 ± 0.0073	$317^{+1.52}_{-1.29}$	83	27 ± 8	0.50 ± 0.48
$O34$	1552	-0.1138 ± 0.0060	$339^{+0.8}_{-0.72}$	98	25 ± 12	$0.4 \ \pm 0.4$
$O35$	1552	-0.2317 ± 0.0106	$340^{+0.15}_{-0.14}$	53	11 ± 4	0.80 ± 0.76
$I20$	1554	-0.6698 ± 3.6510	$35^{+2.43}_{-2.43}$	-125	1000 ± 1000	0.70 ± 0.69
$I21$	1554	-0.3442 ± 82.6510	$189^{+4.38}_{-4.39}$	-750	1000 ± 1000	0.10 ± 0.15
$I22$	1554	-0.1610 ± 0.0158	$191^{+2.09}_{-2.54}$	-227	83 ± 36	0.80 ± 0.85
$I23$	1554	-0.0699 ± 0.0050	$173^{+3.81}_{-4.4}$	-223	93 ± 32	0.60 ± 0.63
$I24$	1554	-0.0536 ± 0.0051	$175^{+8.35}_{-10.09}$	-265	116 ± 21	0.60 ± 0.56
$I25$	1554	-0.2454 ± 0.0155	$233^{+0.71}_{-0.81}$	-182	66 ± 22	0.70 ± 0.66
$O36$	1554	-0.4379 ± 79.8192	$30^{+3.51}_{-3.5}$	750	1000 ± 1000	0.70 ± 0.69
$O37$	1554	-0.0373 ± 0.0007	$149^{+4}_{-3.85}$	239	72 ± 20	0.50 ± 0.46
$O38$	1554	-0.0739 ± 0.0020	$176^{+8.49}_{-8.05}$	162	58 ± 17	0.50 ± 0.51
$O39$	1554	-0.1909 ± 82.6510	$184^{+5.17}_{-5.17}$	750	1000 ± 1000	0.20 ± 0.21
$O40$	1554	-0.6666 ± 10.1086	$233^{+7.5}_{-7.49}$	61	1000 ± 1000	0.90 ± 0.92
$O41$	1554	-0.0547 ± 0.0097	$283^{+6.41}_{-4.5}$	83	25 ± 6	0.70 ± 0.65
$O42$	1554	-0.0005 ± 0.0031	$212^{+211.73}_{-211.73}$	101	41 ± 9	0.30 ± 0.34
$I26$	1555	-0.1796 ± 82.6510	$37^{+4.3}_{-4.3}$	-154	1000 ± 1000	0.10 ± 0.14
$I27$	1555	-1.6194 ± 75.1431	$213^{+2.15}_{-2.15}$	-750	1000 ± 1000	0.40 ± 0.36
$I28$	1555	-0.0934 ± 0.0061	$189^{+2.69}_{-3.06}$	-233	108 ± 27	0.70 ± 0.72
$I29$	1555	-0.0527 ± 0.0029	$162^{+23.97}_{-21.51}$	-284	96 ± 56	0.60 ± 0.59
$I30$	1555	-0.1428 ± 0.0448	$235^{+5.53}_{-10.58}$	-175	85 ± 6	0.60 ± 0.59
$I31$	1555	-0.0373 ± 0.0058	$126^{+24.28}_{-33.19}$	-349	172 ± 56	0.60 ± 0.61
$O43$	1555	-0.1425 ± 0.0020	$32^{+0.68}_{-0.66}$	169	26 ± 8	0.50 ± 0.48
$O44$	1555	-0.0255 ± 0.0006	$156^{+5.42}_{-5.16}$	163	49 ± 12	0.50 ± 0.49
$O45$	1555	-0.0495 ± 0.0012	$177^{+7.48}_{-7.13}$	144	48 ± 10	0.60 ± 0.55
$O46$	1555	-0.0598 ± 0.0072	$188^{+3.49}_{-2.74}$	86	44 ± 11	0.50 ± 0.54
$O47$	1555	-0.1410 ± 0.0105	$237^{+1.24}_{-1.07}$	131	58 ± 66	0.40 ± 0.37
$O48$	1555	-0.0424 ± 0.0021	$290^{+27.5}_{-24.92}$	117	30 ± 15	0.40 ± 0.38
$O49$	1555	-0.0455 ± 0.0030	$330^{+315.05}_{-37.63}$	102	30 ± 10	0.40 ± 0.39
$O50$	1555	-0.0330 ± 0.4261	$106^{+173.83}_{-100}$	135	55 ± 8	$0.4 \ \pm 0.4$
$I32$	1557	-0.0172 ± 0.0079	$15^{+62.29}_{-15.24}$	-50	12 ± 13	0.70 ± 0.67
$I33$	1557	-0.3885 ± 82.6510	$208^{+4.38}_{-4.39}$	-85	1000 ± 1000	$0.7 \ \pm 0.7$
$I34$	1557	-0.1757 ± 0.0169	$215^{+1.06}_{-1.29}$	-117	48 ± 14	0.50 ± 0.55
$I35$	1557	-0.0748 ± 0.0029	$199^{+1.78}_{-1.93}$	-215	81 ± 23	0.60 ± 0.58
$I36$	1557	-8.7260 ± 75.9512	$242^{+2.27}_{-2.28}$	-130	1000 ± 1000	0.80 ± 0.79

$I37$	1557	$-0.0863 \pm\ 0.0041$	$235^{+25.21}_{-22.9}$	-164	54 ± 8	0.60 ± 0.58
$I38$	1557	$-0.0335 \pm\ 0.0009$	$130^{+12.17}_{-11.54}$	-389	140 ± 58	0.50 ± 0.52
$O51$	1557	$-0.1346 \pm\ 0.0039$	$31^{+1.18}_{-1.12}$	193	53 ± 24	0.50 ± 0.46
$O52$	1557	$-0.0253 \pm\ 0.0003$	$155^{+2.41}_{-2.36}$	185	38 ± 14	0.50 ± 0.52
$O53$	1557	$-0.0357 \pm\ 0.0010$	$190^{+9.1}_{-8.6}$	148	45 ± 13	0.60 ± 0.56
$O54$	1557	$-0.0713 \pm\ 0.0070$	$184^{+2.53}_{-2.08}$	111	52 ± 8	0.60 ± 0.61
$O55$	1557	-0.3292 ± 87.3414	$200^{+13.68}_{-13.68}$	116	1000 ± 1000	0.30 ± 0.28
$O56$	1557	-0.2442 ± 83.9584	$230^{+6.02}_{-6.02}$	111	1000 ± 1000	0.30 ± 0.33
$O57$	1557	$-0.0574 \pm\ 0.0016$	$277^{+15.11}_{-14.27}$	139	33 ± 16	0.40 ± 0.37
$O58$	1557	$-0.0647 \pm\ 0.0017$	$315^{+16.78}_{-15.88}$	134	30 ± 16	0.30 ± 0.28
$O59$	1557	$-0.0520 \pm\ 0.1173$	$15^{+329.87}_{-11.54}$	194	55 ± 19	0.30 ± 0.33

Table 6.2.: Surveyed jets numbered by increasing longitude in each mosaic. Each jet has its gradient, base intercept, radial extent, mean width and mean brightness measured as described in Section 6.2. Errors are also described here.

Figure 6.5 shows the distribution in radial extent, R, for the 97 jets. The plot has been truncated at ± 500km to exclude the vertical jets with radial extents greater than the size of the mosaics (19 with R $\geq |750|$ km). Those jets with measured radial extents fall between about 50 and 500 km from the core with a distribution which is relatively flat (especially when considering statistical uncertainties of order the square root of the number of points per column) across this range. Also plotted in Fig. 6.5 are the Δa values of the mini-jets from the survey in Chapter 5 that fall within the jet survey. It is debatable whether they form a single continuous distribution or two discrete populations with a cross-over around $50 - 100$ km. Considering a single population, the distribution resembles a Gaussian with long tails out to hundreds of kilometres. It is also worth remembering that R is a lower estimate and the true maximum extent of some of these jets may be larger. This may enhance the lack of features around the $50 - 100$ km cross-over region but, with the small numbers involved, it is unlikely to be statistically significant. The implication for the total colliding population appears to be that it has a relatively flat, or broad peaked Gaussian distribution in Δa out to several hundred kilometres from the core with a large number of objects with $|\Delta a| < 50$ km.

The distribution in B, the mean brightness of each jet normalised by the mean core brightness in each mosaic, is plotted in Fig. 6.6. The median and mean are both $\sim 0.5 \pm 0.2$ (the standard distribution), i.e. jets are, on average, around half as bright as the F ring core. They vary from ten times smaller to similar to its brightness, with one jet slightly brighter than the core. This is in great contrast to optical depth profiles derived from occultations, as measured by UVIS and VIMS,
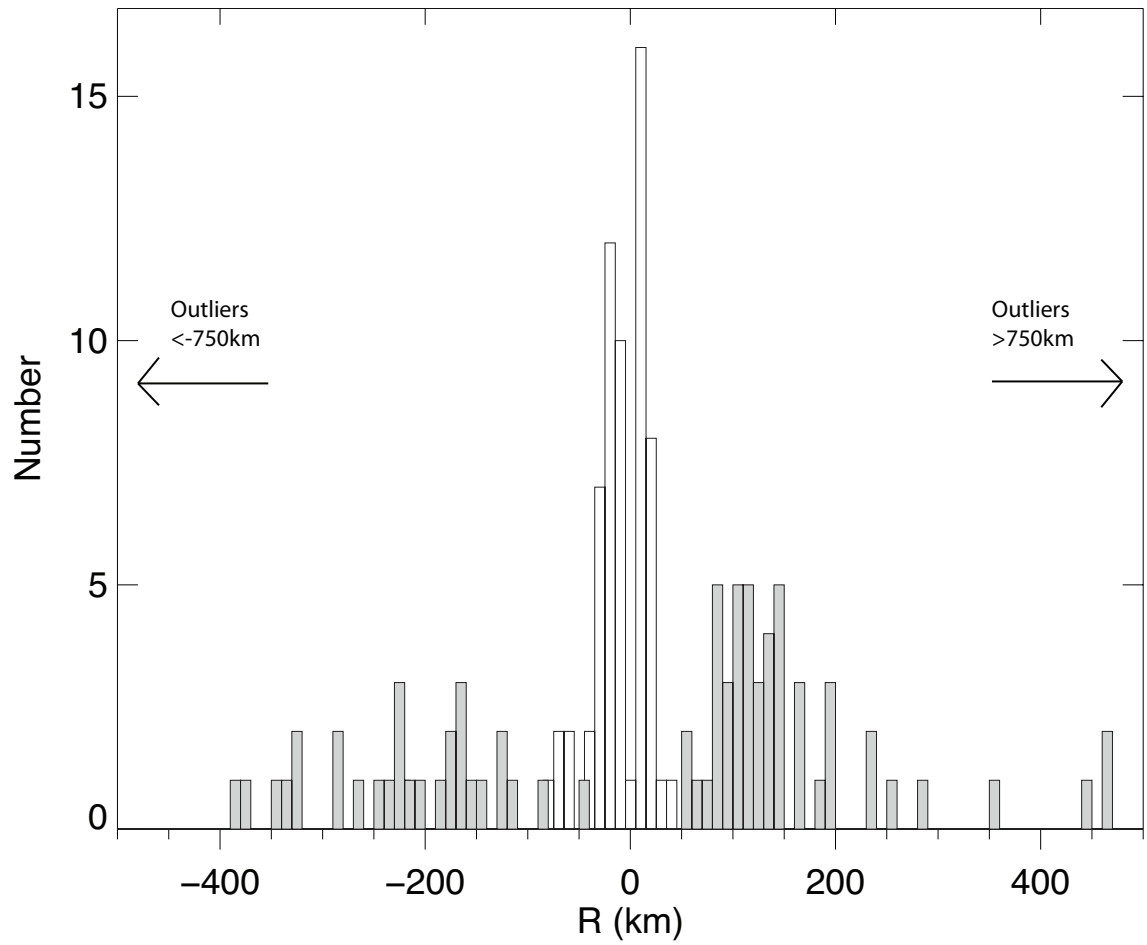
Figure 6.5.: Distribution of R, a minimum estimate of radial extent, of the surveyed jets (filled). Unfilled bins are the distribution of calculated Δa for the mini-jets found in these same sequences (see Chapter 5 above). Data are binned at 10 km.
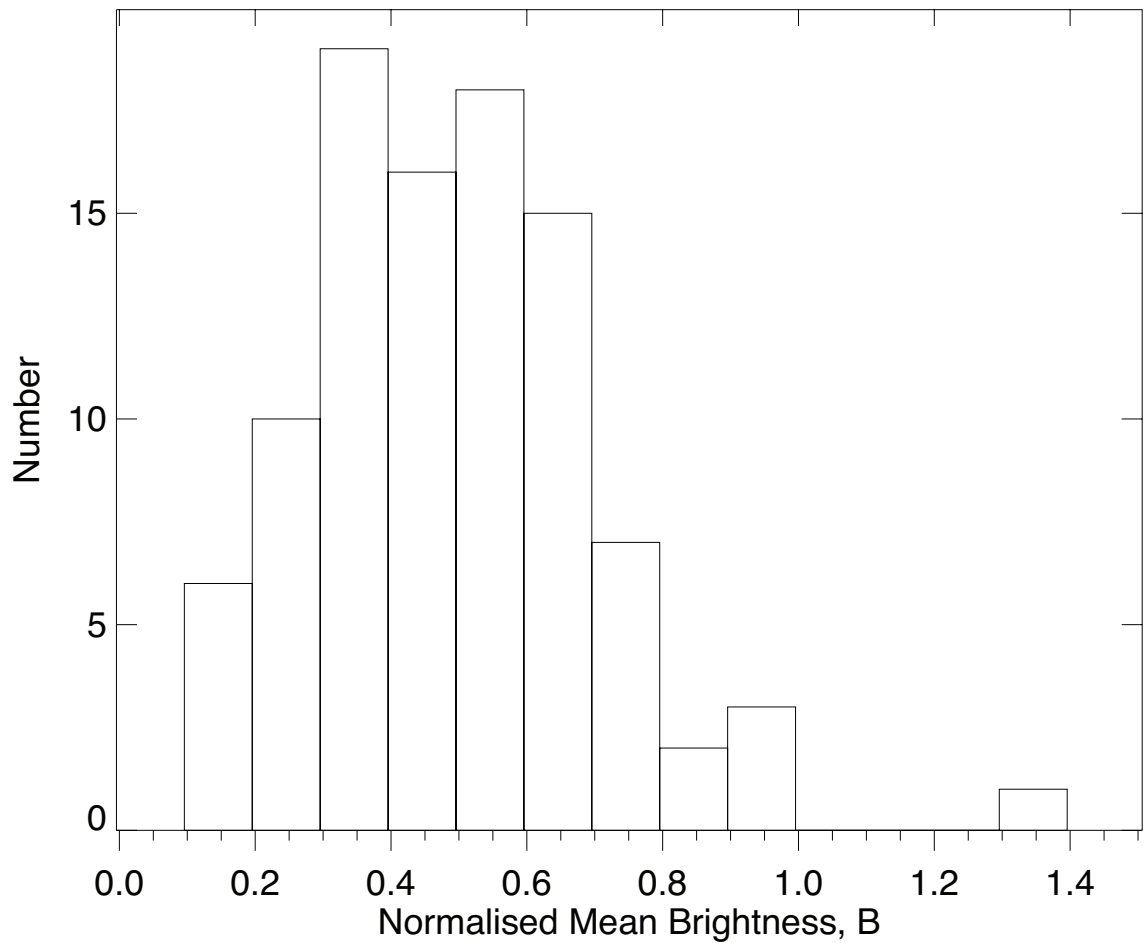
Figure 6.6.: Distribution of B, the mean brightness of each jet normalised by the mean core brightness in that mosaic. The mean and median of the distribution are both $\sim 1/2$ of the core.

where jets have, on average, ten times smaller optical depth than the core (Albers et al., 2012). A differing optical depth-brightness relation between jets and the core may imply different particle size distributions between the two.

Figure 6.7 shows the distribution of the absolute values of the gradients in logarithmic bins. As with Fig. 5.10, for the mini-jets, increasingly more jets are seen at lower gradients which is to be expected as they age and shear over. There is a noticeable cutoff at $0.01°$ however with only a few jets having gradients less than this. As before, it is likely that this represents observational bias, in that jets with this small a gradient must be extremely old, faint and wrapped around the core many times to the point where they may blur into the F ring background.

The distribution of mean jet widths, W, (left-hand side of Fig. 6.8) shows them to be $5 - 10$ times wider than a $10 - 20$ km core, which is marginally consistent
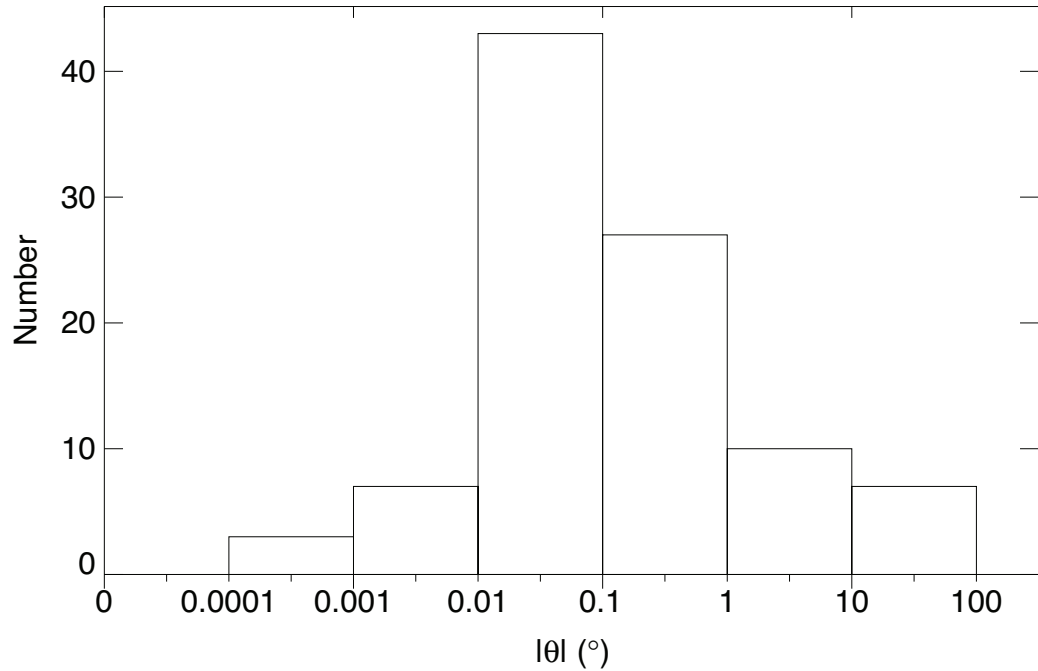
Figure 6.7.: Distribution of the absolute values of θ, the best-fit jet gradients, in logarithmic bins.

with the UVIS observations (Albers et al., 2012). However, the right-hand side of the figure plots the relation between W and the absolute radial extent of the jets $|R|$, showing a clear trend for large widths at large radial extents. Considering the method described in Section 7.1 this is obviously an artefact of the measurement process. The jet 'width' is actually a measurement of the distance between the middle of the jet and the minimum between it and the core. This will naturally be correlated with the distance the jet is from the core and therefore W may not be a good measurement of the jet's real width, i.e. the spread in the particles' positions and velocities from the collision. A Gaussian fit to the jet's radial profile may give a better estimate but the broad F ring background will still be present, making it difficult to detect where the brightness bump from a jet begins. Jets far from the core are inherently easier to spot against the darker background meaning there is likely to always be some correlation between width and radial extent. Subsequent analysis therefore focusses on jet gradients, rather than further consideration of W.

No other significant correlations between jet properties (θ, W, B, R) are detected.
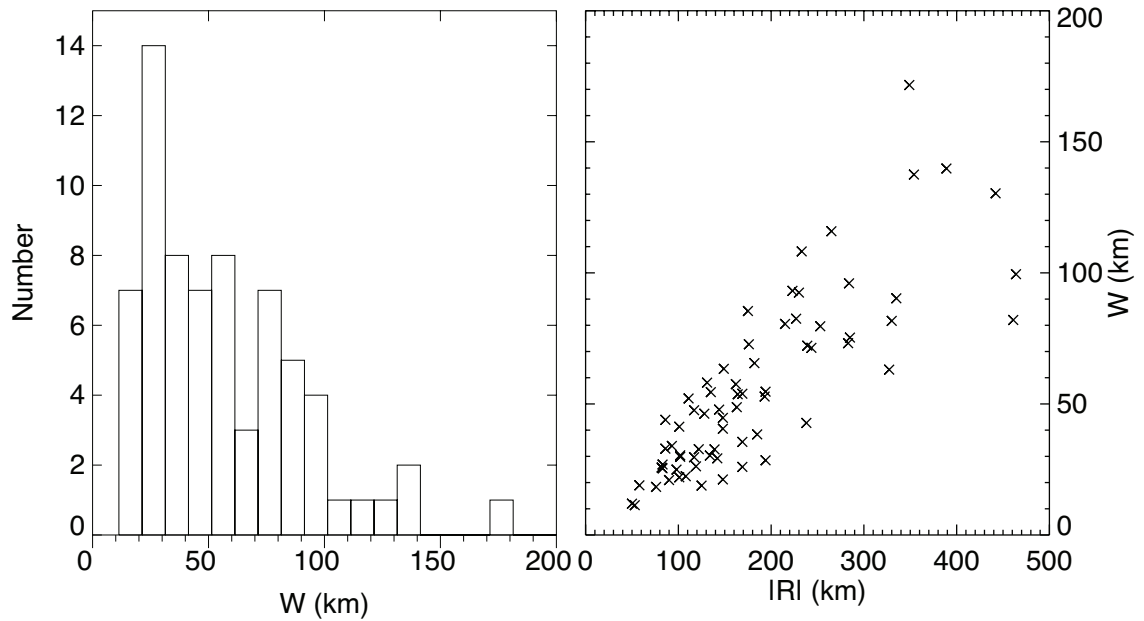
Figure 6.8.: Left: distribution of W, the mean jet widths. Right: W as a function
of absolute value of radial extent, R. There is a clear correlation which
is an artefact of the measurement process, as described in the text.

6.3.1. Repeated Features

Many of these 97 jets are actually the same feature imaged more than once. These
repeated features provide a variety of additional information so efforts are made to
identify them by a combination of matching base longitudes, angles and morphology.

18 repeat features are identified, comprising 85 individual jets from Table 6.2.
Each repeated feature is given a new designation, proceeded by an 'R', and listed
in Table 6.3 below. Upper and lower lifetime estimates are made for each based on
their visibility, as in the previous chapter. The evolution of their gradients, core
intersects and brightnesses are then examined and an estimate of the jet's origin
made.

Lifetimes and locations

The lifetime estimates are poorly constrained as many of the jets survive longer than
the 133 day total observing period. This in itself is an indication that jet lifetimes
are significantly longer than those of mini-jets. Taking the mean of the estimates
suggests jets are visible for ~ 60 days or more. An average of around a dozen jets,
with ~ 60 d lifespans, visible at any one time implies a formation rate of ~ 0.2 d^{-1}.
Assuming all other parameters are the same, Eqn. 5.2 implies a population of ~ 10

Name	1st Obs.	T_{low} (d)	T_{upper} (d)	$T_0 - T_{1545}$ (d)			χ^2/DOF	$\dot{\lambda}_{\text{base}}$ $(\degree \text{d}^{-1})$
$R1$	$O1$	12.9	83.4	-882.12	$\pm$	243.20	0.03	$-$
$R2$	$I1$	83.4	97.7	-1493.12	$\pm$	477.30	0.98	$-$
$R3$	$O2$	132.4	$-$	-7.32	$\pm$	2.50	4.80	0.090 ± 0.015
$R4$	$I6$	119.6	$-$	2.18	$\pm$	1.36	2.02	0.250 ± 0.047
$R5$	$O3$	12.9	48.8	-173.32	$\pm$	11.56	1.42	
$R6$	$O4$	$-$	$-$	$-$			$-$	$-$
$R7$	$I7$	66.7	83.6	38.78	$\pm$	0.73	4.65	-0.080 ± 0.083
$R8$	$O11$	83.7	$-$	40.78	$\pm$	1.94	3.50	0.060 ± 0.084
$R9$	$O14$	83.7	$-$	41.98	$\pm$	1.49	5.31	-0.030 ± 0.040
$R10$	$O15$	83.7	$-$	37.78	$\pm$	2.46	6.01	0.020 ± 0.058
$R11$	$O16$	84.7	$-$	41.38	$\pm$	2.76	1.07	-0.090 ± 0.029
$R12$	$O20$	66.8	$-$	62.18	$\pm$	13.99	0.24	-0.020 ± 0.040
$R13$	$I15$	49.0	$-$	76.98	$\pm$	3.69	0.30	0.020 ± 0.047
$R14$	$I27$	17.0	$-$	110.98	$\pm$	6.16	0.00	0.120 ± 0.144
$R15$	$I14$	49.0	$-$	83.18	$\pm$	0.01	2.07	0.090 ± 0.109
$R16$	$O36$	34.8	$-$	89.78	$\pm$	1.02	8.25	-0.070 ± 0.070
$R17$	$I18$	49.0	$-$	83.380	$\pm$	0.009	0.27	-0.150 ± 0.158
$R18$	$O40$	35.0	$-$	88.78	$\pm$	5.93	0.00	-0.140 ± 0.272

Table 6.3.: Table of repeatedly observed features where 'first observation' is the designation of the first jet making up the feature. T_{low} and T_{upper} are the lower and upper bounds on the feature's observed lifetime, respectively. T_0 is the estimated formation time, with uncertainty, based on fitting its angle evolution, minus the time of the first sequence, 1545. The normalised chi-squared from this fit is shown in the next column. $\dot{\lambda}_{\text{base}}$, the base progression rate, is the relative mean motion which best fits the base longitudes of the feature's constituent jets. Features with missing upper lifetimes lasted longer than the observation period while $R1$, $R2$, $R5$ and $R6$ have anomalous gradient or intercept evolutions and are described in the text.
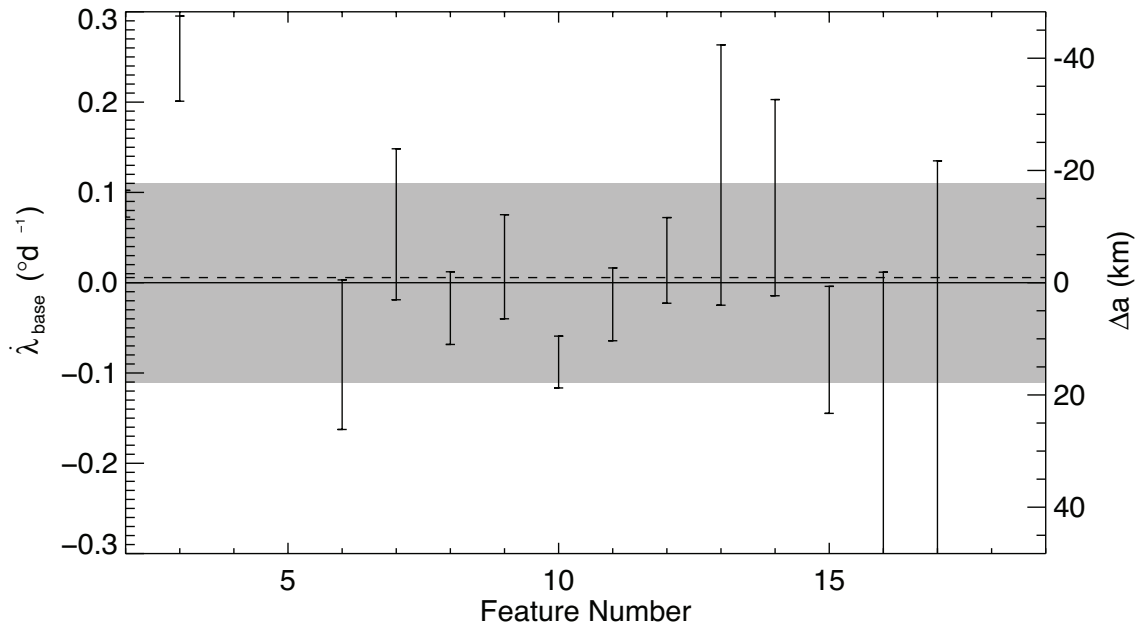
Figure 6.9.: Progression of the base longitudes of the repeated features. Each data point is the relative mean motion that best fits the individual longitudes of jets making up that feature. Errors are the associated uncertainties from the fit. The dashed line is the mean of all the features while the grey shaded region is the standard deviation. The result is consistent with zero relative mean motion.

colliding objects, about one order of magnitude smaller than for mini-jets.

A linear fit to λ_{base} over time for each jet making up a feature in Table 6.3 is performed to check whether the jets as a whole move relative to the core. Longitude errors are the estimates for λ_{upper} and λ_{lower} from above and the times are taken as the mid-times of each observation sequence with no uncertainty used (Cassini timing errors are much smaller than the durations of interest here). The resulting base progression rates, in units of degrees per day with associated fitting uncertainties, are quoted in Table 6.3 and plotted in Fig. 6.9. The results are consistent with zero: the intersection points of each jet with the F ring core do not move relative to the core's own mean motion, n, implying that jet origin points have orbits consistent with the core's. This may be expected but the jets could have had formation points with orbits ± 20 km from the 'core', producing significantly different mean motions, whilst still appearing to come from the bright central region. The fact that jet base locations do not move significantly over time simplifies the process of matching up repeated features and means that their average locations, $\langle \lambda_{base} \rangle$, can be used.

Four features in Table 6.3 do not have base progression fits: $R1, R2, R5$ and $R6$.

$R1$ and 2 are both very old features ($\sim 2 - 4$ years) which have wrapped around multiple times and have very large errors in the intersects. $R5$ has only two longitude measurements and is also quite an old feature (~ 173 d), with large uncertainties, whilst $R6$ will be discussed further below. In addition, only the first three longitude measurements are used for $R11$ as the others have very large uncertainties and are not trusted.

Gradients

Jets will shear over time with their gradient decreasing towards zero. In the short term relative eccentricity will cause the gradient to oscillate on orbital timescales. However, given the average time between observations is 16.6 d $\approx 27P_0$, only the long-term evolution will be fitted here. Consideration of the errors, which are often comparable to- or larger than the magnitude of these gradient oscillations, also supports this. Long-term evolution of θ should follow Keplerian shear as described by Eqn. 3.7 from Chapter 3. A fit to this is performed on θ, for each constituent jet in a feature, over time, fitting for a single parameter; T_0, the jet formation time. Different errors and fit equations are explored using chi-squared statistics with

$$\chi^2 = \sum \frac{(\theta_{obs} - \theta_{pre})^2}{\sigma_\theta^2}, \tag{6.1}$$

where θ_{obs} are the measured gradients and θ_{pre} are those predicted by the model, with σ_θ the uncertainties in gradient as before. Chi-squared is then normalised, or reduced, by dividing by the degrees of freedom (DOF), the number of measurements (between one and eight) minus the number of fitted parameters (one in this case). Values obtained were in most cases > 1 implying underestimated uncertainties or a poor choice of model. Since the average gradient of a jet must follow Keplerian shear (the particles have a range of Δa so must shear over time, even if their short term evolution is complicated by Δe or $\Delta\varpi$) it must be σ_θ that are too small; most likely due to the systematic errors discussed above. Jets are then fitted using errors on their gradients of $3\sigma_\theta$ as pessimistic estimates. This produced more reasonable normalised χ^2 values, with most around 2, but still a large amount of scatter from the desired $\chi^2/DOF \approx 1$. Uncertainties in the formation time, σ_{T_0}, are therefore quite large (and variable) as shown in Table 6.3.

Features $R1$ and $R2$ are both extremely old (estimated at 882 and 1493 days, respectively) with gradients that are essentially flat with time, changing by amounts too small to be confidently detected. Nonetheless their formation time estimates are reasonable given their appearance, with multiple wraps around the core, and

they have been checked by looking at earlier mosaics. Jets in these locations are indeed visible for two to four years previously and, given the large uncertainties, may actually be two sides of the same feature.

$R5$ is estimated at 173 days old but, as discussed above, has an anomalously high relative mean motion and may actually be two separate jets very close to one another. Another possibility is that it is part of an older jet (e.g. $R1$) which has re-collided with the core in several places, forming younger sub-jets. This is a possibility with a number of other features in this region; $R6, 9, 10$ and 11. $R9$ and 10 have gradients which appear to follow the standard curve (albeit with large χ^2) but with odd appearances; having large, bright clumps and seeming to merge from two jets into a single feature. $R6$, on the other hand, has gradients which appear steady or even increasing so its formation time is not fitted. $R6$ also has a bright clump as shown in Fig. 6.10 and $O22$ may also be related. $R1$ is nearby in longitude and radius and the whole region is full of jets which are blurred and overlapping raising the possibility that they are all re-collision features from the older jet. Another possibility is that these features are actually limited arcs of material coming from the bright clumps embedded within them. These could be disrupted by collisions or tidal forces and shed material which will shear either side of the clump whilst moving along with it in longitude. Fitting to the longitudes of the bright clumps over time, in the same way as λ_{base} above, produces relative mean motions of $-0.330 \pm 0.0080°\mathrm{d}^{-1}$ and $-0.26 \pm 0.0144°\mathrm{d}^{-1}$ for $R6$ and $R9$ respectively (assuming longitude errors of approximately the size of the clump). These correspond to Δa values of ~ 53 km and 42 km. Measuring the radii of the clumps relative to the core from the mosaics results in $r_{clump} = 47 \pm 15.6$ km and 49 ± 14.9 km respectively (where the errors are the standard deviations in the r measurements), in close agreement.

The remaining features have formation times that fall within the observing sequence or a few days of the beginning. These have reasonable gradient fits although many still have poor reduced χ^2. For most this is because one or more young, near vertical, jets are included in the fit and their large gradient uncertainties distort the normalised residuals. If these jets are excluded and the fits re-run no significantly improved solutions are obtained. Having a single data point early in the jet's evolution helps pin down its formation date, even if that data point is not particular good: it confirms the jet's existence even if it does not constrain its gradient much. Indeed, checking for features in the mosaics before and after each T_0 confirms these formation time estimates to be plausible.

Fits to Eqn. 3.8, which assumes mini-jet like oscillations with $\Delta a = a\Delta e$, are also tried but, again, no significant improvement to χ^2 are found. Hundreds more
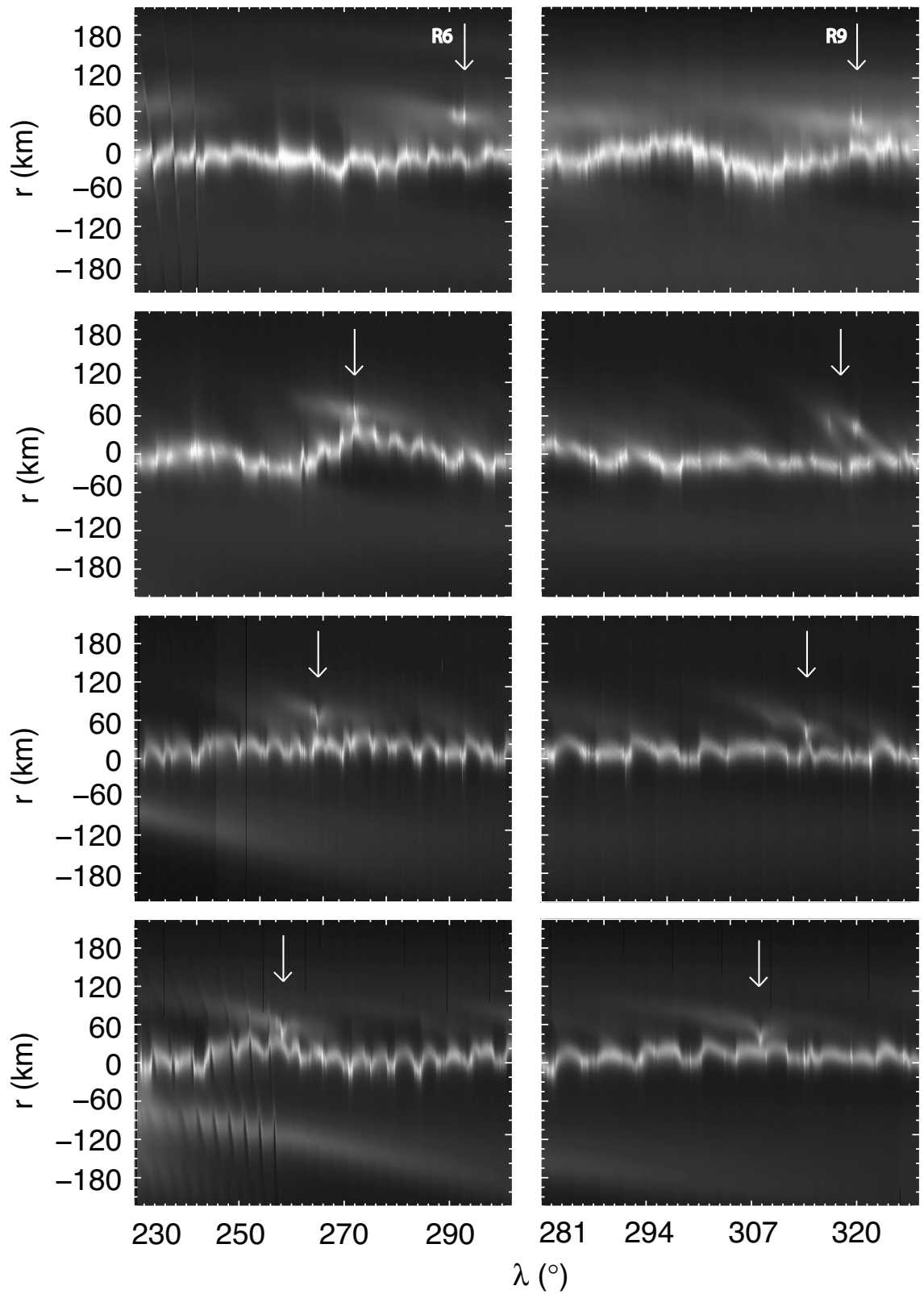
Figure 6.10.: Portions of mosaics 1545, 1546, 1549-A and 1551 showing the evolution of features $R6$ (left) and $R9, 10$ (right) which contain bright clumps. Streamer-channels are visible in the top and bottom left panels along with numerous other features.

T_0 solutions are possible for each jet but iterating the fitting programme to sweep across them generally did little to improve χ^2 or significantly change the formation times. To summarise: long term evolution of the jets fits Keplerian shear but with significant variation which could be accounted for by the biases in the gradient measurements. Alternatively some oscillations in gradient may be occurring on orbital time scales but the time resolution is not good enough to tell.

Brightness

Jet brightness should decrease with time, as described in Chapter 4, as Keplerian shear spreads out the finite number of particles over an ever increasing volume of space. This is generally seen in trends in B but the behaviour is quite variable. For some features $(R1, R9, R10, R11)$ a power-law decrease with time appears a good match to B but for others there seems to be large amounts of scatter or an essentially flat brightness with time $(R2, R3, R6, R12, R15)$. For all features the large variations in core brightness (to which jets are normalised) mean large uncertainties in B resulting in poor χ^2 statistics and large uncertainties in any fitted relations. B is most likely a relatively poor measure of intrinsic jet brightness, being the mean value along its length which can vary quite considerably and can easily be biased upwards by bright clumps. However it does show the general trend of decreasing brightness over time.

As discussed above W is not considered a good measure of jet width so its evolution is not analysed further.

Jet origin and number of objects

Figure 6.11 plots the average location and best-fit formation times of each of the repeated jets, showing the clustering of features into discrete groups.

There are 7 repeat features, plus a further ~ 7 individual jets, which can be positively identified as the S6 complex. This progresses along the core throughout the observations, increasing in longitude from $\sim 150°$ to $\sim 220°$ whilst forming new jets. Just upstream of it, at $\sim 235°$, a second complex of one inward and one outward jet forms mid-way through the observation period. A third complex of inwards and outwards jets forms at about the same time at $\sim 30°$. Finally a fourth cluster is found between about 320 and 340°, containing $R9, 10$ and 11 and possibly also $O35$. In addition to these there are the two older features, $R1$ and $R2$, described above and the anomalous $R5$.

If the anomalous jets are all re-collision features associated with the older $R1$
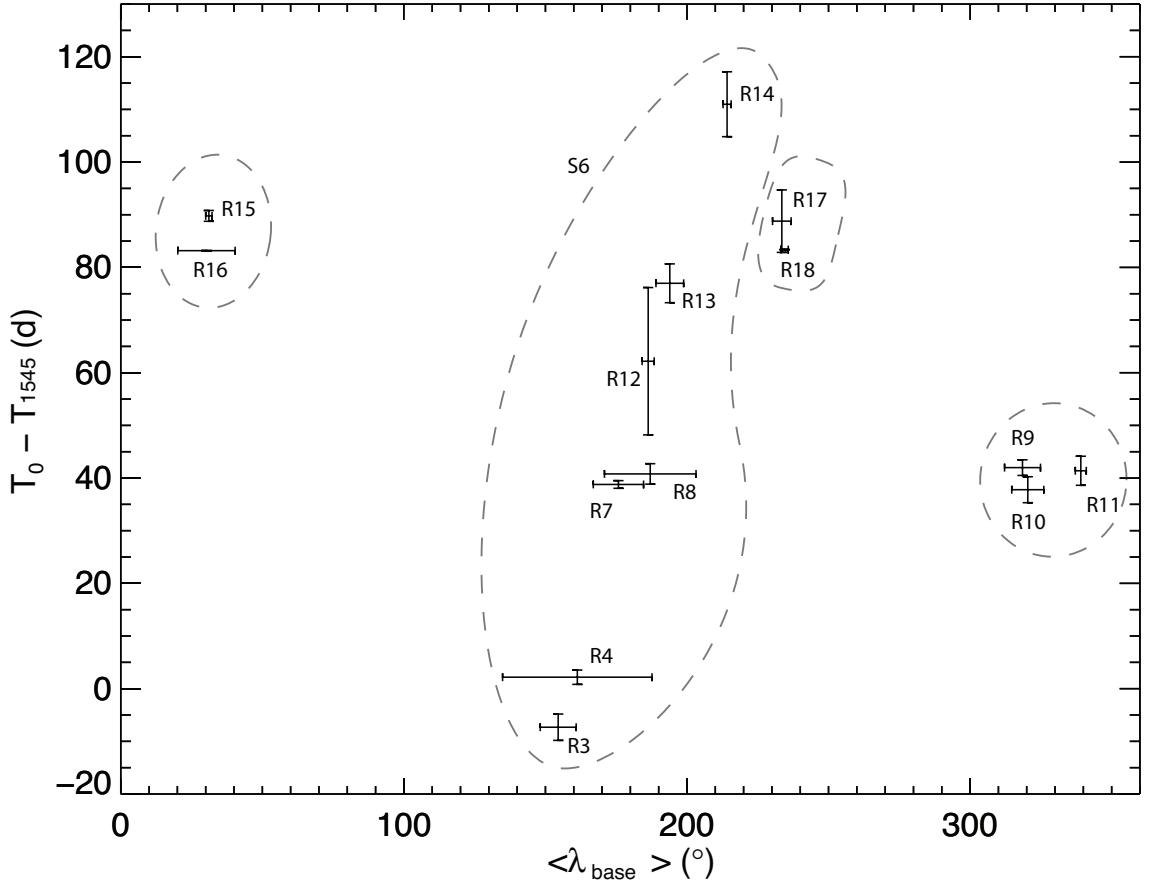
Figure 6.11.: Best-fit jet formation times, T_0, against average base longitudes, $\langle\lambda_{base}\rangle$. Since base locations do not move significantly (see Fig. 6.9) a simple mean of the individual λ_{base} is used with the error bars denoting its standard deviation. Vertical errors are σ_{T_0}. Some of the repeated jets fall outside this plot as described in the text.

and $R2$ and these themselves are previous S6 collisions (possible given the large uncertainty in their base locations and formation times) this suggests a minimum of three colliding objects: S6 and two more producing the second and third jet complexes. More likely there are four or five objects, considering one or two for $R5, 6$ and $R9, 10$ and the other individual jets. This is consistent with the estimate of order ten colliding objects, from the lifetimes, above.

There are a total of 30 individual features (18 repeat features plus the 12 unmatched, single jets) and seven are visible in the first mosaic. Therefore 23 features formed during the 133 day observation period; a formation rate of $\approx 0.17\,\mathrm{d}^{-1}$, again consistent with the previous estimate.

It is tempting to conclude that inwards and outwards jets with similar $\langle\lambda_{base}\rangle$ are two sides of a single double-sided jet; indeed the overlapping error bars of some

of the features in Fig. 6.11 are consistent with them forming at the same time. However not all close pairs can be reconciled in this way (e.g. $R15, 16$ and $R3, R4$) and one inwards feature, $R14$, is unpaired. It seems that some, apparent, jet pairs are actually separate jets, one inwards and one outwards, closely spaced in time. This is entirely consistent with an object with large relative eccentricity, like S6, crossing the core twice per orbit, inwards and outwards, creating closely spaced jets.

6.4. Discussion

Jets have a variety of morphologies, appearing superficially similar to mini-jets but with some differences: many, especially young, features have less pronounced lengths and widths than mini-jets, fading to background levels rather than ending sharply. No analogue to the 'bright-headed' mini-jets are detected which may mean different ejecta distributions or that colliding objects are not located at the head of the feature. On the other hand visible objects are seen when S6 is present and in the second jet complex (see Fig. 6.13). Jets are seen on both sides of the core simultaneously, or very close to one another, implying colliders with large relative eccentricities. Jets also seem to cluster together in complexes, much like repeated mini-jet features. Young jets emerging from these complexes are seen on-top of previous features in a similar way to the formation of 'complex' mini-jets. The search method used here is not optimised for finding 'objects'.

Of the three major jet complexes studied in this chapter, one is associated with a known object, S6, and travels along the core with this object's relative mean motion ($\sim 70°$ in 133 days is close to S6's expected $0.54°$ d^{-1} relative mean motion). French et al. (2014) also identify this jet complex using their clump tracking algorithm as an 'extended clump' (their feature C19/2006) and associate it with S6. New jets form on either side of the core as it passes through it twice per orbit. However, with only 14 new jets forming during this period versus an expected ~ 400 orbit crossings the efficiency of jet formation is clearly low; only 3.5% of collisions result in a jet. Even taking into account the clumpy nature of the core this is extremely small; it may take more than one pass by S6 through the core to form a visible jet. Figure 6.12 shows a close-up of the collision region from the first mosaic, 1545, along with S6's trajectory over the next ten orbits; calculated from Eqn. 3.3 using relative orbital elements derived from the supplementary material of Murray et al. (2008). The extended chain of objects is obvious and the nature of the relative orbits is such that the distance between adjacent collision points ($3\pi\Delta a$) is less than its length.
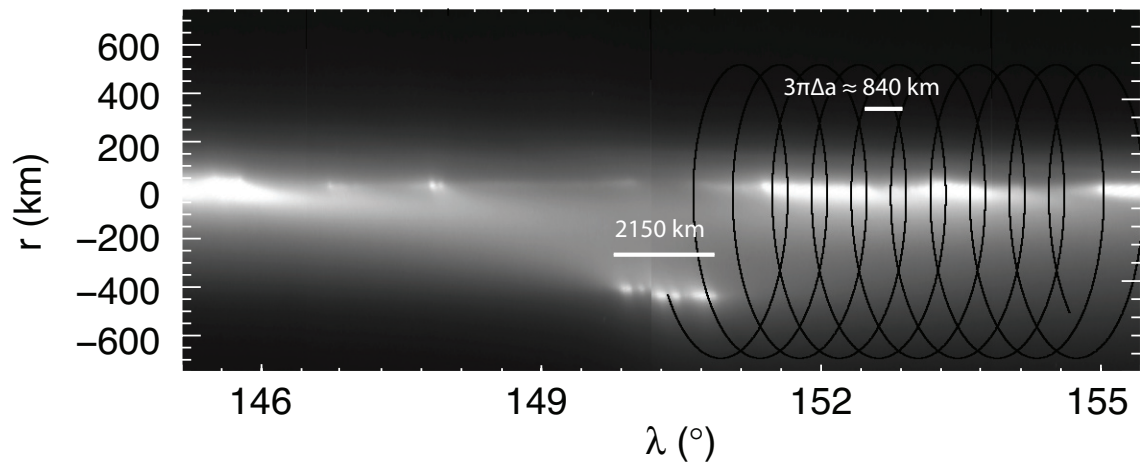
Figure 6.12.: Portion of mosaic 1545 showing S6 and the disturbance in the core it creates. S6's trajectory for the next ten orbits is over-plotted showing how the relative orbits cause segments of ring to be struck multiple times.

Collisions can no longer be approximated as a series of discrete impulses but as a long, drawn out interaction affecting a large section of ring which slowly progresses in longitude.

The other two jet complexes do not appear to move along the core (although they are not observed for as long as the S6 structure). This either implies colliding objects with $a\Delta e \gg \Delta a$ (so small relative mean motions) or objects that are destroyed or placed onto different, non-interacting, orbits by the collisions. The $R15, 16$ feature is also noted by French et al. (2014) (their feature C22) as a 'rapidly spreading extended clump'. French et al. (2014) use a method of integrated width profiles which compresses the feature down to a single brightness bump which spreads with time. Here the individual jets which make up this bump can be resolved and it can be seen (Fig. 6.13) that they are produced by at least two collisions between a small chain of objects and the core. In the last mosaic a new jet is produced at almost exactly the same longitude, presumably by the same chain of objects, confirming they have an orbit with $a\Delta e \gg \Delta a$. Evidence of a previous collision at the same longitude is also visible in 1552 but unfortunately the previous mosaic lacks coverage here. Dark channels in the dust envelope are also visible, much like the N1557026084 feature from the previous chapter. The $R17, 18$ feature is also shown in Fig. 6.13 but is more difficult to identify because of the other prominent jets nearby. It too consists of an inward jet closely followed by an outwards one which both shear away from the collision site. There is also a new jet present in the final mosaic, $I36$,

which is actually previously identified as N1557026084 in the mini-jet survey of the previous chapter. The fact that it is observed in both surveys demonstrates the continuum nature of F ring features from mini-jets up to large jets.

An object with $\Delta a = -20$ km would move from the $R17, 18$ collision point to the location of $I36$/N1557026084 in approximately the time between mosaic 1552 and 1557, raising the possibility that these are caused by the same impactor. Both are primarily inwards jets of similar size but there are morphological differences, $R17$ also having the outwards $R18$ component and being radially more extended and brighter. Additionaly N1557026084 is theorised to have been formed by an impactor with $\Delta a \approx -30$ km rather than -20. Given the closeness of these orbits and the uncertainties, however, it cannot be ruled out that these two features are, in-fact, related.

Subsequent mosaics are dominated by a single large, inwards jet wrapping around multiple times. This unusually prominent strand has also been noted in photometry and stellar occultations and most likely formed from the material ejected by S6 in this sequence. Albers et al. (2012) place this feature in a new category, intermediate in both peak optical depth and width between strands and the core, and name it the F ring 'secondary'. They detect the secondary in UVIS occultations from the beginning of 2008 (but note that occultations are sporadic in time and longitude so can easily miss a jet before it has wrapped all the way around) between $r = -50$ and -250 km. French et al. (2012) note that the appearance of this feature nearly doubles the total brightness of the F ring as seen in ISS image photometry. They model its contribution to this integrated brightness as a linear increase from November 26th, 2006 to a peak at April 16th, 2007 followed by an exponential decay back to normal F ring conditions with a half life of about 90 days. This puts the start of its formation just before mosaic 1545 and the peak brightness between mosaics 1554 and 1555, consistent with the formation of bright jets by S6 in this sequence.

Cooper et al. (2015) measured the orbital elements of parts of this feature, referred to as the strand, from ISS images in streamer-channel movies. Six of these sequences fall after the formation of the strand (between August 9th, 2008 and July 28th 2009), allowing its position to be measured and fitted to a number of precessing ellipses in the same way as the core in Cooper et al. (2013). Each fit is to a separate segment of the strand, essentially sampling it at random, so the ensemble displays a range of orbital elements. Cooper et al. (2015) also track clumps seen in the strand between FMOVIE mosaics 1577 and 1582 and fit their orbital elements. Finally they estimate the strand's formation date as being between late January and late April, 2007, based on its gradient in the mosaics and Eqn. 3.7. This agrees relatively well
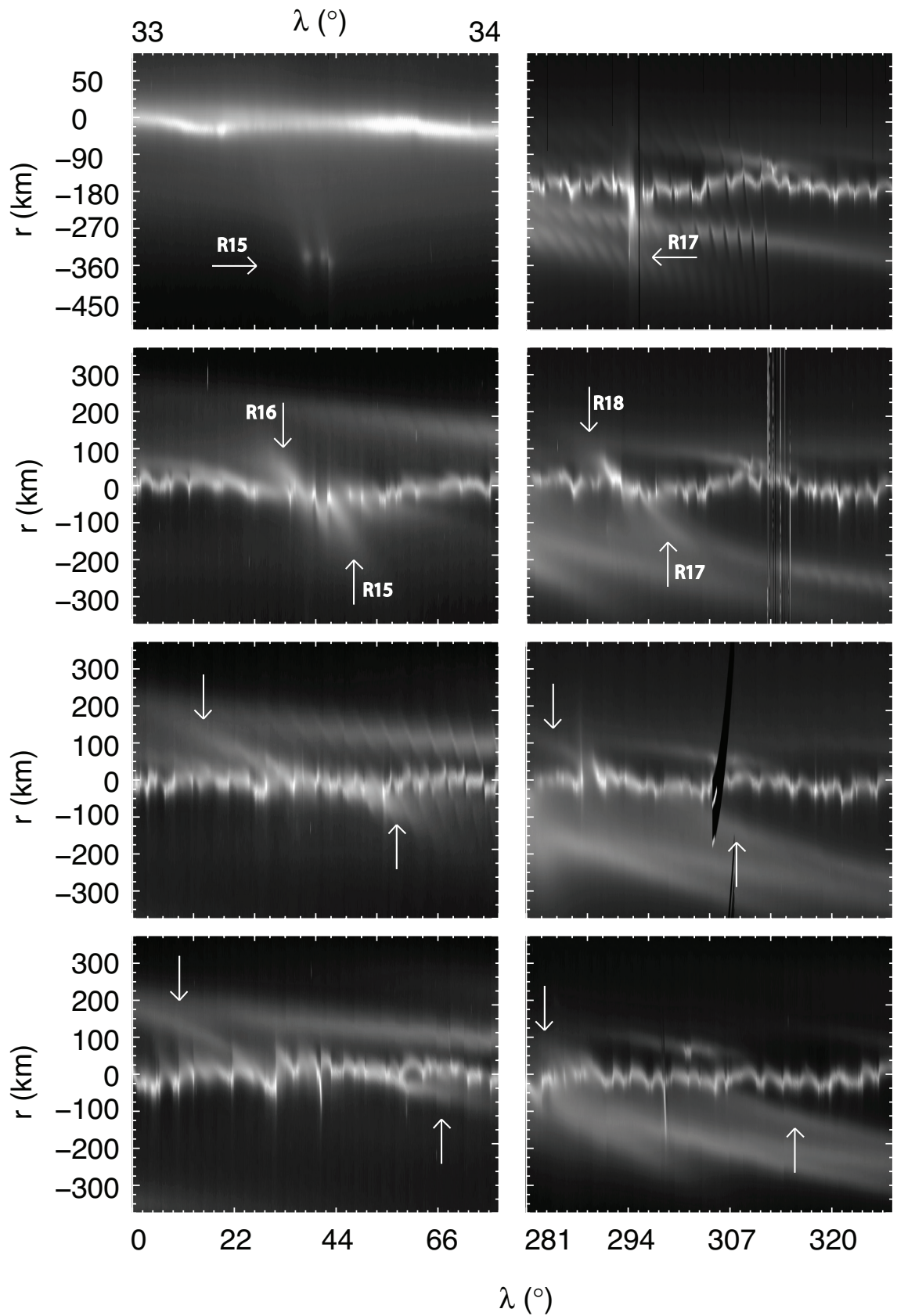
Figure 6.13.: Portions of mosaics 1552, 1554, 1555 and 1557 showing the evolution of features $R15, 16$ (left) and $R17, 18$ (right). Note the different scales in the top left panel and the image artefacts in the middle two right panels.
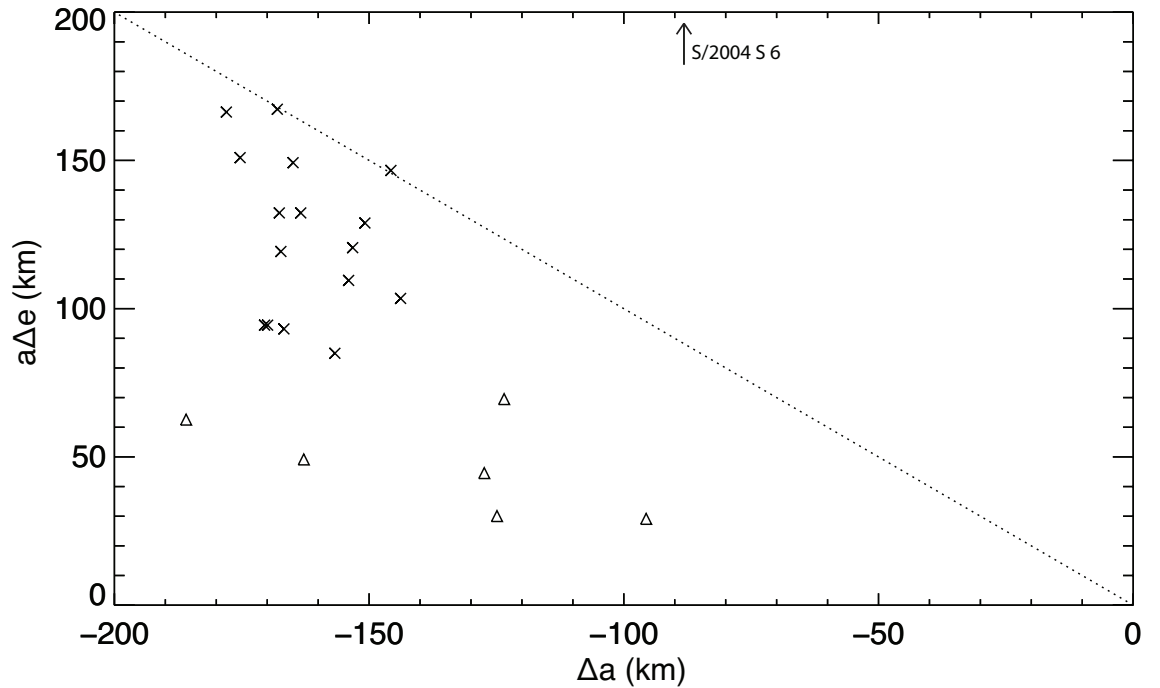
Figure 6.14.: Relative orbital elements of the strand (triangles) and strand clumps
            (crosses) from Cooper et al. (2015). Measurement techniques are de-
            scribed in the text. The dotted line has a gradient of one, i.e. $\Delta a =
            a\Delta e$.

with the estimate from photometry and suggests that all the inwards S6 jets seen
here are associated with it, i.e. $I2$ and 3 and $R4$, 7, 13 and 14. Either these jets
merged together to form the single large feature or the brightest of them survived to
form it whilst the others dissipate. The fact that the date of the start of Keplerian
shear agrees very well with the brightness peak suggests that the jets prior to 1555
may have merged together to form a single feature which then underwent Keplerian
shear together.

Figure 6.14 shows the relative orbital elements for both the strand segments and
clumps (for only the pre-Prometheus encounter clumps). For the strand points Δa
and Δe are calculated relative to the core segment orbit from the corresponding
streamer-channel movie. For the clumps the elements are relative to the standard
Cooper et al. (2013) orbit, precessed to the epoch of observation. The dotted line
has a gradient of one, corresponding to $\Delta a = a\Delta e$. S6's relative eccentricity lies off
the top axis at $a\Delta e = 603$ km.

All but one of the points lie below this line while all the strand segments are
significantly away from it. Considering only these points, the distribution could be

fitted by a line with a smaller gradient, i.e. $a\Delta e \approx (1/2)\Delta a$, or possibly one with a gradient of unity but offset from the origin. Images of the strand, however, do not support such a distribution, which would leave it disconnected from the core. It seems that the bulk of the strand material has orbits with $\Delta a > a\Delta e$, contrary to the expectations of Chapter 3 and observations of the streamer-channel mini-jet.

Clumps within the strand have orbits which are more scattered, with some approaching the dotted line. They could also be fit by a variety of straight lines or curves and may, or may not, follow the same distribution as the strand. Large values of, and scatter in, the eccentricities probably reflect clump formation mechanisms; clumps are formed by the collision and aggregation of material, and possibly with the aid of perturbations from Prometheus. Both should induce extra random velocity which will manifest itself in increased eccentricities, relative to the starting material. It should be noted that subsequently to these observations Prometheus passed through the region, disturbing it further, and that measurements of the perturbed clumps showed even greater eccentricities (Cooper et al., 2015).

In principle the ejecta velocity distribution may be obtained directly from a plot of the relative elements such as this. Zappalà et al.'s (1996) method involves estimating the point in the orbit where the ejection occurred (f) from the proper orbital element distribution, where the proper elements are assumed not to have changed significantly since the perturbation itself. The relative elements shown here are osculating and cannot be assumed constant over long time periods. Nevertheless f at the time of the impact must, in this case, be near the point where S6's orbit intersects that of the F ring. For S6's orbit elements this is $f \approx 120°$ and $282°$. Solving once again the rearranged perturbation equations (Eqns. 4.3 and 4.4) with these values and the Δa and δe of a typical strand measurement from Fig. 6.14 leads to $\Delta v_l \sim \Delta v_r \sim 10$ ms^{-1}, e.g. $\Delta v_l \approx -7.5$ ms^{-1}, $\Delta v_r \approx -14.7$ ms^{-1} for a point in the middle of the range. These are low velocities considering S6's $U \approx 70$ms^{-1} collision velocity but still plausible. On the other hand substituting these velocities back into Eqn. 3.12 results in large differences in pericentre, $\Delta\varpi \sim 20°$, not seen in the measured elements (Cooper et al., 2015). There are no solutions for velocity impulses around $f \approx 120°$ and $282°$ that do not result in Eqns. 3.10, 3.11 and 3.12 producing large $\Delta\varpi$ and therefore a large $a\Delta e$, equal to or greater than Δa.

For the whole strand to have $\Delta a > a\Delta e$ the particles making it up must have been perturbed again, after the original collision with S6 that ejected them from the core. There are a number of possible candidates for this subsequent perturbation including repeated collisions with other ejecta material or S6 itself and a secular gravitational interaction with the F ring core. It is interesting, in this context, to

consider whether other jets follow the orbital distribution of the strand or whether it is somehow special. The measurements made above were relatively insensitive to jets orbital timescale oscillations which might have shed light on this. Observations with coverage at opposite ansae, however, should show this radial motion over an orbit if there is significant Δe. If there is not and $\Delta a > a\Delta e$, like the strand, this should also be obvious. In the next section the evolution of jets on short timescales will be considered before returning to the question of subsequent perturbations.

6.4.1. Opposite Ansa Mosaics

The observation sequences with imaging at either ansa provide useful insights into jet evolution on orbital timescales. One particular opposite ansa sequence is now selected and its jets surveyed using the same methods as above. The sequence selected is ISS_087RF_FMOVIE003_PRIME for which the two mosaics, one at each ansa, are designated 1600-1 and 1600-2, with mid-times 2008-260:02:42:43.20 and 2008-260:09:05:45.60, respectively. This pair of mosaics is chosen because they contain a variety of prominent jets to investigate, both young and old. The mosaics are shown in Fig. 6.15 with the jets labelled using a continuation of the repeated feature numbering system from above.

Seven jets are identified in the first mosaic with six of those visible in the second. The remaining jet may be present in the bright, disturbed region at around 140° but is extremely difficult to find. For each repeated jet the gradient and intersection with the core are measured, as before, and listed in Table 6.4 below. The gradient evolution is then fitted as before and the formation time (in days before the first mosaic mid-time) and its associated chi-squared statistic are also quoted. As before attempts are made to fit mini-jet style gradient evolutions (Eqn. 3.8). In general there is no significant improvement in χ^2 but this is discussed in detail for each jet below.

$R19$ and 20 are both old features from previous collisions that have wrapped around several times. $R20$ is actually the strand measured in Cooper et al. (2015). Gradients here suggest a formation time of late December 2006, somewhat earlier than the other estimates but with error bars that go up to February 2007, and still within the previous survey. This would most closely associate the strand with $R4$. $R19$ is then a later observation of one of the outward parts of the S6 collisions, for example $R3$. The gradient change of $R19$ between the two mosaics is undetectable within the uncertainties (the latter being quite large because of contamination from $R21$; hence the poor χ^2), meaning its relative eccentricity is unknown. $R20$, on the
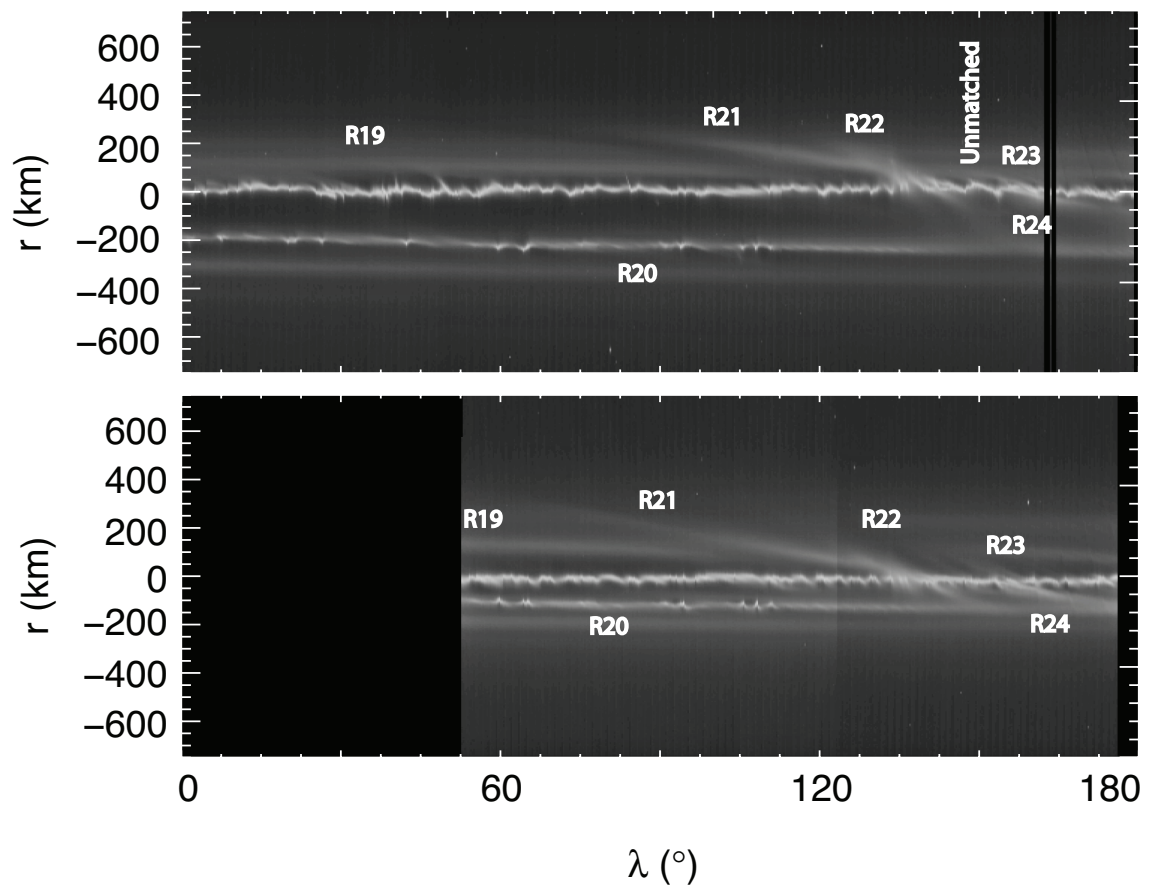
Figure 6.15.: Mosaics 1600-1 and 1600-2, taken at opposite ansae, with jets labelled. Note the restricted longitude coverage.

Name	θ_1 (°)	θ_2 (°)
R19	$-0.006\,10 \pm 0.000\,26$	-0.0080 ± 0.0056
R20	$-0.008\,30 \pm 0.000\,35$	$-0.004\,90 \pm 0.000\,22$
R21	-0.0740 ± 0.0051	-0.0860 ± 0.0037
R22	-0.300 ± 0.034	-0.290 ± 0.058
R23	-0.220 ± 0.022	-0.260 ± 0.017
R24	-0.0890 ± 0.0039	-0.1000 ± 0.0026

Name	λ_{base1} (°)	λ_{base2} (°)	$T_0 - T_{1600-1}$ (d)	χ^2/DOF
R19	323^{+12}_{-11}	353^{+7}_{-145}	560.94 ± 54.42	0.01
R20	116^{+7}_{-6}	158^{+9}_{-8}	639.12 ± 61.75	7.23
R21	159^{+20}_{-17}	140^{+11}_{-10}	45.57 ± 5.01	0.45
R22	139^{+35}_{-28}	135^{+65}_{-44}	12.42 ± 3.67	0.00
R23	$160^{+0.42}_{-0.35}$	153^{+21}_{-19}	15.24 ± 2.54	0.20
R24	154^{+14}_{-13}	147^{+8}_{-7}	37.20 ± 2.39	1.55

Table 6.4.: Features found in both mosaics 1600-1 and 1600-2, taken at opposite ansae. Gradient and base longitude are recorded for each feature in both mosaics and the angle evolution is fitted for a formation time. As before T_0 is quoted in days before the first observation, along with the associated reduced chi-squared statistic. Widths and brightnesses are not analysed.

other hand, changes gradient by significantly more than would be expected for such an old feature with just Keplerian shear; the χ^2 here really is saying that the simple model is inappropriate. With only two observations it is impossible to constrain the relative eccentricity fully but the whole feature does move visibly in radius from a mean $r_{jet} = -272$ km to $r_{jet} = -150$ km implying a significant $a\Delta e \sim 120$km, although still $\Delta a > a\Delta e$.

R21 to 24 are all associated with the bright collision feature at $\lambda \sim 140°$. This feature resembles the large S6 collisions from the previous sequence but progresses along the core from right to left (decreasing co-rotating longitude) so must be from a different object with a positive Δa. R21 and R24 are the oldest visible collisions from this object with implied ages $\sim$ 40 d before the observations. Both have gradients which increase slightly between the two mosaics but within 3σ may also fit the, essentially flat, curve of Eqn. 3.7 at this age. Both are visible at both ansae at roughly the same radius so clearly they do not collapse fully into the core. R22 is a younger feature from a more recent collision by the same object and overlaps the older jets. R23 appears young but is located at a greater longitude implying it formed earlier, if created by an object moving from right to left. It may be a young sub-jet formed by debris from the previous collisions re-colliding, as discussed with R5 and R6, previously. Again, both are consistent with having gradients which do not change, within the errors, or which increase very slightly (the large gradient errors and poor fit statistics are because they are contaminated by other jets in the bright feature). Again the relative eccentricity is hard to measure but the fact that both jets are visible at either ansa suggests they do not behave like mini-jets. A final jet, however, is measured in the first mosaic, between R22 and R23, and is not seen in the second, having apparently collapsed back into the core like a mini-jet.

The conclusion for this pair of observations at opposite ansae is then mixed. Some old jets (e.g. R20) have significant relative eccentricity causing them to oscillate on orbital timescales; $\Delta a > a\Delta e$, however, so they do not reach all the way back in to the core. Other old jets like R19 do not seem to oscillate noticeably. Extended collisional disturbances also show a variety of behaviour with the feature as a whole appearing much the same from ansa to ansa but individual component jets changing gradient and some collapsing fully like mini-jets. Combined with the strand observations it seems that jets have a variety of orbital distributions but with, in many cases, small relative eccentricities, $a\Delta e < \Delta a$, in contrast to mini-jets and the expectation from orbital dynamics.

6.5. Conclusion

Similar numbers of jets and mini-jets are present at any one time in the sequences studied here. Jets have lifetimes which are an order of magnitude longer than mini-jets, however, suggesting an order of magnitude fewer objects (~ 10 rather than ~ 100 mini-jet objects). There is significant overlap in the radial extent of the two types of feature with large mini-jets being mistaken for small jets and *vice-versa*, implying they are probably different extremes of the same population. Figure 6.5 may show a kink or gap in the combined distribution around $|r| = 50 - 100$ km but is, in general, supportive of a single broad spread with a concentration close to the core.

Jet forming objects, like S6, would then just be the most extreme members of a population of objects which probably originates in the core. One can imagine a scenario where Prometheus produces clumps at streamer-channel edges (Beurle et al., 2010) with a slight spread in orbital elements causing them to drift around the ring. Further interactions with Prometheus would then happen at random relative longitudes and distances, inducing random, positive or negative, kicks to the orbit. This, essentially chaotic, evolution is further complicated by collisions with other clumps which might lead to mergers, fragmentations or compaction. The 'lucky' clumps that survive this random process will probably be the largest and most compacted as well as having the greatest spread in orbits from the core. In a similar way to the model of Esposito et al. (2012), these jet-forming objects would then be an order of magnitude less common than their smaller, mini-jet forming, cousins, as observed. Their larger size and cohesiveness means they will go on colliding for some time but eventually they will be worn down, with the material being added back into the general mass of dust around the ring. This may eventually be swept up, back onto the core particles in a recycling reminiscent of the French et al. (2012) and Cuzzi et al. (2014) models.

The orbital distribution of material in jets is interesting in that it does not follow the predicted $\Delta a \approx a \Delta e$ behaviour. The implication being that either external forces are involved or the collisions are even more complicated.

One possible explanation is a secular effect from the averaged (unknown) mass of the F ring core forcing precession and thereby locking the periapse of nearby particles to itself. This would reduce $\Delta \varpi$ and hence Δe, as seen with the major strand feature. For a given core mass, forced periapse precession will fall off with distance in a predictable way (see equation 7.94 from Murray and Dermott, 1999). The effect should therefore be more pronounced in mini-jets than jets, at odds with

measurements of mini-jets in Chapter 4 and Section 5.3.4 (bearing in mind the small $\Delta\varpi$ in these features anyway because of the low-velocity collisions) and the jets seen here. Additionally, S6 is not precessing with the core, being almost exactly anti-aligned with it, so it is questionable whether material spread to similar distances, like the strand, will be. Observations of periapse locking may be a useful tool for probing the mass of the core but it seems unlikely to be the explanation for the anomalous behaviour of jets.

An alternative scenario is perturbations to the jet material by collisions after the initial ejection. Several lines of evidence support this idea. Firstly, the ejected material should have large Δe just after the collision. If it follows roughly the orbit of S6 it will re-impact the core twice per orbit, meaning dozens of successive interactions between each mosaic in this sequence. Secondly, as shown in Fig. 6.12, S6 itself will re-impact the same section of core, repeatedly, in this time. Any material that only received a small kick will still be in the area to receive another, randomly oriented, kick. Thirdly, if each passage of S6, radially outwards and inwards through the core, creates a discrete jet then their radial motions will be out of phase with each-other leading to collisions between the material of the jets themselves. Jets clearly have a significant density of material in them, as shown by their peak brightnesses being comparable to the core and the fact that bright, trackable clumps form in the large 'secondary' feature.

All this points to a messy, complicated formation mechanism. A simple, qualitative model would be this: a single pass by S6 through a dense, clumpy section of core releases a cloud of particles that are placed onto similar orbits to the moonlet (Δa and $a\Delta e$ between $\sim 0 - 600$ km). Further passes though nearby sections of core create additional ejecta clouds. These clouds, with similar orbital distributions but differing phases, re-collide with each-other and the core roughly once per orbit. Collisions are predominately in the radial direction and their dissipative nature serves to slowly damp out the relative radial motions and, therefore, eccentricities. Over the course of a few days the various ejecta clouds from one section of core begin to merge together, damping their relative eccentricities and phases but leaving a large spread in Δa across them. The resulting, merged, structure looks like a jet with a single distribution evolving under Keplerian shear. Individual components, like those oscillating in the opposite ansa sequence, would only be seen near the disturbed, complicated base region of the jet. This would also explain why young jets extend to $\geq |750|$ km but older, classic jets are limited to ~ 400 km, as large initial Δe is damped out, leaving only Δa.

The extended nature of the impact is similar to the explanation for collisional

features seen in the main rings by Tiscareno et al. (2013) but the prolonged impact may be more analogous to cometary debris impacts (Hedman et al., 2007, 2011a; Showalter et al., 2011; Hedman et al., 2015).

This scenario would resolve the discrepancy between the number of jets and the frequency of S6 core-crossings. It would also help explain the difficulty in pinning down jet formation dates and longitudes, which could conceivably be periods of several days or weeks and many degrees long, respectively. Further modelling would need to be done to understand the long term evolution of jets and how they interact and merge with each-other to form the long-lived strand. This scenario could also be tested with better, time-resolved imaging of jet formation regions.

Finally, jets are, on average, half as bright as the F ring core, contrasting with occultation profiles in which they have about a tenth of the core's optical depth (Albers et al., 2012). This may imply different particle size distributions between the two, as would be expected from collisions fragmenting clumps and releasing small particles. Additional photometric observations would be needed to confirm this.

7. Simulating Collisions

This chapter documents a series of numerical simulations performed to investigate collisions in the F ring environment. The open source, N-body code REBOUND (Rein and Liu, 2012), a symplectic integrator with built in collisional modelling, is used to simulate low-velocity collisions between moonlets and F ring particles. The aim is to show that these collisions can form structures like those seen in Cassini images and to place constraints on the colliding moonlets' physical properties by comparing the results to said images. In most cases generic collisions are simulated with the aim of generating a typical mini-jet or jet, rather than attempting to replicate exactly a particular feature.

The simulation method and setup are discussed in Section 7.1 and results shown in Section 7.2. This is broken down into: preliminary results, using the default code, in Section 7.2.1; discussion of the coefficients of restitution, in Section 7.2.2; and results from the collision of aggregates, in Section 7.2.3. Finally, discussions and conclusions, drawn from these results, are presented in Section 7.3.

7.1. Method

7.1.1. REBOUND

REBOUND is an open source N-body code available from `http://github.com/hannorein/rebound`. It was chosen partly because of its ease of use, with collision modelling built-in, and partly because of its choice of integrators; specifically the 'symplectic epicycle integrator' or SEI. In this type of integration particles' positions and velocities are described by Hill's equations, relative to a point co-rotating with angular speed n; appropriate for the local region and short timescales to be considered here.

In the limit of massless particles $R_{\mathrm{Hill}} \to 0$ and the equations of motion have the exact solution of epicyclic motion as described in Chapter 3. A particle on a slightly differing orbit to the co-rotating point (with Δa and/or $a\Delta e$) will always have a position and velocity given by Eqns. 3.3. In the case of massive particles there is

an additional term in the equation of motion, describing their mutual gravitational interaction, and it must be integrated numerically. For the SEI the assumption is that particles have small masses and so this interaction is a small perturbation on the epicycles. The condition for this situation is given in Rein and Tremaine (2011) as $x/R_{\mathrm{Hill}} \gg \min [1, \sqrt{nR_{\mathrm{Hill}}/v}]$, where x is the mutual separation distance, v is velocity and the minimum of the the two terms on the right is selected. At the F ring's location, near the Roche limit, low density, icy bodies should nearly fill their Hill spheres. For two such bodies just touching, their closest separation will be $2R_{\mathrm{Hill}}$ and this condition is just satisfied, even for the largest bodies (radius ~ 1 km) and lowest velocities (1 ms^{-1}) to be considered here. It will be shown later that, in nearly all cases, gravitational forces are much less than those arising in the collisions and that particles do indeed follow epicyclic trajectories with no further interactions following the impulsive collision.

The integrator then works much like a standard N-Body integration with a drift-kick-drift method: for half a time-step, dt, particles 'drift' on their calculated epicycles, given by Eqns. 3.3. A 'kick' is then applied by calculating the accelerations from their mutual perturbations and, with their velocities updated, the particles are allowed to 'drift' for a further half a time-step. Finally collisions are resolved at the end of the time-step when both velocities and positions have been updated and synchronised.

The perturbations due to inter-particle gravity can be calculated exactly by summing over all particles or approximated by an octree method (Rein and Liu, 2012); a hierarchical grouping of particles together so that, at long range, only the total mass of the group is used to compute gravitational forces. Collisions are detected either by searching all particles for nearest neighbours or searching over the octree and are resolved as free slip, hard sphere interactions. A user specified normal coefficient of restitution parameterises how much velocity is lost in each collision; $U_n' = \epsilon_n U_n$, with U_n and U_n' the pre- and post-collision relative velocities as before. Particle spin is ignored and the tangential coefficient of restitution is equal to one (free-slip conditions so there is no change in tangential relative velocity). No other inter-particle forces are modelled and no fragmentation of particles is allowed.

7.1.2. Simulation Setup

The SEI integrator is used with periodic boundary conditions (also known as a shearing sheet setup) but since the focus is on short term evolution and the boundary box is kept large (typically several thousand kilometres) ejecta particles do not leave

the edges and the choice of boundary is arbitrary. The epicycle and vertical epicycle frequencies are set equal to the mean motion at the F ring, n, ignoring the effects of planetary oblateness. No further description of the central body (Saturn) is needed beyond this one parameter and no other forces are modelled.

A constant time-step which is a small fraction of the orbital period is used. For the low velocity collisions a time-step of $dt = 10^{-3}$ times the orbital period, P_0, is used which is equivalent to about 50 s at the F ring. This time-step should be much smaller than the shortest dynamical time in the simulation to fully capture it. In this case dt should be set to ensure that no more than ~ 1 collision happens per time-step. For velocities of 1 ms^{-1} and particle radii of 1 m the time-step should, strictly speaking, be less than 2 s, the time it takes a particle to move its own length, however time-steps of a second or less were deemed too computationally expensive for these, short, simulations. The statistical nature of numerous collisions should allow a representative sample of velocities for a number of particles and the detailed evolution of individual particles is not of great interest. The effects of the time-step are discussed in more detail in Section 7.2.1 below. A gravitational smoothing length of a tenth of the particle radii is used to ensure that unrealistically large interactions do not occur if particles overlap before collisions are resolved.

The coefficient of restitution chosen is the velocity dependent model from Bridges et al. (1984) for the normal component and a constant equal to one for the tangential:

$$\epsilon_n = (U_n/U_c)^{-0.234} \qquad \epsilon_t = 1 \tag{7.1}$$

where $U_c = 0.0077$ cm s^{-1} is the critical velocity for low temperature, frost covered ice (Bridges et al., 1984). $\epsilon \approx 0.1$ for $U_n = 1$ ms^{-1} and $\epsilon \approx 0.04$ for 70 ms^{-1} collisions. This coefficient was chosen primarily for ease of comparison with other work (e.g. Charnoz, 2009) and the effects of varying coefficients are discussed later. Both methods of collision detection and the presence, or not, of intra-particle gravity are also varied and discussed in the following sections.

Except where otherwise stated, a total of 20000 target particles of 1 m radius are used, uniformly distributed in longitude over a section of ring and normally distributed in radius around the origin. A standard deviation in radius of 500 m is generally used to model an inner F ring core of ~ 1 km thickness, made up of the larger particles (Marouf et al., 2010). The simulations are fully three-dimensional but with a thin vertical distribution with a standard deviation of 1 m. This number of particles spread over the simulated volumes is a dynamic optical depth (equal to observed optical depth for low τ Tiscareno, 2013) much less than that of the F

ring. In effect the particles are just tracers of the kind of trajectories that might be expected and their total number is not related to any physically measured quantity. The number and size of impacting objects is varied as described below.

Ring particles are initialised on circular orbits, relative to the co-rotating point, i.e. Eqn. 3.3 with $\Delta e = 0$ and $\Delta a = r_0$, their start radius. Impactors are given positions and velocities appropriate for a range of Δa and Δe with the addition of starting phases and locations, r_0, l_0, M_0, to ensure that they pass through the origin for a collision. All the eccentricity is then contained in the impactors' orbits using the relative eccentricity (Williams, 2009). All particles have a density of $400 \,\mathrm{kg\,m^{-3}}$, representing porous, low density icy bodies.

7.2. Results

7.2.1. Preliminary Results

Figure 7.1 shows the impact of a 200 m radius moonlet on a $\Delta a = a\Delta e = 10$ km orbit into the nominal core segment. A number of particles are given a $\Delta\boldsymbol{v}$ close to the moonlet's own relative velocity, placing them on similar orbits, while others are 'strung-out' on orbits intermediate between those of the object and the core. The resulting feature extends out from the core and shears downstream with an angle that follows Eqn. 3.8. It eventually re-collides with the core but the low particle density means that few particles actually interact and the shape is unaffected. The effect of re-collisions is discussed in more detail later.

During the early stages of evolution the feature points the 'wrong-way', against the direction of Keplerian shear, but Fig. 7.1 shows that its thickness combined with that of the core makes this hard to discern; instead the mini-jet appears as an extended blur on the edge of the core with no discernible angle. This is especially true when the core presents an extended dusty envelope and explains why 'wrong-way' mini-jets are so rarely seen in the Chapter 5 catalogue.

A loop-like structure is evident with a lack of particles filling in the centre of the mini-jet. This is not seen in catalogued features, with the possible exception of the very high-resolution N1537898708, suggesting it may be an artefact. The left-hand side of Fig. 7.2 is the velocity distribution, $\boldsymbol{v}_l$ against $\boldsymbol{v}_r$, of the particles, just after the collider has reached the origin, showing a clear 'loop' of velocities which leads to the shape. This forms because the ring particles are all hit by the impactor with roughly the same velocity and rebound from its spherical surface with similar magnitudes of $\Delta\boldsymbol{v}$ but at a range of angles, leaving a gap in the centre of the
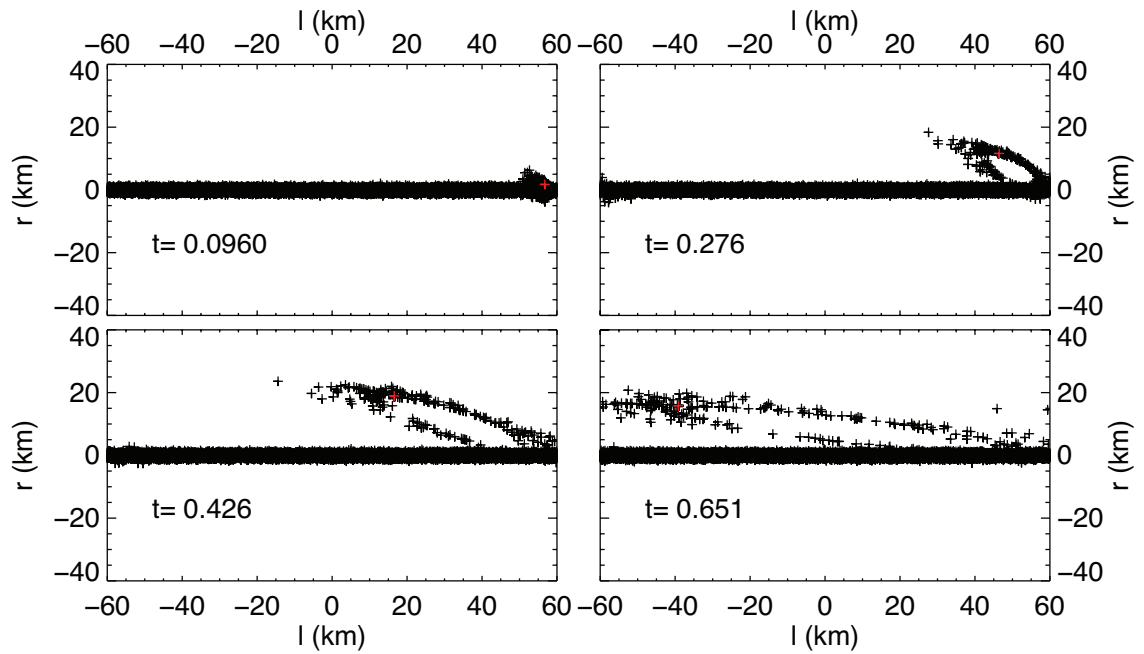
Figure 7.1.: Snapshots from the simulation of a 200 m radius moonlet (red cross) on a $\Delta a = a\Delta e = 10$ km orbit impacting into a segment of ring made up of 1 m radius particles (black crosses). The collision location is shifted longitudinally from the origin so that the resultant feature fits in the frame. Time is shown in each panel in units of orbital periods, P_0, after collision. The loop-like structure of the mini-jet is evident.
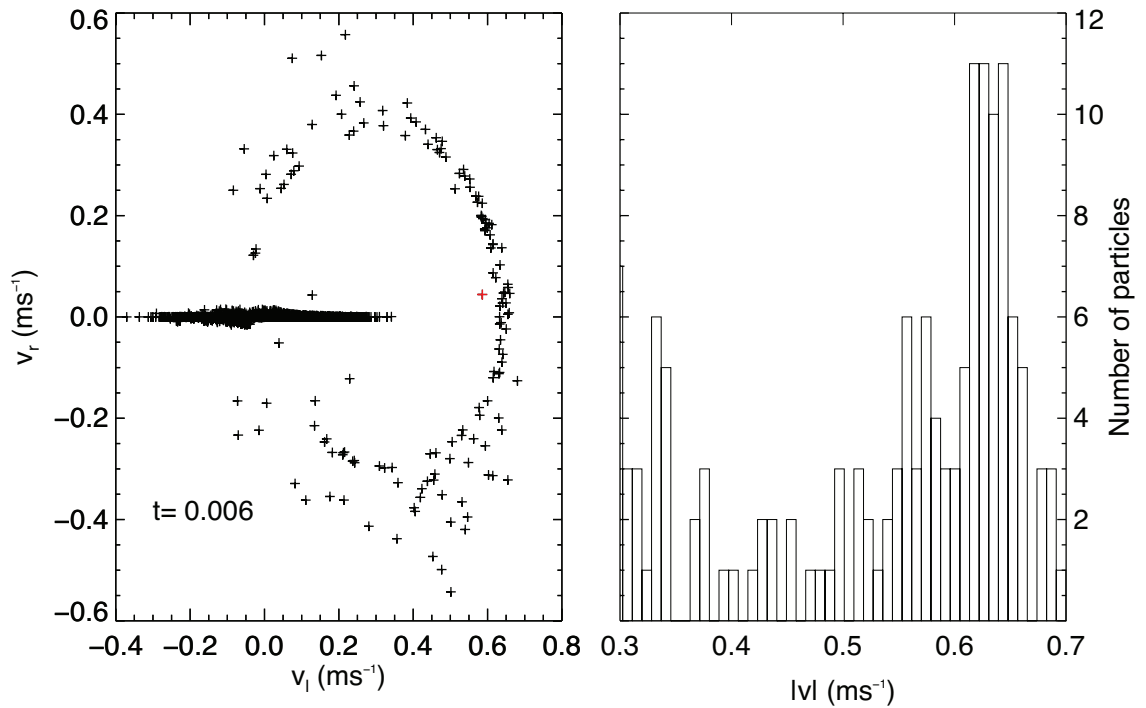
Figure 7.2.: Snapshot of the velocity distribution from the impact of the 200 m radius moonlet (red cross). Left: longitudinal, $\boldsymbol{v}_l$, against radial, $\boldsymbol{v}_r$, velocity. The horizontal bar centred on the origin is made up of the Keplerian velocities of the unperturbed ring particles while the loop-like structure around the impactor is the collision induced Δv. Right: histogram of total speeds from the collision. Note the cut-off in velocity to exclude the unperturbed particles.

distribution. The magnitude of the collision velocity in this case is $U = 0.585 \text{ ms}^{-1}$ and the right-hand side of Fig. 7.2 shows that a large number of particles have their velocity changed by this much ($\Delta v \approx U$ as predicted in Section 3.1). However, it can also be seen that there is a spread in the magnitude of the induced Δv, from the unperturbed velocities ($\lesssim 0.3 \text{ ms}^{-1}$) up to just above U, which is not expected in these dissipative collisions.

Figure 7.3 shows how replacing the single 200 m impactor with a group of ten 50m radius objects on similar orbits helps to fill in the loop. The impactors are given the same orbital parameters but with a normally distributed random component of standard deviation 50 m in Δa to vary slightly their trajectories. This changes the impact velocity magnitudes and directions, slightly varying the rebound $\Delta \boldsymbol{v}$ (shown in 7.4) from the previous, approximately singular value. The resulting mini-jet has a much less pronounced loop shape and is closer in appearance to real features. It is likely that impactors have an extended, irregular shape or are loosely bound clumps, rather than solid, spherical moonlets so the loop structure must be considered a numerical artefact. The right-hand side of Fig. 7.4 shows a more pronounced peak in the velocities around U but there is still a large spread. This will be discussed further in Section 7.2.2.

Radial size of the feature scales with collision velocity (see Section 7.2.1 below) whilst varying the core thickness does little to change the simulation outcomes until it approaches the collider Δa. In this case, of very small mini-jets or thick cores, the object spends more of its epicycle inside the core so that the collision can no longer be approximated as a single impulsive event and the relative velocity vector varies hugely in direction and magnitude over the course of the impact. This leads to far more scatter in the $\Delta \boldsymbol{v}$ values and a broader mini-jet with an angle which is difficult to discern, not-the-least because it is mainly embedded in the core.

Similarly, varying the size of the target and impactor particles also does little to alter the results unless the two become comparable in size. In this case the $\Delta \boldsymbol{v}$ will be shared between the moonlet and the ring particles and the impactor will undergo a change in its velocity, altering its orbit (see Section 7.2.3 below). As long as the mass of the ring particles is much less than the impacting mass then the moonlet's orbit is effectively unaltered and the target particles receive a $\Delta \boldsymbol{v}$ of the same order as the collision velocity and are placed onto similar orbits. The lack of mass dependence means that, in general, impactor sizes cannot be deduced from ISS images of mini-jets, other than to say their mass is much greater than that of a typical ring particle.

Intra-particle gravity was switched off and the simulations repeated with the same
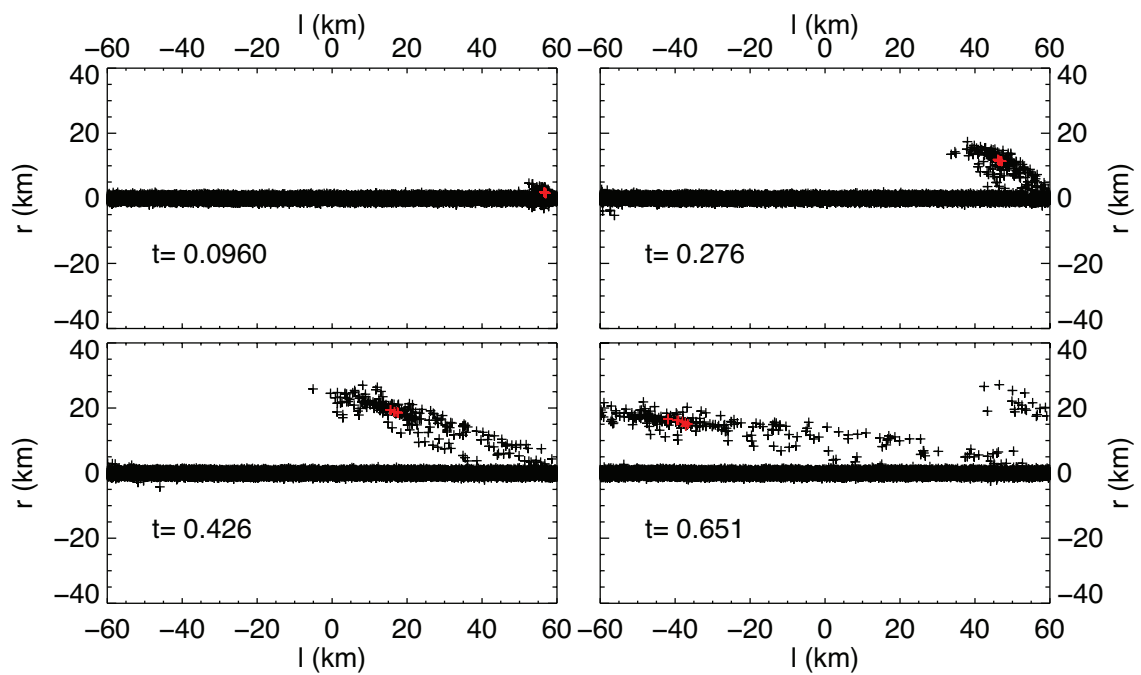
Figure 7.3.: Snapshots from the simulation of ten 50m radius moonlets (red crosses) on $\Delta a = a\Delta e = 10$ km orbits impacting into a segment of ring. The collision location is shifted longitudinally from the origin so that the resultant feature fits in the frame and it begins to wrap-around due to the periodic boundary conditions. The loop structure is less evident.
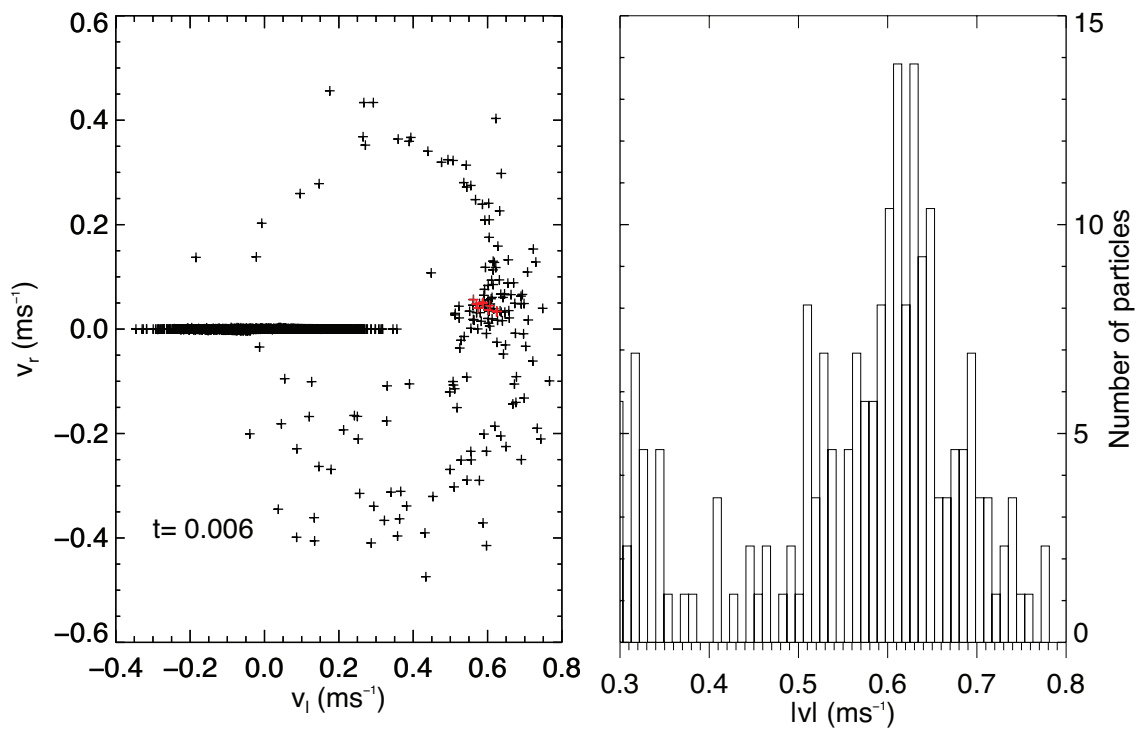
Figure 7.4.: Left: snapshot of the velocity distribution from the impact of ten 50 m radius moonlets (red crosses). The horizontal bar centred on the origin is again made up of the Keplerian velocities of the unperturbed ring particles while the loop-like structure, which is now more closely clustered around the impactors, is the collision induced Δv. Right: histogram of the speeds. Note the cut-off in velocity to exclude the unperturbed particles.

results, demonstrating that this feature is indeed collisional in nature. The exception to this is when large colliders are used and some gravitational scattering occurs (see Section 7.2.3 below), resulting in small versions of the well documented streamer-channel phenomenon. Gravitational scattering from the impactor becomes important only when its escape velocity (~ 1 ms^{-1} for a 1 km sized body) is comparable to the velocity kick from the collisions (a few metres per second). This provides a rough upper limit for impactor size when gravitational features like streamer-channels and fans are not seen.

Finally, identical results are also achieved when using direct detection of collisions, rather than tree-based detection, and when changing the time-step to $P_0 \times 10^{-5}$. Altering the coefficient of restitution, ϵ_n, from a function of velocity to various fixed values also has little effect on the shape of the mini-jet. The major difference is that elastic collisions result in higher $\Delta \boldsymbol{v}$s delivered to the ring particles. The feature then extends past the orbit of the impactor so that it is no longer found at the tip but somewhere in the middle. The angle evolution remains the same however. The effect of a tangential coefficient of restitution is discussed below in Section 7.2.2.

Crossing Orbits

In the above examples the impactor had an orbit with $\Delta a = a\Delta e$ so that it reaches its periapse (or apoapse) in the core, at the origin of the co-rotating coordinate frame. As can be seen in Fig. 7.2 this provides a mostly longitudinal impulse to the ring particles. If $\Delta a \neq a\Delta e$ because, for example, a moonlet has had its eccentricity pumped up by external forces or differential precession has induced a large difference in the longitudes of periapse, then the collision geometry is altered. The impactor will cross through the ring more radially, delivering more of a radial impulse to the target particles. This kind of impact is shown in Fig. 7.5 (for $\Delta a = 10$ km, $a\Delta e = 20$ km), with the velocity distribution at the time of impact shown in Fig. 7.6.

The predominantly radial orientation of the velocity vector results in $\Delta \boldsymbol{v}$ values which are also radial, with the scatter resulting in both positive and negative longitudinal accelerations. This leads to both positive and negative induced Δa values, resulting in a double sided mini-jet. A line connecting both sides through the core still follows the standard angle evolution. The 'loop' structure is also very apparent here. Double-sided features are almost non-existent in Chapter 5 but may occur in the larger jets associated with S6 in Chapter 6. It cannot be concluded that core-crossing mini-jet impactors are not present, however, as several repeated features have been seen to swap sides, implying large relative eccentricities. Further, this
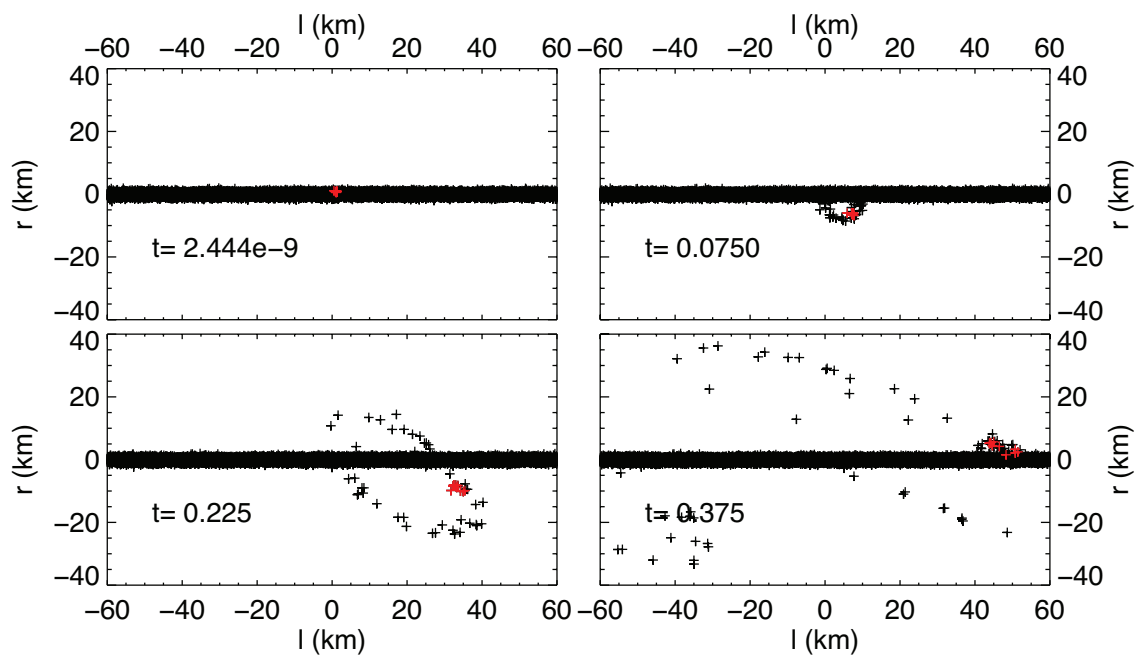
Figure 7.5.: Snapshots from the simulation of ten 50 m radius moonlets (red crosses) on $\Delta a = 10$ km, $a\Delta e = 20$ km orbits impacting into a segment of ring made up of 1 m radius particles (black crosses). The feature begins to wrap-around due to the periodic boundary conditions. The loop-like structure of the mini-jet is evident.
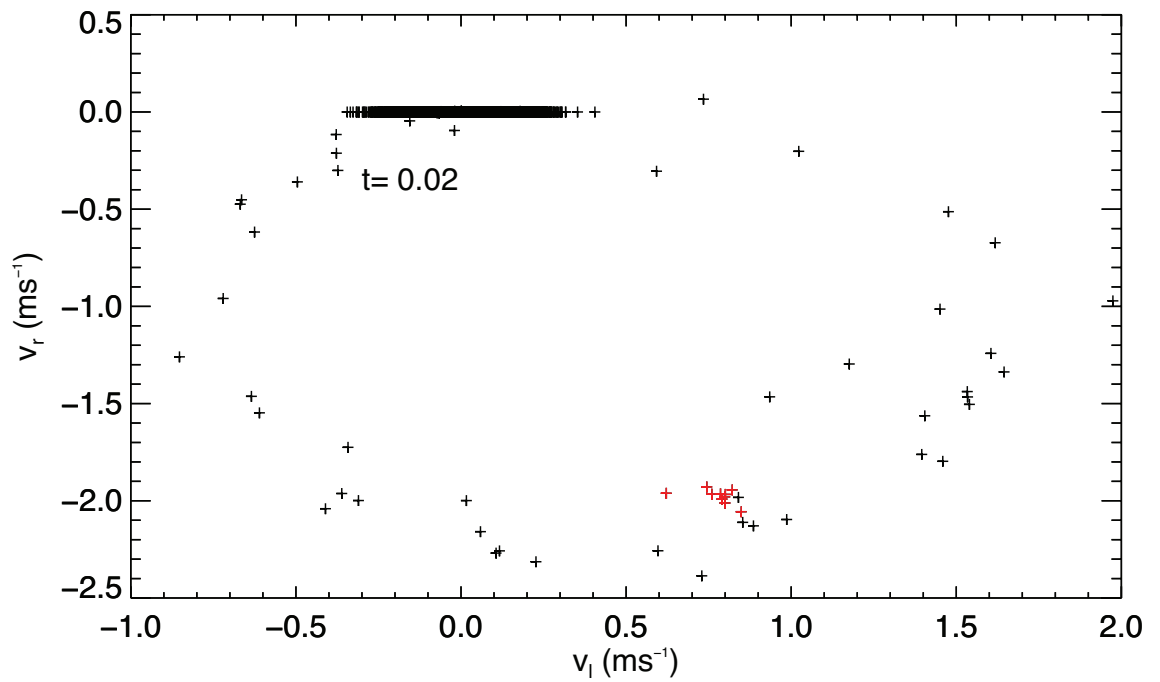
Figure 7.6.: Snapshot of the velocity distribution from the impact of the 50 m radius moonlets (red crosses). The horizontal bar centred on the origin is made up of the Keplerian velocities of the unperturbed ring particles while the loop-like structure around the impactors is the collision induced $\Delta \boldsymbol{v}$.

type of mini-jet, which appears first on one side of the core and then the other, is not reproduced in these simulations; all simulated mini-jets with large Δe appear on both sides of the core at once due to the scatter in $\Delta \boldsymbol{v}$ values seen in Fig. 7.6. Clearly there is a discrepancy between the simulations and the observations.

Higher Velocity Collisions

The simulations are now extended to model the higher velocity jet-forming collisions surveyed in Chapter 6. The orbit of S6 has previously been measured, reducing the number of unknown parameters, so it is taken as typical of the colliding objects. The relative elements used are then those between the fitted orbits for S6 and the F ring core at the epoch of the observations (from the supplementary material of Murray et al., 2008). These are $\Delta a = -89.12$ km, $\Delta e = 7.068 \times 10^{-4}$ and $\Delta \varpi = -159.55°$, therefore $a \Delta e = 603.36$ km. This object is initially taken as a clump generated with the method discussed below in Section 7.2.3. The epicycle integrator is used as before and the ring particles remain the same.

The expectation is that scaling up the velocity will increase the size (radial extent) of the jets but otherwise leave them unaltered from mini-jets. If fragmentation is important in mini-jets then it will be even more so for jets as the velocities increase. S6 encounters the core at around 70 ms^{-1} which should be more than enough to fragment colliding ~ 1 km bodies, even with a low coefficient of restitution (Hyodo and Ohtsuki, 2014). S6 must, therefore, be encountering objects much less massive than itself to explain its continued existence. 70 ms^{-1} is also fast enough that the impactor will pass through the 1 km core, encountering hundreds of particles, in a single time-step with $dt = P_0 \times 10^{-3}$ so the choice of time-step must now be discussed in detail.

Figure 7.7 shows the effect of changing the time-step from $dt = P_0 \times 10^{-3}$ on the left to $dt = P_0 \times 10^{-7}$ on the right for otherwise identical simulations. For these runs the impactor clump was generated just outside the core and given a negative radial velocity of 70 ms^{-1}, rather than using the full relative orbital motion. The simulation is then cut short before the jet properly forms so that the initial particle distributions can be compared in a reasonable amount of computing time. If the time-step is insufficiently small then particles are 'missed' as the change in position of the collider in a single integration step passes over them before collisions can be resolved. For $dt = P_0 \times 10^{-7} \approx 0.01$ s an impactor traveling at 70 ms^{-1} does not move more than the 1 m radius of the smallest particles in a single time-step so all the collisions can be detected and resolved before the next step. This can be seen
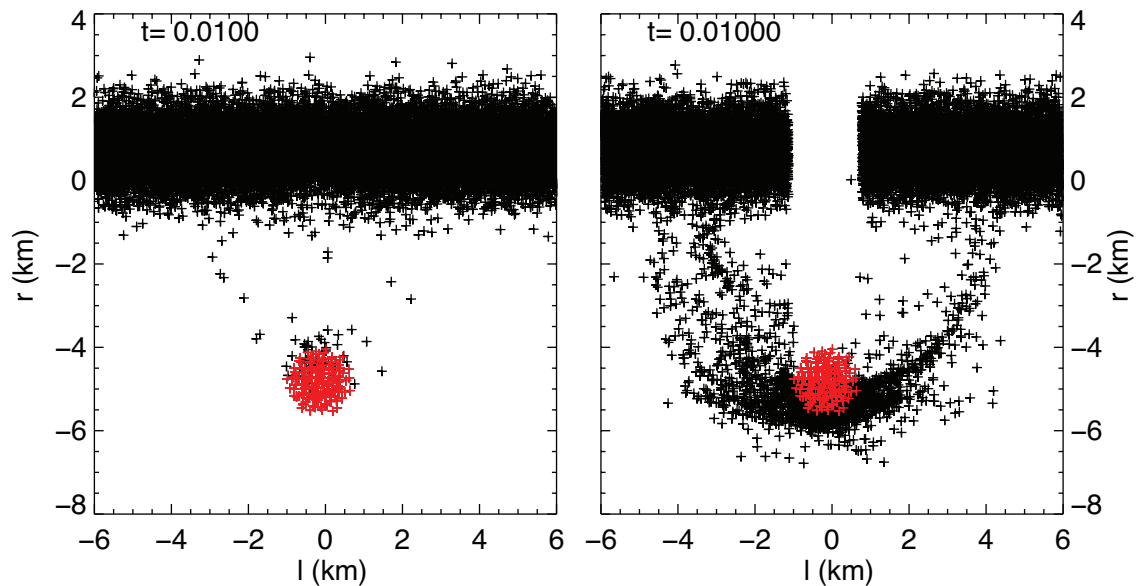
Figure 7.7.: Side-by-side comparison of identical simulations with different time-steps: Left $dt = P_0 \times 10^{-3}$, right $dt = P_0 \times 10^{-7}$. A clump formed from 130 m radius particles (red) is given $v_r = -70$ ms^{-1} and passes through a ring segment of 1 m particles.

clearly in Fig. 7.7 as the impactor has collided with all the particles along its cross section through the core (the gap is swiftly filled in by Keplerian shear).

The velocity distributions after these impacts, and for another identical run with $dt = P_0 \times 10^{-5}$, are shown in Fig. 7.8. With a time-step of $dt = P_0 \times 10^{-5} \approx 1.3$ s the collider can encounter more than one ring particle per step but does not travel more than its own length. Qualitatively the three distributions are similar and the longer time-steps can be seen as an approximation of the fully resolved results. The loop structure is present in each but is much more filled in when an appropriate time-step is used. Magnitudes of Δv clearly still vary between zero and approximately U, the collision velocity. A time-step of $dt = P_0 \times 10^{-5}$ looks, from Fig. 7.8, to be a reasonable approximation and is used as a compromise between computing time and accuracy.

The full motion of the relative orbits is now integrated, with $dt = P_0 \times 10^{-5}$, so that the resulting jet can be seen emerging from the core in Fig. 7.9. The jet shears over and collapses back into the core at $t = P_0$, in the same way as a mini-jet, before rising out again on both sides for a second cycle. It will continue to oscillate back into and out of the core on successive cycles, in contrast to the observed jets which appear to evolve only under keplerian shear. Jet forming collisions clearly cannot be modelled as single, impulsive events with no further forcing or else jets would be
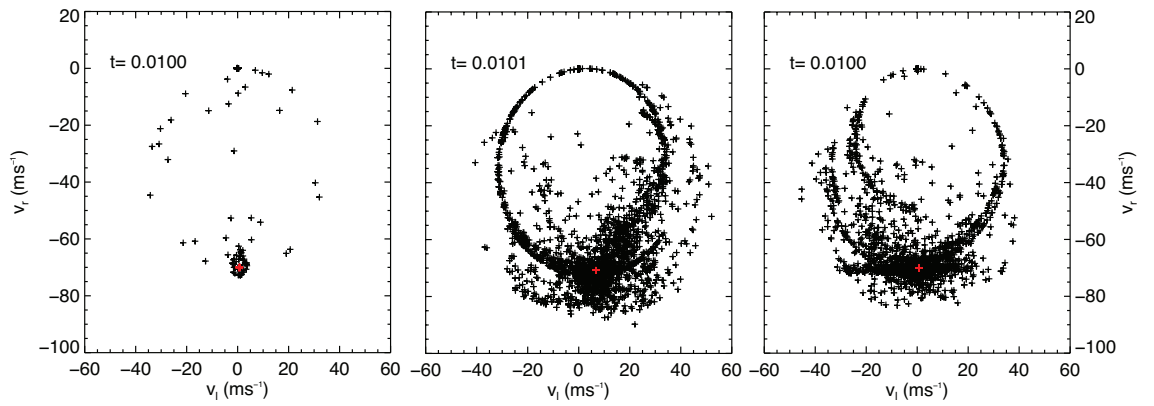
Figure 7.8.: Comparison of the velocity distributions from identical simulations with different time-steps: Left $dt = P_0 \times 10^{-3}$, middle $dt = P_0 \times 10^{-5}$, right $dt = P_0 \times 10^{-7}$. The loop-like structures around the impactors (red) are the collisionally induced $\Delta \boldsymbol{v}$.

seen to oscillate like this.

Neglecting any external forces for the moment there are two scenarios that can be envisaged for collisions which are not a single impulsive event. Collisions which occur over an extended location or collisions which are extended in time or some combination of the two. Both must still involve a series of individual collisions with discrete objects.

In the first scenario, S6 can be thought of as a chain of impactors with identical orbital elements but whose starting positions are all displaced from one another in longitude, l_0. This leads to each object following its own epicycle which intersects the F ring at roughly the same time, with identical geometries, but across a longitudinally extended section of core. This kind of impact is indeed observed at the F ring (see Chapter 6), where S6 is seen as a linear chain of objects, sometimes more than a degree in length. In reality each of these objects will have its own orbit, with its own Δa and Δe relative to the core. If, however, these orbits are all very similar, the objects will impact the core at roughly the same time and a simple longitudinal displacement is a good approximation. Each impactor then behaves identically to the single impactor case above, creating its own ejecta cloud which shears and oscillates as before. The combined effect is a single, unusually wide, classic jet.

The second scenario is the same chain of objects but with a spread in starting phase, M_0, instead of a displacement in longitude . This has the effect of spreading the collisions, which all occur in approximately the same region of ring, over a significant portion of orbital period. A jet formed in this way will be a composite made up of a number of standard jets created by each impactor in turn as it passes
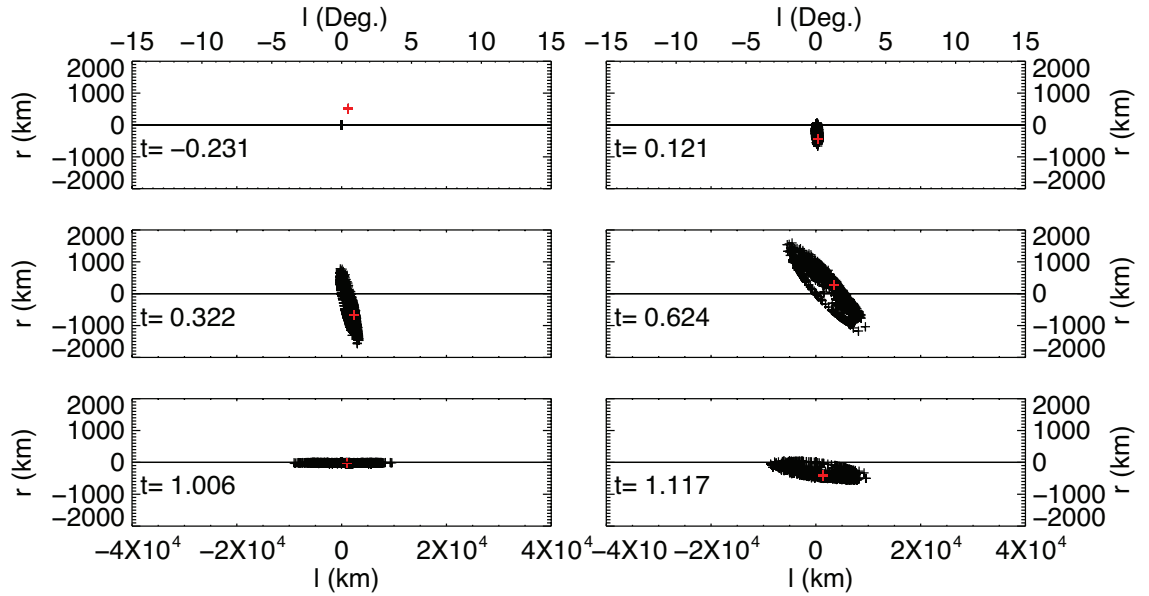
Figure 7.9.: Snapshots of the simulation with $dt = P_0 \times 10^{-5}$. A clump formed from 130 m radius particles (red) on an S6-like orbit impacts into a segment of ring made up of 1 m radius particles (black).

throughout the core. Each jet will have a slightly different phase meaning that some are still radially extended whilst others are collapsing back into the core. This leads to a more complicated jet shape and means that, on average, more material is away from the core at any one time than in previous scenarios. The individual particles will still have large Δe, though, and will therefore still oscillate,

These scenarios are approximations and differing impactor orbits and phases, a clumpy core and interactions between each impactor's ejecta will change the outcome. However the overall jet shape and evolution are clearly not changed that much from the single impactor case: each object produces a standard jet on its own which still oscillates.

7.2.2. Coefficients of Restitution

By default REBOUND uses a free-slip model whereby tangential velocities are unaltered during collisions. This is supported by some experimental evidence (Supulver et al., 1995), which suggests that colliding icy spheres do indeed have high coefficients of tangential restitution. However, this does mean that the effective coefficient of restitution varies with impact angle and is relatively high, approaching elastic, for glancing collisions. It is this which produces the spread in $\Delta \boldsymbol{v}$ seen in Figs. 7.2 and 7.4, etc. For $\epsilon_t = 1$, Eqn. 3.18 reduces to just the first term in the square brackets.

Meanwhile, for a single spherical surface encountering uniformly distributed, approximately static particles the normal component of relative velocity, $\boldsymbol{U}_n$, falls off with impact parameter, b, (defined in Fig. 3.7). Thus the magnitude of the change in particle velocity, Δv, will also fall off with b, from $\sim U$ in head-on collisions to zero for perfectly glancing ones. It is this spread in speed which causes the discrepancy between these simulation results and those of Charnoz (2009), and the predictions of Section 3.1, where all the particles are given approximately the velocity of the collider.

It is unlikely that the real objects are smoothly spherical. As discussed in previous chapters they more likely irregularly shaped, 'fluffy' and under-dense aggregates, possibly with regolith layers. As argued by Charnoz (2009), collisions with such an uneven surface might be expected to damp out relative velocities, independent of original impact angle, and with a damping which is highly inelastic; indeed Hill et al. (2015) found no relation between coefficients of restitution and impact parameter for rough, millimetre-sized ice aggregates. Rolling friction (which is not present with $\epsilon_t = 1$) might also be expected to be important as the component particles of aggregates move across each-other.

Considering the above, REBOUND is modified to include a tangential coefficient of restitution so that $U_t' = \epsilon_t U_t$ where, for symmetry, $\epsilon_t = \epsilon_n = \epsilon$ and Eqn. 7.1 is replaced with $\epsilon = (U/U_c)^{-0.234}$ (i.e. dependent on the total collision velocity, not just the normal component). The code still ignores particle spin, in effect assuming that surface rotation speeds are negligible compared to the translational velocities (Ohtsuki et al., 2013). In addition, the effective tangential coefficient should be a function of the beta parameter, relating to the moments of inertia (see Section 3.1, Charnoz, 2009 and Richardson, 1994), which is itself a function of the shapes and sizes of the particles, but here is set to one. This is because the concern is the effect of a general tangential coefficient of restitution on the ejecta velocities. Neither the specific value of ϵ_t, nor the rotation rates, are of interest, so it is kept as a simple function of U. The modification is tested by having two equal size spheres undergo a grazing collision with no other forces switched on. In default REBOUND there is no change in velocity of the particles whereas with the modification their relative translation velocity is reduced by a factor ϵ. Collisional simulations are then run as above.

Figure 7.10 shows the impact of a single 200 m radius object with $\Delta a = -10$ km, $a\Delta e = 30$ km. Direct detection of collisions, rather than the tree structure, are used here. The addition of ϵ_t leads to all the target particles being given roughly the impactor's velocity, independent of impact parameter. The resulting structure is
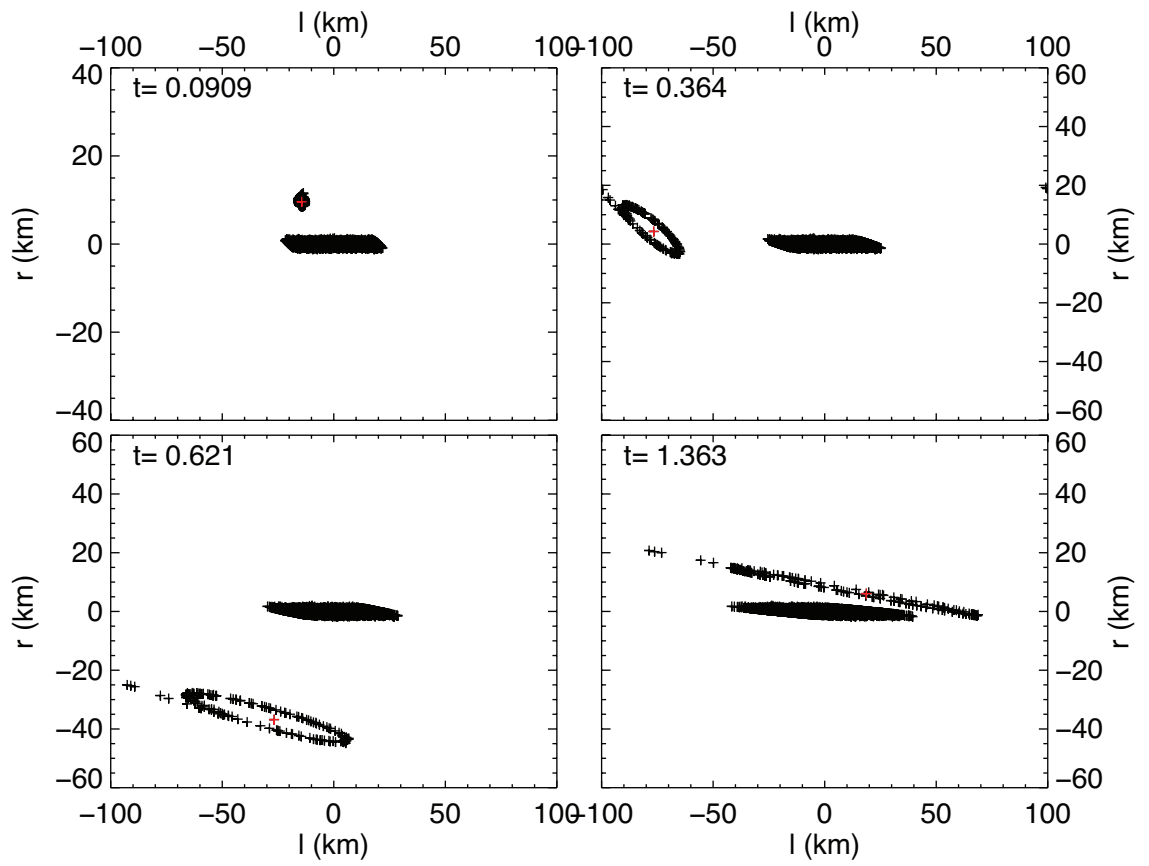
Figure 7.10.: Snapshots from the impact of a 200m radius moonlet (red cross) on a $\Delta a = -10$ km, $a\Delta e = 30$ km orbit where the code has been modified to include a tangential coefficient of restitution, $\epsilon_t = \epsilon_n$.

unlike the ones seen before, taking the form of a sphere of particles which follow the impactor along its orbit whilst slowly shearing out. At times the sheared particles touch the core and look similar to a mini-jet but generally they are detached from it, forming a separate arc of material. Thus the modified code recovers the results of Charnoz (2009) (see his figures 3 and 4) where the 'jet' is centred on the impactor's orbit, rather than the F ring's, and there is no stream of particles linking the two. The feature will eventually shear out along the whole of the impactor's orbital path.

The clustering of velocities is obvious, when compared to Figs. 7.2 and 7.4, in the velocity distribution, shown in Fig. 7.11. The right-hand side shows that nearly all the particles have a velocity of $\Delta v = U = 3.42$ ms^{-1} with a spread of about ± 0.3 ms^{-1} which, from the left-hand side, can be seen to be the same in all directions. This comes from the symmetry in having $\epsilon_t = \epsilon_n$. No particles are given speeds intermediate between this and zero.

To investigate how these new results scale with velocity and time-step the sim-
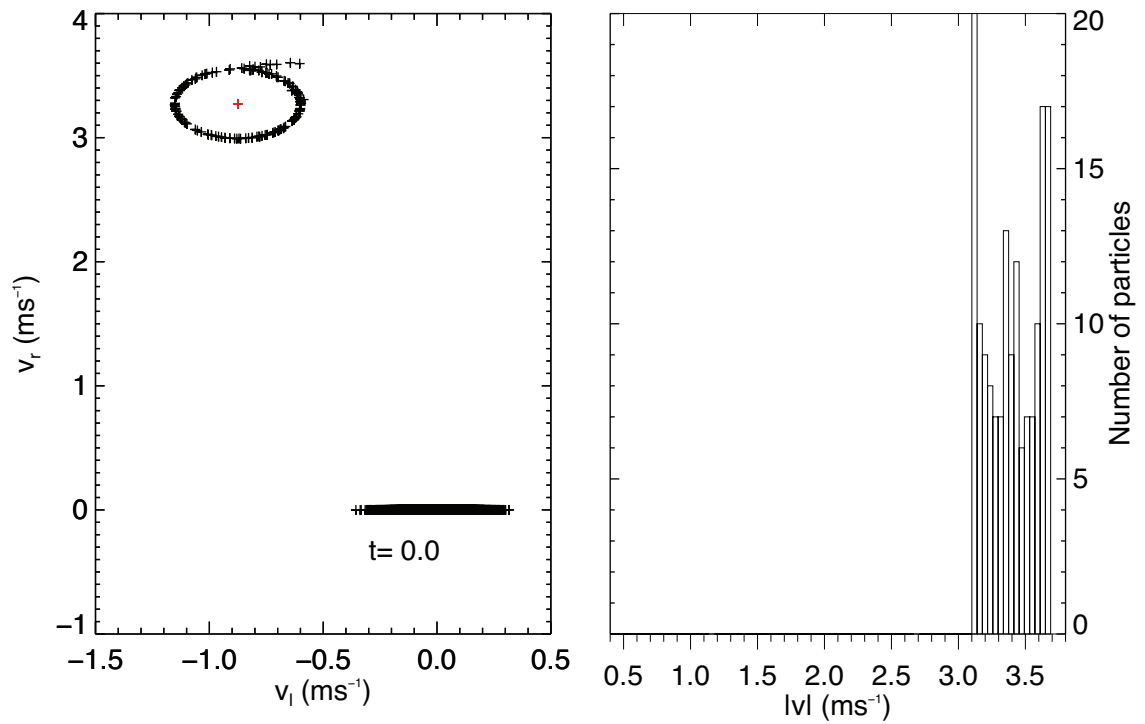
Figure 7.11.: Velocity distribution from the impact of a 200 m radius moonlet where
the code has been modified to include a tangential coefficient of restitu-
tion. The horizontal bar centred on the origin, in the left-hand panel,
is again made up of the Keplerian velocities of the unperturbed ring
particles while the loop-like structure, which is now tightly clustered
around the impactor, is the collision induced Δv. The right hand-
panel shows total speed which is closely clustered around that of the
impactor.

ulation from Section 7.2.1 (with S6 velocities) is repeated but with direct collision detection and a tangential coefficient. Figure 7.12 shows the velocity distribution shortly after impact. $\Delta \boldsymbol{v}$ is, again, much more clustered around that of the impactor when compared to Fig. 7.8. Some particles are given velocities intermediate between zero and those of the impactor but the histogram on the right-hand side shows them to be negligible next to the large number that receive $\Delta v \approx U = 70$ ms^{-1}. Note that the distribution around the impactor is now not a simple sphere due to its extended shape (see Section 7.2.3 below). This velocity distribution will form another extended arc which will follow the collider orbit, gradually shearing out in a feature centred on S6.

These results show that, with a tangential coefficient of restitution, jets are not produced. Ring particles with negligible mass, compared to the impactor, are simply placed on approximately the same orbit as it. The visible result is a bright clump, which elongates with time, but which is separated from the core. This is a possible explanation for the 'Object' category of features seen in Chapter 5 and also supports the idea of objects sweeping up dust when not encountering anything more solid, as discussed in Section 5.3.4.

A possible mechanism for making jets, whilst having a tangential coefficient, is presented in Charnoz (2009): if the colliding object is an unbound, or loosely bound, clump and it encounters a solid moonlet *which is itself embedded in the core* then the scattered material is centred on said moonlet. The result is a shearing jet which is again centred on the core, rather than the impactor orbit. Whilst disruption of loose clumps remains a possible explanation it struggles to explain the presence of repeated collision features and the continued survival of S6. In the next section collisions between aggregates, where partial disruption can occur, are simulated in an effort to find an alternative explanation.

7.2.3. Aggregate Collisions

Introducing structure into the colliding objects allows them to fragment and gain or lose mass whilst also significantly expanding the parameter space. Collision outcomes can now include total disruption, total accretion (i.e. merging) and partial disruptions, either of both clumps or disruption of one clump and survival of the other. Which of these occurs is highly dependent on impact velocity and direction as well as the shapes of the clumps (Walsh and Richardson, 2003; Karjalainen, 2007; Hyodo and Ohtsuki, 2014), their mass ratio and the coefficient of restitution (Barbara and Esposito, 2002; Ohtsuki et al., 2013), all of which are expected to vary
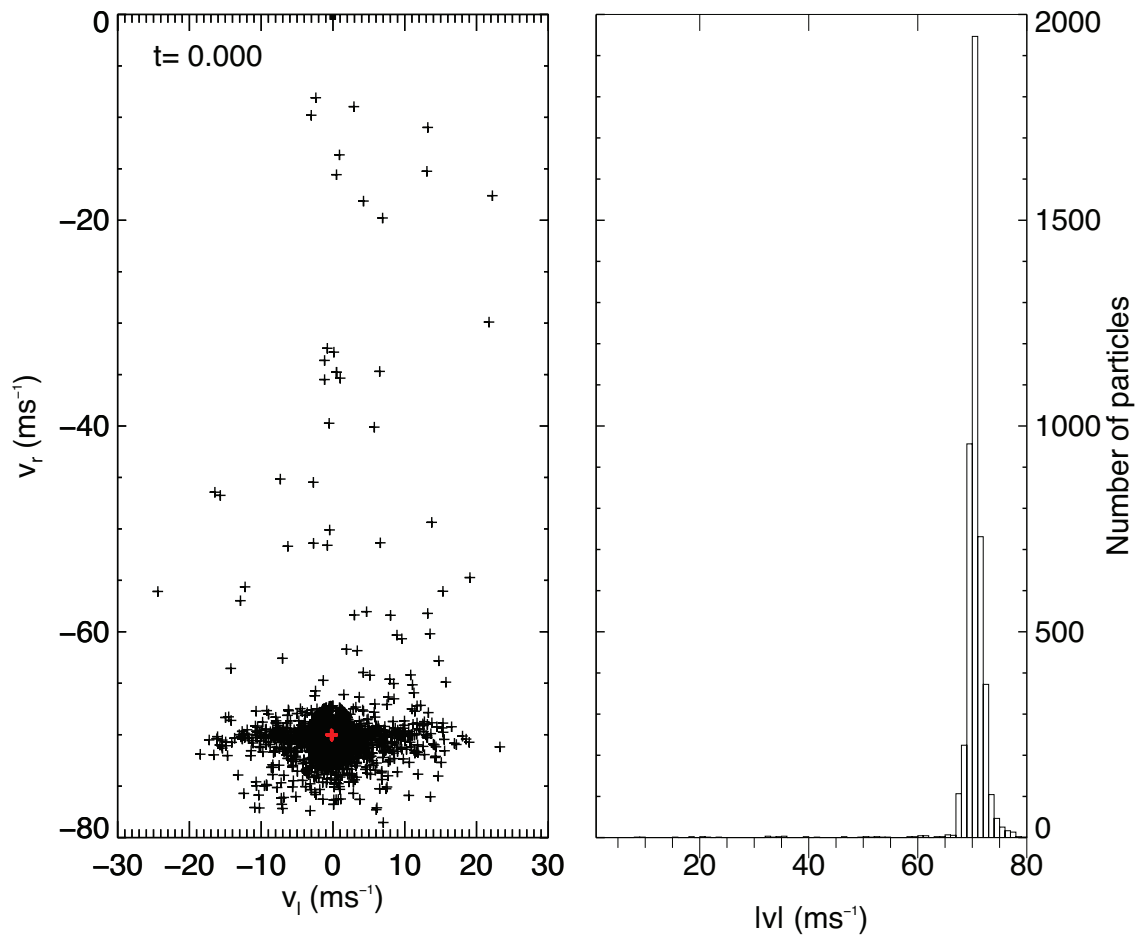
Figure 7.12.: Velocity distribution from the impact of a clump on an S6 type orbit
where the code has been modified to include a tangential coefficient of
restitution. $dt = P_0 \times 10^{-7}$ and collisions are directly detected. Left:
the collision induced $\Delta \boldsymbol{v}$ is clustered around the impactor's $U_r = -70$
ms^{-1}. Right: total speed is also closely clustered around that of the
impactor. Compare with Fig. 7.8

between collisions in the F ring. This parameter space is too large to explore fully so is sampled sporadically to highlight the major trends.

A method based on Hyodo and Ohtsuki (2014) is followed to produce aggregates. Five hundred particles, with radii of 130 m, are placed in a low density sphere with no external forces, i.e. with the gravity of the central body switched off. These then collapse under their own self-gravity to form a randomly packed, loosely bound clump (recall that there are no intra-particle forces except gravity). REBOUND's leap-frog, second order symplectic integrator is used (rather than the SEI) with a constant, and low, coefficient of restitution, $\epsilon = 0.1$ used to facilitate aggregation. The time-step is 0.1 s and all particles are given the density of water ice, $\rho = 900$ $\mathrm{kg\,m^{-3}}$. This is higher than the previous simulations to allow aggregates to survive in the tidal field used in the next part of the process (clumps formed from $\rho = 400$ $\mathrm{kg\,m^{-3}}$ particles are outside their Roche limit at the F ring's radius and tidally disrupt immediately). This increase in density is applied to all particles so mass ratios between them are not altered and collision outcomes should not be affected too drastically. The increased mass does mean, however, that intra-particle gravity becomes more important, as shown below.

When the clump is stable (mutual velocities are $< \mathrm{mms^{-1}}$) the simulation is stopped and the particles positions are saved. The resulting aggregate is shown in the left-hand panel of Fig. 7.13 and is 2492 m by 2228 m by 2343 m across in the r, l and z directions for an average radius of 1177 m.

A new simulation is then started using the epicycle integrator with the F ring parameters from before, a time-step of $dt = P_0 \times 10^{-5}$ and direct collision detection, and the particles are loaded in. Tidal forces begin to affect the particles, and they shift their positions under the new potential, forming a tri-axial ellipsoid which is the expected shape of objects in the Roche zone. The tidally altered clump is shown in the right-hand panel of Fig. 7.13 and now measures 2557 m by 2285 m by 2237 m. This gives an r/l ratio of ~ 1.13 and an overall density and porosity of $\sim 600 \ \mathrm{kg\,m^{-3}}$ and $\sim 33\%$ respectively, intermediate between the individual particles and the previously used densities and comparable to the clump used in Hyodo and Ohtsuki (2014).

Finally, the tidally altered clump is then placed at the origin of a new simulation and a second identical clump is loaded with a relative position and bulk velocity such that it will collide with the first. Figure 7.14 shows the results of a run with significant fragmentation. The impactor clump is here given $\Delta a = -10$ km, $a\Delta e = 30$ km, for a collision velocity of $U = 3.34 \ \mathrm{ms^{-1}}$. An extended ejecta cloud like a mini-jet is formed, but there are a number of differences from the previous simulations. Firstly,
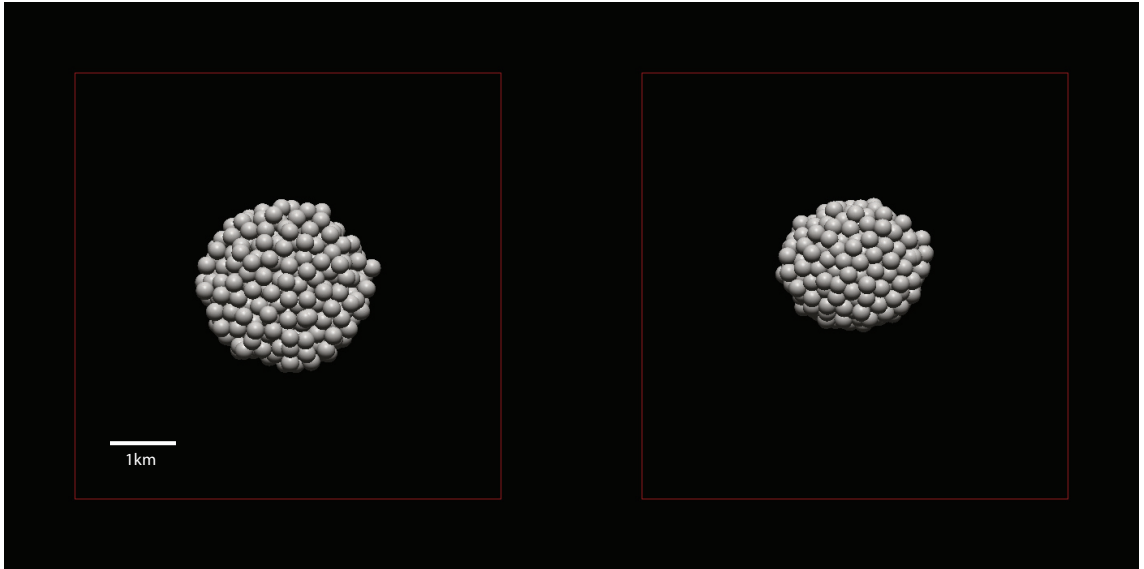
Figure 7.13.: Screenshots from REBOUND simulations showing clumps formed using the method described in Section 7.2.3. Left: The first stage after the particles have collapsed under their own gravity. Right: The second stage after the first clump has been placed in a tidal field appropriate for the F ring and subsequently deformed into a tri-axial ellipsoid.

because all the particles are of equal mass the $\Delta\boldsymbol{v}$ is split evenly between them in each individual collision. This places most of the particles on orbits intermediate between those of the original target and impactor clumps. The result is that both the impactor and target clumps partially disrupt and the mini-jet is made up of particles from both. The mini-jet still oscillates in the classic way but now the whole structure is also slightly displaced from the origin (see panel three in Fig. 7.14) to the centre of mass of the two clumps, which has a slight velocity difference from the reference zero.

These differences are obvious in the velocity distribution, shown in Fig. 7.15. Both the target and impactor particles have a spread of velocities with a large scatter of ~ 1 ms^{-1} or more from their bulk motions, enough to disrupt the clumps. Unlike in the previous simulations, particle speeds (right-hand side) are distributed relatively uniformly between zero and approximately the collision velocity ($U = 3.34$ ms^{-1}), but no loop structure is visible.

Intra-particle gravity is important here due to the much more massive individual particles. This can be seen in Fig. 7.14, fourth panel, where some of the ejecta particles have re-aggregated, forming a large clump in the middle of the mini-jet. This has enough gravity (~ 1 ms^{-1} escape velocity) to visibly perturb part of the
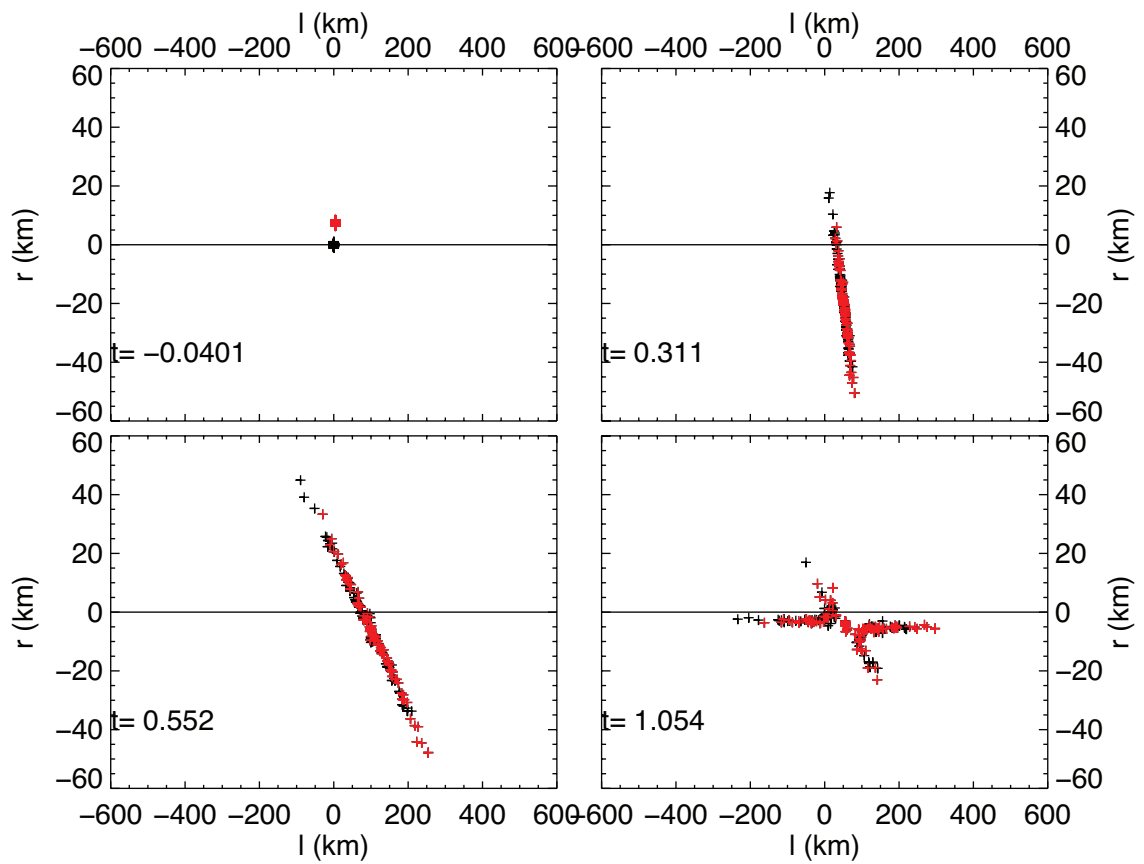
Figure 7.14.: Snapshots from the simulation of a clump made up of five hundred 130 m radius moonlets (red crosses) on a $\Delta a = -10$ km, $a\Delta e = 30$ km orbit impacting into an identical clump (black crosses) at the origin. The resulting structure is determined by both collisions and gravitation.

structure, producing a streamer-channel/fan-like feature which oscillates with the mini-jet but is half a cycle out of phase with it. At lower velocities ($U \sim 1 \text{ ms}^{-1}$) aggregation is further enhanced and the particles merge into a single clump with a velocity, and orbit, intermediate between the two starting aggregates. Any ejected particles form a loose linear structure either side of the object, as above, but their number decreases with decreasing collision velocity. In both complete disruption and merger events particles are ejected in all directions from the clumps, gaining positive and negative Δa values and forming two sided structures.

No attempt is made here to quantify the aggregation at different velocities but figure 5 of Hyodo and Ohtsuki (2014) predicts almost complete disruption for the clumps in Fig. 7.14. However, they use $\epsilon_n = 0.25, \epsilon_t = 1$ as opposed to the $\epsilon \approx 0.08$ in both normal and tangential components here. Their figure 14 shows how increasing ϵ_n shifts the disruption criteria to lower velocities and extrapolating by eye in the opposite direction suggests large remnant fragments are entirely plausible with the lower coefficient used here. Recall that Karjalainen (2007) also noted increased aggregation with smaller coefficients.

Total, or near total, disruption of both clumps is not conducive to the formation of repeated jets and mini-jets. The re-accreted clump seen in the centre of the feature in this simulation also does not fit observations (where the inferred location of the colliding objects is at the tip of the mini-jets). Initial conditions which encourage partial disruption events are now explored to see if these can more accurately reproduce the observations.

Partial Disruptions

A number of previous studies have shown 'bridges' of material stretching out between partially disrupted aggregates after a collision (see for example Leinhardt et al., 2000; Karjalainen, 2007; Walsh and Richardson, 2003 and the middle column of figure 7 of Hyodo and Ohtsuki, 2014). These are a promising candidate for spreading ejecta between the orbits of the two objects. Korycansky and Asphaug (2006) note that, at least in free space, off-centre collisions, those where the clumps are offset by an impact parameter, b, are effective at creating "two re-accreted objects of approximately equal mass, separating at greater than escape speed". Off-centre collisions are simulated now by loading the two aggregates in, as before, but with the second given an additional offset in r_0 or l_0 so that when they collide their centres are slightly displaced. The offset is chosen to be a fraction of the combined clump radii, for example $b = 0.7(R_1 + R_2)$, the most likely impact parameter for randomly
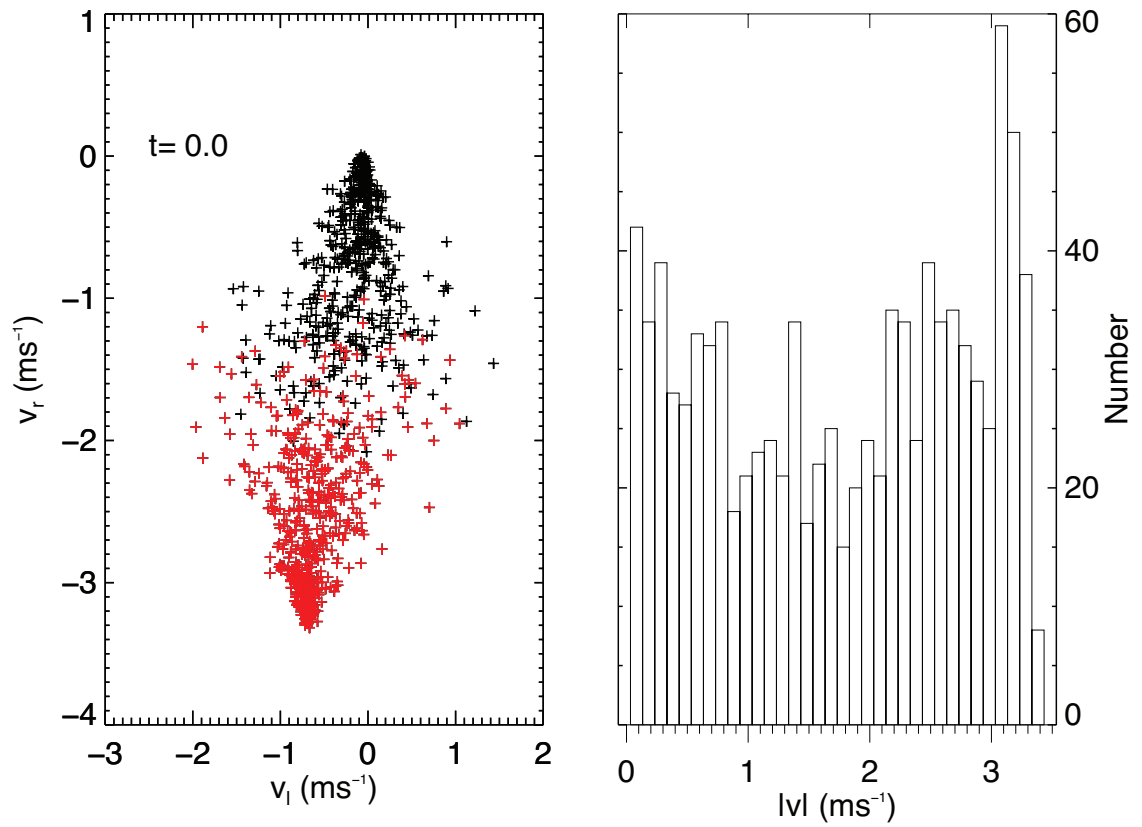
Figure 7.15.: Velocity distribution from the impact of a clump composed of five hundred 130 m radius particles (red crosses) on a $\Delta a = -10$ km, $a\Delta e = 30$ km orbit into an identical clump (black crosses). Left: velocity distribution and right: speed distribution.

moving spheres. Gravitational attraction between the two aggregates slightly alters their trajectories, however, so the final impact parameter will be slightly different and b is only quoted roughly.

Figure 7.16 shows the results for an impactor clump given $\Delta a = -10$ km, $a\Delta e = 20$ km and an impact parameter of $b \approx 0.7$. The glancing collision leads to the release of a number of particles but large remnant clumps survive (visible in both the right hand-panels). The remnant clumps' orbits are slightly changed from their starting orbits, the impactor being slightly decelerated to a smaller Δa and $a\Delta e$ and the target being accelerated so that it now follows its own small epicycle. The ejected material is strung out with orbits which, to first approximation, are between the two, as in the observed mini-jets. The top right-hand panel shows additional structure which is not seen in mini-jets, however, in the form of a radial offset which is out of phase with the main pattern. The shape of the jet, for example in the bottom right panel, is also slightly curved rather than a straight line. The velocity distribution (Fig. 7.17) shows no obvious cause for this structure: the particles all have speeds between zero and the collision velocity of $U = 2.23$ ms^{-1} but with sharp bimodal peaks around the two clumps. The fact that the additional structure is out of phase suggests it forms later due to the subsequent gravitational influence of the surviving clumps on the nearby ejecta. As with the feature in Fig. 7.14 this gravitational effect will be more or less obvious with more or less massive starting clumps and also decrease in importance with increasing collision velocity.

To investigate increased collision velocities the impactor clump is now given $\Delta a = -25$ km, $a\Delta e = 110$ km, approximately that of the feature in Fig. 5.19, Chapter 5 (catalogue number N1557026084). The impact parameter is again $b \approx 0.7$. The results are shown in Fig. 7.18 with the velocity distribution in Fig. 7.19. The increased velocity almost completely disrupts the aggregates, spreading their particles over an extend area of space as can be seen in the two right-hand panels of Fig. 7.18. This can also be seen in the velocity distribution; the spread of ~ 1 ms^{-1} in longitudinal velocity for both the target and impactor particles is enough to disrupt the clumps and spread the material in semi-major axis. The ejecta material still has speeds between zero and U and the distribution is still sharply two-peaked, as before. There is, therefore, still a significant amount of material on orbits similar to the original clumps meaning a repeated impact event could still occur. One final feature to note is the more complicated structure of the resulting jet, as seen in the two right hand panels. The increased spread in velocities has broadened out the feature in both the radial and longitudinal directions whilst the bimodal speed distribution leads to a concentration near the tip at certain times in the orbit.
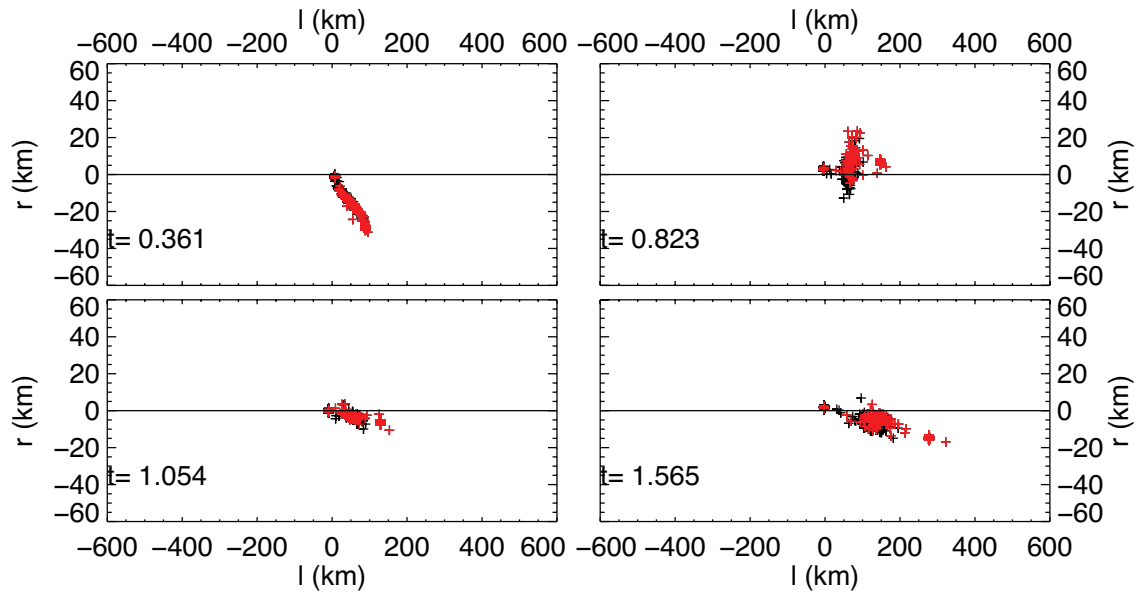
Figure 7.16.: Snapshots from the simulation of two identical clumps undergoing a glancing impact. The impactor clump (red crosses) is given a $\Delta a = -10$ km, $a\Delta e = 20$ km orbit with a small additional offset to generate an impact with $b \approx 0.7$.
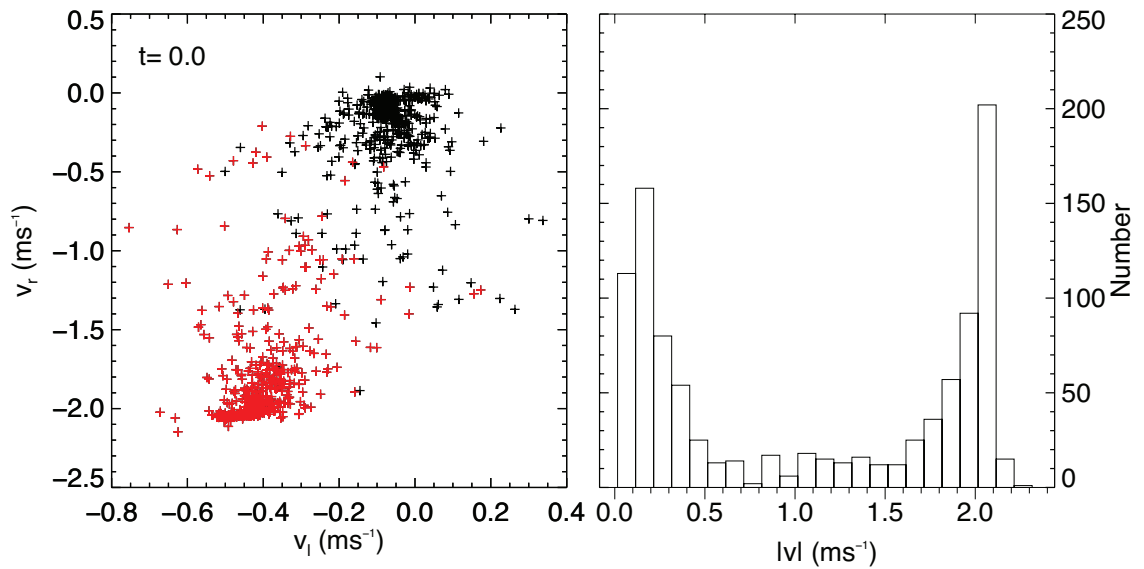
Figure 7.17.: Velocity distribution from the glancing impact of two identical clumps. The impactor clump (red crosses) is given a $\Delta a = -10$ km, $a\Delta e = 20$ km orbit with a small offset to generate an impact with $b \approx 0.7$. Left: velocity distribution and right: speed distribution.
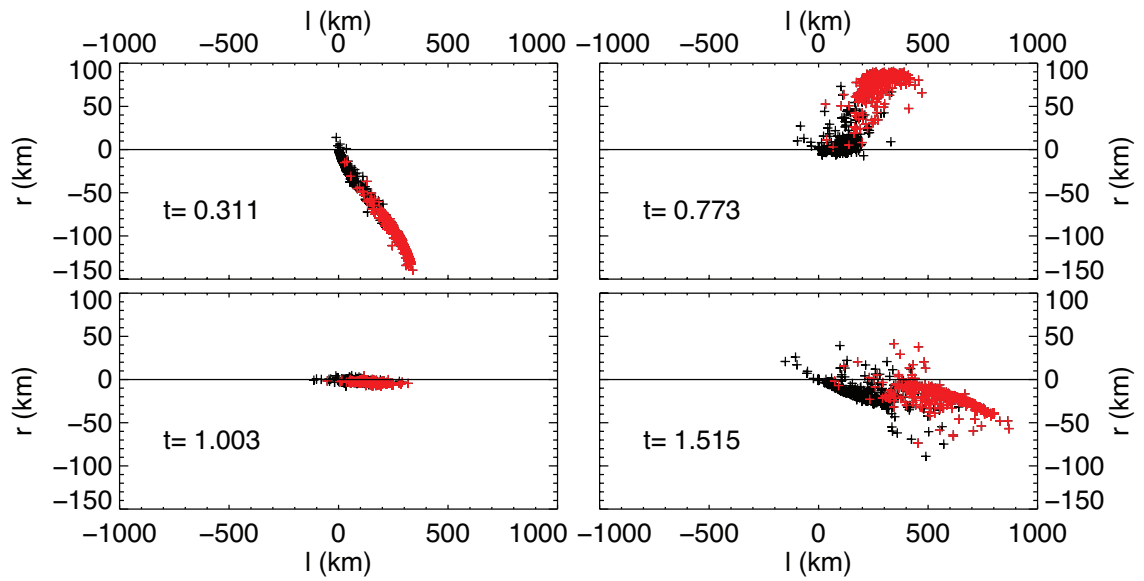
Figure 7.18.: Snapshots from the simulation of two identical clumps undergoing a glancing impact. The impactor clump (red crosses) is given a $\Delta a = -25$ km, $a\Delta e = 110$ km orbit with a small offset to generate an impact with $b \approx 0.7$.
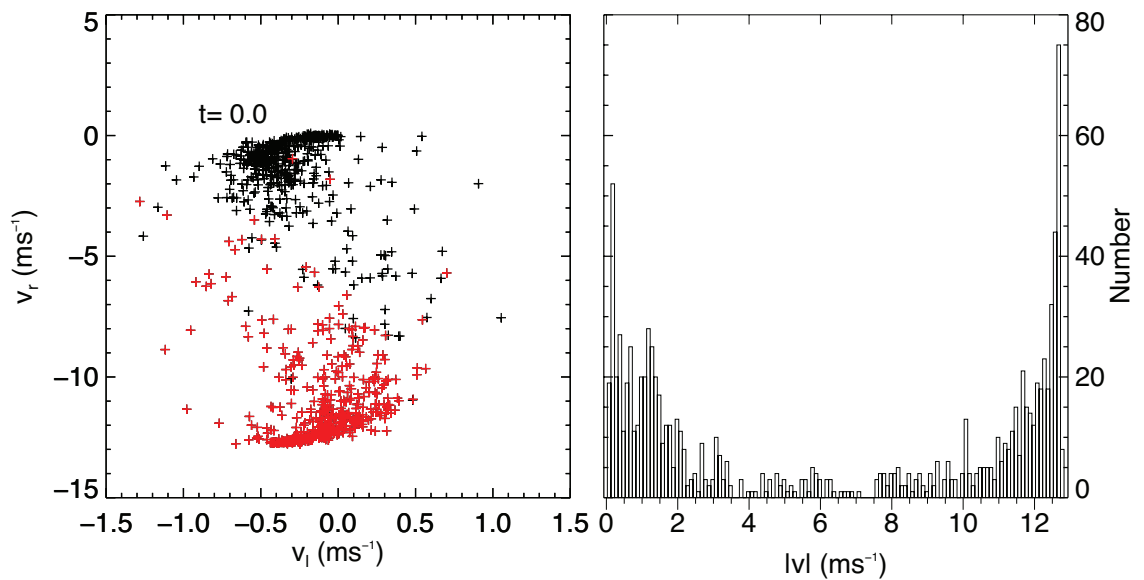
Figure 7.19.: Velocity distribution from the glancing impact of two identical clumps. The impactor clump (red crosses) is given a $\Delta a = -25$ km, $a\Delta e = 110$ km orbit with a small offset to generate an impact with $b \approx 0.7$. Left: velocity distribution and right: speed distribution.

These two simulations show the potential for glancing, partially disruptive collisions to lead to mini-jet like features. Ejecta are spread out into a linear structure with $\Delta a \approx a\Delta e$ which oscillates as mini-jets do. The surviving impactor clump lies at the tip of this structure with an orbit very similar to its pre-collision one and a degree of disruption determined by the impact parameter, speed and relative clump masses. Under certain conditions it can therefore survive to continue colliding with further clumps in the core, forming repeated mini-jets. The concentration of material around the impactor, as seen in the bimodal speed distributions, provides a natural explanation for 'bright-head' mini-jets seen in Chapter 5. Increasing velocity leads to more fragmentation so there should be some relationship between mini-jet size and the presence of bright-heads. However this will depend on the clump masses, shapes and degree of compactness, all of which should vary randomly between collisions, making any relation hard to detect. Further, the visible brightness of mini-jets may be determined mostly by the small particles, rather than the presence of the clump itself. No size distribution is used here so it is hard to compare the relative brightnesses of different parts of a mini-jet between simulations and observations. Finally it can be seen from Figs. 7.16 and 7.18 that the feature swaps sides, following the orbit of the impactor and staying on one side of the core at a time. This is in contrast to the results of the preliminary simulations (Section 7.2.1) and agrees well with the observations, where double-sided features are not observed.

With the above caveat on size distributions in mind, a partially disruptive collision is now compared directly with observations to confirm the visual similarity. Figure 7.20 shows a side-by-side comparison of re-projected images of the ISS_102RF_FRSTRCHAN001_PRIME feature (see Chapter 4) with a simulation. The setup is as before with $\Delta a = a\Delta e = 27$ km, $b \approx 0.7$ and the results displayed as a contour map with particles binned in 5×10 km bins in radius and longitude. The binning is done to improve the visual appearance of the simulation, relative to the observations, and the size of the bins is chosen to be roughly the same as a NAC pixel in this sequence. The results match relatively well; the major difference being the non-continuous, fragmented nature of the simulation feature when compared to the smooth observations. This can be put down to the finite number of, large, particles used, i.e. a resolution issue.
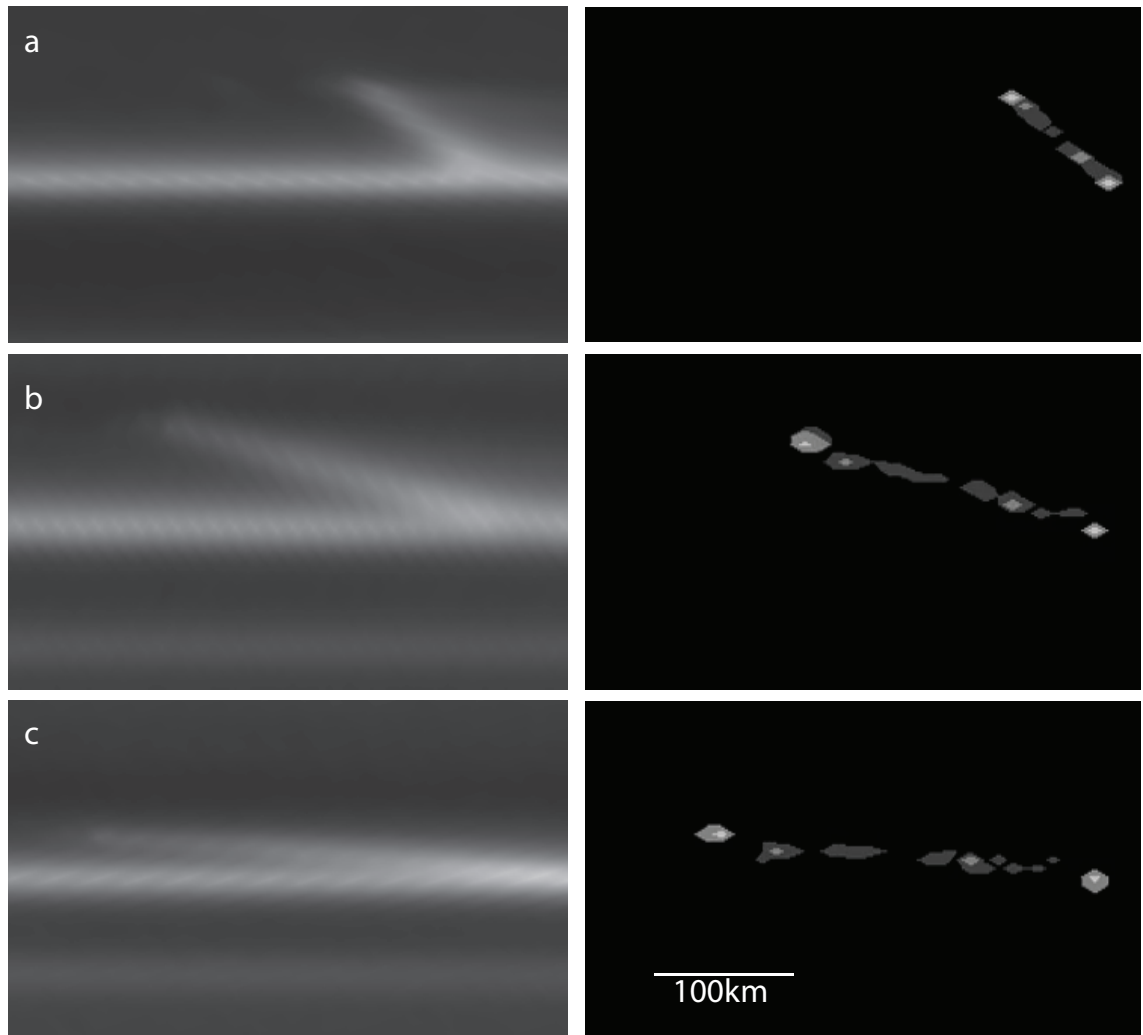
Figure 7.20.: Left: Re-projected ISS NAC images separated by ~ 3 hours. Images are (a) N1612002457 (b) N1612013501 (c) N1612022286. Right: Corresponding frames from a simulation of a clump with $\Delta a = a\Delta e = 27$ km colliding with an identical clump in the F ring with $b \sim 0.7$. The re-projected images and simulation are to the same scale and each covers 400×220 km.

7.3. Discussion and Conclusions

A range of collisional encounters between targets and impactors of varying sizes and forms has been simulated. Nearly all collisions result in jet-like structures, that is clouds of ejecta with roughly linear distributions in relative semi-major axis and eccentricity, with $\Delta a \approx a\Delta e$, and magnitudes of each similar to those of the colliding object. There are, however, a number of important differences between different types of impact. Figure 7.21 summarises these differences. Each row outlines the results of a different collision scenario, sketched in the left-hand column, with the resulting ejecta distributions, at an arbitrary time later, for impacts primarily in the longitudinal (second) and radial (third column) directions. The right-hand column outlines which of the features observed in the F ring can be explained by each scenario.

The first two rows show the impact of a single large body into a loose swarm of much less massive ones (**moonlet-dust** impacts). The top row is the general result using a velocity dependent ϵ_n and $\epsilon_t = 1$, discussed in detail in Section 7.2.1. For the second (and all subsequent) rows $\epsilon_n = \epsilon_t$. The free-slip conditions of the first row may or may not be physically realistic for low temperature ice particles (see discussion in Section 7.2.2) but the noticeable 'loop' of ejecta, where the centre of the feature is left empty, is not observed. It could be argued that resolution plays a role here and that better imagery might resolve such a structure, however the results of radial impacts also argue against this model. $\Delta a = a\Delta e$ impactors produce all positive or all negative longitudinal accelerations resulting in a single sided feature (inwards *or* outwards) with the collider at the tip. Non-aligned colliders pass through the core on more radial trajectories and produce features which are seen on both sides of the core at the same time, a type of feature which is very rarely, if at all, observed. The colliding objects are also no longer located at the mini-jet tip and the loop is even more pronounced.

The second row shows how relaxing the free-slip condition, by adding a non-unity tangential coefficient of restitution, recovers the predictions made in Section 3.1. That is, all the small particles are placed approximately on the orbit of the colliding body, following its epicycle motion but with a small scatter which shears them out around it. This is also the result obtained by Charnoz (2009). This type of behaviour probably explains the sweeping up of fine-grained dust by large objects (S6, Prometheus, etc.) leaving dark, sheared channels in places in the core, strands and dust envelope. It may also explain the bright, extended objects, found completely separate from the core in Chapter 5 as being clumps or moonlets that
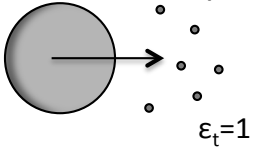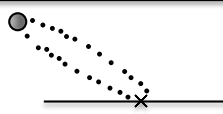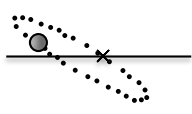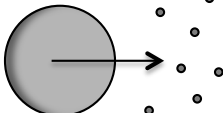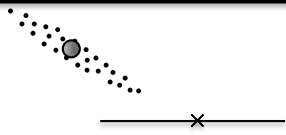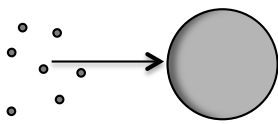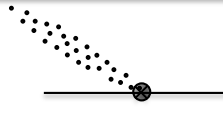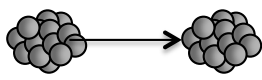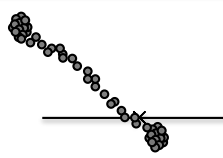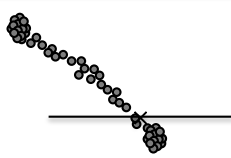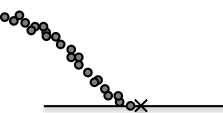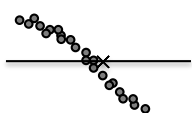
Scenario	Longitudinal Impacts	Radial Impacts	Observed Features
Moonlet-dust $\varepsilon_t=1$			X
Moonlet-dust			Objects and channels
Dust-moonlet			Some jets and mini-jets?
Aggregate-aggregate			Jets and mini-jets incl. bright-heads and repeats
Increasing **v** or decreasing b			Some jets and mini-jets?

Figure 7.21.: Schematic summarising different low-velocity collision outcomes. The left-hand column shows different collision scenarios with **moonlets** represented by large, filled circles, **dust** particles by small filled circles and loosely bound gravitational **aggregates** by clumps. The right-hand object is on an F ring-like orbit and the left-hand one is the impactor with a Δa and Δe. The middle columns show the resulting feature, at some arbitrary time later, with an impact in the longitudinal or radial direction. The right-hand column shows which features, observed by Cassini, can be explained by each scenario.

have picked up a bright swarm of slowly spreading small particles.

Row three shows the inverse situation where the massive object is assumed to be embedded in the F ring core and a loose swarm of small particles, on a differing orbit, impacts it (**dust-moonlet** collisions). This was Charnoz (2009)'s favoured model and, as shown in Fig. 7.21, does produce jet-like features. There are a number of issues with this model however. Firstly the massive object is left unperturbed at the origin and the jet contains essentially no mass, meaning secondary collisional features are unlikely to occur. Secondly the clump itself is completely dispersed into a jet and does not survive a single impact. This is clearly at odds with the observations of S6 which continues to impact the F ring hundreds of times over several years. Finally the right-hand column shows that again, in contrast to observations, double-sided features are created by radial impacts.

The final two rows show the results of disruptive collisions between aggregates, created using the methods outlined in Section 7.2.3 (**aggregate-aggregate** collisions). They differ in the amount of disruption with either increasing collision velocity or decreasing impact parameter (more head-on collisions) causing increased fragmentation. The shape of the resulting feature is similar in all cases, differing only by the amount of clumpiness at the extreme ends. Fig. 7.21 shows only representative examples; in reality a continuum of results exist, ranging between almost complete survival of both clumps to full disruption, with increasing velocity scattering material as per the disruption law of Leinhardt et al. (2000).

In low velocity, head-on cases the clumps merge leaving a concentration of material in the middle of the feature rather than at the ends. This is probably not common for jet-forming collisions but may well be how small clumps can grow. Partial disruptions, on the other hand, seem like a good explanation for jets and mini-jets; they have the right appearance, follow the orbit of the colliding object in the right way and are primarily seen on only one side of the core at a time. Thus impacts by clumps with $\Delta a = a\Delta e$ into core clumps can explain classic mini-jets while those between objects with large relative eccentricities can explain $\Delta a < a\Delta e$ features such as Fig. 5.19 and Fig. 6.13. Bright-heads will naturally form at the feature tip if significant portions of the colliding object survives. It is interesting to note that the 'surviving' clumps, shown above, are often re-accumulated material, i.e. that clumps often disrupt but with low relative velocities, allowing them to re-aggregate under their their own gravity after a collision.

Discrepancies with the observations do exist: simulated features have a curved 'S' shape to them and often have additional structure, in the form of gravitationally scattered ejecta (see Figs. 7.18 and 7.16). Both may occur in real features but

on scales too small to observe, or masses may not be large enough for significant gravitational effects. Simulations can also have a non-continuous appearance when compared to images (see Fig. 7.20) which is probably a numerical resolution effect. Despite these differences partially disruptive collisions between gravitational aggregates present the best model for explaining jets and mini-jets.

There are several implications for the F ring if most mini-jets and jets are formed by collisions between such aggregates. The first, most obvious conclusion is that there must be a large number of clumps with significant mass in the core itself. This is not altogether surprising given the implications of radio science measurements, (Marouf et al., 2010), stellar occultations (Esposito et al., 2008; Meinke et al., 2012) and ISS images themselves. It also supports the clumpy nature of the core inferred from surveying collisional features in Chapter 5. When colliding objects encounter a diffuse, dusty section of the core they pass through, sweeping up material but otherwise leaving little trace. When they enter a region with significant mass, either in the form of another consolidated aggregate or a dense inner core, they collide, shedding material from both impactor and target and dragging out a visible jet. Unfortunately it is difficult to tell where the majority of the material comes from, or to say much about the objects themselves. Collision velocity can be inferred from the feature's Δa but the sizes and orientations of the two clumps are unknown and the results of different collisions are degenerate. Any individual jet could therefore arise from a combination of different impact parameters, clump sizes, orientations or coefficients of restitution (which may vary randomly between collisions - Hill et al., 2015). Further, any particular jet, observed only once, could be the result of the complete disruption of one or both aggregates or even the dispersal of a loose cloud in the style of the Charnoz (2009) model. It is only the presence of repeated and secondary collisions (and possibly bright-heads) that suggests the survival of the impactor. Nevertheless, the ubiquity of these features implies high survival rates among colliding clumps. Perhaps only the most massive or densely consolidated aggregates survive long enough to be placed on colliding orbits. S6 must be especially consolidated or massive to survive many F ring encounters.

To summarise:

- **Moonlet-dust** collisions with $\epsilon_t = 1$ do not produce structures like those seen in observations.

- **Moonlet-dust** collisions without $\epsilon_t = 1$ can explain dark channels in the core and bright, extended objects seen separate from it.

- **Dust-moonlet** collisions may produce some of the observed jets and mini-jets but cannot explain those with multiple, repeated collisions. Likewise for **aggregate-aggregate** collisions in which both aggregates completely disrupt.

- **Aggregate-aggregate** collisions with partial disruptions produce jet and mini-jet-like features from collisions in any direction and provide a natural explanation for bright-heads and repeated collisions. As such they represent the best model for the majority of jets and mini-jets.

With regards to the high velocity collisions, even partial clump disruptions struggle to replicate the orbital properties of the strand and the observed behaviour of some jets (i.e. ejecta distributions with $\Delta a > a\Delta e$). This is not found in *any* of the simulations presented in this chapter nor is it expected from the elementary dynamics of a single collision. Material drawn out in a collision involving a clump with $\Delta a > a\Delta e$ could theoretically have elements with the same distribution but such a clump would not collide with the core in the first place! Furthermore S6 is known to have an orbit with much larger relative eccentricity. As discussed in Chapter 6, the implication is that further perturbations to the ejecta orbits must be occurring after the initial collision. This may take the form of secular perturbations from a massive F ring core or re-collisions between ejecta and the core, or between different jets. All will be difficult to simulate within REBOUND given the constraints on particle number and computing resources.

For a more global model one approach might be to abandon hard spheres and allow individual particles to fragment, reducing the initial number of particles needed. This is the approach taken in some versions of the PKDGRAV N-body code, where look-up tables of rubble pile collisions (e.g. see Leinhardt et al., 2000 and Stewart and Leinhardt, 2009) are used to determine the outcomes of each interaction, including replacing a single disrupted particle with a size distribution of ejecta. One would need to bear in mind the large variation in collision outcomes seen here, however, and also that most look-up tables will be for collisions in free-space, not the tidal environment.

A different approach would be to consider the interaction between two clumps in more detail, extrapolating the results to a global model. In this work, clumps have been considered gravitationally bound aggregates of identical particles but more complicated structures may occur in the F ring. Constituent particles will undoubtedly have a size distribution, not to mention irregular shapes, and inter-particle forces other than gravity (such as ice sticking, van der Waals, etc.) may be important. A more realistic model of an F ring clump may be a single large, compacted

moonlet surrounded by a deep regolith of smaller particles, as suggested by occultations (Esposito et al., 2008; Meinke et al., 2012). One attempt to model collisions in a more realistic way is the Soft Sphere Discrete Element (SSDE) approach. Here particles are allowed to penetrate into one another and rebound velocities are calculated from the material's elastic and frictional properties (Schwartz et al., 2012). SSDE has been incorporated into PKDGRAV and used to investigate interactions between granular matter (Ballouz et al., 2014), a regime that probably applies to the loose, clumpy F ring objects. The disadvantages of SSDE are that the mechanical properties of the material must be well characterised, possibly not the case for low temperature ice, and that very small time-steps must be used to fully resolve the collisions (multiple time-step per collision - Schwartz et al., 2012).

8. Conclusions

8.1. Summary

This thesis investigated the role of physical collisions in shaping Saturn's F ring. Collisional features have been imaged using the Cassini spacecraft and their distribution and morphology analysed. Computer simulations were then compared directly to these observations. Good agreement was found for low-velocity ($1 - 100$ ms^{-1}) collisions between loosely bound aggregates. Repeated collisions by the same object are found to be very important, explaining a number of properties of the observed features. Overall, much of the F ring's uniquely complex morphology can be explained by physical collisions with a population of, mostly unseen, objects.

Chapter 2 gave an overview of the F ring system, detailing its morphology, structure, particle sizes and orbit, based on observations from Earth and spacecraft.

Chapter 3 reviewed the orbital and collisional dynamics needed to understand the rest of the thesis. Motion of small objects in Hill's coordinate frame, which rotates around a larger primary, was described as well as the effect of a small perturbing force on this motion. The hard spheres model of physical collisions was then described and compared to evidence from laboratory experiments and computer simulations.

Chapter 4 introduced the Imaging Science Subsystem of the Cassini spacecraft and the process of using it to acquire images of the F ring. Analysis of a particularly interesting feature was then presented. This feature, termed a 'mini-jet', was observed for half an orbital period, revealing its evolution with time and showing it to be the ejecta cloud from a recent collision. Low-velocity impacts by local objects are suggested as the cause.

In Chapter 5 similar features were cataloged by visually identifying them in individual ISS images. Over one thousand features were found throughout the dataset and their statistics were analysed. They are found to be distributed randomly in time and around the F ring, with little correlation to the nearby moon Prometheus or other brightness features in the core. This lack of correlation with visible ring features supports the idea of a, mostly unseen, inner core of larger particles which

is important in collisions. Mini-jet morphology supports the idea of low-velocity impacts and suggests a population of order one hundred objects on slightly different orbits from the core, colliding with it at speeds of several metres per second. Many of these objects appear to collide more than once, forming 'repeated mini-jets', implying that they have enough self-gravity or physical strength to survive passage through the core, and many are clustered together, forming multiple structures.

In Chapter 6 mosaics of ISS images were used to identify and measure the larger collisional features known as jets. Their morphology and distribution were compared to the smaller mini-jets and found to be very similar. Thus it appears likely that they are two extremes of a single population. Differences are noted, however, with some of the larger features having differing orbital distributions, with small relative eccentricity, contrary to the expectations of theory. Secular effects from the mass of the core or damping from the repeated, overlapping nature of the collisions are suggested to explain this. The especially prominent strand or 'F ring secondary', noted in other works, is confirmed in this survey to be the result of collisions by the object S6.

Finally, in Chapter 7, computer simulations of jet and mini-jet forming collisions were undertaken. These were performed using the REBOUND N-body code at a range of impact velocities and geometries. Results ware found to be strongly dependent on the coefficient of restitution, and in particular the presence of a tangential component. In general, large objects impacting dust merely sweep it up meaning there must be significant mass in the impactor *and* target to form a jet-like feature. A single population of loosely bound gravitational aggregates, with some embedded in the core and others on nearby orbits, is implied.

8.2. Other Collisional Systems and Future Work

The processes described in this thesis are generic; features similar to those studied here are expected to occur wherever aggregates physically collide with one another at low velocities. One example may be the recent discovery of an object at the edge of the A ring (Murray et al., 2014). Nicknamed 'Peggy', the object itself is not seen directly but its presence is inferred from a localised disturbance at the ring edge, visible in ISS images. This disturbance has been tracked over several years and, at times, resembles a mini-jet feature protruding from the ring, suggesting physical collisions. Interpretation of the feature is hampered, however, by its small size (compared to the pixel resolution) and by the complex dynamics of the region, which

is shaped by the 7:6 resonance with the co-orbital moons Janus and Epimetheus. The Peggy feature may represent a combination of collisional and gravitational interactions with surrounding ring material. Other locations in Saturn's rings where collisions could be important are the B ring edge; where perturbations by Mimas may be inducing clumping of material (Esposito et al., 2012), and the edge of the Keeler gap; where localised, irregular structures, called 'wisps' and 'spikes', are seen extending $\sim$ 1 km into the gap from the outer edge (Tiscareno et al., 2005; Porco et al., 2005). Perturbations from the gap-opening moon Daphnis are expected but the structures do not seem directly related, raising the possibility that they are secondary features caused by objects aggregated by the moon-induced clumping.

Apart from Saturn, Uranus has a system of narrow, dusty rings interspersed with small moons. Several of these inner moons are unstable on relatively short timescales (compared to the age of the solar system), raising the possibility that the ν ring, which lies between two of them, is a collisional remnant (see review in Tiscareno, 2013). High-resolution imaging of the Uranian ring system might reveal collisional structures.

Finally the discovery of rings around two Centaurs (small solar system bodies with orbits between the giant planets and properties of both asteroids and comets) extends the realm of planetary rings from the gas giants to other objects as well. Dense, narrow rings were discovered by stellar occultations around Chariklo (Braga-Ribas et al., 2014) and are inferred around Chiron (Ortiz et al., 2015). The narrowness of Chariklo's rings suggests a shepherding mechanism by small moons and collisions may be involved in their formation and evolution.

Returning to the F ring of Saturn, additional work could be done to characterise further collisional features. Photometry of jets and mini-jets, using calibrated ISS images, would allow a more quantitative analysis of their brightness. Only raw images have been used here but converting from DN to measured flux would allow estimates of the volume of material contained within specific features. Photometry would be especially revealing if jets and strands have different phase functions to the core, implying different particle size distributions, as suggested in Chapter 6.

Another area for future work is the anomalous behaviour of jets, with respect to mini-jets and basic orbit theory, also discussed in Chapter 6. The small relative eccentricity of these large features is puzzling given the relatively high-velocity collisions that formed them. The possible solutions, proposed in Chapter 6, include periapse locking from the gravitational attraction of the core; which would require additional description using secular perturbation theory, and damping via re-collisions with the core and other jets. This second option could be investigated

with additional computer simulations with the challenges briefly discussed in Section 7.3.

Finally, the so-called 'F ring' and 'proximal orbits' , towards the end of the Cassini mission, will provide unprecedented close-up views of the ring system. Imaging resolution at the F ring will be sub-kilometre at various times during these phases, beginning in late 2016, potentially revealing intricate structure within collisional features as well as the colliding objects themselves. It must be noted, however, that the most enlightening observations discussed in this thesis are those which capture the evolution of a feature over time; in other words time resolution is equally, if not more, important than spatial resolution in investigating orbital structures. Nevertheless, the F ring orbits should provide a spectacular view of Saturn's most active and diverse ring.

A. Measurements of the Streamer-Channel Feature

Image Number	Date (year-DOY-time)	r_{base} (km)	λ_{base} (°)	r_{tip} (km)	λ_{tip} (°)
N1612002457	2009-030-09:47:26.471	140407.1	108.705	140461.6	108.675
N1612002708	2009-030-09:51:37.469	140412.5	110.383	140462.0	110.365
N1612002959	2009-030-09:55:48.467	140422.0	112.077	140471.6	112.046
N1612003210	2009-030-09:59:59.466	140428.7	113.762	140481.7	113.732
N1612003461	2009-030-10:04:10.464	140428.8	115.449	140488.4	115.415
N1612003712	2009-030-10:08:21.462	140434.2	117.137	140493.6	117.097
N1612003963	2009-030-10:12:32.460	140443.0	118.824	140499.2	118.784
N1612004214	2009-030-10:16:43.458	140443.2	120.506	140506.9	120.472
N1612004465	2009-030-10:20:54.457	140452.4	122.193	140514.8	122.154
N1612004716	2009-030-10:25:05.455	140459.9	123.877	140519.2	123.837
N1612004967	2009-030-10:29:16.453	140466.6	125.557	140529.1	125.518
N1612005218	2009-030-10:33:27.451	140478.6	127.244	140531.6	127.204
N1612005469	2009-030-10:37:38.450	140484.1	128.928	140546.7	128.883
N1612005720	2009-030-10:41:49.448	140487.0	130.617	140545.6	130.566
N1612005971	2009-030-10:46:00.446	140496.2	132.293	140546.3	132.252
N1612006222	2009-030-10:50:11.444	140498.7	133.979	140549.6	133.928
N1612006473	2009-030-10:54:22.442	140500.4	135.665	140560.4	135.615
N1612006724	2009-030-10:58:33.441	140504.2	137.346	140558.5	137.290
N1612006975	2009-030-11:02:44.439	140505.7	139.030	140564.5	138.979
N1612007226	2009-030-11:06:55.437	140509.6	140.714	140564.6	140.663
N1612007477	2009-030-11:11:06.435	140511.7	142.398	140566.4	142.342
N1612007728	2009-030-11:15:17.433	140508.9	144.088	140572.1	144.031
N1612007979	2009-030-11:19:28.432	140514.0	145.769	140575.9	145.707
N1612008230	2009-030-11:23:39.430	140522.5	147.454	140576.2	147.393
N1612008481	2009-030-11:27:50.428	140515.6	149.141	140576.9	149.074
N1612008732	2009-030-11:32:01.426	140517.8	150.822	140574.3	150.755
N1612008983	2009-030-11:36:12.425	140525.0	152.504	140582.9	152.436
N1612009234	2009-030-11:40:23.423	140520.1	154.184	140584.1	154.119
N1612009485	2009-030-11:44:34.421	140519.3	155.869	140578.9	155.804
N1612009736	2009-030-11:48:45.419	140517.6	157.556	140585.7	157.480
N1612009987	2009-030-11:52:56.417	140514.4	159.238	140582.5	159.170

N1612010238	2009-030-11:57:07.416	140519.5	160.920	140588.6	160.851
N1612010489	2009-030-12:01:18.414	140518.5	162.606	140582.5	162.528
N1612010740	2009-030-12:05:29.412	140520.4	164.284	140579.7	164.210
N1612010991	2009-030-12:09:40.410	140518.3	165.964	140577.5	165.897
N1612011242	2009-030-12:13:51.408	140523.1	167.648	140578.2	167.574
N1612011493	2009-030-12:18:02.407	140514.6	169.336	140575.6	169.258
N1612011744	2009-030-12:22:13.405	140518.2	171.026	140570.8	170.940
N1612011995	2009-030-12:26:24.403	140514.8	172.698	140573.0	172.622
N1612012246	2009-030-12:30:35.401	140512.9	174.382	140566.4	174.307
N1612012497	2009-030-12:34:46.400	140507.1	176.063	140560.9	175.986
N1612012748	2009-030-12:38:57.398	140508.6	177.750	140562.4	177.671
N1612012999	2009-030-12:43:08.396	140509.2	179.436	140575.3	179.357
N1612013250	2009-030-12:47:19.394	140497.3	181.116	140563.4	181.035
N1612013501	2009-030-12:51:30.392	140501.0	182.798	140553.1	182.720
N1612013752	2009-030-12:55:41.391	140496.4	182.800	140557.7	182.718
N1612014003	2009-030-12:59:52.389	140491.2	186.165	140546.2	186.087
N1612014254	2009-030-13:04:03.387	140489.5	187.849	140544.1	187.768
N1612014505	2009-030-13:08:14.385	140485.6	189.527	140535.6	189.452
N1612014756	2009-030-13:12:25.384	140480.3	191.216	140533.6	191.131
N1612015007	2009-030-13:16:36.382	140479.0	192.895	140523.8	192.817
N1612015258	2009-030-13:20:47.380	140471.7	194.588	140526.5	194.497
N1612015509	2009-030-13:24:58.378	140467.0	196.269	140513.9	196.185
N1612015760	2009-030-13:29:09.376	140456.7	197.953	140511.0	197.868
N1612016011	2009-030-13:33:20.375	140448.5	199.639	140504.6	199.549
N1612016262	2009-030-13:37:31.373	140442.0	201.320	140495.1	201.235
N1612016513	2009-030-13:41:42.371	140436.3	203.009	140490.9	202.919
N1612016764	2009-030-13:45:53.369	140425.4	204.684	140480.1	204.604
N1612017015	2009-030-13:50:04.367	140429.0	206.377	140476.1	206.291
N1612017266	2009-030-13:54:15.366	140421.5	208.061	140466.4	207.972
N1612017517	2009-030-13:58:26.364	140411.0	209.746	140459.6	209.658
N1612017768	2009-030-14:02:37.362	140409.9	211.438	140446.7	211.345
N1612018019	2009-030-14:06:48.360	140406.4	213.118	140446.8	213.026
N1612018270	2009-030-14:10:59.359	140381.0	214.814	140442.7	214.712
N1612018521	2009-030-14:15:10.357	140386.5	216.496	140429.1	216.398
N1612018772	2009-030-14:19:21.355	140379.7	218.183	140425.3	218.085
N1612019023	2009-030-14:23:32.353	140367.4	219.868	140412.1	219.773
N1612019274	2009-030-14:27:43.351	140363.7	221.561	140409.5	221.456
N1612019525	2009-030-14:31:54.350	140355.6	223.251	140396.5	223.142
N1612019776	2009-030-14:36:05.348	140343.0	224.936	140384.7	224.829
N1612020027	2009-030-14:40:16.346	140337.7	226.614	140376.5	226.516
N1612020278	2009-030-14:44:27.344	140332.4	228.301	140372.8	228.204
N1612020529	2009-030-14:48:38.342	140326.3	229.991	140361.5	229.890
N1612020780	2009-030-14:52:49.341	140317.3	231.682	140355.5	231.577
N1612021031	2009-030-14:57:00.339	140307.2	233.367	140338.1	233.264

N1612021282	2009-030-15:01:11.337	140300.5	235.062	140334.5	234.949
N1612021533	2009-030-15:05:22.335	140283.6	236.751	140326.6	236.640
N1612021784	2009-030-15:09:33.334	140282.3	238.443	140310.0	238.330
N1612022035	2009-030-15:13:44.332	140272.2	240.126	140300.9	240.022
N1612022286	2009-030-15:17:55.330	140268.4	241.814	140298.3	241.707
N1612022537	2009-030-15:22:06.328	140252.5	243.509	140290.4	243.393
N1612022788	2009-030-15:26:17.326	140248.4	245.192	140280.6	245.083
N1612023039	2009-030-15:30:28.325	140236.9	246.879	140271.2	246.773
N1612023290	2009-030-15:34:39.323	140228.4	248.579	140260.2	248.462
N1612023541	2009-030-15:38:50.321	140217.1	250.271	140248.5	250.151
N1612023792	2009-030-15:43:01.319	140206.2	251.960	140242.3	251.848
N1612024043	2009-030-15:47:12.317	140196.5	253.653	140229.1	253.532
N1612024294	2009-030-15:51:23.316	140189.9	255.333	140214.1	255.224
N1612024545	2009-030-15:55:34.314	140180.7	257.029	140216.4	256.910
N1612024796	2009-030-15:59:45.312	140170.6	258.716	140197.6	258.606
N1612025047	2009-030-16:03:56.310	140164.8	260.412	140188.5	260.296
N1612025298	2009-030-16:08:07.309	140154.7	262.105	140179.3	261.988
N1612025549	2009-030-16:12:18.307	140145.8	263.800	140171.2	263.683
N1612025800	2009-030-16:16:29.305	140135.3	265.485	140161.2	265.374
N1612026051	2009-030-16:20:40.303	140131.7	267.167	140150.1	267.064
N1612026302	2009-030-16:24:51.301	140120.6	268.864	140137.5	268.757
N1612026553	2009-030-16:29:02.300	140112.1	270.552	140128.3	270.450
N1612026804	2009-030-16:33:13.298	140103.1	272.252	140117.5	272.146
N1612027055	2009-030-16:37:24.296	140094.7	273.940	140109.2	273.838
N1612027306	2009-030-16:41:35.294	140086.5	275.639	140096.6	275.520
N1612027557	2009-030-16:45:46.292	140076.4	277.322	140093.3	277.230
N1612027808	2009-030-16:49:57.291	140068.8	279.005	140078.8	278.929
N1612028059	2009-030-16:54:08.289	140058.6	280.710	140075.3	280.611
N1612028310	2009-030-16:58:19.287	140054.3	282.396	140067.6	282.326
N1612028561	2009-030-17:02:30.285	140044.8	284.118	140053.0	283.979
N1612028812	2009-030-17:06:41.284	140036.5	285.806	140054.1	285.706
N1612029063	2009-030-17:10:52.282	140030.1	287.492	140040.6	287.391
N1612029314	2009-030-17:15:03.280	140017.2	289.201	140031.8	289.093
N1612029565	2009-030-17:19:14.278	140014.7	290.889	140021.8	290.781
N1612029816	2009-030-17:23:25.276	140007.0	292.583	140012.1	292.476
N1612030067	2009-030-17:27:36.275	140001.0	294.268	140006.7	294.159
N1612030318	2009-030-17:31:47.273	139992.3	295.972	139998.4	295.875
N1612030569	2009-030-17:35:58.271	139986.5	297.682	139991.3	297.603
N1612030820	2009-030-17:40:09.269	139980.9	299.343	139982.9	299.256
N1612031071	2009-030-17:44:20.267	139975.2	301.062	139976.8	300.851

Table A.1.: Mini-jet measurements from ISS_102RF_FRSTRCHAN001_PRIME sequence (see Chapter 4. All image exposures are 1500 ms and uncertainties from pixel size are ~ 5 km radial by $\sim 0.01°$ longitudinal.

B. Survey Data of Low-Velocity Collisional Features

Designation	Date (year-DOY-time)	r_{base} (km)	λ_{base} (°)	r_{tip} (km)	λ_{tip} (°)	Class (°)	Phase (°)
N1467350502	2004-183-04:57	140405.58	23.80	140349.66	23.88	BH	126.2
N1492066743	2005-103-06:28	140485.97	43.53	-	-	O	37.4
N1493639016a	2005-121-11:16	-	-	139921.01	226.32	Co	32.4
N1493639016b	2005-121-11:16	-	-	139930.84	224.87	Co	32.4
N1495325540a	2005-140-23:45	-	-	139885.80	276.03	Co	13.2
N1495325540b	2005-140-23:45	-	-	139887.85	274.90	Co	13.2
N1498727393	2005-180-08:42	140571.29	162.05	140505.13	162.25	C	99.3
N1498730990	2005-180-09:46	140706.06	160.52	-	-	O	98.9
N1501710723	2005-214-21:24	139850.34	126.34	-	-	O	146.4
N1503280408a	2005-233-01:25	-	-	140093.12	113.85	Co	151.3
N1503280408b	2005-233-01:25	-	-	140136.33	108.87	Co	151.3
N1503287403	2005-233-03:21	140118.44	107.43	140157.66	107.38	C	145.4
N1503915081	2005-240-09:43	139990.57	179.33	-	-	O	78.3
W1504631966	2005-248-16:51	140649.75	326.30	-	-	O	144.2
N1537877405	2006-268-11:38	139901.62	176.68	-	-	O	100.3
N1537877613	2006-268-11:41	139893.29	175.49	139904.74	175.48	C	100.0
N1537878025	2006-268-11:48	139890.64	172.25	139904.09	172.24	C	99.3
N1537878429a	2006-268-11:55	139975.10	170.84	-	-	O	98.8
N1537878429b	2006-268-11:55	139987.82	170.64	139994.24	170.64	C	98.8
N1537878429c	2006-268-11:55	139990.78	170.01	139997.27	170.01	C	98.7
N1537878628	2006-268-11:58	139892.76	168.65	139898.91	168.48	C	98.3
N1537882528a	2006-268-13:03	139931.48	153.23	-	-	O	89.8
N1537882528b	2006-268-13:03	139929.90	153.11	-	-	O	89.8
N1537883378	2006-268-13:17	-	-	139958.97	150.07	Co	87.3
N1537883920	2006-268-13:26	-	-	139939.20	148.86	Co	85.8
N1537884053	2006-268-13:29	-	-	139976.15	148.19	Co	85.8
N1537884703	2006-268-13:39	-	-	139968.07	148.06	Co	83.2
N1537884830	2006-268-13:42	-	-	139955.73	147.80	Co	82.9
N1537887254	2006-268-14:22	139966.74	142.00	-	-	O	75.3
N1537888059	2006-268-14:35	139960.65	140.85	-	-	O	72.6
N1537888287	2006-268-14:39	-	-	139968.41	140.48	Co	71.7

N1537889523	2006-268-15:00	139964.61	138.93	139969.30	138.90	C	67.3
N1537889634	2006-268-15:02	-	-	139973.90	138.86	Co	66.9
N1537890408	2006-268-15:14	139971.44	138.47	-	-	O	64.3
N1537891831	2006-268-15:38	139971.41	138.17	139981.58	138.09	C	59.5
N1537892812	2006-268-15:55	-	-	139987.31	137.78	Co	56.0
N1537893575	2006-268-16:07	139975.48	137.80	-	-	O	53.4
N1537895899	2006-268-16:46	139967.66	137.43	-	-	O	45.4
N1537897861	2006-268-17:19	-	-	139981.84	137.65	Co	39.8
N1537898100	2006-268-17:23	-	-	139980.46	137.37	Co	39.1
N1537898220	2006-268-17:25	139975.69	137.45	139985.97	137.44	C	38.8
N1537898708	2006-268-17:33	-	-	139995.04	137.31	Co	37.7
N1537899083	2006-268-17:39	-	-	139978.98	137.17	Co	36.9
N1537899854	2006-268-17:52	-	-	139996.50	137.05	Co	35.6
N1537900808	2006-268-18:08	140002.52	136.50	-	-	O	34.5
N1537900950	2006-268-18:10	139987.05	136.41	140003.08	136.39	C	34.4
N1537906905	2006-268-19:49	-	-	140056.50	122.28	Co	40.1
N1537910819	2006-268-20:55	140117.54	91.43	-	-	O	41.2
N1538184238	2006-272-00:52	140147.22	267.12	140108.38	267.15	C	159.6
N1538204682	2006-272-06:32	140364.82	270.27	-	-	O	160.9
N1538283887	2006-273-04:32	140244.39	82.82	-	-	O	159.9
N1541029450	2006-304-23:12	-	-	140549.26	97.14	Co	157.8
N1541035680	2006-305-00:55	140537.00	95.41	-	-	O	158.2
N1541044580	2006-305-03:24	140516.92	95.85	140543.47	95.77	C	158.9
N1541050365	2006-305-05:00	140584.90	97.04	-	-	O	159.4
N1541111925	2006-305-22:06	-	-	139901.65	293.00	Co	159.9
N1541116275	2006-305-23:19	139845.36	295.90	139894.43	295.86	C	159.9
N1541118015	2006-305-23:48	139850.18	296.86	139885.14	296.65	C	159.9
N1541118885	2006-306-00:02	-	-	139892.34	295.89	Co	160.0
N1541374579	2006-308-23:04	139895.54	118.50	-	-	O	163.4
N1542050711	2006-316-18:52	140354.06	93.67	140469.28	93.61	C	156.1
N1542057386	2006-316-20:44	140327.02	93.99	140459.02	93.86	BH	156.7
N1542058721	2006-316-21:06	140503.80	93.74	140463.41	93.77	C	156.8
N1542064061	2006-316-22:35	-	-	140477.62	94.99	Co	157.3
N1542076966	2006-317-02:10	139874.96	95.15	-	-	O	158.3
N1543174303	2006-329-18:59	140397.40	293.00	-	-	O	160.0
N1543216384	2006-330-06:40	140342.62	292.68	-	-	O	160.8
N1545564642	2006-357-10:58	140023.47	288.28	-	-	O	158.8
N1545576684	2006-357-14:18	140553.48	287.42	-	-	O	159.4
N1545580252	2006-357-15:18	140057.89	287.11	-	-	O	159.6
N1545589618	2006-357-17:54	140403.42	288.64	140461.68	288.61	C	159.9
N1545608350	2006-357-23:06	140492.90	288.63	-	-	O	160.7
N1546703299	2007-005-15:15	-	-	140508.02	250.02	Co	131.5
N1546704045	2007-005-15:27	-	-	140495.58	250.66	Co	131.5
N1546734631	2007-005-23:57	-	-	140358.79	255.40	Co	134.3

N1549804474	2007-041-12:41	140066.15	242.21	140019.41	242.29	BH	125.8
N1549805288	2007-041-12:55	140182.77	241.76	-	-	O	125.9
N1549808137	2007-041-13:42	139982.85	244.41	140003.94	244.38	C	126.2
N1549820347	2007-041-17:06	140236.64	247.47	-	-	O	127.5
N1549821568	2007-041-17:26	139965.93	247.65	140007.78	247.61	C	127.7
N1549830522	2007-041-19:55	140230.56	248.36	-	-	O	128.8
N1549833778	2007-041-20:49	-	-	140043.51	250.36	Co	129.1
N1549842325	2007-041-23:12	140178.13	252.94	-	-	O	130.0
N1550419818a	2007-048-15:37	140167.93	144.72	140154.05	144.94	C	125.9
N1550419818a	2007-048-15:37	-	-	140147.02	143.05	Co	125.9
N1551265033	2007-058-10:23	140367.21	200.22	-	-	O	102.7
N1551268606	2007-058-11:23	-	-	139979.04	200.74	Co	103.2
N1551269400	2007-058-11:36	-	-	139999.46	200.93	Co	103.3
N1551271782	2007-058-12:16	-	-	139999.27	200.69	Co	103.5
N1551275752	2007-058-13:22	-	-	139985.02	199.79	Co	104.0
N1551287669	2007-058-16:41	139914.72	202.39	-	-	O	105.4
N1551303946	2007-058-21:12	139924.73	206.57	139954.20	206.56	C	107.3
N1552434512	2007-071-23:15	140361.38	161.74	-	-	O	70.6
N1552730884	2007-075-09:34	139847.66	200.58	-	-	O	99.7
N1552809157	2007-076-07:19	140005.92	208.91	-	-	O	107.5
N1552818877	2007-076-10:01	-	-	140196.09	208.39	Co	108.5
N1552825357	2007-076-11:49	-	-	140174.45	209.88	Co	109.2
N1552826077	2007-076-12:01	-	-	140172.61	211.54	Co	109.2
N1552839757	2007-076-15:49	139848.25	213.67	-	-	O	110.7
N1554032873	2007-090-11:14	140525.44	176.19	140489.83	176.24	C	82.6
N1554034273	2007-090-11:37	140417.82	176.73	-	-	O	82.7
N1554037423	2007-090-12:30	-	-	140522.95	174.27	Co	82.9
N1554038123	2007-090-12:41	-	-	140461.15	176.11	Co	83.1
N1554038823	2007-090-12:53	140508.68	176.11	-	-	O	83.1
N1554044073a	2007-090-14:21	140438.62	177.14	140486.16	177.06	C	83.5
N1554044073b	2007-090-14:21	-	-	140473.42	173.70	Co	83.4
N1554045123	2007-090-14:38	-	-	140485.60	177.46	Co	83.5
N1554046873a	2007-090-15:07	140490.53	177.19	140526.39	177.16	C	83.7
N1554046873b	2007-090-15:07	140490.58	177.18	140526.39	177.16	C	83.7
N1554047573	2007-090-15:19	140544.24	175.02	140518.12	175.04	C	83.7
N1554052823	2007-090-16:46	140485.92	177.85	140497.79	177.82	C	84.1
N1554064723	2007-090-20:05	140168.45	177.42	-	-	O	85.0
N1555566013	2007-108-05:06	-	-	140537.09	178.93	Co	84.0
N1555575013	2007-108-07:36	-	-	140551.82	181.34	Co	84.7
N1555579213	2007-108-08:46	140584.02	180.87	140521.89	180.93	C	84.9
N1555583413	2007-108-09:56	-	-	140520.70	180.27	Co	85.2
N1555585813	2007-108-10:36	-	-	140555.64	182.89	Co	85.4
N1555587013	2007-108-10:56	139868.48	181.36	-	-	O	85.4
N1555588213	2007-108-11:16	140512.00	185.85	-	-	O	85.6

N1555590613	2007-108-11:56	140498.29	179.81	140525.15	179.78	C	85.6
N1555591213	2007-108-12:06	-	-	140519.21	182.65	Co	85.7
N1555592413	2007-108-12:26	140574.37	184.01	140528.35	184.04	C	85.8
N1555594813	2007-108-13:06	-	-	140497.18	183.04	Co	86.0
N1555595413	2007-108-13:16	-	-	140511.65	183.67	Co	86.0
N1555600813a	2007-108-14:46	-	-	140547.23	184.81	Co	86.4
N1555600813b	2007-108-14:46	140581.94	183.79	140546.62	183.82	C	86.4
N1555600813c	2007-108-14:46	-	-	140541.28	181.80	Co	86.4
N1555607413	2007-108-16:36	140539.64	184.74	140562.34	184.72	C	86.8
N1556209323	2007-115-15:48	140008.35	85.24	-	-	O	14.3
N1556209778	2007-115-15:55	140011.11	80.64	140026.87	80.62	C	13.7
N1556544478a	2007-119-12:58	-	-	140067.83	334.87	Co	46.9
N1556544478b	2007-119-12:58	140148.71	328.72	140112.84	328.84	C	46.9
N1557026084a	2007-125-02:40	140228.40	179.02	140365.01	178.97	BH	79.8
N1557026084b	2007-125-02:40	140228.40	179.02	140353.01	178.86	BH	79.8
N1557033152	2007-125-04:38	140311.76	179.47	140373.69	179.40	C	80.2
N1557035012	2007-125-05:09	140304.66	177.96	140344.68	177.92	C	80.3
N1557054728	2007-125-10:38	140289.81	179.81	-	-	O	81.5
N1557056960	2007-125-11:15	-	-	140367.15	179.30	Co	81.6
N1557058448	2007-125-11:40	-	-	140378.33	181.21	Co	81.7
N1557072956	2007-125-15:42	-	-	140389.68	180.96	Co	82.6
N1557080024	2007-125-17:39	140230.35	182.51	140362.30	182.22	BH	83.0
N1558547650	2007-142-17:20	139909.39	159.26	140013.96	159.18	BH	79.2
N1571450847	2007-292-01:32	139931.89	179.05	140009.07	179.04	C	55.8
N1577813677a	2007-365-16:58	140563.73	168.39	140533.49	168.38	C	63.3
N1577813677b	2007-365-16:58	140526.89	165.69	140567.42	165.66	C	63.3
N1577813677c	2007-365-16:58	140598.84	165.61	140568.38	165.63	C	63.3
N1577813677d	2007-365-16:58	140603.17	165.49	140552.21	165.53	C	63.3
N1577818269	2007-365-18:15	140523.20	169.21	140574.19	168.92	C	63.7
N1577820565	2007-365-18:53	140562.91	167.96	140545.61	168.02	C	63.9
N1577823189a	2007-365-19:37	140516.78	169.15	-	-	O	64.2
N1577823189b	2007-365-19:37	140504.09	168.46	140546.98	168.32	BH	64.2
N1577824501a	2007-365-19:58	-	-	140555.02	171.70	Co	64.3
N1577824501b	2007-365-19:58	140575.77	169.28	140558.09	169.30	C	64.3
N1577825157a	2007-365-20:09	140534.00	169.12	140550.99	169.08	C	64.3
N1577825157b	2007-365-20:09	140525.85	168.61	140534.91	168.59	C	65.3
N1577825813	2007-365-20:20	-	-	140522.45	170.04	Co	64.4
N1577826797	2007-365-20:37	-	-	140333.35	168.75	Co	64.5
N1577828765a	2007-365-21:09	140500.18	171.14	140568.32	169.48	C	64.7
N1577828765b	2007-365-21:09	-	-	140342.73	169.94	Co	64.7
N1577828765c	2007-365-21:09	140480.58	169.46	140560.66	168.95	BH	64.7
N1577832373	2007-365-22:10	140576.63	169.52	140559.25	169.55	C	65.0
N1577832701	2007-365-22:15	-	-	140551.57	167.48	Co	65.0
N1577841885	2008-001-00:48	140378.79	170.42	-	-	O	66.0

N1577846477	2008-001-02:05	-	-	140551.41	171.53	Co	66.5
N1577848445a	2008-001-02:37	140537.97	171.98	-	-	O	66.7
N1577848445b	2008-001-02:37	140547.42	171.32	-	-	O	66.7
N1577857301	2008-001-05:05	140611.07	174.43	140580.29	174.61	C	67.7
N1577857629	2008-001-05:11	-	-	140536.68	175.55	Co	67.8
N1578389757	2008-007-08:59	140354.16	118.56	140326.08	118.65	C	19.2
N1578395134	2008-007-10:29	140367.82	121.35	140331.80	121.55	C	19.6
N1578398813	2008-007-11:30	140257.86	121.09	-	-	O	19.9
N1578399379	2008-007-11:40	140313.75	122.55	140350.98	122.53	C	20.0
N1578403907	2008-007-12:55	140253.05	121.95	140338.42	121.80	BH	20.2
N1578405605	2008-007-13:23	-	-	140362.63	121.95	Co	20.4
N1578406454	2008-007-13:38	140307.57	125.62	140344.85	125.50	C	20.5
N1578409567a	2008-007-14:29	140224.66	122.81	140338.89	121.54	BH	20.6
N1578409567b	2008-007-14:29	140282.88	127.19	140336.83	122.25	C	20.7
N1578410416	2008-007-14:44	140316.83	122.66	140353.98	122.59	C	20.7
N1578411831	2008-007-15:07	140314.25	122.80	140350.16	122.70	C	20.8
N1578414095	2008-007-15:45	140308.06	121.96	140348.38	121.86	C	20.9
N1578420038	2008-007-17:24	-	-	140372.82	122.36	Co	21.3
N1578424283	2008-007-18:35	140392.95	122.24	140371.70	123.08	C	21.6
N1578424849	2008-007-18:44	140514.04	121.56	-	-	O	21.6
N1578427113	2008-007-19:22	140295.46	123.39	140353.15	123.31	C	21.8
N1578427679	2008-007-19:31	140281.91	122.30	140333.04	122.24	C	21.8
N1578439565	2008-007-22:49	140339.67	125.69	140378.30	124.90	BH	22.7
N1578439848	2008-007-22:54	140363.52	125.58	140352.28	125.88	C	22.7
N1579792956	2008-023-14:46	-	-	140210.26	143.43	Co	42.7
N1579819522a	2008-023-22:08	140239.05	142.82	140209.56	142.84	C	44.6
N1579819522b	2008-023-22:08	140239.99	142.87	140220.71	142.90	C	44.6
N1579819522c	2008-023-22:08	140232.85	143.00	140223.52	143.02	C	44.6
N1579819522d	2008-023-22:08	140204.98	143.36	140223.90	143.34	C	44.6
N1579819881	2008-023-22:14	140178.96	142.77	140208.56	142.74	C	44.6
N1579821676	2008-023-22:44	-	-	140206.70	145.88	Co	44.9
N1579823471	2008-023-23:14	140184.28	145.45	140210.03	145.42	C	45.0
N1579831010	2008-024-01:20	140178.54	144.96	140214.42	144.91	C	45.5
N1581948682	2008-048-13:34	-	-	140538.98	313.86	Co	43.4
N1581955370	2008-048-15:26	140589.43	313.26	140560.55	313.27	C	44.0
N1581963312	2008-048-17:38	140571.37	313.91	140543.65	313.91	C	44.6
N1581965820	2008-048-18:20	-	-	140571.80	314.48	Co	44.7
N1581967910a	2008-048-18:55	140624.19	314.93	140559.07	314.96	C	44.9
N1581967910b	2008-048-18:55	140525.25	315.93	140537.71	315.83	C	44.8
N1581969164	2008-048-19:16	-	-	140541.08	314.09	Co	45.0
N1582552048	2008-055-13:10	140467.66	291.87	140521.81	290.47	C	23.9
N1582566906	2008-055-17:18	140469.78	289.82	140498.46	289.71	C	24.7
N1582588319	2008-055-23:15	140520.75	290.07	140503.27	290.22	C	26.0
N1582589630	2008-055-23:37	140470.72	291.10	140513.16	291.05	C	26.1

N1582599244	2008-056-02:17	140456.24	288.37	140492.02	288.29	C	26.7
N1584274022	2008-075-11:30	139988.44	116.12	-	-	O	13.0
N1584280862	2008-075-13:24	-	-	140149.25	115.44	Co	13.6
N1584282002	2008-075-13:43	140116.15	116.08	-	-	O	13.7
N1584283332	2008-075-14:05	140205.64	113.96	140181.60	114.06	C	13.8
N1584286942	2008-075-15:05	140009.03	115.75	140034.75	115.65	C	14.1
N1584288082	2008-075-15:24	-	-	140158.62	116.52	Co	14.2
N1584289412	2008-075-15:46	140197.47	115.46	140153.93	116.16	C	14.3
N1584294542	2008-075-17:12	140176.75	116.70	140145.70	116.84	C	14.8
N1584316392	2008-075-23:16	140183.52	116.75	140148.94	117.73	C	16.7
N1584316772	2008-075-23:22	-	-	140166.33	117.66	Co	16.7
N1586514693	2008-101-09:54	139909.40	265.75	139896.05	265.76	C	88.0
N1589096022	2008-131-06:56	139929.08	0.54	-	-	O	79.5
N1589115538	2008-131-12:21	140260.05	249.29	-	-	O	83.4
N1589117017	2008-131-12:46	140345.32	239.73	140334.35	239.74	C	83.0
N1589117591a	2008-131-12:55	140376.03	235.67	140338.23	235.76	C	82.7
N1589117591b	2008-131-12:55	140383.99	235.43	-	-	O	82.7
N1589117847	2008-131-12:59	140352.74	233.91	-	-	O	82.6
N1589117976	2008-131-13:01	-	-	140335.40	233.50	Co	82.4
N1589118555	2008-131-13:11	-	-	140357.99	229.87	Co	82.0
N1589118812	2008-131-13:15	-	-	140342.19	228.59	Co	81.8
N1589119327a	2008-131-13:24	-	-	140385.57	224.92	Co	81.3
N1589119327b	2008-131-13:24	140401.87	229.87	-	-	O	82.0
N1589120162	2008-131-13:38	140355.36	220.26	-	-	O	80.4
N1589598184	2008-137-02:25	140390.78	130.37	140445.84	130.25	C	45.8
N1589609758	2008-137-05:38	-	-	140449.24	133.04	Co	48.2
N1589614902a	2008-137-05:38	140460.31	134.50	140449.90	134.50	C	49.3
N1589614902b	2008-137-07:04	140428.17	134.32	140440.79	134.31	C	49.3
N1589614902c	2008-137-07:04	140418.36	133.89	140434.14	133.89	C	49.3
N1589614902d	2008-137-07:04	140134.39	134.90	140190.47	133.79	BH	49.3
N1589616188	2008-137-07:25	-	-	140433.18	136.26	Co	49.7
N1589620046a	2008-137-08:29	140399.67	137.86	140448.10	137.76	C	50.6
N1589620046b	2008-137-08:29	-	-	140449.31	133.91	Co	50.6
N1589625190	2008-137-09:55	140418.06	136.84	140441.99	136.83	C	51.7
N1589626476	2008-137-10:17	140420.11	137.63	140453.44	137.56	C	52.0
N1589638050a	2008-137-13:29	140498.11	139.03	140484.41	139.04	C	54.9
N1589638050b	2008-137-13:29	140496.51	138.96	140478.62	138.98	C	54.9
N1589639336	2008-137-13:51	140508.09	140.96	140478.53	140.97	C	55.4
N1590848295	2008-151-13:40	140330.76	158.32	140371.62	158.20	C	31.7
N1593917852	2008-187-02:19	140385.81	119.45	-	-	O	29.2
N1593921457	2008-187-03:19	139870.05	120.68	139902.67	120.66	C	29.7
N1593923002	2008-187-03:45	139857.05	121.51	-	-	O	30.0
N1593929182	2008-187-05:28	139860.62	119.69	-	-	O	30.7
N1593933817	2008-187-06:45	139873.38	121.78	139909.87	121.74	BH	31.4

N1593940512	2008-187-08:37	139878.45	120.79	139902.54	120.73	C	32.3
N1593942057	2008-187-09:02	139884.70	121.40	-	-	O	32.6
N1593943602a	2008-187-09:28	139884.89	123.74	-	-	O	32.9
N1593943602b	2008-187-09:28	139926.71	122.47	139902.06	123.06	C	34.1
N1593952357	2008-187-11:54	139874.79	123.18	-	-	O	34.2
N1593952872	2008-187-12:03	-	-	139903.56	123.52	Co	34.3
N1593964202	2008-187-15:11	139872.82	122.07	-	-	O	35.3
N1595325557	2008-203-09:21	140530.80	355.97	-	-	O	101.8
N1595325677a	2008-203-09:23	-	-	140544.44	355.95	Co	102.3
N1595325677b	2008-203-09:23	-	-	140540.85	356.03	Co	102.2
N1595325997	2008-203-09:28	-	-	140532.28	355.99	Co	103.6
N1595326037	2008-203-09:29	140551.33	356.03	-	-	O	103.7
N1595329125	2008-203-10:20	-	-	140391.34	356.01	Co	123.2
N1595501977	2008-205-10:21	140191.43	101.05	140171.69	101.07	C	13.4
N1595503327	2008-205-10:43	-	-	140190.87	100.29	Co	13.3
N1595504452	2008-205-11:02	140157.23	103.15	140168.22	103.11	C	13.2
N1596423029	2008-216-02:12	139810.24	216.50	139822.16	216.48	C	56.3
N1596427925	2008-216-03:33	-	-	139895.14	216.13	Co	58.0
N1596428660a	2008-216-03:46	139877.06	217.02	139889.58	217.03	C	58.2
N1596428660b	2008-216-03:46	139895.52	217.18	139889.65	217.18	C	58.2
N1596429640a	2008-216-04:02	139914.41	216.42	139892.40	216.44	C	58.6
N1596429640b	2008-216-04:02	139914.84	216.89	139887.56	216.90	C	58.6
N1596429640c	2008-216-04:02	-	-	139896.57	217.42	Co	58.6
N1596430130	2008-216-04:10	-	-	139892.54	216.65	Co	58.7
N1596431600	2008-216-04:35	-	-	139881.89	217.01	Co	59.2
N1596432090	2008-216-04:43	-	-	139834.78	217.15	Co	59.4
N1596433070	2008-216-04:59	139891.50	216.88	139870.22	216.89	C	59.8
N1596435765	2008-216-05:44	-	-	139910.50	216.13	Co	60.8
N1596436255	2008-216-05:52	139867.75	216.50	139880.83	216.53	C	61.0
N1596437725	2008-216-06:17	-	-	139887.30	216.41	Co	61.5
N1596439195	2008-216-06:41	139868.31	216.68	139892.34	216.66	C	62.1
N1596447770	2008-216-09:04	139867.29	216.22	139896.51	216.18	BH	65.6
N1596451690a	2008-216-10:09	139882.47	216.93	139895.30	216.92	C	67.4
N1596451690b	2008-216-10:09	139887.81	216.98	139895.75	216.97	C	67.4
N1596682272a	2008-219-02:12	140137.05	149.70	-	-	O	27.4
N1596682272b	2008-219-02:12	-	-	140095.88	150.94	Co	27.4
N1596689037a	2008-219-04:05	-	-	140098.70	150.65	Co	25.9
N1596689037b	2008-219-04:05	-	-	140093.33	150.82	Co	26.0
N1596689242a	2008-219-04:09	140007.29	150.84	140026.95	150.85	C	25.9
N1596689242b	2008-219-04:09	140009.59	150.92	-	-	O	25.9
N1596690062	2008-219-04:22	-	-	140009.98	150.65	Co	25.7
N1596710562	2008-219-10:04	140070.18	150.98	140109.36	150.99	C	21.8
N1596711587	2008-219-10:21	-	-	140106.33	150.55	Co	21.6
N1597394201	2008-227-07:58	140490.56	106.69	140466.36	107.23	C	14.6

N1597396028	2008-227-08:28	140546.25	107.33	140448.06	107.49	BH	14.5
N1597402118	2008-227-10:10	140424.85	109.58	140478.56	109.35	BH	14.3
N1597886915	2008-233-00:50	140565.46	106.04	-	-	O	46.8
N1597890485a	2008-233-01:49	-	-	140506.12	106.89	Co	45.1
N1597890485b	2008-233-01:49	-	-	140502.43	106.56	Co	45.0
N1597892375	2008-233-02:21	140486.28	106.33	-	-	O	44.0
N1597892795	2008-233-02:28	140472.46	105.82	140503.28	105.77	BH	43.7
N1597893425	2008-233-02:38	140568.41	105.69	140532.04	105.76	C	43.4
N1597894685	2008-233-02:59	140474.39	105.94	140519.75	105.88	C	42.9
N1597897625	2008-233-03:48	140485.61	105.92	-	-	O	41.5
N1597898045	2008-233-03:55	140555.14	105.86	-	-	O	41.3
N1597899305	2008-233-04:16	140484.67	106.53	-	-	O	40.8
N1597901825a	2008-233-04:58	140543.54	106.17	140527.19	106.22	C	39.7
N1597901825b	2008-233-04:58	140504.44	106.69	-	-	O	39.8
N1597902245a	2008-233-05:05	140476.44	106.35	140532.01	106.19	C	39.5
N1597902245b	2008-233-05:05	140487.55	106.56	140531.17	106.33	C	39.5
N1597902245c	2008-233-05:05	140483.43	106.72	140528.25	106.46	C	39.5
N1597902665	2008-233-05:12	140628.63	106.49	-	-	O	39.4
N1597903295	2008-233-05:23	140597.32	106.25	-	-	O	39.1
N1597903925	2008-233-05:33	140529.89	105.69	-	-	O	38.8
N1597904975a	2008-233-05:51	140543.02	106.57	140525.26	106.52	C	38.5
N1597904975b	2008-233-05:51	140549.39	106.31	140522.74	106.43	C	38.4
N1597905815a	2008-233-06:05	140503.97	106.44	140529.12	106.39	C	38.1
N1597905815b	2008-233-06:05	140488.11	106.37	-	-	O	38.1
N1597906445a	2008-233-06:15	140558.25	105.90	140536.65	106.03	C	37.8
N1597906445b	2008-233-06:15	140481.00	106.40	-	-	O	37.6
N1597907075	2008-233-06:26	140492.33	104.68	-	-	O	37.4
N1597907285a	2008-233-06:29	140441.87	107.42	-	-	O	37.5
N1597907285b	2008-233-06:29	140484.91	106.52	140506.78	106.39	C	37.5
N1597907285c	2008-233-06:29	140484.91	106.52	-	-	O	37.5
N1597907705	2008-233-06:36	140541.23	105.27	140506.69	105.29	C	37.3
N1597910645	2008-233-07:25	140472.81	106.37	-	-	O	36.3
N1597910855	2008-233-07:29	140556.44	106.36	140537.83	106.54	C	36.2
N1597916735	2008-233-09:07	140474.17	106.25	-	-	O	34.2
N1597916945	2008-233-09:10	-	-	140482.38	106.19	Co	34.1
N1597919045	2008-233-09:45	-	-	140503.74	107.21	Co	33.5
N1597919255	2008-233-09:49	140566.40	104.53	-	-	O	33.2
N1597921145	2008-233-10:20	140494.76	106.83	140536.57	106.74	BH	32.8
N1597921565	2008-233-10:27	140487.45	106.52	-	-	O	32.7
N1597921775	2008-233-10:31	140579.69	107.09	-	-	O	32.7
N1597933115	2008-233-13:40	-	-	140507.04	108.24	Co	29.5
N1598806665	2008-243-16:19	140585.83	110.63	-	-	O	20.8
N1598808971	2008-243-16:57	140604.39	113.77	140559.80	113.85	C	21.1
N1598811701	2008-243-17:43	140530.86	117.96	-	-	O	21.5

N1598811911	2008-243-17:46	-	-	140550.74	114.16	Co	21.5
N1598812121	2008-243-17:50	140668.98	110.73	-	-	O	21.4
N1598818001	2008-243-19:28	140577.99	119.14	-	-	O	22.3
N1598818841	2008-243-19:42	140575.64	117.53	140539.65	117.65	C	22.3
N1598819051a	2008-243-19:45	140503.78	112.53	140535.63	112.58	C	22.2
N1598819051b	2008-243-19:45	140507.93	112.82	-	-	O	22.2
N1598829341	2008-243-22:37	140596.59	115.52	140562.18	115.62	C	23.5
N1598829971	2008-243-22:47	140595.12	115.66	140569.75	115.83	C	23.5
N1598839211	2008-244-01:21	140530.75	116.16	-	-	O	24.7
N1598840681	2008-244-01:46	-	-	140527.90	114.07	Co	24.8
N1598841731	2008-244-02:03	140561.17	116.00	-	-	O	25.0
N1598841941	2008-244-02:07	-	-	140549.28	116.13	Co	25.0
N1598850551	2008-244-04:30	140603.38	116.32	140568.19	116.36	C	26.1
N1598851181	2008-244-04:41	140543.66	115.17	140554.36	114.90	C	26.2
N1600213404	2008-259-23:04	140500.96	128.34	-	-	O	41.4
N1600213830	2008-259-23:11	140558.62	128.96	140518.01	128.99	C	41.6
N1600214895	2008-259-23:29	140498.23	127.49	140525.06	127.47	C	41.7
N1600219794	2008-260-00:51	140674.98	128.01	-	-	O	42.9
N1600220007	2008-260-00:54	140665.48	129.44	-	-	O	43.0
N1600221285	2008-260-01:15	140566.20	128.94	140535.04	128.96	C	43.3
N1600221924	2008-260-01:26	140444.27	128.10	-	-	O	43.3
N1600222350	2008-260-01:33	140498.10	128.65	-	-	O	43.5
N1600226397a	2008-260-02:41	140470.00	128.43	-	-	O	44.4
N1600227249a	2008-260-02:41	140526.79	130.00	140541.31	129.98	C	44.8
N1600227249b	2008-260-02:55	140599.97	127.81	140546.21	128.52	C	44.8
N1600232148	2008-260-04:17	140538.04	128.24	140521.62	128.27	C	45.8
N1600232361	2008-260-04:20	140502.53	128.59	140524.13	128.58	C	45.9
N1600232574	2008-260-04:24	140614.44	127.97	-	-	O	45.9
N1600233852	2008-260-04:45	140593.34	128.33	140533.64	128.35	BH	46.2
N1600234065a	2008-260-04:48	140497.46	129.17	140529.18	129.14	C	46.4
N1600234065b	2008-260-04:48	140483.26	128.26	140506.19	128.20	C	47.4
N1600234491a	2008-260-04:48	140543.10	128.49	140521.12	128.52	C	46.4
N1600234491b	2008-260-04:48	140541.64	128.29	140519.33	128.33	C	46.4
N1600234491c	2008-260-04:56	140545.79	128.14	140518.08	128.17	C	46.4
N1600235343	2008-260-05:10	140481.70	128.48	140516.80	128.37	C	46.6
N1600239816	2008-260-06:24	140298.58	128.88	-	-	O	47.9
N1601485634	2008-274-16:28	140231.24	285.12	-	-	O	44.8
N1601486840	2008-274-16:48	140238.50	285.31	140200.07	285.92	C	45.0
N1601488050	2008-274-17:08	140262.64	284.48	140210.21	284.54	BH	45.3
N1601492164	2008-274-18:17	140128.99	285.26	140092.42	285.60	C	46.0
N1601502328	2008-274-21:06	139855.83	285.39	-	-	O	48.1
N1601508620	2008-274-22:51	140249.66	285.95	140208.34	286.01	C	49.5
N1601508862	2008-274-22:55	140000.44	286.27	-	-	O	49.5
N1601511040	2008-274-23:31	140256.63	286.12	140215.88	286.17	BH	50.0

N1601511282	2008-274-23:35	140142.98	285.94	140109.23	286.38	C	50.1
N1601512734	2008-274-23:59	-	-	140209.91	285.46	Co	50.5
N1601513944	2008-275-00:20	140236.62	286.14	140201.09	286.18	C	50.7
N1601516848a	2008-275-01:08	140202.72	285.64	140218.22	285.65	C	51.5
N1601516848b	2008-275-01:08	-	-	140210.69	285.97	Co	51.4
N1601516848c	2008-275-01:08	140291.28	286.13	-	-	O	51.4
N1601606582	2008-276-02:04	-	-	140143.62	299.55	Co	99.3
N1601607555	2008-276-02:20	140158.42	299.46	140152.18	299.55	C	100.8
N1602719343a	2008-288-23:09	140295.64	283.57	140276.73	283.59	C	39.3
N1602719343b	2008-288-23:09	140291.12	283.69	140278.27	283.69	C	39.3
N1602720801	2008-288-23:34	140255.61	282.17	140277.29	282.12	C	39.6
N1602725904	2008-289-00:59	-	-	140424.31	282.04	Co	40.3
N1602727119	2008-289-01:19	140469.13	283.97	140420.86	284.06	C	40.4
N1602731007	2008-289-02:24	140474.77	283.54	140418.83	283.59	C	41.0
N1602734409	2008-289-03:21	-	-	140419.09	283.40	Co	41.5
N1602734895	2008-289-03:29	140419.50	284.14	140407.61	284.17	C	41.5
N1602735138	2008-289-03:33	140438.13	283.94	140419.66	283.93	C	41.6
N1602738054	2008-289-04:21	-	-	140434.63	284.36	Co	42.0
N1602739026a	2008-289-04:38	140336.73	284.19	140312.66	284.21	C	42.2
N1602739026b	2008-289-04:38	140336.15	284.13	140312.04	284.15	C	42.2
N1602739755	2008-289-04:50	140477.52	284.24	140459.73	284.26	C	42.3
N1602742185a	2008-289-05:30	140461.38	284.82	140433.19	284.88	C	42.7
N1602742185b	2008-289-05:30	-	-	140417.73	285.21	Co	42.6
N1602745587	2008-289-06:27	140437.86	283.97	-	-	O	43.3
N1602746802	2008-289-06:47	140451.69	283.76	140433.19	283.81	C	43.5
N1602751662	2008-289-08:08	140493.51	284.15	140434.54	284.23	C	44.3
N1602752877a	2008-289-08:08	140422.03	285.13	140444.19	285.09	C	44.5
N1602752877b	2008-289-08:28	-	-	140452.99	285.47	Co	44.5
N1602753120	2008-289-08:32	140471.57	283.74	140435.42	283.79	C	44.6
N1602753363	2008-289-08:36	140463.21	283.70	-	-	O	44.7
N1602754092a	2008-289-08:49	140472.30	283.99	140443.10	284.00	BH	44.8
N1602754092b	2008-289-08:49	140473.38	283.93	140449.56	283.97	BH	44.8
N1602754092c	2008-289-08:49	140475.06	283.86	140444.99	283.91	BH	44.8
N1602758466	2008-289-10:02	-	-	140427.79	284.00	Co	45.6
N1603489199	2008-297-21:00	140496.59	254.44	-	-	O	93.1
N1603489547	2008-297-21:06	140577.00	254.41	140541.56	254.53	C	93.5
N1603491983	2008-297-21:47	139878.39	254.66	-	-	O	96.0
N1603492425	2008-297-21:54	139878.08	255.13	-	-	O	96.3
N1603493295	2008-297-22:09	139881.23	255.14	-	-	O	97.3
N1603493991	2008-297-22:20	139890.92	254.62	-	-	O	98.2
N1603496333	2008-297-22:59	140530.01	254.91	140574.84	254.57	C	101.0
N1603502075	2008-298-00:35	140598.48	254.37	140568.33	254.40	C	108.7
N1604009928	2008-303-21:39	-	-	140339.32	199.12	Co	44.6
N1604011524a	2008-303-22:06	140292.67	198.20	140320.52	198.09	C	44.9

N1604011524b	2008-303-22:06	140289.51	198.05	140311.48	198.00	C	44.9
N1604015172	2008-303-23:06	140206.96	198.17	-	-	O	45.7
N1604023152	2008-304-01:19	-	-	140325.25	199.36	Co	47.7
N1604025432	2008-304-01:57	140232.50	198.64	140346.64	198.55	BH	48.3
N1604026572	2008-304-02:16	140245.13	198.42	-	-	O	48.6
N1604027028	2008-304-02:24	140271.90	198.56	-	-	O	48.7
N1604028396	2008-304-02:47	140361.13	198.65	140341.35	198.65	C	49.1
N1604028624	2008-304-02:51	140311.86	198.42	-	-	O	49.1
N1604030448	2008-304-03:21	140289.02	198.83	-	-	O	49.6
N1604038884a	2008-304-05:42	140356.46	198.08	140335.72	198.10	C	52.0
N1604038884b	2008-304-05:42	-	-	140331.82	198.97	Co	52.0
N1604038884c	2008-304-05:42	140318.06	199.53	140331.10	199.52	C	52.0
N1604039340a	2008-304-05:49	140352.28	198.26	140320.75	198.30	C	52.1
N1604039340b	2008-304-05:49	140140.35	198.41	-	-	O	52.1
N1604040024	2008-304-06:01	140361.53	198.63	-	-	O	52.3
N1604040252	2008-304-06:04	140288.37	198.58	140301.50	198.56	C	52.4
N1604720757	2008-312-03:06	140650.12	301.78	-	-	O	49.1
N1604721303	2008-312-03:15	140593.58	301.90	140556.27	301.95	C	49.2
N1604723103	2008-312-03:45	-	-	140517.18	301.97	Co	49.5
N1604725303	2008-312-04:22	140570.80	302.19	140545.65	302.20	C	49.9
N1604725553	2008-312-04:26	-	-	140535.90	302.41	Co	49.9
N1604725653	2008-312-04:28	-	-	140561.67	302.14	Co	50.0
N1604726853	2008-312-04:48	140605.31	302.11	140528.72	302.14	BH	50.2
N1604727053	2008-312-04:51	-	-	140548.79	301.36	Co	50.3
N1604730253	2008-312-05:44	140595.17	302.03	-	-	O	50.9
N1604809621	2008-313-03:47	140350.38	241.75	-	-	O	88.9
N1604816005	2008-313-05:34	140526.13	241.91	-	-	O	93.8
N1605368928	2008-319-15:09	139797.50	126.75	-	-	O	40.2
N1605369778	2008-319-15:23	139867.25	127.06	-	-	O	40.4
N1605375558	2008-319-16:59	-	-	139896.43	127.06	Co	41.3
N1605383718a	2008-319-19:15	139857.42	129.26	139895.16	129.24	C	42.9
N1605383718b	2008-319-19:15	-	-	139897.39	129.07	Co	42.9
N1605390518	2008-319-21:09	-	-	139877.45	130.06	Co	44.2
N1605392388	2008-319-21:40	139877.15	129.46	139895.93	129.46	C	44.5
N1605393238	2008-319-21:54	139865.86	130.20	139890.78	130.19	C	44.8
N1605396128a	2008-319-22:42	139882.93	130.75	139913.79	130.73	C	45.4
N1605396128b	2008-319-22:42	139870.33	130.66	139913.65	130.64	C	45.4
N1605396298	2008-319-22:45	139859.17	131.09	-	-	O	45.4
N1605531275	2008-321-12:15	-	-	140547.14	324.80	Co	96.9
N1605531856	2008-321-12:24	-	-	140535.72	324.86	Co	97.6
N1605531939	2008-321-12:26	140598.13	324.78	-	-	O	97.7
N1605535342	2008-321-13:22	-	-	140565.67	324.54	Co	102.5
N1606006222	2008-327-00:10	139906.16	122.20	139933.38	122.19	C	37.9
N1606031442	2008-327-07:11	140482.16	303.20	140505.57	303.16	C	45.4

N1606032022	2008-327-07:20	-	-	140517.17	302.02	Co	45.6
N1606033182	2008-327-07:40	140614.83	304.06	140507.07	304.11	BH	45.7
N1606033762	2008-327-07:49	140527.33	302.15	140512.00	302.23	C	45.9
N1607469729	2008-343-22:42	139865.69	207.45	139882.05	207.43	C	93.5
N1607473453	2008-343-23:44	-	-	139905.04	207.15	Co	96.4
N1607483253	2008-344-02:27	140024.64	207.35	-	-	O	104.8
N1607485115	2008-344-02:58	139849.76	207.64	-	-	O	106.5
N1607486487	2008-344-03:21	139828.55	207.38	-	-	O	107.7
N1607625791	2008-345-18:03	140101.40	135.38	-	-	O	73.8
N1607628707a	2008-345-18:52	140090.69	135.56	140081.46	135.57	C	72.1
N1607628707b	2008-345-18:52	140091.39	135.52	140080.30	135.53	C	72.1
N1607629355a	2008-345-19:02	140094.54	136.06	140090.25	136.09	C	71.9
N1607629355b	2008-345-19:02	140110.74	135.59	140095.46	135.70	C	71.8
N1607629517	2008-345-19:05	140077.65	135.97	140095.03	135.97	C	71.7
N1607629679	2008-345-19:08	140095.27	135.25	-	-	O	71.5
N1607630003	2008-345-19:13	140088.91	135.20	140105.26	135.19	C	71.3
N1607630813	2008-345-19:27	-	-	140117.56	135.74	Co	71.0
N1607633081	2008-345-20:05	-	-	140103.41	136.02	Co	69.8
N1607636159	2008-345-20:56	140085.51	136.08	140098.35	135.97	C	68.2
N1607638265	2008-345-21:31	140105.41	136.08	-	-	O	67.1
N1607645393	2008-345-23:30	140094.90	136.10	-	-	O	63.6
N1607648957	2008-346-00:29	140109.36	135.44	140096.39	135.52	C	61.8
N1607665643	2008-346-05:07	140079.33	135.95	140096.07	135.94	C	55.0
N1610370206	2009-011-12:23	140596.39	125.75	140549.35	125.79	C	37.6
N1610371543	2009-011-12:45	140601.24	127.33	140556.51	127.37	C	38.0
N1610373453a	2009-011-13:17	-	-	140565.19	129.21	Co	38.6
N1610373453b	2009-011-13:17	140617.70	126.95	140547.30	127.00	C	38.4
N1610373453c	2009-011-13:30	140584.44	126.37	140551.87	126.39	C	38.6
N1610374217	2009-011-13:30	140577.00	126.22	140550.83	126.23	C	38.6
N1610374408	2009-011-13:33	-	-	140549.83	126.76	Co	38.7
N1610375554	2009-011-13:52	140609.49	128.60	140542.65	128.64	C	39.1
N1610377655	2009-011-14:27	140510.58	127.84	-	-	O	39.5
N1610381093	2009-011-15:24	140515.94	127.76	-	-	O	40.4
N1610385486a	2009-011-16:38	140495.00	129.76	140512.41	129.75	C	41.6
N1610385486b	2009-011-16:38	140501.25	129.68	140518.97	129.67	C	41.6
N1610387205	2009-011-17:06	-	-	140331.71	129.53	Co	42.0
N1610387587	2009-011-17:13	140540.79	131.24	-	-	O	42.3
N1610390452	2009-011-18:00	140510.03	131.19	-	-	O	43.0
N1610391789	2009-011-18:23	140487.74	131.09	-	-	O	43.4
N1610394081	2009-011-19:01	140580.73	131.68	-	-	O	44.0
N1610401148a	2009-011-20:59	140522.44	132.98	140535.85	132.96	C	46.0
N1610401148b	2009-011-20:59	140471.98	132.84	140534.84	132.77	C	46.0
N1610401339	2009-011-21:02	140463.77	133.67	140527.83	133.61	C	46.2
N1610403822	2009-011-21:43	140543.58	133.94	140516.11	133.98	C	46.9

N1610584086	2009-013-23:48	-	-	139905.53	285.43	Co	143.3
N1610591166	2009-014-01:46	140093.95	287.42	-	-	O	149.5
N1610593686	2009-014-02:28	140078.12	288.38	-	-	O	151.6
N1610595366	2009-014-02:56	139969.90	288.92	-	-	O	153.1
N1610598606	2009-014-03:50	140388.33	289.96	-	-	O	155.9
N1610598966	2009-014-03:56	140390.70	289.71	-	-	O	156.2
N1610600046	2009-014-04:14	140394.64	290.86	-	-	O	157.1
N1610600166	2009-014-04:16	140389.87	290.53	-	-	O	157.2
N1612005469	2009-030-10:37	140540.26	128.88	140484.10	128.93	C	33.7
N1612969737	2009-041-14:28	140466.78	168.43	140536.18	168.37	C	69.9
N1612970258	2009-041-14:37	140483.54	167.96	140499.76	167.89	C	70.0
N1612970958	2009-041-14:49	140466.14	168.25	140504.45	167.94	C	70.2
N1612980233a	2009-041-17:23	140465.66	173.86	-	-	O	73.2
N1612980233b	2009-041-17:23	-	-	140540.78	173.53	Co	73.2
N1612980233c	2009-041-17:23	-	-	140533.99	173.44	Co	73.2
N1612980583	2009-041-17:29	140297.04	174.61	-	-	O	73.3
N1612982333	2009-041-17:58	140607.00	175.70	-	-	O	73.9
N1612984608	2009-041-18:36	140538.63	177.27	-	-	O	74.6
N1612984958	2009-041-18:42	140526.65	176.93	-	-	O	74.7
N1612986008	2009-041-18:59	140540.28	177.43	-	-	O	75.0
N1612986183a	2009-041-19:02	140524.28	178.16	140539.95	178.13	C	75.2
N1612986183b	2009-041-19:02	140549.05	177.39	-	-	O	75.1
N1612987758a	2009-041-19:29	-	-	140560.31	179.06	Co	75.7
N1612987758b	2009-041-19:29	-	-	140534.59	179.16	Co	75.7
N1612987758c	2009-041-19:29	-	-	140552.52	178.95	Co	75.7
N1612987933a	2009-041-19:31	140584.58	178.90	140535.12	178.93	C	75.7
N1612987933b	2009-041-19:31	140569.42	178.69	140530.30	178.71	C	75.7
N1612989683a	2009-041-20:01	140560.33	180.42	140526.83	180.46	C	76.3
N1612989683b	2009-041-20:01	140585.69	180.01	140535.14	180.06	C	76.3
N1612991433	2009-041-20:30	140485.65	181.15	140523.57	181.02	C	76.9
N1612994408a	2009-041-21:19	140577.70	183.57	140555.26	183.96	C	77.9
N1612994408b	2009-041-21:19	140509.43	183.54	-	-	O	77.9
N1612997648a	2009-041-22:13	140602.21	185.38	140562.94	185.39	C	78.9
N1612997648b	2009-041-22:13	140588.43	185.27	140553.79	185.27	C	78.9
N1612998373	2009-041-22:25	140598.22	186.86	140540.73	186.89	C	79.2
N1613000473	2009-041-23:00	140581.56	188.52	-	-	O	79.9
N1613001523	2009-041-23:18	140605.26	188.34	140570.75	188.66	C	80.2
N1613002923	2009-041-23:41	140349.34	189.14	-	-	O	80.7
N1613003098	2009-041-23:44	140613.69	189.09	140567.30	189.11	C	80.7
N1613003273	2009-041-23:47	140508.26	190.62	140545.08	190.58	C	80.9
N1614216471	2009-056-00:47	140386.63	280.28	140434.66	280.19	C	143.9
N1614218231	2009-056-01:16	140399.15	281.01	140445.08	280.92	C	144.6
N1614218451	2009-056-01:20	140391.04	279.68	140430.12	278.71	C	144.7
N1614219771	2009-056-01:42	140496.80	279.17	140435.35	279.28	C	145.3

N1614219991	2009-056-01:46	140457.79	281.56	140420.98	281.60	C	145.3
N1614220211	2009-056-01:49	140511.75	280.87	140432.04	280.99	C	145.4
N1614857435	2009-063-10:50	140470.31	284.41	-	-	O	34.2
N1614857913	2009-063-10:58	-	-	140508.58	285.40	Co	34.3
N1614858630	2009-063-11:09	140540.38	285.39	140502.27	285.52	C	34.3
N1614858869	2009-063-11:13	-	-	140493.98	285.94	Co	34.3
N1614865800	2009-063-13:09	140529.98	286.57	-	-	O	34.9
N1615467346	2009-070-12:15	-	-	140074.78	148.00	Co	111.6
N1615468963	2009-070-12:42	-	-	139984.90	150.14	Co	111.2
N1615469887	2009-070-12:57	-	-	140073.14	150.92	Co	110.9
N1615483516	2009-070-16:44	140102.57	163.26	140122.88	163.26	C	107.4
N1615485364	2009-070-17:15	140156.33	164.53	140136.28	164.53	C	106.9
N1615488367	2009-070-18:05	140090.09	167.97	140135.01	167.94	C	106.2
N1615488598	2009-070-18:09	-	-	140105.82	168.35	Co	106.1
N1615489291	2009-070-18:20	-	-	140136.55	168.07	Co	105.8
N1615491601	2009-070-18:59	140129.13	170.09	140156.54	170.07	C	105.2
N1615492756	2009-070-19:18	-	-	140176.43	171.64	Co	104.9
N1615495066	2009-070-19:57	-	-	140168.10	172.98	Co	104.2
N1615495297	2009-070-20:01	-	-	140166.73	174.63	Co	104.3
N1615498300a	2009-070-20:51	-	-	140190.65	177.54	Co	103.5
N1615498300b	2009-070-20:51	-	-	140195.64	177.39	Co	103.5
N1615498300c	2009-070-20:51	-	-	140191.01	177.22	Co	103.5
N1615503382	2009-070-22:15	140195.81	182.17	140220.90	182.15	C	102.1
N1615506616	2009-070-23:09	140187.08	186.28	140231.52	186.25	C	101.2
N1615511698	2009-071-00:34	140218.07	191.11	140283.87	191.08	C	99.7
N1616505395	2009-082-12:35	140207.67	151.28	139957.70	151.40	C	110.9
N1616506283	2009-082-12:50	140308.13	151.68	-	-	O	110.7
N1616507837a	2009-082-13:16	140392.84	153.03	-	-	O	110.3
N1616507837b	2009-082-13:16	140348.02	153.47	-	-	O	110.3
N1616523599a	2009-082-17:39	139920.25	168.41	-	-	O	106.3
N1616523599b	2009-082-17:39	139924.97	168.32	-	-	O	106.3
N1616524487	2009-082-17:54	140017.61	168.95	139984.56	168.97	C	106.0
N1616529149	2009-082-19:11	139980.76	173.43	-	-	O	104.8
N1616532479	2009-082-20:07	-	-	140037.20	177.47	Co	103.9
N1616539583	2009-082-22:05	140326.07	183.78	-	-	O	101.9
N1616541581	2009-082-22:38	140061.19	186.11	140103.19	186.10	C	101.4
N1616543135a	2009-082-23:04	139987.00	187.55	-	-	O	100.9
N1616543135b	2009-082-23:04	-	-	140053.37	187.10	Co	100.9
N1616543357	2009-082-23:08	140102.10	187.32	-	-	O	100.9
N1617040240	2009-088-17:09	140355.66	151.76	-	-	O	55.2
N1617044815	2009-088-18:26	-	-	139891.69	152.29	Co	56.3
N1617050122	2009-088-19:54	139889.68	155.38	139911.49	155.35	C	57.8
N1618581563	2009-106-13:18	140045.27	241.09	140022.68	241.15	C	102.7
N1618591933	2009-106-16:11	140035.84	244.18	-	-	O	104.7

N1618599753	2009-106-18:21	140013.47	246.78	140043.15	246.70	C	106.2
N1618601283	2009-106-18:47	140180.71	246.87	-	-	O	106.5
N1618603153	2009-106-19:18	-	-	140043.28	245.78	Co	106.9
N1620641087	2009-130-09:23	-	-	139802.32	251.01	Co	65.8
N1620642842	2009-130-09:52	139862.57	252.19	139880.78	252.18	C	65.1
N1620646157a	2009-130-10:48	139939.95	253.46	-	-	O	63.9
N1620646157b	2009-130-10:48	139860.43	253.20	139874.43	253.12	C	63.9
N1620646157c	2009-130-10:48	139860.83	253.03	139875.77	252.97	C	63.9
N1620651617	2009-130-12:19	140051.54	254.14	-	-	O	62.0
N1620663902	2009-130-15:43	139877.64	258.01	-	-	O	57.6
N1622023663	2009-146-09:26	-	-	139922.42	275.09	Co	38.0
N1622025992	2009-146-10:05	-	-	139912.47	275.53	Co	37.6
N1622032568	2009-146-11:54	140005.01	274.51	-	-	O	36.4
N1622035719	2009-146-12:47	139884.11	269.62	139909.30	269.54	C	35.8
N1622044761	2009-146-15:17	139847.71	274.78	139892.79	274.69	BH	34.8
N1623224391a	2009-160-06:58	140422.45	108.10	140438.09	108.09	C	95.0
N1623224391b	2009-160-06:58	140477.78	107.92	140444.69	107.94	C	94.9
N1623224706a	2009-160-07:03	140469.86	107.76	140440.39	107.80	C	94.6
N1623224706b	2009-160-07:03	140456.03	107.61	140439.36	107.71	C	94.6
N1623225651a	2009-160-07:19	-	-	140441.24	108.64	Co	93.9
N1623225651b	2009-160-07:19	-	-	140445.33	107.96	Co	93.8
N1623225861	2009-160-07:22	-	-	140446.47	107.85	Co	93.5
N1623226176	2009-160-07:28	140395.14	108.11	-	-	O	93.3
N1623226701	2009-160-07:36	-	-	140453.86	107.81	Co	92.7
N1623227646a	2009-160-07:52	140399.77	108.63	-	-	O	92.0
N1623227646b	2009-160-07:52	140393.49	108.52	-	-	O	92.0
N1623227856	2009-160-07:56	139903.57	108.00	-	-	O	91.7
N1623228066	2009-160-07:59	140498.79	107.73	140462.04	107.75	C	91.4
N1623228591	2009-160-08:08	-	-	140461.39	108.52	Co	91.1
N1623282318	2009-160-23:03	140437.61	161.91	-	-	O	48.9
N1623284964	2009-160-23:47	140633.23	162.34	140568.73	162.46	C	46.4
N1623287218	2009-161-00:25	139888.46	161.59	-	-	O	44.0
N1623328380a	2009-161-11:51	140437.74	123.09	140469.73	123.07	BH	17.2
N1623328380b	2009-161-11:51	140533.11	121.32	140490.94	121.35	C	17.2
N1623328380c	2009-161-11:51	140467.58	121.06	140489.16	120.93	C	17.2
N1623329280d	2009-161-12:06	140234.30	112.88	-	-	O	17.1
N1623330636a	2009-161-12:29	140456.17	120.08	140467.86	120.01	C	17.2
N1623330636b	2009-161-12:29	140447.39	118.90	140466.02	118.89	C	17.1
N1623330636c	2009-161-12:29	-	-	140459.04	116.79	Co	17.1
N1623331766a	2009-161-12:47	140451.06	119.64	140469.61	119.63	C	17.2
N1623331766b	2009-161-12:47	140490.01	118.12	140474.22	118.26	C	17.2
N1623331766c	2009-161-12:47	140534.87	117.72	140480.81	117.91	C	17.2
N1623331766d	2009-161-12:47	-	-	140460.76	115.25	Co	17.1
N1623331766e	2009-161-12:47	-	-	140460.50	114.39	Co	17.1

N1623331766f	2009-161-12:47	140471.40	113.29	140453.87	113.35	C	17.1
N1623332218a	2009-161-12:55	140423.34	114.55	140451.60	114.46	C	17.2
N1623332218b	2009-161-12:55	140490.37	114.10	140451.95	114.21	C	17.1
N1623332896a	2009-161-13:06	140490.52	116.45	140458.44	116.51	C	17.2
N1623332896b	2009-161-13:06	140478.77	116.28	140459.66	116.43	C	17.2
N1623332896c	2009-161-13:06	140484.34	115.19	140458.52	115.38	C	17.2
N1623333348a	2009-161-13:14	-	-	140446.95	114.13	Co	17.2
N1623333348b	2009-161-13:14	-	-	140447.74	113.66	Co	17.2
N1623334704	2009-161-13:36	-	-	140468.54	119.24	Co	17.4
N1623335156a	2009-161-13:44	140427.84	122.39	140439.81	122.38	C	17.6
N1623335156b	2009-161-13:44	-	-	140468.62	118.22	Co	17.4
N1623335834	2009-161-13:55	-	-	140444.26	118.34	Co	17.5
N1623336512	2009-161-14:07	140537.89	117.97	140495.26	118.01	C	17.6
N1623336964a	2009-161-14:14	140513.47	118.32	140471.17	118.32	C	17.7
N1623336964b	2009-161-14:14	-	-	140451.23	117.39	Co	17.6
N1623338094a	2009-161-14:33	-	-	140471.94	118.29	Co	17.8
N1623338094b	2009-161-14:33	140473.94	117.84	-	-	O	17.8
N1623342840	2009-161-15:52	140185.42	118.07	-	-	O	18.7
N1623344422	2009-161-16:18	-	-	140448.46	115.92	Co	19.0
N1623345100	2009-161-16:30	-	-	140450.24	117.15	Co	19.2
N1623345778a	2009-161-16:41	140454.07	118.21	140468.05	118.16	C	19.3
N1623345778b	2009-161-16:41	140361.12	118.14	-	-	O	19.3
N1623346456	2009-161-16:52	140420.08	117.46	-	-	O	19.5
N1623347134a	2009-161-17:04	-	-	140465.48	119.35	Co	19.7
N1623347134b	2009-161-17:04	-	-	140284.89	117.79	Co	19.7
N1623347134c	2009-161-17:04	-	-	140494.23	116.77	Co	19.6
N1623347812	2009-161-17:15	-	-	140478.66	117.15	Co	19.8
N1623349620a	2009-161-17:45	-	-	140477.11	118.38	Co	20.3
N1623349620b	2009-161-17:45	-	-	140477.41	117.58	Co	20.3
N1623350072	2009-161-17:53	140436.50	116.92	140459.24	116.88	C	20.4
N1623350750a	2009-161-18:04	140492.32	118.98	140474.72	119.08	C	20.6
N1623350750b	2009-161-18:04	140497.74	118.26	140473.09	118.80	C	20.6
N1623350750c	2009-161-18:04	-	-	140460.74	117.74	Co	20.6
N1623351202a	2009-161-18:11	140495.49	117.35	140465.86	117.37	C	20.7
N1623351202b	2009-161-18:11	140440.83	115.52	140461.88	115.50	C	20.6
N1623351880	2009-161-18:23	140408.80	118.33	-	-	O	20.9
N1623353010	2009-161-18:41	140461.91	119.72	140470.05	119.47	C	21.3
N1623353236	2009-161-18:45	-	-	140289.36	117.59	Co	21.3
N1623353688a	2009-161-18:53	140425.08	117.43	-	-	O	21.4
N1623353688b	2009-161-18:53	140435.79	117.05	140461.26	117.04	BH	21.3
N1623355648	2009-161-19:25	139869.15	296.55	-	-	O	33.9
N1623357230a	2009-161-19:52	-	-	139967.11	297.67	Co	33.8
N1623357230b	2009-161-19:52	-	-	139969.11	295.60	Co	33.9
N1623360620	2009-161-20:48	139984.25	297.05	139973.44	297.04	C	33.9

N1623362428	2009-161-21:18	140378.86	297.42	-	-	O	33.9
N1623369434	2009-161-23:15	-	-	139875.42	296.97	Co	34.3
N1623372372	2009-162-00:04	140044.74	296.90	139971.08	296.97	BH	34.6
N1624155508	2009-171-01:36	140415.40	251.36	140336.33	251.40	C	127.3
N1624897464	2009-179-15:42	140249.48	260.47	-	-	O	80.9
N1626207601	2009-194-19:38	140081.17	331.10	-	-	O	80.3
N1626214461	2009-194-21:32	140549.74	224.73	140531.45	224.79	C	88.7
N1626220902a	2009-194-23:19	140483.04	222.66	140518.67	222.63	C	89.3
N1626220902b	2009-194-23:19	140549.00	224.72	140533.73	224.80	C	88.7
N1626224970	2009-195-00:27	140521.27	223.46	140529.10	223.41	C	89.7
N1626225648	2009-195-00:38	140291.52	223.06	-	-	O	89.8
N1626234123	2009-195-03:00	-	-	140520.93	224.20	Co	90.5
N1626236835	2009-195-03:45	140557.20	224.15	140510.36	224.19	C	90.8
N1626241581	2009-195-05:04	140550.39	223.98	140531.78	223.97	C	91.2
N1626248361	2009-195-06:57	140479.59	223.43	140532.25	222.54	C	91.8
N1627610575	2009-211-01:20	-	-	140445.05	237.97	Co	99.0
N1627612717	2009-211-01:56	-	-	140449.05	236.74	Co	99.1
N1627615165	2009-211-02:37	140215.27	239.31	140224.09	239.19	C	99.3
N1627623427	2009-211-04:55	140380.34	237.49	140405.67	237.40	C	99.8
N1627625263	2009-211-05:25	-	-	140415.01	237.07	Co	100.0
N1627631383	2009-211-07:07	140373.37	236.23	140399.43	236.17	C	100.4
N1627632607	2009-211-07:28	-	-	140239.62	236.81	Co	100.4
N1627636585	2009-211-08:34	-	-	140425.69	237.09	Co	100.7
N1627639033	2009-211-09:15	-	-	140424.68	236.80	Co	100.9
N1627639951	2009-211-09:30	140383.23	236.29	140396.89	236.23	C	100.9
N1627640563	2009-211-09:40	-	-	140442.93	237.31	Co	100.9
N1627642093	2009-211-10:06	140453.80	236.86	140434.58	236.87	C	101.0
N1627643011	2009-211-10:21	140358.51	236.32	140390.60	236.27	C	101.1
N1628596720a	2009-222-11:16	-	-	139961.33	102.61	Co	149.4
N1628596720b	2009-222-11:16	139937.92	100.66	139961.57	100.45	C	149.5
N1628932441a	2009-226-08:31	140088.85	230.33	140136.33	230.29	C	100.6
N1628932441b	2009-226-08:31	-	-	140136.64	228.42	Co	100.6
N1629353989	2009-231-05:37	140064.48	241.69	140132.45	241.57	C	119.5
N1629517865	2009-233-03:08	140182.49	265.89	140238.98	265.64	C	126
N1629518885a	2009-233-03:25	-	-	140262.31	269.89	Co	126.0
N1629518885b	2009-233-03:25	-	-	140260.87	267.84	Co	126.0
N1629518885c	2009-233-03:25	-	-	140227.51	260.19	Co	126.0
N1654040868a	2010-151-23:02	139992.50	265.28	-	-	O	119.9
N1654040868b	2010-151-23:02	-	-	139995.77	265.63	Co	119.9
N1654057184a	2010-152-03:34	-	-	139997.00	267.53	Co	121.7
N1654057184b	2010-152-03:34	139975.86	268.11	139991.62	268.08	C	121.7
N1654057184c	2010-152-03:34	139972.27	267.81	139996.60	267.76	C	121.7
N1654062944	2010-152-05:10	139983.96	268.99	140022.51	268.93	C	122.4
N1654064384	2010-152-05:34	139971.52	268.08	140011.70	266.88	BH	122.6

N1654065824	2010-152-05:58	139981.99	269.47	140026.91	269.37	C	122.8
N1654068224	2010-152-06:38	-	-	140034.94	270.26	Co	123.1
N1654070624	2010-152-07:18	139993.08	269.06	-	-	O	123.4
N1654072544	2010-152-07:50	-	-	140034.74	270.02	Co	123.6
N1654073504	2010-152-08:06	140059.59	269.93	140029.09	269.99	C	123.8
N1654074944	2010-152-08:30	139992.80	269.49	140033.22	269.41	C	123.9
N1654075904a	2010-152-08:46	139988.48	271.32	140022.84	271.06	C	124.1
N1654075904b	2010-152-08:46	-	-	140031.58	269.62	Co	124.1
N1654079264	2010-152-09:42	139973.01	273.58	140004.26	273.47	C	124.5
N1654085984	2010-152-11:34	140073.42	274.05	140033.53	274.16	C	125.4
N1662091567a	2010-245-03:20	139969.24	101.96	-	-	O	139.6
N1662091567b	2010-245-03:20	-	-	139901.83	101.66	Co	139.6
N1662092767	2010-245-03:39	-	-	139890.83	100.84	Co	139.9
N1716476180a	2012-144-14:04	140469.62	203.72	140516.77	203.61	C	46.2
N1716476180b	2012-144-14:04	140489.06	205.36	140528.63	205.25	C	46.2
N1716476180c	2012-144-14:04	140494.21	205.59	140540.07	205.50	C	46.2
N1716483035	2012-144-15:58	140570.40	203.45	140514.13	204.33	C	46.7
N1716483035	2012-144-15:58	-	-	140505.01	209.43	Co	47.0
N1716489890a	2012-144-17:52	140483.23	206.51	140551.73	206.29	C	47.1
N1716489890b	2012-144-17:52	140610.46	205.83	140541.08	206.93	C	48.1
N1716493546	2012-144-18:53	140490.35	209.32	140534.18	209.11	C	47.3
N1716496288a	2012-144-19:39	-	-	140512.77	211.12	Co	47.5
N1716496288b	2012-144-19:39	-	-	140544.18	206.88	Co	47.5
N1716498573	2012-144-20:17	140433.67	212.46	140514.35	211.54	C	47.6
N1719296954	2012-177-05:37	-	-	140521.43	281.98	Co	109.5
N1719298554	2012-177-06:03	140479.15	281.45	-	-	O	109.7
N1719301354	2012-177-06:50	140452.85	277.56	140531.78	276.51	C	109.9
N1719306154	2012-177-08:10	140493.38	282.12	140543.16	282.01	C	110.3
N1719307354	2012-177-08:30	140517.11	279.43	140536.04	279.17	C	110.4
N1719308554	2012-177-08:50	-	-	140531.66	280.01	Co	110.5
N1719316954	2012-177-11:10	140582.33	281.36	140558.97	281.47	C	111.3
N1719320154	2012-177-12:03	-	-	140543.57	276.58	Co	111.6
N1719541260	2012-180-01:28	140115.49	115.84	-	-	O	135.1
N1719632331a	2012-181-02:46	140270.99	201.04	140257.43	201.04	C	97.8
N1719632331b	2012-181-02:46	140272.58	201.08	140259.02	201.09	C	97.8
N1719632331c	2012-181-02:46	140270.79	201.10	140256.06	201.10	C	97.8
N1721660740	2012-204-14:13	140561.59	13.09	140533.16	13.11	C	156.6
N1721662310	2012-204-14:39	140563.29	16.50	140530.93	16.49	BH	153.9
N1721666235	2012-204-15:44	140501.07	24.16	-	-	O	146.7
N1723508317	2012-225-23:25	-	-	140214.40	147.62	Co	147.6
N1723510237	2012-225-23:57	140110.67	159.67	-	-	O	122.3
N1723511197	2012-226-00:13	140089.26	165.74	-	-	O	121.9
N1726540620	2012-261-01:43	140095.20	261.71	140059.46	261.79	C	91.1
N1726686691	2012-262-18:18	140185.87	238.75	140225.70	238.55	C	98.3

N1726861257a	2012-264-18:47	140017.22	277.59	140037.78	277.56	C	111.3
N1726861257b	2012-264-18:47	140022.31	277.45	140043.33	277.43	C	111.3
N1726861257c	2012-264-18:47	140018.24	277.33	140050.42	277.32	C	111.3
N1726861257d	2012-264-18:47	-	-	140036.62	277.22	Co	111.3
N1726861728	2012-264-18:55	-	-	140036.11	277.15	Co	111.3
N1726864083	2012-264-19:35	140132.88	273.61	140043.48	274.15	C	111.5
N1726877742	2012-264-23:22	-	-	140054.09	273.56	Co	112.8
N1726882452	2012-265-00:41	-	-	140044.39	275.20	Co	113.3
N1726885278	2012-265-01:28	140070.22	277.36	140024.91	277.44	C	113.6
N1726890459	2012-265-02:54	-	-	140036.80	279.21	Co	114.1
N1726895169	2012-265-04:13	-	-	140052.49	276.23	Co	114.6
N1726901763a	2012-265-06:03	139992.74	280.95	140022.83	280.95	C	115.3
N1726901763b	2012-265-06:03	-	-	140025.66	279.62	Co	115.3
N1726901763c	2012-265-06:03	140066.85	278.93	140033.35	279.00	C	115.3
N1727132335a	2012-267-22:05	140566.61	151.97	140513.67	152.00	C	153.4
N1727132335b	2012-267-22:05	140566.61	151.97	140516.88	152.20	C	154.4
N1727132335c	2012-267-22:05	-	-	140517.11	152.56	Co	153.4
N1727132605	2012-267-22:10	140539.29	150.57	140518.82	150.63	C	153.5
N1727795094	2012-275-14:11	140456.69	234.37	140437.51	234.42	C	72.0
N1727800548	2012-275-15:42	140392.02	233.87	140449.69	233.74	C	72.3
N1727809032	2012-275-18:04	140389.68	233.98	140427.68	233.57	C	72.7
N1727814486	2012-275-19:34	140464.49	234.43	140451.98	235.58	C	73
N1727825394a	2012-275-22:36	140431.26	240.60	140393.02	240.55	C	73.6
N1727825394b	2012-275-22:36	140454.41	236.64	140432.48	236.70	C	73.6
N1727829030	2012-275-23:37	-	-	140400.10	237.88	Co	73.8
N1727835696	2012-276-01:28	140422.13	238.19	140392.27	238.24	C	74.1
N1727836908	2012-276-01:48	140389.98	237.49	140425.59	237.44	C	74.2
N1729025684	2012-289-20:01	140263.86	139.09	140248.60	139.16	C	137.6
N1729028870	2012-289-20:54	140131.89	135.87	-	-	O	138.0
N1729030994	2012-289-21:29	-	-	140231.67	132.38	Co	138.2
N1729035773	2012-289-22:49	140228.33	127.61	140208.45	128.11	C	138.9
N1729037366a	2012-289-23:16	140197.44	123.92	140176.45	123.94	C	139.1
N1729037366b	2012-289-23:16	140196.32	123.84	140177.49	123.87	C	139.1
N1729040021	2012-290-00:00	-	-	140120.53	123.38	Co	139.6
N1729041083a	2012-290-00:18	-	-	140169.65	122.74	Co	139.7
N1729041083b	2012-290-00:18	140168.87	121.22	140161.50	121.90	C	139.7
N1729043207	2012-290-00:53	-	-	140149.53	121.43	Co	140.1
N1729046393	2012-290-01:46	140078.12	116.18	140116.95	116.01	C	140.7
N1729046924a	2012-290-01:55	140104.73	114.30	140120.52	114.30	C	140.8
N1729046924b	2012-290-01:55	-	-	140131.16	117.13	Co	140.8
N1729047455	2012-290-02:04	140425.25	114.00	140115.14	114.26	BH	140.9
N1729057850	2012-290-04:57	140164.99	330.58	-	-	O	154.6
N1729059974a	2012-290-05:32	-	-	140143.42	327.03	Co	155.2
N1729059974b	2012-290-05:32	-	-	140139.82	325.96	Co	155.2

N1729062629	2012-290-06:17	-	-	140136.10	323.69	Co	155.9
N1729063691	2012-290-06:34	-	-	140159.43	323.80	Co	156.2
N1729064753	2012-290-06:52	140198.99	322.14	140143.52	322.76	C	156.4
N1729072187	2012-290-08:56	140268.71	315.98	140205.37	316.08	C	158.3
N1729075373	2012-290-09:49	140279.64	311.90	140228.11	311.96	C	159.1
N1729259467a	2012-292-12:57	140458.79	179.91	140437.60	179.93	C	71.2
N1729259467b	2012-292-12:57	140451.17	179.83	140432.86	179.90	C	71.2
N1729259467c	2012-292-12:57	140451.99	179.93	140435.40	179.97	C	71.2
N1729261283	2012-292-13:28	140461.84	190.87	140484.33	190.85	C	72.1
N1729264143	2012-292-14:15	-	-	140555.47	208.81	Co	73.2
N1729266353a	2012-292-14:52	140600.31	221.53	140567.10	221.77	C	73.5
N1729266353b	2012-292-14:52	-	-	140567.10	221.77	Co	74.5
N1730569356	2012-307-16:49	140424.45	349.57	140277.58	349.80	C	101.2
N1731107237	2012-313-22:13	140520.77	318.38	140480.58	318.63	C	150.7
N1731107648	2012-313-22:20	140543.94	317.92	140479.35	319.74	C	150.7
N1731108470	2012-313-22:34	140459.63	320.12	140483.44	320.02	C	150.9
N1731109703	2012-313-22:54	140460.22	321.11	140479.37	321.08	C	151.1
N1731110114	2012-313-23:01	140455.57	321.15	140494.28	320.93	C	151.2
N1731112169a	2012-313-23:35	140473.95	318.74	140486.99	318.68	C	151.7
N1731112169b	2012-313-23:35	140527.75	319.06	140497.98	319.09	C	151.7
N1731113813	2012-314-00:03	-	-	140497.45	319.87	Co	152.0
N1731119567	2012-314-01:39	140522.29	320.66	140488.34	321.08	C	153.2
N1731119978	2012-314-01:46	140438.02	320.96	140501.22	320.91	C	153.3
N1731126143	2012-314-03:28	140450.01	320.95	140491.82	319.56	C	154.7
N1731129842a	2012-314-04:30	-	-	140509.40	319.68	Co	155.5
N1731129842b	2012-314-04:30	140483.21	319.17	140512.59	319.12	C	155.6
N1731140093	2012-314-07:21	-	-	139954.90	136.97	Co	145.4
N1731152834	2012-314-10:53	139917.05	134.35	139900.64	135.54	C	148.1
N1731153656	2012-314-11:07	139901.21	134.10	139913.55	134.06	C	148.3
N1731155300	2012-314-11:34	139935.58	134.61	-	-	O	148.7
N1731156122	2012-314-11:48	139886.01	134.27	139923.14	134.29	C	148.9
N1731157355	2012-314-12:09	-	-	139924.85	137.38	Co	148.9
N1733157232a	2012-337-15:40	140501.79	23.15	140525.03	23.11	C	59.8
N1733157232b	2012-337-15:40	140496.10	19.16	140528.94	19.07	C	60.8
N1733160448	2012-337-16:33	-	-	140016.41	218.99	Co	67.0
N1733513734	2012-341-18:41	140548.81	357.27	140578.62	357.13	C	103.5
N1733517926a	2012-341-19:51	140620.52	356.28	140581.82	356.30	C	104.3
N1733517926b	2012-341-19:51	-	-	140597.19	356.37	Co	104.3
N1733518974a	2012-341-20:09	140542.73	358.34	140565.30	358.30	C	104.2
N1733518974b	2012-341-20:09	140552.24	358.64	140563.52	358.60	C	104.2
N1733522118	2012-341-21:01	140684.80	357.30	140619.46	357.37	BH	104.9
N1733524214a	2012-341-21:36	140706.08	356.97	140614.65	357.03	C	105.3
N1733524214b	2012-341-21:36	140715.09	356.97	140609.64	357.20	C	105.3
N1733529454	2012-341-23:03	-	-	140537.42	0.94	Co	105.7

N1733533122	2012-342-00:04	140663.23	359.31	140586.69	359.34	BH	106.5
N1733549366	2012-342-04:35	-	-	140589.42	4.54	Co	108.9
N1733553558b	2012-342-05:45	-	-	140591.41	6.56	Co	109.3
N173355355a8	2012-342-05:45	-	-	140593.92	7.63	Co	109.3
N1733554082	2012-342-05:54	140621.73	7.16	140584.51	7.24	C	109.4
N1733555654	2012-342-06:20	140582.14	5.96	140592.37	5.95	C	109.9
N1733556702	2012-342-06:37	-	-	140572.64	8.57	Co	109.8
N1733557750	2012-342-06:55	140568.97	8.53	140588.28	8.51	C	110.0
N1733559846	2012-342-07:30	140654.96	8.38	140586.09	8.40	C	110.4
N1733564562	2012-342-08:48	140536.45	9.42	140563.33	9.38	C	111.2
N1734571074	2012-354-00:24	139823.19	239.08	139886.88	239.04	C	95.5
N1734573588	2012-354-01:05	140109.04	238.49	139908.74	238.55	C	95.8
N1734591596	2012-354-06:06	140613.73	23.64	140565.97	23.65	C	90.9
N1734593691	2012-354-06:40	140528.96	24.15	140564.36	24.02	C	91.2
N1734595367a	2012-354-07:08	140610.57	24.57	140581.82	24.62	C	91.4
N1734595367b	2012-354-07:08	140610.27	24.82	140600.18	24.90	C	91.3
N1734596624a	2012-354-07:29	140551.17	23.87	140574.82	23.85	C	91.6
N1734596624b	2012-354-07:29	140549.74	23.95	140570.91	23.93	C	91.6
N1735117974	2012-360-08:18	139929.37	197.54	139962.04	197.49	C	20.6
N1735135905	2012-360-13:17	140427.28	358.90	140391.62	358.97	C	13.5
N1735584151	2012-365-17:48	140660.25	41.59	140612.09	41.64	C	72.5
N1735592203	2012-365-20:02	-	-	140546.74	42.89	Co	72.5
N1736802961	2013-013-20:21	139907.41	260.43	139929.24	260.42	C	88.1
N1737159287a	2013-017-23:20	-	-	140477.22	147.53	Co	151.9
N1737159287b	2013-017-23:20	140478.42	147.29	140502.68	147.27	C	151.9
N1737159287c	2013-017-23:20	-	-	140472.88	147.58	Co	151.9
N1737159287d	2013-017-23:20	140497.08	146.60	140462.28	146.63	C	151.9
N1737159287e	2013-017-23:20	-	-	140497.92	146.46	Co	151.9
N1737159819	2013-017-23:29	-	-	140494.64	147.38	Co	152.2
N1737162231a	2013-018-00:09	140462.16	149.78	140493.59	149.38	C	153.7
N1737162231b	2013-018-00:09	140460.89	149.44	140486.27	149.32	C	153.7
N1737164643	2013-018-00:49	140455.21	150.66	140472.60	150.62	C	155.1
N1737165715	2013-018-01:07	140484.97	150.29	140474.22	150.32	C	155.8
N1737166787a	2013-018-01:25	140495.42	152.01	140479.56	152.08	C	156.5
N1737166787b	2013-018-01:25	-	-	140473.26	151.58	Co	156.5
N1737167591a	2013-018-01:39	140473.71	151.21	140486.07	151.05	C	156.9
N1737167591b	2013-018-01:39	140462.24	151.06	140486.07	151.05	C	157.5
N1737168395a	2013-018-01:52	-	-	140489.95	152.67	Co	157.5
N1737168395b	2013-018-01:52	140495.72	152.77	140476.00	152.72	C	157.5
N1737168395c	2013-018-01:52	140486.69	153.04	140480.10	152.79	C	157.5
N1737170271	2013-018-02:23	-	-	140493.04	154.71	Co	158.7
N1738426745	2013-032-15:24	140496.60	193.73	140481.94	193.85	C	65.2
N1738431345	2013-032-16:41	-	-	140482.44	195.05	Co	59.6
N1738434105	2013-032-17:27	140487.62	195.18	140480.34	195.21	C	56.4

N1738434841	2013-032-17:39	140489.25	195.50	140475.77	195.72	C	55.6
N1739126746	2013-040-17:51	140284.56	270.37	140213.29	270.57	BH	97.3
N1739132486	2013-040-19:27	140188.04	271.25	140221.00	271.22	C	91.3
N1739134126	2013-040-19:54	140238.59	270.34	140221.01	270.36	C	91.5
N1739151346	2013-041-00:41	140237.47	270.15	140225.85	270.13	C	93.6
N1739153806	2013-041-01:22	140160.08	270.62	140213.16	270.57	C	93.9
N1739165696	2013-041-04:40	-	-	140217.50	270.08	Co	95.4
N1739169796a	2013-041-05:48	140270.61	271.79	140204.24	271.97	C	95.9
N1739169796b	2013-041-05:48	140274.85	269.51	140210.99	269.77	C	95.9
N1739169796c	2013-041-05:48	140246.32	268.78	140216.74	268.82	C	95.9
N1739173076	2013-041-06:43	140238.22	269.77	140219.46	269.78	C	96.4
N1739180046	2013-041-08:39	140297.85	269.16	140234.41	269.59	BH	97.3
N1739459522	2013-044-14:17	140479.95	148.17	140463.87	148.19	C	152.1
N1739460567	2013-044-14:35	-	-	140430.68	149.49	Co	152.8
N1739461403	2013-044-14:49	140349.66	149.08	-	-	O	153.2
N1739467882a	2013-044-16:36	140430.43	152.46	140464.73	152.44	C	157.2
N1739467882b	2013-044-16:36	140430.43	152.46	140464.37	152.40	C	157.2
N1739473107	2013-044-18:04	140410.75	153.94	140482.17	153.92	BH	158.6
N1739473107	2013-044-18:04	-	-	140478.27	156.85	Co	160.7
N1739473525	2013-044-18:11	-	-	140485.55	155.32	Co	160.9
N1739476869a	2013-044-19:06	140518.87	157.47	140483.93	157.52	C	163.1
N1739476869b	2013-044-19:06	140504.18	157.46	140491.70	157.54	C	163.1
N1739476869c	2013-044-19:06	140491.46	157.37	140484.38	157.38	C	163.1
N1739476869d	2013-044-19:06	140493.85	157.30	140486.94	157.32	C	163.1
N1739476869e	2013-044-19:06	140495.80	157.19	140485.16	157.20	C	163.1
N1739494832	2013-045-00:06	-	-	139902.35	19.82	Co	156.6
N1739504240	2013-045-02:42	-	-	139916.33	24.62	Co	147.2
N1741148227	2013-064-03:22	-	-	139813.76	44.85	Co	71.2
N1741150670	2013-064-04:03	-	-	139802.17	46.93	Co	71.4
N1741159706	2013-064-06:33	140416.98	190.25	140402.93	190.27	C	78.7
N1742332190	2013-077-20:15	140559.37	269.81	140549.02	269.82	C	104.3
N1742334246	2013-077-20:49	140524.66	271.28	140544.10	271.26	C	104.7
N1742337336	2013-077-21:40	140553.17	269.36	-	-	O	105.3
N1742348151	2013-078-00:41	140529.61	270.96	140546.44	270.96	C	107.4
N1743085105a	2013-086-13:23	140293.37	10.26	140327.67	10.22	C	55.8
N1743085105b	2013-086-13:23	140302.47	10.20	140318.52	10.17	C	55.8
N1743085105c	2013-086-13:23	140334.27	10.09	140377.51	10.04	C	55.8
N1743085105d	2013-086-13:23	140326.19	9.79	140375.76	9.71	C	55.8
N1743085105e	2013-086-13:23	140359.28	8.30	140324.44	8.36	C	55.8
N1743085481a	2013-086-13:29	140320.04	7.28	140345.55	6.95	C	55.9
N1743085481b	2013-086-13:29	140339.78	5.64	140350.18	5.63	C	56.0
N1743085481c	2013-086-13:29	140372.15	5.55	140351.41	5.56	C	56.0
N1743085861	2013-086-13:36	140390.30	7.35	140348.28	7.50	C	56.0
N1743086621	2013-086-13:48	140348.46	7.96	140365.53	7.79	C	56.1

N1743087381	2013-086-14:01	140411.70	6.67	140371.85	6.71	C	56.2
N1743089281	2013-086-14:33	140388.17	5.69	140357.02	5.71	C	56.5
N1743091181	2013-086-15:04	140326.46	7.06	140345.18	7.02	C	56.7
N1743092321a	2013-086-15:23	140359.82	6.98	140329.84	7.00	C	56.9
N1743092321b	2013-086-15:23	140357.50	6.92	140337.40	6.93	C	56.9
N1743092321c	2013-086-15:23	140356.62	6.89	140336.73	6.91	C	56.9
N1743092321d	2013-086-15:23	140355.55	6.86	140345.59	6.87	C	56.9
N1743094981	2013-086-16:08	140130.38	7.68	140347.97	7.54	BH	57.2
N1743096501	2013-086-16:33	140311.24	7.18	140356.42	6.73	C	57.4
N1743107901	2013-086-19:43	-	-	140364.00	9.12	Co	58.8
N1743113981	2013-086-21:24	140325.35	6.00	140350.04	5.73	C	59.8
N1743114741	2013-086-21:37	140194.48	8.63	-	-	O	59.8
N1743115501a	2013-086-21:50	140342.44	9.65	140358.00	9.62	C	59.8
N1743115501b	2013-086-21:50	140339.01	9.09	140356.81	9.07	C	59.8
N1743116641	2013-086-22:09	140301.34	7.77	-	-	O	60.1
N1743117401	2013-086-22:21	140431.64	7.01	140363.40	7.12	C	60.2
N1743123481	2013-087-00:03	-	-	140376.44	5.76	Co	61.1
N1743477293	2013-091-02:20	140566.84	307.43	140553.19	307.46	C	130.7
N1743637951	2013-092-22:57	140178.14	49.74	-	-	O	115.5
N1743776395	2013-094-13:25	-	-	140535.22	321.30	Co	17.4
N1746570747a	2013-126-21:37	139905.94	239.99	139919.86	239.60	C	57.9
N1746570747b	2013-126-21:37	139894.57	239.42	-	-	O	57.9
N1746571495	2013-126-21:49	-	-	139955.40	241.61	Co	58.0
N1746581593a	2013-127-00:38	-	-	139890.89	241.97	Co	59.6
N1746581593b	2013-127-00:38	-	-	139880.76	241.59	Co	59.6
N1746584959	2013-127-01:34	-	-	139899.29	241.62	Co	60.1
N1746588325	2013-127-02:30	139879.78	241.37	139901.76	241.38	C	60.7
N1748346788	2013-147-10:57	-	-	139916.80	266.41	Co	85.6
N1748350636	2013-147-12:01	139955.70	265.07	139917.96	265.22	C	86.3
N1748368433	2013-147-16:58	-	-	139935.92	265.93	Co	89.7
N1748388154	2013-147-22:27	139850.04	266.02	139914.26	265.98	C	93.5
N1748458409	2013-148-17:58	139931.10	270.72	139895.43	271.11	C	108.1
N1748763019	2013-152-06:34	-	-	140241.85	54.01	Co	107.6
N1748770357	2013-152-08:37	140206.18	40.93	140216.26	40.93	C	102.5
N1748782796	2013-152-12:04	-	-	140345.27	193.14	Co	105.7
N1748790648	2013-152-14:15	-	-	140195.87	239.87	Co	105
N1748900003	2013-153-20:38	-	-	140000.31	246.77	Co	31.4
N1750385279	2013-171-01:12	140392.76	46.26	-	-	O	70.9
N1750397121	2013-171-04:29	-	-	140032.37	46.08	Co	73.0
N1750398649	2013-171-04:55	140046.93	44.82	140033.59	44.88	C	73.3
N1750400177	2013-171-05:20	-	-	140023.12	45.64	Co	73.5
N1750404379	2013-171-06:30	140049.59	45.98	140037.86	46.01	C	74.2
N1750425806	2013-171-12:27	-	-	140389.15	238.94	Co	87.1
N1750427716	2013-171-12:59	140368.67	238.49	140344.09	238.57	C	87.5

N1750428862	2013-171-13:18	-	-	140347.12	238.35	Co	87.7
N1750433064	2013-171-14:28	-	-	140332.79	238.73	Co	88.4
N1751430721a	2013-183-03:36	140300.68	276.02	140310.35	276.00	C	82.2
N1751430721b	2013-183-03:36	140294.38	275.96	140320.04	275.94	C	82.2
N1751440679	2013-183-06:22	140376.76	276.36	140313.67	276.44	BH	84.0
N1751446807	2013-183-08:04	-	-	140362.87	277.01	Co	85.1
N1751451403	2013-183-09:21	140317.50	277.67	140297.68	277.72	C	86.0
N1751452552	2013-183-09:40	140264.33	277.30	140286.94	277.20	C	86.2
N1751456327	2013-183-10:43	140060.67	111.62	140182.20	111.58	C	77.1
N1751459391	2013-183-11:34	-	-	140168.40	109.64	Co	77.6
N1751475477	2013-183-16:02	-	-	140133.35	110.61	Co	80.3
N1751478541a	2013-183-16:53	140235.27	108.85	140187.01	108.98	C	80.7
N1751478541b	2013-183-16:53	140183.13	108.89	140187.01	108.98	C	80.7
N1751481222	2013-183-17:38	140160.38	111.00	140178.43	110.87	C	81.3
N1755734445	2013-232-23:04	-	-	140163.32	238.89	Co	59.5
N1755734859	2013-232-23:11	140146.54	240.12	140177.80	240.12	C	59.6
N1755738171	2013-233-00:06	140203.37	240.59	140193.93	240.58	C	60.4
N1755746037	2013-233-02:17	-	-	140189.35	240.51	Co	62.1
N1755752661	2013-233-04:08	140152.85	238.57	140163.06	238.54	C	63.4
N1755755559	2013-233-04:56	140238.44	239.29	140166.09	239.32	C	64.0
N1755769221	2013-233-08:44	-	-	140281.63	238.75	Co	66.7
N1755772947	2013-233-09:46	-	-	140179.05	240.45	Co	67.6
N1755775017	2013-233-10:20	140145.43	241.22	140174.35	241.17	C	68.0
N1755775845	2013-233-10:34	-	-	140197.07	239.08	Co	68.2
N1756041827	2013-236-12:27	-	-	140368.41	276.87	Co	109.7
N1756045967a	2013-236-13:36	-	-	140347.26	279.80	Co	109.9
N1756045967b	2013-236-13:36	-	-	140352.70	278.74	Co	110.2
N1756047209	2013-236-13:57	140304.02	278.14	140316.38	278.09	C	110.3
N1756047623	2013-236-14:04	140296.94	277.91	140325.93	277.74	C	110.4
N1756048865	2013-236-14:24	-	-	140341.17	278.04	Co	110.5
N1756060871	2013-236-17:45	-	-	140320.13	277.72	C	112.0
N1756061285	2013-236-17:51	-	-	140336.64	279.26	Co	112.1
N1756064597	2013-236-18:47	-	-	140356.68	279.43	Co	112.5
N1756066667	2013-236-19:21	140368.09	276.59	140319.09	276.85	BH	112.7
N1756069565	2013-236-20:09	140298.13	277.25	140333.96	277.23	C	113
N1756079087	2013-236-22:48	140325.35	277.41	140324.46	277.41	C	114.2
N1756082813	2013-236-23:50	140285.56	274.99	140308.15	274.99	C	114.6
N1756207084a	2013-238-10:21	140311.84	285.36	140345.33	285.25	C	128.3
N1756207084b	2013-238-10:21	-	-	140343.05	283.99	Co	128.3
N1756208724	2013-238-10:49	140320.75	286.23	140351.59	286.11	C	128.5
N1756209134	2013-238-10:56	140342.18	285.74	140335.47	285.85	C	128.5
N1756209954	2013-238-11:09	-	-	140347.52	283.35	Co	128.6
N1756212004	2013-238-11:43	140278.14	285.61	140338.04	285.55	BH	128.8
N1756218154	2013-238-13:26	140346.05	283.92	140331.57	283.92	C	129.5

N1756222664	2013-238-14:41	-	-	140341.24	287.58	Co	130.0
N1756222664	2013-238-14:41	-	-	140348.25	286.29	Co	129.9
N1756228404a	2013-238-16:17	140391.81	285.66	140318.93	285.70	C	130.5
N1756228404b	2013-238-16:17	140391.81	285.66	140333.64	285.97	C	130.5
N1756240294	2013-238-19:35	-	-	140318.73	283.50	Co	131.7
N1756244394	2013-238-20:43	140297.48	283.67	140320.13	283.53	C	132.1
N1756257104	2013-239-00:15	-	-	140384.13	286.52	Co	133.4
N1756377239a	2013-240-09:37	140451.42	302.73	140397.55	302.78	C	145.3
N1756377239b	2013-240-09:37	140451.42	302.73	140390.02	302.87	C	145.3
N1756379305	2013-240-10:12	-	-	140373.00	299.77	Co	145.5
N1756380961	2013-240-10:39	140413.56	300.37	140382.10	300.80	C	145.6
N1756384687	2013-240-11:41	-	-	140373.05	299.00	Co	146.0
N1756385101	2013-240-11:48	-	-	140387.69	300.39	Co	146.0
N1756390069	2013-240-13:11	140329.75	298.62	140365.47	298.57	C	146.5
N1756390897	2013-240-13:25	140416.27	299.83	140367.60	299.88	C	146.6
N1756394209	2013-240-14:20	-	-	140396.58	299.58	Co	146.9
N1756402903	2013-240-16:45	-	-	140368.64	298.85	Co	147.7
N1756405387a	2013-240-17:26	140494.81	300.75	140375.70	300.77	BH	148.0
N1756405387b	2013-240-17:26	140494.81	300.75	140376.26	301.06	BH	148.0
N1756407043	2013-240-17:54	-	-	140364.36	299.17	Co	148.1
N1756419463	2013-240-21:21	-	-	140415.56	300.55	Co	149.3
N1756424845	2013-240-22:51	140350.34	302.22	140388.91	302.14	C	149.8
N1756427743a	2013-240-23:39	140289.28	299.24	140357.65	299.03	C	150.1
N1756427743b	2013-240-23:39	140289.28	299.24	140366.74	299.17	C	150.1
N1757251551	2013-250-12:29	140071.77	254.45	140035.95	254.49	C	110.7
N1757255731	2013-250-13:39	-	-	140012.36	255.12	Co	109.8
N1757268689	2013-250-17:15	-	-	140142.42	256.80	Co	107.0
N1757883329	2013-257-19:59	139914.43	255.10	139941.71	255.11	C	81.9
N1757952511	2013-258-15:12	139950.15	269.83	139961.41	269.35	C	94.8
N1757959693	2013-258-17:11	139970.90	270.72	140019.22	270.70	C	96.1
N1757965678	2013-258-18:51	-	-	140020.32	270.44	Co	97.1
N1757967274	2013-258-19:18	-	-	139987.06	270.83	Co	97.3
N1760818744	2013-291-19:22	139951.99	279.03	139979.63	279.01	C	119.5
N1760826534	2013-291-21:32	139984.58	280.08	139969.98	280.09	C	120.5
N1760841674	2013-292-01:44	140533.90	111.73	140483.70	111.83	C	114.1
N1760844134	2013-292-02:25	140530.44	110.92	140485.75	110.95	C	114.5
N1760846184a	2013-292-02:59	140376.87	112.42	140483.95	112.26	C	114.8
N1760846184b	2013-292-02:59	140376.87	112.42	140477.02	112.08	C	114.8
N1760846184c	2013-292-02:59	140376.87	112.42	140470.76	111.65	C	114.8
N1760851924	2013-292-04:35	140511.60	111.62	140475.63	111.65	C	115.5
N1760853154a	2013-292-04:55	140317.46	110.50	140471.12	110.36	C	115.7
N1760853154b	2013-292-04:55	140317.46	110.50	140447.58	109.68	C	115.7
N1760853154c	2013-292-04:55	140317.46	110.50	140454.13	109.09	C	115.7
N1760864634	2013-292-08:07	140558.92	110.83	140500.81	110.87	C	117.1

Table B.1.: Measurements from the survey of low-velocity collisional features (see Chapter 5). Features are named after the image that they first appear in, followed by an alphabetical character for multiple features in the same image. Classification is by morphology in the re-projected images into one of the following classes: classic (C), bright-headed classic (BH), complex (Co), or objects (O). Phase is the Sun to feature ring-plane coordinate to spacecraft phase angle. Uncertainties from pixel size are typically ~ 5 km radial by $\sim 0.01°$ longitudinal.

C. Repeatedly Observed Survey Features

Designation	Date (year-DOY-time)	θ (°)	Class	Phase (°)	Exposure (ms)
N1538204682	2006-272-06:32:50.814	-	O	160.9	680
N1538283887	2006-273-04:32:55.309	-	O	159.9	680
N1557026084a	2007-125-02:40:53.219	-46	BH	79.8	1000
N1557026084b	2007-125-02:40:53.219	-18	BH	79.8	1000
N1557080024	2007-125-17:39:52.877	-11	BH	83.0	1000
N1577828765a	2007-365-21:09:57.025	-1	C	64.7	1200
N1577828765c	2007-365-21:09:57.025	-4	BH	64.7	1200
N1578409567a	2008-007-14:29:55.038	-2	BH	20.6	1000
N1578409567b	2008-007-14:29:55.038	0	C	20.7	1000
N1595326037	2008-203-09:29:05.444	-	O	103.7	1500
N1595501977	2008-205-10:21:24.905	-24	C	13.4	100
N1606006222	2008-327-00:10:55.278	-55	C	37.9	1200
N1606033182	2008-327-07:40:15.087	-43	BH	45.7	1200
N1623224391a	2009-160-06:58:20.565	-43	C	95.0	1800
N1623224391b	2009-160-06:58:20.565	-32	C	94.9	1800
N1623332218a	2009-161-12:55:27.199	-8	C	17.2	1000
N1623332218b	2009-161-12:55:27.199	-8	C	17.1	1000
N1623224706a	2009-160-07:03:35.563	-17	C	94.6	1800
N1623224706b	2009-160-07:03:35.563	-4	C	94.6	1800
N1623332896a	2009-161-13:06:45.194	-13	C	17.2	1000
N1623332896b	2009-161-13:06:45.194	-3	C	17.2	1000
N1623225651a	2009-160-07:19:20.556	-47	Co	93.9	1800
N1623333348a	2009-161-13:14:17.190	-12	Co	17.2	1000
N1623225651b	2009-160-07:19:20.556	-27	Co	93.8	1800
N1623360620	2009-161-20:48:48.597	26	C	33.9	1800
N1623226701	2009-160-07:36:50.548	-11	Co	92.7	1800
N1623335156b	2009-161-13:44:25.178	-13	Co	17.4	1000
N1623329280d	2009-161-12:06:29.219	-	O	17.1	1000
N1623355648	2009-161-19:25:56.632	-	O	33.9	1800
N1623330636b	2009-161-12:29:05.210	-40	C	17.1	1800
N1623357230a	2009-161-19:52:18.621	-23	Co	33.8	1800

N1623330636c	2009-161-12:29:05.210	-42	Co	17.1	1000
N1623357230b	2009-161-19:52:18.621	-25	Co	33.9	1000
N1623342840	2009-161-15:52:29.123	-16	O	18.7	1000
N1623369434	2009-161-23:15:42.534	90	Co	34.3	1800
N1623345778b	2009-161-16:41:27.102	78	O	19.3	1000
N1623372372	2009-162-00:04:40.513	-23	BH	34.6	1800
N1629353989	2009-231-05:37:35.278	-13	C	119.5	1200
N1629517865	2009-233-03:08:50.432	-5	C	126.0	560
N1729028870	2012-289-20:54:33.308	-	O	138.0	1800
N1729057850	2012-290-04:57:33.424	-	O	154.6	1200
N1729030994	2012-289-21:29:57.295	23	Co	138.2	1800
N1729059974a	2012-290-05:32:57.411	-7	Co	155.2	1200
N1729059974b	2012-290-05:32:57.411	-5	Co	155.2	1200
N1729035773	2012-289-22:49:36.264	-1	C	138.9	1800
N1729064753	2012-290-06:52:36.380	-2	C	156.4	1200
N1729037366a	2012-289-23:16:09.254	-30	C	139.1	1800
N1729037366b	2012-289-23:16:09.254	-17	C	139.1	1800
N1729259467a	2012-292-12:57:49.144	-21	C	71.2	1200
N1729259467b	2012-292-12:57:49.144	-6	C	71.2	1200
N1729259467c	2012-292-12:57:49.144	-9	C	71.2	1200
N1729043207	2012-290-00:53:30.217	-18	Co	140.1	1800
N1729072187	2012-290-08:56:30.333	-14	C	158.3	1200
N1731113813	2012-314-00:03:23.367	-4	Co	152	1200
N1731140093	2012-314-07:21:23.200	23	Co	145.4	1200
N1731126143	2012-314-03:28:53.288	-1	C	154.7	1200
N1731152834	2012-314-10:53:44.119	0	C	148.1	1200
N1731129842a	2012-314-04:30:32.265	-5	Co	155.5	1200
N1731129842b	2012-314-04:30:32.265	-14	C	155.6	1200
N1731157355	2012-314-12:09:05.090	89	Co	148.9	1200
N1734573588	2012-354-01:05:56.394	-54	C	95.8	1200
N1734595367a	2012-354-07:08:55.255	-12	C	91.4	1200
N1734595367b	2012-354-07:08:55.255	-3	C	91.3	1200
N1739126746	2013-040-17:51:25.327	-8	BH	97.3	1500
N1739180046	2013-041-08:39:44.988	-3	BH	97.3	1500
N1739169796a	2013-041-05:48:55.053	-9	C	95.9	1500
N1739169796b	2013-041-05:48:55.053	-6	C	95.9	1600
N1739169796c	2013-041-05:48:55.053	-15	C	95.9	1600
N1739473107	2013-044-18:04:04.744	20	Co	160.7	380
N1739473525	2013-044-18:11:02.741	20	Co	160.9	380
N1739173076	2013-041-06:43:35.032	-33	C	96.4	1600
N1739476869a	2013-044-19:06:46.720	-17	C	163.1	380
N1739476869b	2013-044-19:06:46.720	-4	C	163.1	380
N1739476869c	2013-044-19:06:46.720	-22	C	163.1	380

N1739476869d	2013-044-19:06:46.720	-9	C	163.1	380
N1739476869e	2013-044-19:06:46.720	-16	C	163.1	380
N1739460567	2013-044-14:35:04.824	21	Co	152.8	380
N1739494832	2013-045-00:06:09.621	71	Co	156.6	380
N1739473107	2013-044-18:04:04.744	-56	BH	158.6	380
N1739504240	2013-045-02:42:57.546	6	Co	147.2	380
N1748350636	2013-147-12:01:56.873	-6	C	86.3	1200
N1748458409	2013-148-17:58:09.463	-2	C	108.1	680
N1748763019	2013-152-06:34:57.250	47	Co	107.6	1200
N1748790648	2013-152-14:15:26.074	13	Co	105.0	1200
N1750397121	2013-171-04:29:48.930	51	Co	73.0	1200
N1750425806	2013-171-12:27:53.748	14	Co	87.1	1200
N1751446807	2013-183-08:04:28.263	12	Co	85.1	1200
N1751475477	2013-183-16:02:18.081	27	Co	80.3	1200
N1750398649	2013-171-04:55:16.920	-5	C	73.3	1200
N1750427716	2013-171-12:59:43.735	-8	C	87.5	1200
N1750400177	2013-171-05:20:44.910	51	Co	73.5	1200
N1750428862	2013-171-13:18:49.728	14	Co	87.7	1200
N1750404379	2013-171-06:30:46.884	-9	C	74.2	1200
N1750433064	2013-171-14:28:51.701	14	Co	88.4	1200
N1751430721a	2013-183-03:36:22.365	-15	C	82.2	1200
N1751430721b	2013-183-03:36:22.365	-30	C	82.2	1200
N1751459391	2013-183-11:34:12.183	28	Co	77.6	1200
N1751452552	2013-183-09:40:13.227	-6	C	86.2	1200
N1751481222	2013-183-17:38:03.045	-3	C	81.3	1200
N1755734445	2013-232-23:04:39.032	13	Co	59.5	1200
N1756060871	2013-236-17:45:02.959	12	C	112.0	1200
N1756222664	2013-238-14:41:34.932	11	Co	130.0	1200
N1756384687	2013-240-11:41:56.903	11	Co	146.0	1200
N1755734859	2013-232-23:11:33.030	86	C	59.6	1200
N1756061285	2013-236-17:51:56.957	12	Co	112.1	1200
N1756222664	2013-238-14:41:34.932	11	Co	129.9	1200
N1756385101	2013-240-11:48:50.900	11	Co	146	1200
N1755738171	2013-233-00:06:45.009	23	C	60.4	1200
N1756064597	2013-236-18:47:08.936	12	Co	112.5	1200
N1755752661	2013-233-04:08:14.917	-7	C	63.4	1200
N1756079087	2013-236-22:48:38.844	-3	C	114.2	1200
N1756240294	2013-238-19:35:24.820	11	Co	131.7	1200
N1756402903	2013-240-16:45:32.787	11	Co	147.7	1200
N1755769221	2013-233-08:44:14.812	14	Co	66.7	1200
N1756041827	2013-236-12:27:39.080	12	Co	109.7	1200
N1756257104	2013-239-00:15:34.713	11	Co	133.4	1200
N1756419463	2013-240-21:21:32.682	11	Co	149.3	1200
N1757268689	2013-250-17:15:13.288	13	Co	107.0	1200

N1757965678	2013-258-18:51:37.862	12	Co	97.1	1200
N1755772947	2013-233-09:46:20.788	13	Co	67.6	1200
N1756045967a	2013-236-13:36:39.054	12	Co	109.9	1200
N1756207084a	2013-238-10:21:55.031	-7	C	128.3	1200
N1755775017	2013-233-10:20:50.775	-14	C	68.0	1200
N1756047623	2013-236-14:04:15.043	-4	C	110.4	1200
N1756209134	2013-238-10:56:05.018	-1	C	128.5	1200
N1755775845	2013-233-10:34:38.769	13	Co	68.2	1200
N1756048865	2013-236-14:24:57.036	12	Co	110.5	1200
N1756209954	2013-238-11:09:45.012	11	Co	128.6	1200
N1756045967b	2013-236-13:36:39.054	12	Co	110.2	1201
N1756207084b	2013-238-10:21:55.031	11	Co	128.3	1200
N1756047209	2013-236-13:57:21.046	-7	C	110.3	1200
N1756208724	2013-238-10:49:15.020	-6	C	128.5	1200
N1756424845	2013-240-22:51:14.648	-11	C	149.8	1200
N1756066667	2013-236-19:21:38.922	-4	BH	112.7	1200
N1756228404a	2013-238-16:17:14.895	-36	C	130.5	1200
N1756228404b	2013-238-16:17:14.895	-4	C	130.5	1200
N1756390897	2013-240-13:25:26.863	-20	C	146.6	1200
N1756082813	2013-236-23:50:44.820	84	C	114.6	1200
N1756244394	2013-238-20:43:44.794	-4	C	132.1	1200
N1756407043	2013-240-17:54:32.761	11	Co	148.1	1200
N1756212004	2013-238-11:43:54.999	-25	BH	128.8	1200
N1756427743a	2013-240-23:39:32.629	-7	C	150.1	1200
N1756427743b	2013-240-23:39:32.629	-23	C	150.1	1200
N1756218154	2013-238-13:26:24.960	-45	C	129.5	1200
N1756380961	2013-240-10:39:50.926	-2	C	145.6	1200
N1757255731	2013-250-13:39:15.371	13	Co	109.8	1200
N1757952511	2013-258-15:12:10.945	-1	C	94.8	1200

Table C.1.: Repeatedly observed features, grouped together and ordered by time of first appearance. Some new features have appeared on the second observation and these are given new designations, whilst others have disappeared or merged. The time between observations ranges from ~ 15 hours to ~ 6.7d. Classes are determined by visual appearance as classic (C), bright-headed classic (BH), complex (Co), or objects (O). Errors in θ are $\sim 2°$.

References

Albers, N., Sremcevic, M., Colwell, J. E., Esposito, L. W., 2012. Saturn's F ring as seen by Cassini UVIS: Kinematics and statistics. Icarus 217 (1), 367–388.

Attree, N. O., Murray, C. D., Cooper, N. J., Williams, G. A., 2012. Detection of low-velocity collisions In Saturn's F ring. ApL 755 (2), L27.

Attree, N. O., Murray, C. D., Williams, G. A., Cooper, N. J., 2014. A survey of low-velocity collisional features in Saturn's F ring. Icarus 227 (0), 56 – 66.

Ballouz, R.-L., Richardson, D. C., Michel, P., Schwartz, S. R., 2014. Rotation-dependent Catastrophic Disruption of Gravitational Aggregates. ApJ 789, 158.

Barbara, J. M., Esposito, L. W., 2002. Moonlet collisions and the effects of tidally modified accretion in Saturn's F ring. Icarus 160 (1), 161–171.

Benz, W., Asphaug, E., 1999. Catastrophic Disruptions Revisited. Icarus 142, 5–20.

Beurle, K., Murray, C. D., Williams, G. A., Evans, M. W., Cooper, N. J., Agnor, C. B., 2010. Direct evidence for gravitational instability and moonlet formation in Saturn's rings. ApL 718, L176–L180.

Bosh, A., Olkin, C., French, R., Nicholson, P., 2002. Saturn's F ring: Kinematics and particle sizes from stellar occultation studies. Icarus 157 (1), 57–75.

Braga-Ribas, F., Sicardy, B., Ortiz, J. L., Snodgrass, C., Roques, F., Vieira-Martins, R., Camargo, J. I. B., Assafin, M., Duffard, R., Jehin, E., Pollock, J., Leiva, R., Emilio, M., Machado, D. I., Colazo, C., Lellouch, E., Skottfelt, J., Gillon, M., Ligier, N., Maquet, L., Benedetti-Rossi, G., Gomes, A. R., Kervella, P., Monteiro, H., Sfair, R., El Moutamid, M., Tancredi, G., Spagnotto, J., Maury, A., Morales, N., Gil-Hutton, R., Roland, S., Ceretta, A., Gu, S.-H., Wang, X.-B., Harpsøe, K., Rabus, M., Manfroid, J., Opitom, C., Vanzi, L., Mehret, L., Lorenzini, L., Schneiter, E. M., Melia, R., Lecacheux, J., Colas, F., Vachier, F., Widemann, T., Almenares, L., Sandness, R. G., Char, F., Perez, V., Lemos, P., Martinez, N., Jørgensen, U. G., Dominik, M., Roig, F., Reichart, D. E., Lacluyze, A. P., Haislip, J. B., Ivarsen, K. M., Moore, J. P., Frank, N. R., Lambas, D. G., 2014. A ring system detected around the Centaur (10199) Chariklo. Nature 508, 72–75.

Bridges, F. G., Hatzes, A., lin, D., 1984. Structure, Stability And Evolution Of Saturns Rings. Nature 309 (5966), 333–335.

Burns, J. A., 1976. Elementary derivation of the perturbation equations of celestial mechanics. AmJPh 44, 944–949.

Burns, J. A., Hamilton, D. P., Showalter, M. R., 2001. Dusty Rings and Circumplanetary Dust: Observations and Simple Physics. Springer, p. 641.

Burns, J. A., Lamy, P. L., Soter, S., 1979. Radiation forces on small particles in the solar system. Icarus 40, 1–48.

Canup, R. M., Esposito, L. W., 1995. Accretion in the Roche zone - Coexistence of rings and ringmoons. Icarus 113 (2), 331–352.

Charnoz, S., 2009. Physical collisions of moonlets and clumps with the Saturn's F-ring core. Icarus 201 (1), 191–197.

Charnoz, S., Porco, C. C., Deau, E., Brahic, A., Spitale, J. N., Bacques, G., Baillie, K., 2005. Cassini discovers a kinematic spiral ring around Saturn. Science 310 (5752), 1300–1304.

Colwell, J. E., 2003. Low velocity impacts into dust: results from the COLLIDE-2 microgravity experiment. Icarus 164, 188–196.

Colwell, J. E., Nicholson, P. D., Tiscareno, M. S., Murray, C. D., French, R. G., Marouf, E. A., 2009. Saturn From Cassini-Huygens. Springer, Ch. 14.

Colwell, J. E., Sture, S., Cintala, M., Durda, D., Hendrix, A., Goudie, T., Curtis, D., Ashcom, D. J., Kanter, M., Keohane, T., Lemos, A., Lupton, M., Route, M., 2008. Ejecta from impacts at 0.2 2.3 m/s in low gravity. Icarus 195, 908–917.

Cooper, N. J., Murray, C. D., Attree, N. O., Williams, G. A., 2015. The morphology and dynamics of Saturns F ring: III. An analysis of the 2008 prominent jet. In Preparation.

Cooper, N. J., Murray, C. D., Williams, G. A., 2013. Local Variability in the Orbit of Saturn's F Ring. AJ 145, 161.

Cuzzi, J. N., Burns, J. A., 1988. Charged-particle depletion surrounding Saturns F-ring - evidence for a moonlet belt. Icarus 74 (2), 284–324.

Cuzzi, J. N., Durisen, R. H., 1990. Bombardment of planetary rings by meteoroids - General formulation and effects of Oort Cloud projectiles. Icarus 84, 467–501.

Cuzzi, J. N., Whizin, A. D., Hogan, R. C., Dobrovolskis, A. R., Dones, L., Showalter, M. R., Colwell, J. E., Scargle, J. D., 2014. Saturn's F Ring core: Calm in the midst of chaos. Icarus 232, 157–175.

Durda, D. D., Greenberg, R., Jedicke, R., 1998. Collisional Models and Scaling Laws: A New Interpretation of the Shape of the Main-Belt Asteroid Size Distribution. Icarus 135, 431–440.

Esposito, L. W., Albers, N., Meinke, B. K., Sremcevic, M., Madhusudhanan, P., Colwell, J. E., Jerousek, R. G., 2012. A predator-prey model for moon-triggered clumping in Saturn's rings. Icarus 217 (1), 103–114.

Esposito, L. W., Meinke, B. K., Colwell, J. E., Nicholson, P. D., Hedman, M. A., 2008. Moonlets and clumps in Saturn's F ring. Icarus 194 (1), 278–289.

French, R. S., Hicks, S. K., Showalter, M. R., Antonsen, A. K., Packard, D. R., 2014. Analysis of clumps in Saturn's F ring from Voyager and Cassini. Icarus 241, 200–220.

French, R. S., Showalter, M. R., Sfair, R., Argelles, C. A., Pajuelo, M., Becerra, P., Hedman, M. M., Nicholson, P. D., 2012. The brightening of Saturns F ring. Icarus 219 (0), 181–193.

Gehrels, T., Baker, L. R., Beshore, E., Blenman, C., Burke, J. J., Castillo, N. D., Dacosta, B., Degewij, J., Doose, L. R., Fountain, J. W., Gotobed, J., Kenknight, C. E., Kingston, R., McLaughlin, G., McMillan, R., Murphy, R., Smith, P. H., Stoll, C. P., Strickland, R. N., Tomasko, M. G., Wijesinghe, M. P., Coffeen, D. L., Esposito, L. W., 1980. Imaging photopolarimeter on Pioneer Saturn. Science 207, 434–439.

Goldreich, P., Rappaport, N., 2003a. Chaotic motions of prometheus and pandora. Icarus 162, 391–399.

Goldreich, P., Rappaport, N., 2003b. Origin of chaos in the Prometheus-Pandora system. Icarus 166, 320–327.

Goldreich, P., Tremaine, S., 1979. Towards a theory for the Uranian rings. Nature 277, 97–99.

Guimarães, A. H. F., Albers, N., Spahn, F., Seiß, M., Vieira-Neto, E., Brilliantov, N. V., 2012. Aggregates in the strength and gravity regime: Particles sizes in Saturn's rings. Icarus 220, 660–678.

Gundlach, B., Blum, J., 2015. The Stickiness of Micrometer-sized Water-ice Particles. ApJ 798, 34.

Hedman, M. M., Burns, J. A., Evans, M. W., Tiscareno, M. S., Porco, C. C., 2011a. Saturn's Curiously Corrugated C Ring. Science 332, 708–.

Hedman, M. M., Burns, J. A., Showalter, M. R., 2015. Corrugations and eccentric spirals in Saturn's D ring: New insights into what happened at Saturn in 1983. Icarus 248, 137–161.

Hedman, M. M., Burns, J. A., Showalter, M. R., Porco, C. C., Nicholson, P. D., Bosh, A. S., Tiscareno, M. S., Brown, R. H., Buratti, B. J., Baines, K. H., Clark, R., 2007. Saturn's dynamic D ring. Icarus 188, 89–107.

Hedman, M. M., Nicholson, P. D., Showalter, M. R., Brown, R. H., Buratti, B. J., Clark, R. N., Baines, K., Sotin, C., 2011b. The Christiansen Effect in Saturn's narrow dusty rings and the spectral identification of clumps in the F ring. Icarus 215, 695–711.

Heißelmann, D., Blum, J., Fraser, H. J., Wolling, K., 2010. Microgravity experiments on the collisional behavior of saturnian ring particles. Icarus 206, 424–430.

Hill, C. R., Heißelmann, D., Blum, J., Fraser, H. J., 2015. Collisions of small ice particles under microgravity conditions. A&A 573 (A49), 11.

Hill, G. W., 1878. Researches in the lunar theory. AmJM 1 (1), pp. 5–26.

Høg, E., Fabricius, C., Makarov, V. V., Urban, S., Corbin, T., Wycoff, G., Bastian, U., Schwekendiek, P., Wicenec, A., 2000. The Tycho-2 catalogue of the 2.5 million brightest stars. A&A 355, L27–L30.

Hyodo, R., Ohtsuki, K., 2014. Collisional Disruption of Gravitational Aggregates in the Tidal Environment. ApJ 787, 56.

Karjalainen, R., 2007. Aggregate impacts in Saturn's rings. Icarus 189 (2), 523–537.

Korycansky, D. G., Asphaug, E., 2006. Low-speed impacts between rubble piles modeled as collections of polyhedra. icarus 181, 605–617.

Korycansky, D. G., Asphaug, E., 2009. Low-speed impacts between rubble piles modeled as collections of polyhedra, 2. Icarus 204, 316–329.

Leinhardt, Z. M., Richardson, D. C., Quinn, T., 2000. Direct N-body Simulations of Rubble Pile Collisions. Icarus 146, 133–151.

Markwardt, C. B., 2009. Non-linear Least-squares Fitting in IDL with MPFIT. In: Bohlender, D. A., Durand, D., Dowler, P. (Eds.), Astronomical Data Analysis Software and Systems XVIII. Vol. 411 of Astronomical Society of the Pacific Conference Series. p. 251.

Marouf, E., Wong, K., French, R., Rappaport, N. J., McGhee, C., 2010. Saturn's F-Ring Discontinuous Core and Orbit Model. In: 38th COSPAR Scientific Assembly. Vol. 38 of COSPAR Meeting. p. 699.

Marouf, E. A., Tyler, G. L., Rosen, P. A., 1986. Profiling Saturn's rings by radio occultation. Icarus 68, 120–166.

McGhee, C. A., Nicholson, P. D., French, R. G., Hall, K. J., 2001. HST observations of saturnian satellites during the 1995 ring plane crossings. Icarus 152 (2), 282–315.

Meinke, B. K., Esposito, L. W., Albers, N., Sremevi, M., 2012. Classification of F ring features observed in Cassini UVIS occultations. Icarus 218 (1), 545 – 554.

Melosh, H. J., 1989. Impact cratering: A geologic process. Oxford University Press.

Murray, C. D., Beurle, K., Cooper, N. J., Evans, M. W., Williams, G. A., Charnoz, S., 2008. The determination of the structure of Saturn's F ring by nearby moonlets. Nature 453 (7196), 739–744.

Murray, C. D., Chavez, C., Beurle, K., Cooper, N., Evans, M. W., Burns, J. A., Porco, C. C., 2005. How Prometheus creates structure In Saturn's F ring. Nature 437 (7063), 1326–1329.

Murray, C. D., Cooper, N. J., Williams, G. A., Attree, N. O., Boyer, J. S., 2014. The discovery and dynamical evolution of an object at the outer edge of Saturn's A ring. Icarus 236, 165–168.

Murray, C. D., Dermott, S. F., 1999. Solar System Dynamics. Cambridge University Press.

Murray, C. D., Giuliatti Winter, S. M., 1996. Periodic collisions between the moon Prometheus and Saturn's F ring. Nature 380, 139–141.

Nakazawa, K., Ida, S., 1988. Chapter 15. Hill's Approximation in the Three-Body Problem. PTnPS 96, 167–174.

Ohtsuki, K., 1993. Capture probability of colliding planetesimals - Dynamical constraints on accretion of planets, satellites, and ring particles. Icarus 106, 228.

Ohtsuki, K., Yasui, Y., Daisaka, H., 2013. Accretion Rates of Moonlets Embedded in Circumplanetary Particle Disks. AJ 146, 25.

Ortiz, J. L., Duffard, R., Pinilla-Alonso, N., Alvarez-Candal, A., Santos-Sanz, P., Morales, N., Fernández-Valenzuela, E., Licandro, J., Campo Bagatin, A., Thirouin, A., 2015. Possible ring material around centaur (2060) Chiron. A&A 576, A18.

Porco, C. C., Baker, E., Barbara, J., Beurle, K., Brahic, A., Burns, J. A., Charnoz, S., Cooper, N., Dawson, D. D., Del Genio, A. D., Denk, T., Dones, L., Dyudina, U., Evans, M. W., Giese, B., Grazier, K., Helfenstein, P., Ingersoll, A. P., Jacobson, R. A., Johnson, T. V., McEwen, A., Murray, C. D., Neukurn, G., Owen, W. M., Perry, J., Roatsch, T., Spitale, J., Squyres, S., Thomas, P., Tiscareno, M., Turtle, E., Vasavada, A. R., Veverka, J., Wagner, R., West, R., 2005. Cassini imaging science: Initial results on Saturn's rings and small satellites. Science 307 (5713), 1226–1236.

Porco, C. C., West, R. A., Squyres, S., McEwen, A., Thomas, P., Murray, C. D., Del Genio, A., Ingersoll, A. P., Johnson, T. V., Neukum, G., Veverka, J., Dones, L., Brahic, A., Burns, J. A., Haemmerle, V., Knowles, B., Dawson, D., Roatsch, T., Beurle, K., Owen, W., 2004. Cassini Imaging Science: Instrument Characteristics And Anticipated Scientific Investigations At Saturn. SSRv 115, 363–497.

Rein, H., Liu, S.-F., 2012. REBOUND: An open-source multi-purpose N-body code for collisional dynamics. A&A 537, A128.

Rein, H., Tremaine, S., 2011. Symplectic integrators in the shearing sheet. MNRAS 415, 3168–3176.

Richardson, D. C., 1994. Tree code simulations of planetary rings. MNRAS 269 (2), 493–511.

Scharringhausen, B. R., Nicholson, P. D., 2013. The vertical structure of the F ring of Saturn from ring-plane crossings. Icarus 226, 1275–1293.

Schwartz, S. R., Richardson, D. C., Michel, P., 2012. An implementation of the soft-sphere discrete element method in a high-performance parallel gravity tree-code. Granular Matter 14, 363–380.

Shimaki, Y., Arakawa, M., 2012. Low-velocity collisions between centimeter-sized snowballs: Porosity dependence of coefficient of restitution for ice aggregates analogues in the Solar System. Icarus 221, 310–319.

Showalter, M. R., 1998. Detection of centimeter-sized meteoroid impact events in Saturn's F ring. Science 282, 1099.

Showalter, M. R., 2004. Disentangling Saturn's F Ring. I. Clump orbits and lifetimes. Icarus 171, 356–371.

Showalter, M. R., Burns, J. A., 1982. A numerical study of Saturn's F-ring. Icarus 52, 526–544.

Showalter, M. R., Hedman, M. M., Burns, J. A., 2011. The Impact of Comet Shoemaker-Levy 9 Sends Ripples Through the Rings of Jupiter. Science 332, 711–.

Showalter, M. R., Pollack, J. B., Ockert, M. E., Doyle, L. R., Dalton, J. B., 1992. A photometric study of Saturn's F Ring. Icarus 100, 394–411.

Smith, B. A., Soderblom, L., Batson, R. M., Bridges, P. M., Inge, J. L., Masursky, H., Shoemaker, E., Beebe, R. F., Boyce, J., Briggs, G., Bunker, A., Collins, S. A., Hansen, C., Johnson, T. V., Mitchell, J. L., Terrile, R. J., Cook, A. F., Cuzzi, J. N., Pollack, J. B., Danielson, G. E., Ingersoll, A. P., Davies, M. E., Hunt, G. E., Morrison, D., Owen, T., Sagan, C., Veverka, J., Strom, R., Suomi, V. E., 1982. A new look at the Saturn system - The Voyager 2 images. Science 215, 504–537.

Smith, B. A., Soderblom, L., Beebe, R. F., Boyce, J. M., Briggs, G., Bunker, A., Collins, S. A., Hansen, C., Johnson, T. V., Mitchell, J. L., Terrile, R. J., Carr, M. H., Cook, A. F., Cuzzi, J. N., Pollack, J. B., Danielson, G. E., Ingersoll, A. P., Davies, M. E., Hunt, G. E., Masursky, H., Shoemaker, E. M., Morrison, D., Owen, T., Sagan, C., Veverka, J., Strom, R., Suomi, V. E., 1981. Encounter with Saturn - Voyager 1 imaging science results. Science 212, 163–191.

Stewart, S. T., Leinhardt, Z. M., 2009. Velocity-Dependent Catastrophic Disruption Criteria for Planetesimals. ApL 691, L133–L137.

Supulver, K. D., Bridges, F. G., Lin, D. N. C., 1995. The coefficient of restitution of ice particles in glancing collisions: Experimental results for unfrosted surfaces. Icarus 113, 188–199.

Supulver, K. D., Bridges, F. G., Tiscareno, S., Lievore, J., Lin, D. N. C., 1997. The Sticking Properties of Water Frost Produced under Various Ambient Conditions. Icarus 129, 539–554.

Tiscareno, M. S., 2013. Planetary Rings. Springer, p. 309.

Tiscareno, M. S., Burns, J. A., Hedman, M. M., Porco, C. C., Weiss, J. W., Dones, L., Richardson, D. C., Murray, C. D., 2006. 100-metre-diameter moonlets in Saturn's A ring from observations of 'propeller' structures. Nature 440, 648–650.

Tiscareno, M. S., Burns, J. A., Hedman, M. M., Spitale, J. N., Porco, C. C., Murray, C. D., Cassini Imaging Team, 2005. Wavy Edges and Other Disturbances in Saturn's Encke and Keeler Gaps. In: AAS/Division for Planetary Sciences Meeting Abstracts #37. Vol. 37 of Bulletin of the American Astronomical Society. p. 767.

Tiscareno, M. S., Mitchell, C. J., Murray, C. D., Di Nino, D., Hedman, M. M., Schmidt, J., Burns, J. A., Cuzzi, J. N., Porco, C. C., Beurle, K., Evans, M. W., 2013. Observations of Ejecta Clouds Produced by Impacts onto Saturn's Rings. Science 340, 460–464.

Vahidinia, S., Cuzzi, J. N., Hedman, M., Draine, B., Clark, R. N., Roush, T., Filacchione, G., Nicholson, P. D., Brown, R. H., Buratti, B., Sotin, C., 2011. Saturn's F ring grains: Aggregates made of crystalline water ice. Icarus 215, 682–694.

Walsh, K. J., Richardson, D. C., 2003. Direct N-body Simulations of Rubble Pile Collisions in Strong Tidal Fields: Applied to Saturn's F Ring. In: AAS/Division for Planetary Sciences Meeting Abstracts #35. Vol. 35 of Bulletin of the American Astronomical Society. p. 1486.

Williams, G. A., 2009. The three body problem applied to close ring-satellite encounters. Ph.D. thesis, Queen Mary, University of London.

Winter, O. C., Mourão, D. C., Giuliatti Winter, S. M., Spahn, F., da Cruz, C., 2007. Moonlets wandering on a leash-ring. MNRAS 380, L54–L57.

Zacharias, N., Urban, S. E., Zacharias, M. I., Wycoff, G. L., Hall, D. M., Monet, D. G., Rafferty, T. J., 2004. The Second US Naval Observatory CCD Astrograph Catalog (UCAC2). AJ 127, 3043–3059.

Zappalà, V., Cellino, A., Dell'oro, A., Migliorini, F., Paolicchi, P., 1996. Reconstructing the Original Ejection Velocity Fields of Asteroid Families. Icarus 124, 156–180.